Dissolution Behaviour of Innovative Inert Matrix Fuels for Recycling of Minor Actinides

Elena Laura Mühr-Ebert

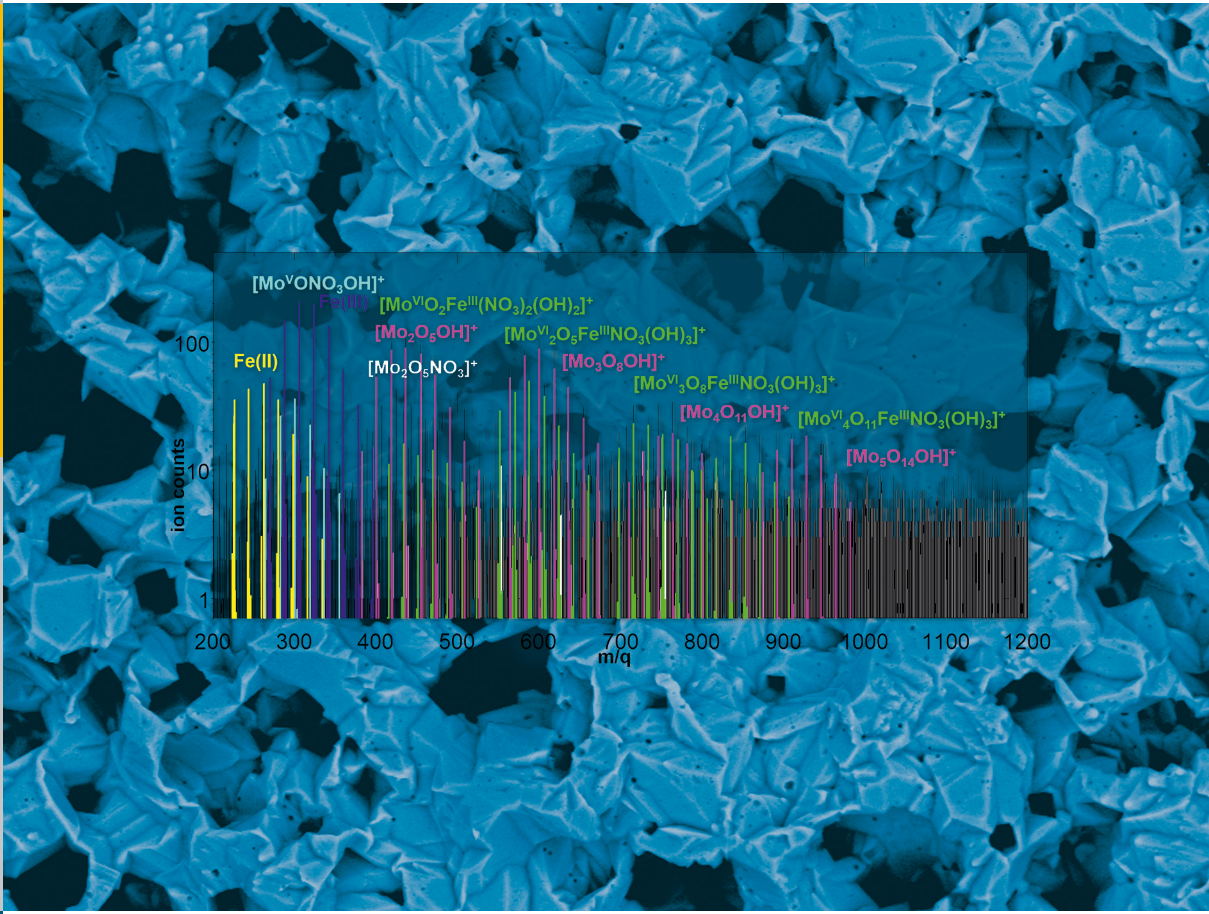

Energie & Umwelt / Energy & Environment
Band / Volume 378
ISBN 978-3-95806-238-2

JÜLICH
FORSCHUNGSZENTRUM

Schriften des Forschungszentrums Jülich
Reihe Energie & Umwelt / Energy & Environment Band / Volume 378

Forschungszentrum Jülich GmbH
Institut für Energie- und Klimaforschung
Nukleare Entsorgung und Reaktorsicherheit (IEK-6)

Dissolution Behaviour of Innovative Inert Matrix Fuels for Recycling of Minor Actinides

Elena Laura Mühr-Ebert

Schriften des Forschungszentrums Jülich
Reihe Energie & Umwelt / Energy & Environment Band / Volume 378

ISSN 1866-1793 ISBN 978-3-95806-238-2

Bibliographic information published by the Deutsche Nationalbibliothek.
The Deutsche Nationalbibliothek lists this publication in the Deutsche
Nationalbibliografie; detailed bibliographic data are available in the
Internet at http://dnb.d-nb.de.

Publisher and Distributor: Forschungszentrum Jülich GmbH
Zentralbibliothek
52425 Jülich
Tel: +49 2461 61-5368
Fax: +49 2461 61-6103
Email: zb-publikation@fz-juelich.de
www.fz-juelich.de/zb

Cover Design: Grafische Medien, Forschungszentrum Jülich GmbH

Printer: Grafische Medien, Forschungszentrum Jülich GmbH

Schriften des Forschungszentrums Jülich
Reihe Energie & Umwelt / Energy & Environment, Band / Volume 378

D 82 (Diss. RWTH Aachen University, 2017)

ISSN 1866-1793
ISBN 978-3-95806-238-2

The complete volume is freely available on the Internet on the Jülicher Open Access Server (JuSER)
at www.fz-juelich.de/zb/openaccess.

Die Neugier steht immer an erster Stelle des Problems, das gelöst werden will.

Galileo Galilei

Abstract

During the peaceful use of nuclear energy high level wastes, which contain long-lived radionuclides (plutonium, minor actinides) with high radiotoxicity, are generated worldwide. About 10,000 t of spent fuel are unloaded from commercial reactors each year. Most countries including Germany favour the direct disposal of spent fuel in deep geological formations. Other countries prefer the reprocessing of the spent fuel to recycle uranium and plutonium. In Europe commercial reprocessing is currently performed in La Hague and Sellafield. A future alternative would be provided by closing the fuel cycle in the context of the partitioning and transmutation strategy (P&T). This method separates and converts the long-lived radionuclides into stable or short-lived nuclides via neutron induced reactions in dedicated facilities. The P&T strategy has potential to significantly reduce the radiotoxicity and the volume of the radioactive waste; however it cannot obviate the need of a final repository. The transmutation of minor actinides can be performed in different reactor types, including accelerator driven systems, which consist of a subcritical reactor core and an external accelerator. The accelerator driven system (ADS) fuel consists of the fissile material (AnO_2) which is spread in an inert matrix to improve the thermal properties of the fuel. Within this work two different fuels containing actinide oxides as fissile material and ceramic magnesium oxide (CerCer) or metallic molybdenum (CerMet) as matrix material are under investigation. The dissolution and separation issues for inert matrix fuels (IMF) have not yet been investigated coherently. It is of crucial importance to take into account the behaviour of the matrix elements in the dissolution and separation processes and to check their compatibility with future waste management requirements. The dissolution and the subsequent hydro or pyrometallurgical treatment of the fuel are crucial steps in the reprocessing process.

A complete dissolution of the actinide oxide and the matrix material, or a selective dissolution, where one of the components remains undissolved, can be considered. To investigate the reprocessability of molybdenum and magnesia based inert matrix fuels reference samples containing variable amounts of CeO_2, which serves as surrogate for plutonium dioxide, have been prepared based on a comprehensive compactibility and sinterability investigation. The pellets were thoroughly characterized by means of density measurements, micro hardness measurements, scanning electron microscopy (SEM) investigation, and X-ray diffraction (XRD). The dissolution rate was studied in macroscopic experiments as a function of acid concentration and temperature.

Magnesium oxide is soluble even under mild conditions. The dissolution rates of MgO at different acid concentrations are rather similar, whereas the dissolution rate is strongly dependent on the temperature. Additionally, the MgO dissolution process was investigated following a microscopic approach. Detailed SEM investigations show a heterogeneous reactivity of the MgO pellet's surface. A model was developed to describe the evolution of the pellet surface area and a surface normalized dissolution rate was calculated. The activation energies of MgO dissolution in nitric acid have been calculated from the Arrhenius plot for different acid concentrations and indicate a surface controlled dissolution mechanism. During the dissolution of MgO/CeO_2 pellets the MgO dissolves completely, while the bulk of CeO_2 remains undissolved, allowing a separation of the actinides and the matrix during the dissolution process.

The dissolution of molybdenum is more complex due to its specific aqueous redox chemistry (Mo(-II) – Mo(VI)). Molybdenum metal is soluble in nitric acid. However, it is oxidized to MoO_3, which then precipitates. The dissolution rate strongly depends on the acid concentration. Higher acid concentrations or temperatures result in faster dissolution but also in more precipitation. The addition of ferric nitrate to the acid improves the dissolution properties and prevents precipitations at low acid concentrations. However, the addition of a great amount of Fe^{3+} to the solution might influence the extraction process. To get closer to the real system, unirradiated PuO_2/Mo pellets were dissolved in collaboration with NRG and the Karlsruher Institut für Technologie, Institut für Nukleare Entsorgung. The presence of Fe(III) increases the solubility of Mo as described above, while the solubility of the actinides is decreased. In 1 and 3 mol/L HNO_3 without the addition of iron about 2 and 3% of the plutonium dissolved respectively, while less than 0.1% of the Pu dissolved in the presence of iron.

Dissolution in nitric acid is the first step in the head end of the reprocessing of spent fuel. Therefore, detailed knowledge of the speciation of molybdenum in nitric acid medium is crucial on the one hand to understand this dissolution process and on the other hand as a basis for the design of a tailored extraction process. The solution species of Mo in strongly acidic media have been characterized and quantified comprehensively. For this purpose electrospray ionization mass spectrometry (ESI-MS), which can probe the stoichiometry and relative abundances of solution species, was applied in collaboration with the Leibniz Universität Hannover, Institut für Radioökologie und Strahlenschutz. The method delivers unique insights into the solution speciation of molybdenum as a function of acid- and Fe(III)-concentration. The solution species Mo forms in the presence of iron were investigated in order to understand the effect of Fe(III) on the dissolution. The ESI-MS reveals the formation of mixed Mo-Fe species which explains the increased solubility. Moreover, a method to analyse solutions of molybdenum with natural isotopic composition with a commercially available ESI/MS/MS instrument (QTrap) was developed in collaboration with the Forschungszentrum Jülich, Zentralinstitut für Engineering, Elektronik und Analytik 3. The commercial instrument permits routine measurements due to significantly reduced measurement times.

As an alternative to the very complex dissolution of Mo based IMF the separation of the matrix material from the fuel by thermal treatment was considered. This exploits that molybdenum is oxidized in air at temperatures from 400 °C and the resulting MoO_3 sublimes at 800 °C. It is expected that the volatile components of the fuel are not deposited together with the molybdenum and the remaining components of the fuel do not evaporate at these temperatures. Molybdenum was quantitatively evaporated and recovered as MoO_3, confirmed by XRD. In the case of thermal treatment of Mo/CeO_2 mixtures a solid state reaction of MoO_3 and CeO_2 occurs at 674 °C. Depending on the temperature and Mo-Ce ratio $CeMo_5O_8$, $Ce_8Mo_{12}O_{49}$, and $Ce_2Mo_4O_{15}$ form. In the case of thermal treatment of Mo/PuO_2 mixtures at equivalent conditions a mixed oxide $PuMo_2O_8$ is expected to form, which will affect the evaporation in a way similar to the MoO_3 and CeO_2 solid state reaction. However, the bulk of the Mo should be evaporated and the mixed oxide $PuMo_2O_8$ can be easily dissolved in nitric acid. The thermal treatment of the fuel is a promising method for the separation of the bulk molybdenum to simplify the dissolution and minimize the effect on the liquid-liquid extraction.

Kurzzusammenfassung

Bei der friedlichen Nutzung der Kernenergie fallen weltweit hochradioaktive Abfälle an, die langlebige Radionuklide (Plutonium, Minore Actinide) mit hoher Radiotoxizität enthalten. Über 10.000 t abgebrannter Brennelemente werden jährlich aus kommerziellen Reaktoren entladen. Die meisten Länder, darunter Deutschland, bevorzugen die direkte Endlagerung abgebrannter Brennelemente in tiefen geologischen Formationen. Andere Länder bevorzugen die Wiederaufbereitung des verbrauchten Brennstoffs, um Uran und Plutonium zu recyceln. Eine zukünftige Alternative wäre die Schließung des Brennstoffkreislaufs im Rahmen der Partitioning- und Transmutationsstrategie (P&T). Diese Methode trennt und wandelt die langlebigen Radionuklide über neutroneninduzierte Reaktionen in entsprechenden Einrichtungen in stabile, kurzlebige Nuklide um. Die P&T-Strategie hat Potenzial, die Radiotoxizität und das Volumen der radioaktiven Abfälle zu verringern; kann aber nicht die Notwendigkeit des Endlagers erübrigen. Die Umwandlung von Minoren Actiniden kann in verschiedenen Reaktortypen, einschließlich beschleunigergetriebenen Systemen, die aus einem unterkritischen Reaktorkern und einem externen Beschleuniger bestehen, durchgeführt werden. Der Brennstoff für beschleunigergetriebene Systeme besteht aus dem spaltbaren Material (AnO_2), das in einer inerten Matrix verteilt wird, um die thermischen Eigenschaften des Brennstoffs zu verbessern. Im Rahmen dieser Arbeit werden zwei verschiedene Brennstoffe, die Actinidenoxide als spaltbares Material und keramisches Magnesiumoxid (CerCer) oder metallisches Molybdän (CerMet) als Matrixmaterial enthalten, untersucht. Die Auflösung und Trennung von Inertmatrixbrennstoffen (IMF) wurde bisher nicht umfassend untersucht. Es ist von entscheidender Bedeutung, das Verhalten der Matrixelemente bei der Auflösung und Abtrennung und ihre Kompatibilität mit zukünftigen Immobilisierungsmethoden zu berücksichtigen. Die Auflösung und die anschließende hydro- oder pyrometallurgische Behandlung des Brennstoffs sind entscheidende Schritte des Wiederaufbereitungsprozesses.

Eine vollständige Auflösung der Actinidenoxide und des Matrixmaterials oder eine selektive Auflösung eines Bestandteils können in Betracht gezogen werden. Um die Reprozessierbarkeit von Mo- und MgO-basierten IMF zu untersuchen, wurden Referenzproben, die unterschiedliche Mengen von CeO_2 enthalten, das als Surrogat für PuO_2 dient, auf der Grundlage einer umfassenden Verdichtbarkeits- und Sinterfähigkeitsstudie hergestellt. Die Pellets wurden mit Hilfe von Dichtemessungen, Mikrohärtemessungen, REM-Untersuchung und XRD umfassend charakterisiert. Die Auflösungsgeschwindigkeit wurde in makroskopischen Experimenten als Funktion der Säurekonzentration und der Temperatur untersucht. Magnesiumoxid ist bereits unter milden Bedingungen löslich. Die Auflösungsraten von MgO bei verschiedenen Säurekonzentrationen sind relativ ähnlich, während sie stark von der Temperatur abhängen. Zusätzlich wurde der Auflösungsprozess mit einem mikroskopischen Ansatz untersucht. Detaillierte REM-Untersuchungen zeigen eine heterogene Reaktion der Pelletoberfläche, zu deren Beschreibung ein Modell entwickelt wurde. Die mittels Arrhenius-Plot berechnete Aktivierungsenergie der Auflösung von MgO in Salpetersäure weist auf eine oberflächenkontrollierte Auflösung hin. Während der Auflösung von MgO/CeO_2 Pellets löst sich MgO vollständig, indessen bleibt der Großteil des CeO_2 (> 99%) ungelöst; sodass eine Trennung der Actiniden und der Matrix während der Auflösung erreicht wird. Die Auflösung von Mo ist aufgrund seiner

spezifischen wässrigen Redoxchemie (Mo -II - + VI) komplexer. Molybdänmetall ist in HNO_3 löslich, wird jedoch zu MoO_3 oxidiert, welches dann ausfällt. Die Auflösungsgeschwindigkeit ist stark abhängig von der Säurekonzentration und der Temperatur. Deren Erhöhung führt nicht nur zu einer schnelleren Auflösung, sondern auch zu vermehrter Niederschlagsbildung. Die Zugabe von Eisen(III)-Nitrat zu der Säure verbessert die Auflösungseigenschaften und verhindert die Niederschlagsbildung, kann allerdings den Extraktionsprozess beeinflussen. Um eine weitere Annäherung an das reale System zu erreichen, wurden in Zusammenarbeit mit NRG und dem Karlsruher Institut für Technologie, Institut für Nukleare Entsorgung Auflösungsversuche an unbestrahlten Mo/PuO_2 Pellets durchgeführt. Die Anwesenheit von Eisen erhöht die Löslichkeit von Molybdän, während die Löslichkeit der Actiniden verringert wird. In 1 bzw. 3 mol/L HNO_3 ohne die Zugabe von Eisen lösen sich etwa 2 bzw. 3% des Plutoniums, während sich in Gegenwart von Fe weniger als 0.1% des Pu lösen.

Die Auflösung in Salpetersäure ist der erste Schritt in der Wiederaufarbeitung abgebrannter Brennelemente. Daher ist eine detaillierte Kenntnis der Speziation von Mo in HNO_3 entscheidend, auf der einen Seite um die Auflösung zu verstehen und andererseits als Basis für den Entwurf eines maßgeschneiderten Extraktionsverfahrens. Die Molybdänspezies in stark sauren Medien wurden umfassend charakterisiert und quantifiziert. Hierzu diente die Elektrosprayionisations-Massenspektrometrie (ESI-MS), welche die Stöchiometrie und die relativen Häufigkeiten der Spezies in Lösung ermitteln kann, in Zusammenarbeit mit der Leibniz Universität Hannover, Institut für Radioökologie und Strahlenschutz. Das Verfahren lieferte einzigartige Einblicke in die Speziation von Mo in Lösung als Funktion der Säure- und Fe(III)-Konzentration. Die in Gegenwart von Eisen gebildeten Mo-Spezies wurden untersucht, um die Wirkung von Fe(III) auf den Prozess zu verstehen. Die ESI-MS offenbart die Bildung von gemischten Mo-Fe Spezies, was die erhöhte Löslichkeit erklärt. Außerdem wurde in Zusammenarbeit mit dem Forschungszentrum Jülich, Zentralinstitut für Engineering, Elektronik und Analytik 3 ein Verfahren entwickelt, um Lösungen von Mo mit natürlicher Isotopenzusammensetzung mit einem handelsüblichen Instrument (QTrap) analysieren zu können.

Als Alternative zu der sehr komplexen Auflösung der Mo-basierten IMF wurde die Möglichkeit der Abtrennung des Molybdäns durch thermische Behandlung betrachtet. Dabei wird ausgenutzt, dass Mo an Luft bei Temperaturen ab 400 °C oxidiert wird und das erhaltene MoO_3 bei 800 °C sublimiert. Es wird erwartet, dass die flüchtigen Bestandteile des Brennstoffes sich nicht zusammen mit dem Mo abscheiden und die übrigen Komponenten der Brennelemente nicht bei diesen Temperaturen verdampfen. Molybdän wurde quantitativ verdampft und als blassgelbe Kristalle zurückgewonnen, die mittels XRD als MoO_3 identifiziert wurden. Im Fall der thermischen Behandlung von Mo/CeO_2-Gemischen erfolgt bei 674 °C eine Festkörperreaktion zwischen MoO_3 und CeO_2. In Abhängigkeit von der Temperatur und dem Mo-Ce-Verhältnis bilden sich $CeMo_5O_8$, $Ce_8Mo_{12}O_{49}$ und $Ce_2Mo_4O_{15}$. Für Mo/PuO_2-Mischungen wird bei äquivalenten Bedingungen die Bildung eines ein Mischoxids $PuMo_2O_8$ erwartet, welche die Verdampfung in ähnlicher Weise beeinflussen wird. Der Großteil des Mo sollte dennoch verdampften, und $PuMo_2O_8$ kann leicht in Salpetersäure aufgelöst werden. Die thermische Behandlung ist eine vielversprechende Methode zur Abtrennung des Molybdäns, um dessen Einfluss auf die Flüssig-Flüssig-Extraktion zu minimieren.

Content

List of Abbreviations

%TD	quotient of the theoretical density in percent
a	lattice parameter a
a.u.	arbitrary unit
AcN	acetonitrile
ADS	accelerator driven system
An	actinide
ANKA	Angströmquelle Karlsruhe
ASGARD	advanced fuels for generation IV reactors: reprocessing and dissolution
b	lattice parameter b
BET	Brunauer Emmett Teller: method of specific surface area measurement
B_i	brittleness index
c	lattice parameter c
CCD	charge coupled device
CDTA	cyclohexylenedinitrilotetraacetic acid
CE	collision energy
CerCer	ceramic ceramic
CerMet	ceramic metal
CHON	carbon, hydrogen, oxygen and nitrogen
c_i	average length of cracks
CN	coordination number
COEX^{TM}	co-extraction of actinides
cps	counts per second
CYANEX	registered trademark of Cytec Inc.
d	average length of the diagonals of the Vickers indents
D	diameter
D	distribution ratio
D2EHPA	di-2-ethylhexyl phosphate
D_{av}	average grain size
DIAMEX	diamide extraction
D_{max}	maximal diameter
DMDBTDMA	N,N’-dimethyl-N,N’-dibutyltetradecylmalonamide
DMDOHEMA	N,N’-dimethyl-N,N’-dioctylhexylethoxymalonamide
D_{min}	minimal diameter
DP	declustering potential
DSC	differential scanning calorimetry
E	young’s modulus
EDX	energy-dispersive X-ray spectroscopy
EFIT	european facility for industrial transmutation
eq.	equivalent
ESI	electrospray ionization

EUROTRANS	european research programme for the transmutation of high level nuclear waste in an accelerator driven system
EXAFS	extended X-ray absorption fine structure
F	load
fcc	face centred cubic
FP	fission products
FR	fast reactor
g	surface tension
GANEX	group actinide extraction process
h	height
HAW	high active waste
HLLW	high level liquid waste
HLW	high level waste
HTR	high temperature reactor
H_V	micro hardness
I	ionic strength
ICP	inductive coupled plasma mass spectrometry
IEK-6	Institut für Energie- und Klimaforschung, Nukleare Entsorgung und Reaktorsicherheit, within the Forschungszentrum Jülich GmbH
IMF	inert matrix fuel
Inc.	incorporation
IS	ionspray voltage
K_{1c}	fracture toughness
KIT-INE	Institute für Nukleare Entsorgung (INE) within the Karlsruher Institut für-Technologie (KIT)
LLFP	long lived fission products
Ln	lanthanides
LUH-IRS	Institut für Radioökologie und Strahlenschutz at the Leibnitz Universität Hannover
LWR	light water reactor
m	mass
M	mol/L
m/z	mass to charge ratio
MA	minor actinides (Np, Am, Cm)
MCA	accumulation of several mass spectra
MOX	mixed oxide fuel
MS	mass spectrometry
MWe	megawatt electrical
n	number of sides of the grain
NRG	Nuclear Research and Consultancy Group
OS	oxidation state
P	pressure
P&C	partitioning and conditioning

P&T	partitioning and transmutation
$\mathrm{P_C}$	compaction pressure
P_{opt}	optimal pressure
PUREX	plutonium-uranium-recovery by extraction
PWR	pressurized water reactor
Q	quadrupole
r_{At}	atomic radius
RT	room temperature
SANEX	selective actinide extraction
SEM	scanning electron microscope
SI	saturation index
SiC	silicon carbide
SLFP	short lived fission products
SSD	silicon drift detector
t	time
T	temperature
T_b	boiling point
TBP	tri-n-butyl-phosphate
T_c	calcination temperature
TG	thermogravimetry
T_m	melting point
TODGA	N,N,N’,N’-tetraoctyldiglocylamide
ToF	time of flight
TPH	hydrogenated tetrapropene
TRISO	tristructural-isotropic
TRU	transuranium elements
T_S	sintering temperature
TW·h	terra watt hours
UOX	uranium dioxide
V	volume
vol.%	percent by volume
VSI	vertical scanning interferometry
wt.%	percent by weight
XAFS	X-ray absorption fine structure
XANES	X-ray absorption near edge structure
XRD	X-ray diffraction
XT-ADS	experimental facility demonstrating the technical feasibility of transmutation in ADS
Z	atomic number
z	charge
β	angle ≠ 90° in the monoclinic system
λ	wavelength
ρ_G	green density

ρ_{geo}	geometrical density
ρ_S	sintered density
$\rho(H_2O)$	density of water
$\rho(liq)$	density of a liquid
$\rho(p)$	density of paraffin

1 Introduction and Background

1.1 The Role of Nuclear Energy

The increasing economic growth of the developing countries in the last decades has led to a rapid increase in world energy consumption. A trend which is expected to further increase in the near future.[1] With 12.7 billion tons of oil equivalent the world energy consumption was almost twice as high in 2010 as at the beginning of the seventies, according to the International Energy Agency (IEA)[2]. The industrialized countries (OECD) currently account for 45% of global energy consumption, the newly industrialized countries for 9%, and the developing and emerging countries account for 46%.[3] The most important source of energy is oil (32%) prior to coal (27%) and gas (22%). Renewable energies cover almost 13% of global energy consumption. Nuclear energy has a share of almost 6%. In 2050 the world will consume 44.6 billion tons of oil equivalents. About two-thirds of the increase will come from developing countries where the economic and population growth is the highest. In OECD countries, however, stagnating energy consumption and the observable trend that more and more is set to natural gas and renewable energy. Fossil fuels will continue to dominate in the power supply and cover about 75% of the projected increase in primary energy consumption. The share of nuclear power (7%) rises slightly, while that of hydropower remains almost constant. Other renewable energy sources such as geothermal, solar and wind energy grow faster than all other energy sources. Nevertheless, they will cover only about 25% of the world’s electricity generation in 2040.[1] Concerns about environmental protection have additionally extended the demand for more efficient management and environmentally sound and sustainable development of nuclear energy. Appropriate management of radioactive waste arising at the back end of the fuel cycle is regarded as a crucial issue of long term environmental burden with respect to the nuclear fuel cycle.[4] In 2014 there were 435 reactors operating in 30 countries with a total generating capacity of 2359 terawatt-hours (TW·h). A further 72 units were under construction.[5] Whether the harmful components of this waste can be isolated from the biosphere for at least tens of thousands of years or even longer is the basis of environmental concerns. The reduction of waste volume and radiotoxicity is expected to be obtained with the development of Generation IV nuclear systems, which would allow closing the fuel cycle.[4] The solution of the nuclear waste problem plays an important role in the future of nuclear energy. This is especially true for the high level radioactive waste (HLW).

1.2 The Nuclear Fuel Cycle

The nuclear fuel cycle is a series of industrial processes, which involve the production of electricity from uranium in nuclear power reactors. It consists of front-end activities (mining, conversion, enrichment, and fabrication) and back-end activities of the nuclear waste management, as shown in Figure 1.

The nuclear fuel cycle starts with the mining of uranium ore. The uranium ore content is increased from a few tenth of percent (in the ore) to 85-95% (in a semi-refined concentrate known as "yellowcake"), while eliminating other elements that are present (the "tailings"), in mills, which are located near the mines. While very high grade pitchblende deposits can be concentrated by physical techniques involving their specific gravity, most concentration of uranium involves chemical leaching from the ore. For this purpose, the ore is crushed and roasted (to destroy organic material), chemically leached, followed by a separation of the liquids and solids, and finally concentrated/purified for final product recovery. The normal choice for chemical leaching is sulfuric acid; for ores with high carbonate content, an alkaline leach with sodium carbonate is used to prevent high acid consumption. Since only U(VI) is dissolved, any U(IV) present must be oxidized prior to leaching. After leaching a purification/concentration is performed by ion exchange or solvent extraction. The refined uranium is converted to uranium hexafluoride for enrichment from 0.7 to 3.3% ^{235}U by gaseous diffusion or gas centrifuges prior to fuel fabrication. The UF_6 is then converted to UO_2 by precipitation with ammonium hydroxide, calcination in air to produce U_3O_8 and reduction with hydrogen. The UO_2 powder is pressed into pellets, which are sintered, ground to size, and loaded into zircalloy tubing. The tubes are helium filled and then sealed and assembled into fuel bundles.[6]

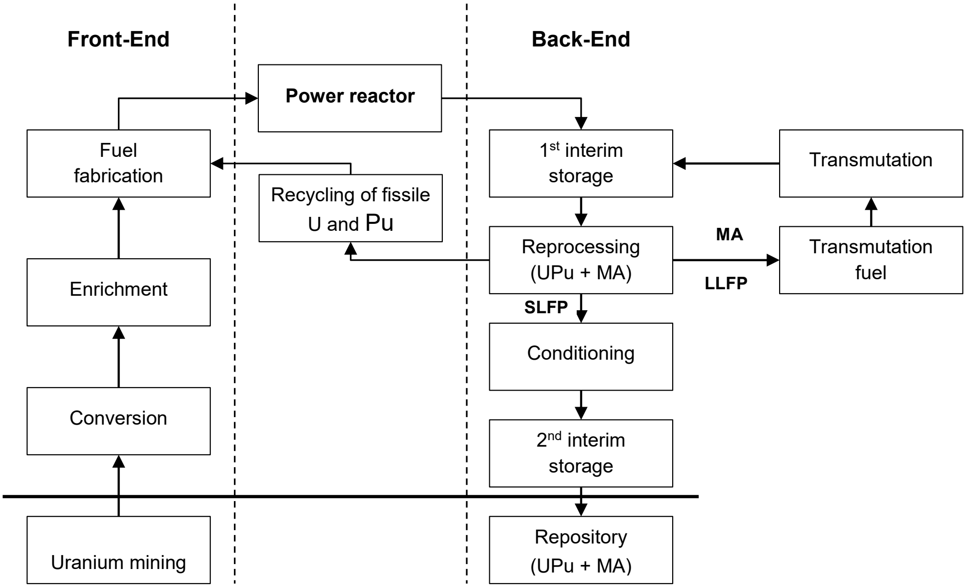

Figure 1: Schematic representation of the nuclear fuel cycle (MA = minor actinides, LLFP = long lived fission products, SLFP = short lived fission products).[7]

More than 80% of the existing commercial power reactors are light water reactors (LWR). The reactor core is made up of several hundred uranium dioxide fuel assemblies. A typical core of a reactor with an output of 1000 MWe contains about 75 t of low-enrichment uranium. Periodically a portion of the fuel is removed from the reactor core and replaced with fresh fuel to maintain the efficient performance. The average lifetime of fuel in the reactor is three years with one third being removed each year. During the lifetime of fuel elements in the reactor the percentage of fissile ^{235}U decreases, and short and long lived fission products and considerable quantities of bred plutonium (1 wt.%) and minor actinides (MA = Np, Am, Cm, 0.1 wt.%) are generated by neutron capture (compare Figure 2).[8] Plutonium and minor actinides are of particular concern with respect to long term radio toxicity, heat load issues and proliferation risks. It is estimated that in the year 2006 about 110 tons of minor actinides were contained in the spent fuel storages worldwide and 40 tons were contained in high level waste products from reprocessing. This amount will double by the year 2020 as demonstrated in Figure 3.[4]

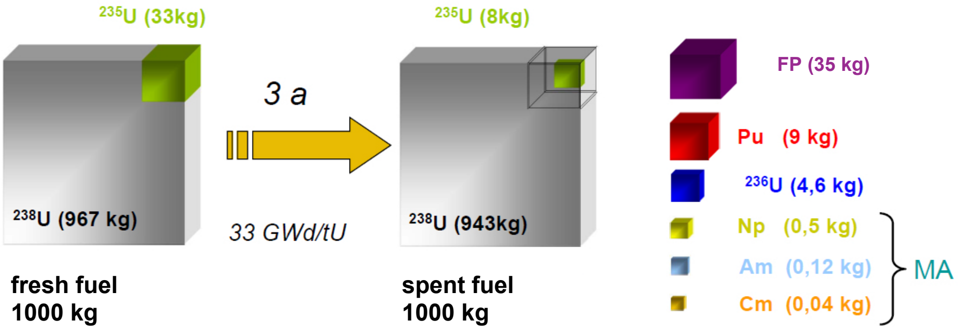

Figure 2 : Element composing UO_2 fuel (3.3% enrichment) before and after irradiation for 3 a at 33 GWd/t in PWR.[9]

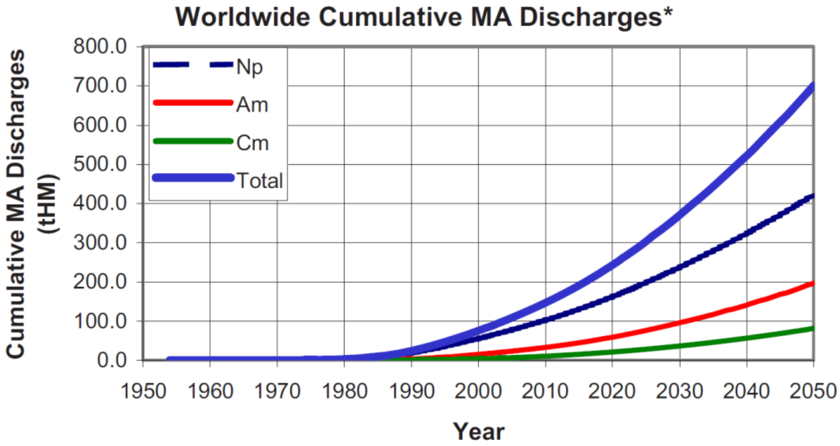

Figure 3: Estimated inventory of minor actinides worldwide. Taken from IAEA[4]

After the discharge the fuel elements are stored initially in an interim storage facility where the heat load and the radioactivity decrease. For the management of the used fuel two options can be distinguished: intermediate storage until final repository (open cycle) and reprocessing for further usage (closed cycle). In the framework of the closed fuel cycle approach two complementary strategies can be discussed: the partitioning and conditioning (P&C) and the partitioning and transmutation (P&T) strategies.

In the partitioning and conditioning strategy the separated radionuclides are embedded into a suitable matrix and disposed in a deep geological repository. This strategy does not lead to a reduced radiotoxicity of the waste, but the immobilization of the radionuclides in the host matrix increases the safety of the final disposal.[10] Glasses and ceramics are suitable structures for the conditioning of radionuclides. Due to their chemical durability, their tolerance to radiation, and their natural analogues that show stability, ceramic matrices are regarded to be advantageous for this purpose.[11]

The reduction of the radiotoxicity of the final waste is the aim of the P&T strategy. The influence of the different recycling strategies on the requisite storage time is depicted in Figure 4. It is clearly shown that in the overall context the actinides determine the hazard potential of the irradiated fuel from the beginning and the reference level is not reached within the first 100000 years due to the long half-lives. The fission products, however, contribute only in the first hundred years and due to decay of particularly ^{137}Cs and ^{90}Sr the hazard potential is reduced by five orders of magnitude within 1,000 years. Among the actinides, plutonium con-tributes most to the hazard potential, followed by americium. The contributions of curium, uranium and neptunium are less important. In summary it can be said that primarily the actinides and only secondarily the few long-lived fission products (for example, ^{129}I, ^{99}Tc) are decisive for the long-term radiotoxicity. In modern reprocessing plants the separation rates for uranium and plutonium are approximately 99.9%. It is apparent that with the concept of reprocessing the reference level of the fresh UO_2 fuel is undercut after several 10,000 years. The hazard potential after reprocessing decreases by two orders of magnitude as compared to direct disposal, but a geological confinement of the remaining waste is still required. The concept of an advanced fuel cycle (AFC) including P&T has the aim of placing only small amounts of radiotoxic inventory from the fuel cycle in a repository so that the reference level is reached within a technically manageable period of about 1,000 years. This objective is achieved by an additional separation of minor actinides and their subsequent destruction by transmutation. After the separation of long term radiotoxic elements (e.g. Pu, MA) they are embedded into a stable matrix to form the transmutation target which is then irradiated in a dedicated reactor to convert the long-lived elements into short lived or stable nuclides. Many studies have shown that if all plutonium is recycled and fissioned, the radiotoxic inventory can be reduced by a factor of 10. If the minor actinides are recycled, in addition, reduction factors higher than 100 can be obtained.[12] One can clearly see that the long-term toxicity of the residual waste is reduced considerably and the reference level is reached after 1000 years. However, this implies the almost complete separation and transmutation of transuranic elements. Partitioning and transmutation are essentially "back end processes", whose aim is to improve the options for the disposal of nuclear waste. Because plutonium and minor actinides are also responsible for the medium- and long-term heat transfer into the repository, the P&T method allows to significantly reduce the footprint of a final repository after a decay time of about 100 years.[8] However, short and long-lived fission products must still be disposed of in deep geological formations.[13] The P&T strategy not only reduces the necessary effort for the final repository construction, but also increases efficiency of the resource exploitation.**[14]**

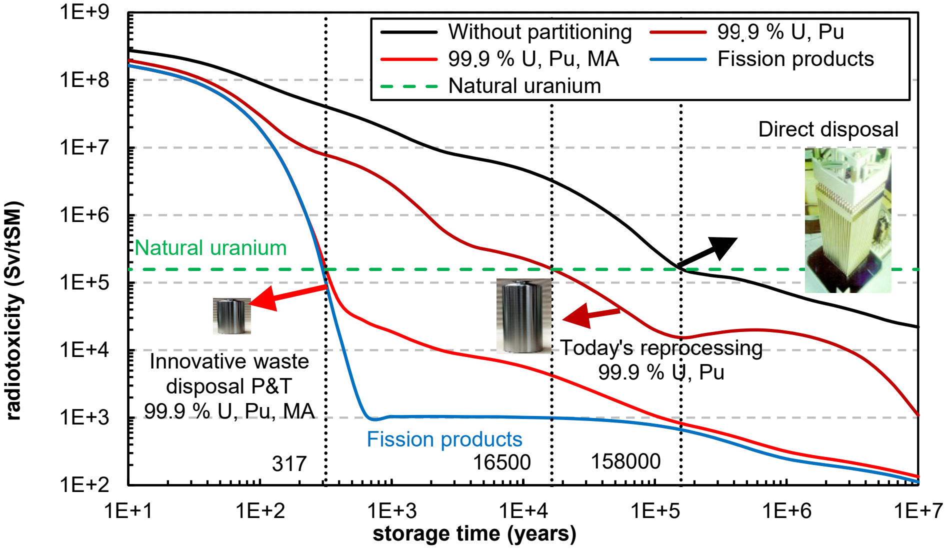

Figure 4: The influence of the different recycling strategies on the requisite storage time.[14]

1.3 Hydrometallurgical Separation of Actinides

Hydrometallurgical processes using solvent extraction technology are the industry standard for used commercial reactor fuel reprocessing with the PUREX (Plutonium Uranium Reduction Extraction) process as the basis for all current commercial scale reprocessing plants.[12, 15-16] The PUREX process is based on the initial dissolution of fuel into nitric acid and the consecutive separation. The fuel is dissolved in hot concentrated HNO_3. A solution of 30% tri-n-butyl-phosphate (TBP) in kerosene type diluent is used initially to separate U and Pu from the vast majority of the fission products.[6]

The first step is to prepare the irradiated fuel for dissolution by mechanically chopping it into small pieces (~ 1 – 5 cm). This opening of the cladding causes the release of ~ 10% of the Kr and Xe fission products as well as some ^3H and volatile fission products. These off-gases are combined with those from the dissolution step. The fuel pieces are dissolved in near boiling 8 mol/L HNO_3. This step, which takes a few hours, dissolves the uranium, plutonium, and fission products, leaving the cladding to be recovered. The chemical reactions for the dissolution of uranium involve processes like

$$3UO_2 + 8HNO_3 \rightarrow 3UO_2(NO_3)_2 + 2NO + 4H_2O \quad \textbf{(1)}$$

and

$$UO_2 + 4HNO_3 \rightarrow UO_2(NO_3)_2 + 2NO_2 + 2H_2O \quad \textbf{(2)}$$

The plutonium is oxidized to Pu(IV) and Pu(VI), while the neptunium ends up in the pentavalent or hexavalent state. Small amounts of plutonium and fission products may not dissolve, and can be leached with acid solutions containing the oxidant Ce^{4+}. A solution of TBP in a hydrocarbon with low vapour pressure, such as n-dodecane, is used to selectively extract the hexavalent $UO_2(NO_3)_2$ and the tetravalent $Pu(NO_3)_4$ from the other actinides and fission products in the aqueous phase. The overall reactions are

$$UO_2^{2+}(aq) + 2NO_3^-(aq) + 2TBP(org) \rightarrow UO_2(NO_3)_2 \cdot 2TBP(org) \quad \textbf{(3)}$$

or

$$Pu^{4+}(aq) + 4NO_3^-(aq) + 2TBP(org) \rightarrow Pu(NO_3)_4 \cdot 2TBP(org) \quad \textbf{(4)}$$

In a second step, the U and Pu loaded TBP solution is treated with a dilute nitric acid solution of a reducing agent, such as ferrous sulfamate or U(IV), which reduces the plutonium to a trivalent state but leaves the uranium in a hexavalent state. Plutonium will then transfer to the aqueous phase, leaving uranium in the organic phase. The uranium is stripped from the organic phase with 0.01 mol/L HNO_3. It is purified by a series of solvent extraction cycles until the Pu/U ratio is $<10^{-8}$ and the total β/γ activity is less than twice that of aged natural uranium. Am and Cm are not extracted and Np is partially extracted. Because of the high radiation levels, there are radiolysis problems with TBP, leading to solvent degradation. Primary products of the radiolysis of TBP are the dibutyl- and monobutylphosphoric acids along with phosphoric acid. These degradation products are removed in the solvent purification steps.[6, 17-18]

In order to achieve a significant reduction in long-term radio-toxicity of the high active waste, Am and Cm must also be separated from the PUREX raffinate, which is currently vitrified for subsequent disposal in deep geological repositories, for the fabrication of transmutation dedicated targets. That turns out to be difficult, because lanthanides make up about one third of the fission products. Therefore, depending on the burn-up the mass ratio of Ln/An is greater than 20. In addition, the lanthanides have the same oxidation state (+III), and the chemical behaviour is very similar to that of trivalent actinides. Some lanthanides have very large neutron capture cross sections and therefore act as neutron poisons during transmutation. The processes that have been developed over the past 20 years, are mainly based on the co-extraction of trivalent actinides and lanthanides and their subsequent separation.[7, 13] The separation of An(III) + Ln(III) from PUREX raffinate in a process called DIAMEX (Diamide Extraction) was proposed in the 1980s.[19] Compared to the formerly used phosphorus based extractants modern solvents aspire to contain only carbon, hydrogen, oxygen and nitrogen (CHON principle), which prevails complete combustion without the generation of salts, thereby minimising secondary waste generation.[12] N,N'-dimethyl-N,N'-dioctylhexylethoxymalon-amide (DMDOHEMA) has become the reference molecule for DIAMEX process[20-21] enhancing the extractive properties towards trivalent elements and reducing degradation compounds formed by acidic hydrolysis and radiolysis.[22] Recently, a new process for recovery of trivalent actinides from PUREX type raffinate utilizing *N*,*N*,*N'*,*N'*-tetraoctyldiglycolamide (TODGA) was developed (SANEX).[23-29] The chemical structures of these ligands, which are used for the extraction experiments within this work, are depicted in Figure 5. In a first step a very efficient extraction of An(III) and Ln(III) from acidic medium is performed, followed by their stripping using diluted nitric acid.[26]

Special attention of international research is the development of proliferation-resistant processes that do not allow isolation of fissile material (plutonium) and thus nuclear weapons-grade material in pure form. The COEX^{TM} method represents an innovative concept that could replace the proven PUREX process in the near future.[30] The GANEX (group actinide extraction process) simultaneously removes all the actinides from the dissolved spent fuel. This allows for the separation of the actinides from the lanthanides, fission and corrosion/activation products in a single process, and offers process-options to avoid separation of weapon-grade plutonium.[31-32]

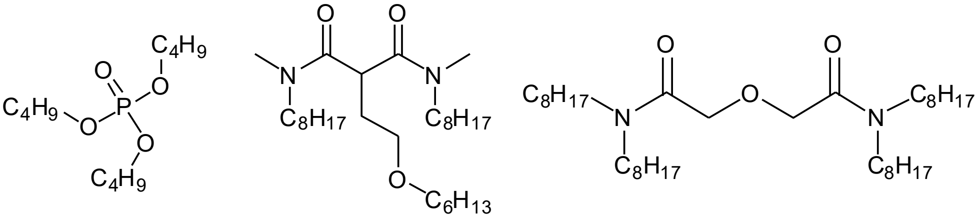

TBP DMDOHEMA TODGA

Figure 5: Structures of DMDOHEMA, TBP, and TODGA, which are used for the extraction experiments within this work.

1.4 Transmutation

Transmutation refers to the transformation of long-lived radionuclides (e.g. MA) into nonradioactive elements or elements with a much shorter half-life under a neutron flux. These processes may be achieved by:

- Fission-reactions: the nucleus is transformed into fission products (FP), which are largely short-lived (< 50 years)

$$^{239}\mathrm{Pu} + \mathrm{n} \rightarrow {}^{98}\mathrm{Mo} + {}^{141}\mathrm{Ba} \qquad \textbf{(5)}$$

- Neutron-capture reactions: the nucleus is transformed into another radionuclide, which does not necessarily allow significant reduction of the long- or medium-term radiotoxicity

$$^{239}\mathrm{Pu} + \mathrm{n} \rightarrow {}^{240}\mathrm{Pu} \qquad \textbf{(6)}$$

Thus, the fission reaction is needed for efficient transmutation of MA. When one moves from the neutron spectrum of a pressurized water reactor (PWR) (thermal or epithermal) to that of a fast reactor (FR) the probability of capture (σ_c) rather than fission (σ_f) is reduced by a factor of 5 for most radionuclides. So a FR is more suitable for this purpose than a PWR, but of course the safety question is an issue. Actinide transmutation in high temperature reactors (HTR) has been studied for many years and is currently reconsidered with focus on the use of TRISO coated particle fuels. In a thermal spectrum of e.g. a light water reactor (LWR) minor actinide transmutation reactions only consume neutrons. However, homogeneous recycling of MA in the MOX is an option considering that it is only worth transmuting minor actinides if plutonium is also recycled. In a pressurized water reactor (PWR) heterogeneous recycling can be performed in various ways depending on the arrangement of the target pins. The fast neutron spectrum from a fast reactor allows fissioning MA, thereby significantly reducing the MA production thermal reactors. However, the minor actinide content is restricted by safety reasons. Homogeneous recycling, where the MAs are introduced in to the standard (MOX, nitride, metallic or carbide) fuel, and heterogeneous recycling, where MA targets are placed either in the core or in the first layer of the blanket, is possible.[8] The higher content of minor actinides, results in a higher transmutation capacity. Many countries like Germany, Belgium, and recently Japan decided to stop their Nuclear Power plants in future. So the chance that they will build new reactors for transmutation is very unlikely. Another option to produce a fast neutron spectrum similar to that of a fast reactor, but subcritical, so inherently safe, is to use an accelerator driven system (ADS) which is described in the following section.[33-39]

1.5 Accelerator Driven System

An ADS consists of a sub-critical reactor-core with an accelerator driven spallation neutron source and may be more suitable and efficient for MA transmutation than critical FR with respect to safety and transmutation capacity.[34, 36, 40] However, the multirecycling of the ADS-MA fuel is needed in order to achieve the high transmutation level, as in the case of MA transmutation in FR. In the framework of the EUROTRANS project[35] two ADS concepts were under development: XT-ADS (experimental facility demonstrating the technical feasibility of transmutation in ADS) cooled by PbBi with power between 50 and 100 MW(th) and EFIT (European facility for Industrial transmutation) with power ~400 MW(th) cooled by Pb.[8, 37, 41] In transmutation-dedicated reactors, MAs are the fuel as they fundamentally contribute to core reactivity. A large target of molten heavy metal (e.g., Pb) is bombarded with a beam of protons (energy: 1 - 1.6 GeV, beam current: 5 - 20 mA), providing intense source of neutrons. About 30 MeV of proton energy are required to produce a free neutron (as a result of a sequence of spallation reactions). Hence, a proton beam of 1 GeV and 10 mA will produce a total number of about $2 \cdot 10^{20}$ n/s (corresponding to a neutron flux of about $6 \cdot 10^{15}$ $cm^{-2}s^{-1}$ at a distance of 50 cm).[42] These neutrons fed into a fissioning system may be used (1) for (n,γ)-reactions with the purpose to breed new fissioning nuclei or to transform long-lived radioactive isotopes into shorter-lived ones; (2) to operate the reactor in a subcritical state; (3) to selectively destroy undesired nuclides like some isotopes of plutonium or other transuranium elements, that have a potential for weapons and are ecologically problematic.[42] The target is surrounded by a blanket, which contains actinides to be burned in the high neutron flux and fission products to be converted into less long-lived products by neutron capture. Outside the inner region a subcritical assembly of fissile material produces the thermal energy required to drive the turbines. The operation of the core in a subcritical state increases the safety of the reactor. About 10% of the electricity produced from the reactor is sufficient to operate the accelerator. The long term radiotoxic inventory of geological repositories may be reduced by a factor of 200 by multi-recycling of americium and curium in addition to plutonium.[4, 42-43]

However, because the loaded transuranium elements cannot be completely burned in one reactor cycle, transmutation fuels must be reprocessed by a further step and the recovered actinides are used for the production of new transmutation fuels. For a limited period, i.e. several years, nuclear fuels containing transuranium elements can be irradiated in a transmutation facility. During this time, only a portion of the transuranic elements is transmuted into other isotopes, whereby energy is generated by nuclear fission. As only about ten to twenty percent of total transmutation fuel can be converted in a transmutation facility for physical reasons in a single irradiation cycle, the irradiated transmutation fuel is treated again so that the unconverted plutonium and minor actinides can be recovered. They are then used to produce new transmutation fuel and then once again fed into the P&T cycle. The non-transmuted transuranic elements from the transmutation fuel are extracted, and then mixed with the transuranium elements extracted from spent LWR fuel and irradiated again. A conversion of twenty percent is desired for the future, with the result that the number of cycles is reduced. This recycling must be carried out several times, with the number of recycling steps being very much dependent on the respective transmutation system and the scenario. The treatment of irradiated transmutation fuel for the recovery of plutonium and minor actinides is a chemical process which is similar to partitioning of irradiated LWR fuel. For reasons of stability and thermomechanics fuels for transmutation cannot be made exclusively from transuranium elements.[44]

The ADS fuel cycle is capable of recycling a high content of minor actinides. Due to the subcriticality of the core and the influence of the external neutron source accelerator driven systems exhibit a significantly increased neutron-physical stability. This feature provides the ability to use non-fertile fuel and thus enables very high rates of transmutation. [44] However, multi recycling cycles are needed. Additionally these transmutation dedicated fuels are not easily compatible with existing recycling processes and the development of specialized processes or at least the alteration of existing processes is therefore necessary. The inert matrix material should not give rise to new radioactive waste that must be safely disposed of as low or medium active waste and therefore needs to be separated.[44]

1.6 *Inert Matrix Fuels*

The ADS fuel is a very innovative concept with respect to the fuel of a critical core and a promising candidate for minor actinide transmutation within the concept of heterogeneous recycling. The fuel has to contain a high concentration of actinides (of 45 - 70%). It is nonfertile, that is to say free of uranium, so as to increase the transmutation performance by preventing the production of higher actinides through neutron capture of the uranium. The design of ADS fuels involves dilution of actinide compounds in an inert matrix to form either a composite (multiphase compound) or a solid solution (one-phase compound). The actinide compounds are spread in an inert matrix to better control their power and thermics while avoiding higher actinide production.[45]

It is very challenging to choose the matrix as it must comply with restrictive specifications:

- good thermal properties (high melting point, high thermal conductivity, and expansion property close to that of the actinide compounds);
- low activation under neutron flux;
- resistance to irradiation (low swelling, structural and dimensional stability, isotropic behaviour, preservation of original properties, etc.);
- Integration by a simple and robust manufacturing process.[45]

On the basis of these criteria materials were preselected and are listed in Table 1. The inventory of high potential matrices was narrowed down to a few matrices of which the most studied were oxide composites, among others: MgO and Mo (enriched in isotope ^{92}Mo)[46-47]. Both materials are highlighted in green in the table. Their suitability is discussed below.

Table 1: Selection of inert matrices for composite transmutation fuels and targets.[45]

Inert matrices		**Crystal structure**	**Thermal properties**	**Neutron activation**	**Compatibility with**				
					AnO_2	**Cladding**		**Coolant**	
						Zry	**Steel**	**Na**	**H_2O**
Oxides	st-ZrO_2	+	-	+	+(solid solution)	+	+	+	+
	MgO	+	+	+	-(eutectic)	?	+	+	-
	Al_2O_3	-(hexagonal)	+	+	-(eutectic)	+	+	+	+
	Y_2O_3	+	-	+	+(solid solution)	?	+	-	-
	CeO_{2-X}	+	-	+	+(solid solution)	-	+	-	+
	$MgAl_2O_4^+$	+	+	+	-(eutectic)	+	+	+	+
	$Y_3Al_5O_{12}^-$	-(monoclinic)	+	+	+	+	+	+	+
	$CePO_4$	-(monoclinic)	-	+	+	?	?	-	+
	$ZrSiO_4$	-(tetragonal)	-(decomposition)	+	+	?	?	-	+
Carbides, nitrides	SiC	-(hex/cubic)	+	+	-	-	-	+	+
	$^{11}B_4C$	-(rhomb.)	-(vapour pressure)	+			-	+	+
	^{11}BN	-(hex/cubic)	-(vapour pressure)	-(^{14}C)				+	+
	Si_3N_4	-(hexagonal)	-(vapour pressure)	-(^{14}C)			+	+	+
	TiN	+	+	-(^{14}C)	+		?	+	?
	YN	+	+	-(^{14}C)			?	?	-(hygroscopic)
	ZrN	+	+	-(^{14}C)	-		-	+	+
	CeN	+	+	-(^{14}C)			?	?	-
	AlN	-(hexagonal)	-(vapour pressure)	-(^{14}C)	-(?)		+	+	-
Metal	Cr	+	+	+	-(eutectic)	+	+	+	-(H_2 issue)
	V	+	+	+	-(eutectic)	+	+	+	-(H_2 issue)
	W	+	+	+	+	+	+	+	-(H_2 issue)
	Mo	+	+	-(^{95}Mo)	+	+	+	+	-(H_2 issue)
	Nb	+	+	-(^{94}Nb)		-		+	-(H_2 issue)
	Steel	+	-	+	-(eutectic)	+	+	+	-(H_2 issue)

The fabrication of the ADS fuel should result in desirable thermal and mechanical properties of the fuel. The production process itself needs to be simple and robust, with losses no larger than the expected reprocessing losses (0.1%) and should be feasible in a wet route to prevent dust formation. The VIPAC or SPHEREPAC technologies should allow a significant reduction of the number of fabrication, control and maintenance steps and therefore reduce the radiation exposure time and fabrication cost.[43] Carbides are considered as unsuitable for MA transmutation due to the volatility of americium carbide.[48] Americium in metallic form may be fabricated by arc-casting, which is however at present not adaptable to mass-flows of industrial scale.[49] Americium nitrides are more stable than carbides, however large americium losses are to be expected during sintering above 1600 °C.[50-51] Alternative production routes currently do not provide acceptable densities.[43] The most stable Am compound is americium oxide, which therefore enables fabrication with less concern of volatility. The density of composite oxide fuels decreases with increasing matrix fraction. The use of an inert matrix to improve the thermal properties is needed due to the poor thermal conductivity of actinide oxides.[43] Co-precipitation of oxalates allows the fabrication of $(Pu,Am)O_2$ with MA contents of up to 80%, but does not yet allow the fabrication of granules sufficiently dense to be directly vibropacked. Other coprecipitation routes should be considered. The infiltration of Am and Cm into a porous medium could provide an alternative.[5] The stability of AmO_{2-x}-MgO depends on the oxygen potential. An eutectic melting of $AmO_{1.8}$-MgO is expected to occur at 2300 K.[43, 52] Molybdenum and tungsten based oxide CerMet are expected to provide the best high temperature stability. The cost for Mo enrichment may be high.[43]

The solubility rate of TRU oxides in nitric acid is lower than that of nitrides, especially for higher plutonium fractions. Zirconia is insoluble in nitric acid. Losses of actinides during industrial scale reprocessing of industrial fuel have to be no larger than those achieved for Pu in established processes (i.e. processing of spent LWR fuel at La Hague, < 0.1%) to achieve a factor of 100 reduction of the radiotoxic inventory. Pyro chemical processes have not been able to provide loss rates below 1% except under laboratory conditions. The metallic fuel option is not readily compatible to aqueous processes due to the necessary use of sodium bonding to keep the fuel temperature below the melting point.[43] An additional sodium cleaning step would be needed. Actinide nitrides can be easily dissolved in nitric acid.[53] Zirconium- and thorium oxide are insoluble in nitric acid without the help of aggressive catalysts like hydrofluoric acid, which is not acceptable in the process of existing industrial facilities. MgO and Mo are expected to be compatible with dissolution in nitric acid.[43]

The most important objective for developing and deploying ADS is its potential for high minor actinide burning rates. Therefore matrix materials which absorb neutrons are disadvantageous. This is especially true for composite fuels, which should contain at least 50 vol.% of matrix. The 50% matrix criterion is difficult to fulfil using a tungsten matrix, but may be achievable with MgO. Molybdenum is on the limit, ^{92}Mo has a smaller absorption cross section compared to natural Mo.[43] An initial plutonium fraction of 40% is compatible with a minimum matrix fraction of 50% for the MgO based composite fuel. The absorption cross section of ^{92}Mo is slightly larger than that of MgO, and the Pu/MA ratio has to be raised to about 1/1 to obtain the same reactivity.[43]

A special property of fuels dedicated to transmutation is the high production rate of helium, which is of the same magnitude as the fission gas production. Helium bubble formation would accelerate fuel swelling, if retained in the fuel, and increases pin pressure if released, but may also alleviate the degradation of gap conductance caused by fission gas release. Experimental data indicate higher helium release rates in ceramic fuels than for xenon[54].

An additional complication in composite fuels is the reduction of matrix thermal conductivity due to radiation damage, which can be quite substantial for MgO[55]. In the case of molybdenum even a large relative degradation of thermal conductivity would retain sufficiently large heat conduction for the matrix to provide excellent heat removal. The burnup of nitride fuel is limited by pellet clad mechanical interaction in the case of helium bonded fuel pins, while liquid metal bonded pins may operate without failure up to the irradiation damage limit of the clad.[56]

The overall assessment of the matrices resulted in a higher ranking for the molybdenum based CerMet fuel, as compared to the magnesium oxide based CerCer fuel. In particular, the safety case looked better for the CerMet. Therefore, the composite CerMet fuel $(Pu,Am)O_{2-x}$-^{92}Mo is recommended as primary candidate within the EUROTRANS project. The composite CerCer fuel $(Pu,Am)O_{2-x}$-MgO is recommended as a backup solution. The major advantages of this fuel are a higher transmutation rate and lower cost of fabrication.[43] Both options are under investigation within the ASGARD project.[57]

1.6.1 Potential Problems during Reprocessing of IMF

Due to the necessity of multi recycling to achieve appropriate transmutation levels, a recycling of the transmutation targets is inevitable. For this purpose, methods of separating the matrix from the fission products to be vitrified and stored in a final repository need to be developed. This separation is necessary because otherwise the volume of the heat-generating waste would rise to multiples. The central challenge is to minimize actinide losses. Based on experience from the commercial reprocessing the main losses in the case of a hydrometallurgical separating are not likely to originate from the actual separation process, but in the head-end (i.e. the fuel crushing and dissolution). This plays a major role, in particular for fuels with high plutonium content, due to the poor solubility of plutonium oxide. The hydrometallurgical processing of fuels with high burnup and short cooling time leads to a higher radiolytic stress of the extracting agent used. This requires a further improvement of the extraction agents with regard to their radiolytic stability or the use of pyrometallurgical methods.[12, 39, 44]

The presence of large amounts of matrix material poses additional challenges with respect to the various reprocessing steps of the transmutation target (Figure 6).[58] A major difficulty will be to optimize the dissolution process of the used fuel after ADS operation. The well-known hydrometallurgical PUREX process is used today for the industrial reprocessing of used fuel and serves as a reference[59]. The PUREX process utilizes HNO_3 for the dissolution step. A complete dissolution of the inert matrix and the actinide oxide, or a selective dissolution, where the actinides remain undissolved, can be considered. Mo as an inert matrix poses additional challenges with respect to its redox-chemistry. There is a need to avoid coprecipitation with Pu, thus leading to Pu losses. Iron(III) nitrate is known to significantly increase the solubility of uranyl molybdate in nitric acid.[60-61] The specific chemistry of the actinide oxides and the matrix materials will be discussed in the following sections.

However, the target contains a significant amount of inert matrix which will interfere and disturb the recycling of Pu and MA using innovative hydrometallurgical processes, such as DIAMEX/SANEX concepts[20-29, 58]. To prevent Mo extraction, oxalic acid was identified as the best complexing agent in former partitioning processes[62]. Too much oxalic acid in solution induces precipitation of fission products (including Zr and Mo as main elements), lanthanides, and actinides elements. Magnesium is not known as being involved in precipitation during FP concentration, before vitrification. During FP concentration, Mo precipitates, possibly trapping actinides. If Mo is not separated before, dilution of the high active raffinate is the only solution to avoid too much concentration of Mo in this flux leading to a lot of precipitates. However, this process option reduces the throughput of vitrification process downstream, increasing the amount of water and acid to be evaporated during calcination and vitrification. Since enriched ^{92}Mo is used to limit the build-up of ^{99}Tc and because of its favourable neutronic parameters[47] it is necessary to recover the Mo, which is a challenging task. Although the separation of Mg should be considered, it is not known for generating troubles during the vitrification process, but MgO content is limited to a low part (1 to 7.5 wt.%) of matrix glass composition to prevent the degradation of the lixiviation resistance of the matrix. The selected fuel and inert matrix should not give rise to new waste that must be isolated from the biosphere.[58]

Therefore, multiple recycling of plutonium and minor actinides is a key step of the P&T concept. It is necessary, since the actinides can be burned only partially - to around ten per cent - in an ADS or fast reactor (FR). The irradiated transmutation fuel must then be reprocessed again; separated plutonium and minor actinides must be irradiated again in the form of fresh transmutation fuel. [44]

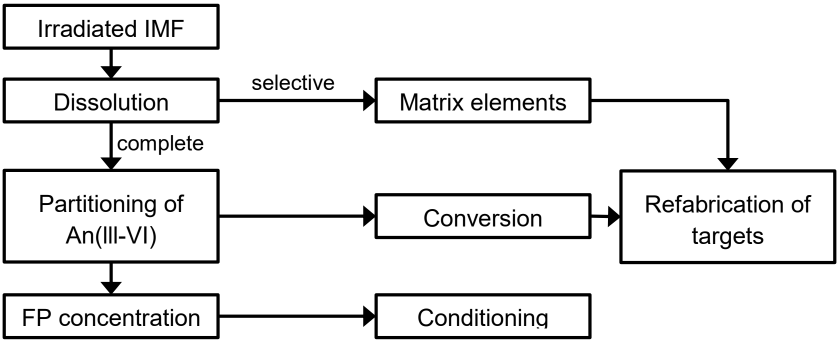

Figure 6: Schematic flow sheet for the hydrometallurgical reprocessing of used IMF targets.

1.7 Dissolution

Dissolution is the first step in reprocessing of spent nuclear fuels and will therefore be a major aspect of this work. The chemical dissolution reaction, the surface changes of the solute, and the mechanism of dissolution are the key factors in studying the dissolution behaviour of a solute.

Usually, the dissolution rate is normalized to the surface area of the solute. Therefore, the changes of the surface are important to calculate the dissolution rate of a solid in a certain solvent.[63] Changes in surface area depend on the solute and the dissolution conditions (*e.g.* temperature or pH). The dissolution rate R is defined as change of dissolved solute concentration dc per time normalized to the surface area A and is given by equation (7)[64]:

$$R= \frac{dc}{dt \cdot A} \tag{7}$$

The definition of the dissolution rate R by Brantley *et al.* [65] considers the rate constant k, the surface area A, the difference in Gibbs free energy between the solid and the dissolved molecules ΔG, and the surface area A:

$$R = A \cdot k \cdot f(\Delta G) \tag{8}$$

The solution pH and temperature also play a significant role in the determination of the overall dissolution rate, this is considered by Lasaga[66]. Furthermore, it is pointed out that the rate changes with deviation from the equilibrium. Equation (9) represents a general form of the rate law which considers the rate constant k_0, the reactive surface area A_{min}, the activation energy E_a, the activity of protons in solution $a_{H^+}^{n_{H+n}}$, the ionic strength g(I), the sum of the activity of other species in solution $\Pi_i \cdot a_i^{n_i}$, and the variation of the rate with deviation from equilibrium $f(\Delta G_r)$[66]:

$$R = k_0 \cdot A_{min} \cdot e^{-\frac{E_a}{RT}} \cdot a_{H^+}^{n_{H+n}} \cdot g(I) \cdot \Pi_i \cdot a_i^{n_i} \cdot f(\Delta G_r) \tag{9}$$

Since all these approaches consider the surface area of the solid in their dissolution rate calculations, a definition of the term surface area is necessary. Three types of surface area are described in the literature: 1) the geometric surface area, 2) the total or BET surface area and 3) the reactive surface area[65]. The geometric surface area can be described by a simple model because it is typically calculated from the dimensions of the solid. To calculate the surface of a solid it is a necessity to assume that the solid has a defined geometry. The topography of the solid surface is not considered here. Therefore, the calculated value is smaller than the total surface area.[65] To mitigate this problem a surface roughness factor can be included in the calculations to obtain the so-called total surface[67]. The surface roughness λ describes the correlation between the geometric surface area A_{geo} and the total surface area A_{total}[68]:

$$\lambda = \frac{A_{total}}{A_{geo}} \tag{10}$$

Gas adsorption can be utilized to measure the total surface area[65] based on the Brunauer–Emmett–Teller (BET) theory[69]. Highly rough surfaces, containing *e.g.* step and kink sides, have a higher probability of reaction than a surface that is completely smooth this is incorporated in the reactive surface area, which assesses that parts of the solid surface are more reactive than others[65, 68].

These approaches of an overall dissolution rate calculations discussed previously are raised to question by Lüttge *et al.*[63] and Fischer *et al.*[70]. The overall dissolution rate poorly describes the dissolution as demonstrated by Fischer *et al.* through comparing dissolution rates of single crystals to their equivalent polycrystallines[70]. Therefore, the calculation of rate spectra to evaluate the frequency of their occurrence on the surface is proposed, because the current dissolution rate of a certain site is dependent on its particular energy and the surface energy is heterogeneously distributed.[63, 70]

The dissolution mechanism can be either controlled by transport or by surface reaction depending on the rate determining step. If transport of dissolved ions away from the bulk solution and the transport of protons to the bulk solution is slow the dissolution is transport controlled. In surface controlled dissolutions the surface dissolution reaction is the rate determining step. Therefore, the dissolution of solids which are highly soluble is more likely to be transport controlled. The agitation velocity dependence of the dissolution rate provides information on the dissolution mechanism. In the case of surface controlled dissolution the rate is independent on the agitation.[65] The formation of etch pits on a mineral surface indicates that the dissolution occurs far from equilibrium which denotes that the dissolution is surface controlled[65]. In transport controlled dissolution the mineral becomes rounded, because the dissolution occurs at near-equilibrium conditions within the boundary layer and consequently just the high-energy surface sites are dissolved.[65] The activation energy of a dissolution reaction, which is given by the Arrhenius equation (11), can also be used to differentiate between transport and surface control.

$$k=Ae^{-E_a/RT} \tag{11}$$

Were A is the pre-exponential factor, E_a is the activation energy, k is the rate constant, R is the gas constant and T is the temperature (in Kelvin). The activation energy can be determined by plotting the dissolution rate as a function of 1/T. The determined activation energy, which correlates to the slope of the curve, then gives information about the dissolution mechanism.[71] In case of a transport controlled dissolution the activation energy is equal to the activation energy of diffusion[72], a value of below 20 kJ/mol should be expected in aqueous media. Activation energies significantly higher indicate a surface-controlled dissolution.[71]

1.8 Background Chemistry

1.8.1 Nitric Acid

Nitric acid (HNO_3) is a strong acid with p*K*s = -1.44.

$$HNO_3 + H_2O \rightleftharpoons H_3O^+ + NO_3^- \quad \textbf{(12)}$$

It can be used as an oxidizing agent in an aqueous solution under standard conditions to all materials whose oxidation potential is less than +0.96 V (compare Figure 7) according to

$$NO_3^- + 4H^+ + 3e^- \rightleftharpoons NO + 2H_2O. \quad \textbf{(13)}$$

The oxidizing power is particularly strong in concentrated nitric acid. Refractory metals (such as aluminium, chromium, and iron) is not attacked by nitric acid. This phenomenon (passivation) is due to the formation of an extremely thin but dense and adherent oxide film which shelters the subjacent metal from further attack by the oxidizing acid. The appearance of the passivation phenomenon provides the possibility to work with concentrated nitric acid in vessels of iron or aluminium.**[73]**

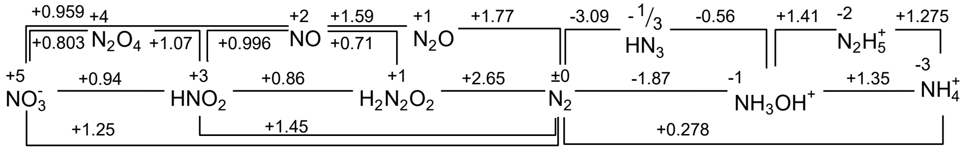

Figure 7: Standard reduction potentials (V) for nitric acid and other nitrogen species at pH = 0.[73]

Appreciable concentrations of nitrous acid (HNO_2) and lower concentrations of nitrogen oxides (NO, NO_2, N_2O_3, and N_2O_4) are present in nitric acid. As nitrogen oxides have an appreciable vapour pressure[73-74] (equation (14)-(26)), the concentrations of nitrous acid and nitrogen oxides in solution depend upon the solution conditions.

Solution phase equilibria

$$2NO \rightleftharpoons N_2O_2 \quad \textbf{(14)}$$

$$2NO_2 \rightleftharpoons N_2O_4 \quad \textbf{(15)}$$

$$NO + NO_2 \rightleftharpoons N_2O_3 \quad \textbf{(16)}$$

$$NO + NO_2 + H_2O \rightleftharpoons 2HNO_2 \quad \textbf{(17)}$$

$$N_2O_3 + H_2O \rightleftharpoons 2HNO_2 \quad \textbf{(18)}$$

$$2NO_2 + H_2O \rightleftharpoons HNO_2 + H^+ + NO_3^- \quad \textbf{(19)}$$

$$N_2O_4 + H_2O \rightleftharpoons HNO_2 + H^+ + NO_3^- \quad \textbf{(20)}$$

$$NO + O_2 \rightleftharpoons NO_3 \quad \textbf{(21)}$$

$$NO_3 + NO \rightleftharpoons N_2O_4 \quad \textbf{(22)}$$

Solution-gas phase equilibria

$$NO_{(aq)} \rightleftharpoons NO_{(g)} \quad \textbf{(23)}$$

$$NO_{2\,(aq)} \rightleftharpoons NO_{2\,(g)} \quad \textbf{(24)}$$

$$N_2O_{3\,(aq)} \rightleftharpoons N_2O_{3\,(g)} \quad \textbf{(25)}$$

$$N_2O_{4\,(aq)} \rightleftharpoons N_2O_{4\,(g)} \quad \textbf{(26)}$$

The **dissolution mechanism and kinetics of metals** in nitric acid have been studied by different authors using batch and flow dissolution experiments and electrochemical techniques.[75-83] Metals dissolve in nitric acid according to an autocatalytic mechanism involving the formation of nitrous acid. The undissociated HNO_3 but not the dissociated $NO_3^- \cdot H_3O^+$ acts oxidizing to metals.[75] The first step in metal dissolution by nitric acid is an adsorption desorption step.[75, 79, 82]

$$M + HNO_3 \rightleftharpoons M{:}HNO_3 + 2H^+ \rightarrow M^{2+} + HNO_2 + H_2O \qquad \textbf{(27)}$$

The first adsorption-desorption step (27) is considered to be rate determining for the dissolution of copper[79]; a slow induction period followed by a more rapid dissolution was observed. This adsorption-desorption step is eliminated by stirring. The higher the speed of stirring and the lower the acid concentration, the longer the period during which no interaction takes place between the metal and HNO_3. The adsorption-desorption of the intermediate HNO_2 on the metal surface is much faster than that of HNO_3. Therefore the addition of small amounts of NO_2^- or its generation during the dissolution causes the metal dissolution to start. The first step (27) plays an important role in the initial formation of HNO_2 by reduction of the absorbed HNO_3 on the metal surface. At the time of a measurable decrease in HNO_3 concentration relatively faster step starts to be predominant. This step involves the reduction of HNO_2 to NO on the metal surface:[79]

$$HNO_2 + M + H^+ \rightarrow M^+ + NO + H_2O \qquad \textbf{(28)}$$

$$HNO_2 + M^+ + H^+ \rightarrow M^{2+} + NO + H_2O \qquad \textbf{(29)}$$

The gases formed during dissolution of metals in nitric acid, mainly nitrogen oxides NO and NO_2, are poorly dissolved in hot nitric acid and the formation of bubbles at the reaction interface is observed under the microscope.[80] NO formed in reactions (28) and (29) reacts rapidly with HNO_3 forming HNO_2. This reaction takes place at the metal surface as well as in the bulk solution.[79]

$$2NO + HNO_3 + H_2O \rightarrow 3HNO_2 \qquad \textbf{(30)}$$

Zinc dissolves in nitric acid follows the same mechanism. However, in the case of zinc the first adsorption-desorption step (27) is fast. This is due to the difference in the electrochemical potential of zinc (-0.763 V) and copper (0.337 V), after which the zinc metal should be chemically more active than the copper metal.[82] The dissolution of cobalt in dilute nitric acid solution also proceeds according to an autocatalytic mechanism which involves the formation of nitrous acid as an intermediate step. However, a passivation process takes place on the cobalt surface as a result of the formation of an oxide film on the metal surface in concentrated nitric acid solutions, further complicating the dissolution kinetics.[83]

1.8.2 Magnesium Oxide

Magnesium oxide (MgO) is generally obtained by annealing readily decomposable magnesium compounds, such as the hydroxide, nitrate, oxalate, and carbonate. The physical and chemical properties depend to a large extent on the fabrication route, namely the starting material and the annealing temperature and time. The size of MgO crystallites at alike conditions depends on the starting material. The observed decrease in reactivity with increasing annealing temperature and annealing time is due to the increase of the crystal size. Magnesium oxide crystallizes in the form of colourless crystals of sodium chloride structure.[84]

Table 2: Properties of MgO.[85-86]

Property	Value
Molar mass	40.31 g/mol
Melting point	2642 °C
Density (20 °C)	3.58 g/cm³
Ionic radius	Mg^{2+} 0.86 Å, O^{2-} 1.266 Å
Crystal structure	NaCl
Space group	$Fm\overline{3}m$
Lattice parameter a	4.211 Å

If MgO is exposed to air, different amounts of magnesium hydroxide and carbonate are formed depending on the temperature and moisture. Water is initially only absorbed and only gradually forms the hydroxide; as long as it is only absorbed the water can be withdrawn by energetic acting desiccants.[84]

At high temperatures MgO is recognized to be stable against neutron irradiation. The dimensional changes in macro dispersed MgO + UO_2 composite samples of about 90% theoretical density irradiated to high burnup (thus subjected to the combined effects of neutron and fission product impact) at a temperature of 700 - 1000 K are limited (0.9 ± 1.0 $\Delta V/V$ (%)).[87] MgO has a very high melting point of 3100 K, a total vapour pressure of 100 Pa at 2000 K, and its thermal conductivity of 13 W/m·K at 1273 K is relatively low, but suitable for the application.[53, 88] However the formation of hydroxides with water makes fuel based on MgO alone not attractive for water-cooled reactors. Since MgO does not react with liquid sodium, it is favourable for use in sodium-cooled reactors.[88]

1.8.2.1 Dissolution of Magnesium Oxide

The dissolution of MgO has been investigated by various authors[89-93], including determination of dissolution rates, morphology evaluation and chemical reaction. MgO powder was used in the majority of these studies.

According to Segall *et al.*[89] the important factors for the determination of the dissolution kinetics of MgO are atomic surface detail, surface morphology, and bond strength for the solid and diffusion, pH, and electrolyte concentration for the solution. At low pH (2-5) MgO (periclase) dissolves in HNO_3 by first forming a brucite-like ($Mg(OH)_2$) hydrous oxide layer on the surface.[90, 92] The formation of a brucite or brucite-like layer on the periclase surface during dissolution explains why the dissolution rates of brucite and periclase are identical in the acidic pH region.[92] A two-step protonation of periclase is introduced by Wogelius *et al.*[92] and Fedorocková *et al.*[94] In a first fast step, surface oxygen is protonated whereby a brucite-like layer is formed followed by a second protonation, which is rate determining.[94]

$$Mg{=}O + H^+ \rightarrow Mg^{2+} + OH^- \qquad \textbf{(31)}$$

$$Mg\text{-}OH^+ + H^+ \rightarrow Mg^{2+} + H_2O \qquad \textbf{(32)}$$

$$Mg{=}O + 2H^+ \rightarrow Mg^{2+} + H_2O \qquad \textbf{(33)}$$

Suárez *et al.*[93] observed different surface developments at the different crystal surfaces of MgO crystals dissolved in hydrochloric acid by atomic force microscopy studies. The (110) plane shows circular and square shaped etch pits, the (110) plane evolves ridges and the (111) plane triangular etch pits. The (100) plane is postulated to be the most stable.[93] Investigations of the dissolution of perfect MgO crystals by Segall *et al.*[89] show that surface changes due to roughening result in rate changes. Step formation at the surface resulting from dissolution moving across the surface has been observed additionally to the development of pits and channels. According to Segall *et al.*[89] protons attack preferentially at kink sites. The surface increases during dissolution because of surface roughening and particle size decrease. Suárez *et al.*[93] postulate that the dissolution mechanism of MgO is a surface controlled because the dissolution was independent on the flow rate at which the experiments were carried out. They propose that the surface hydroxylation is fast and the detachment of the dissolution products is the rate determining step. According to Segall *et al.*[89] the dissolution of MgO below a pH of 5 is surface controlled. Vermilyea *et al.*[90], Wogelius *et al.*[92], Segall *et al.*[89], and Fedorocková *et al.*[94] propose that MgO is protonated in two steps, the second being rate determining.

1.8.3 Molybdenum

Molybdenum is a hard, white lustrous, in the pure state ductile metal of great mechanical strength which melts at 2620 °C and boils at 4825 °C.[73] The theoretical density of molybdenum amounts to 10.28 g/cm^3 [95]. It crystallizes body-centred cubic.[73] The physical properties of molybdenum are summarized in Table 3.

Table 3: Physical properties of molybdenum.[73, 96]

Property	Value
colour	white lustrous
atomic number (Z)	42
atomic mass	95.94 amu
density	10.28 g/cm^3
atomic volume	9.32 cm^3/mol
crystal structure	body-centred cubic
melting point	2620 °C
boiling point	4825 °C

Molybdenum is a natural mixture of six stable isotopes and twenty nine radioisotopes are known. The stable and the most important radioactive molybdenum isotopes are summarized in Table 4. Molybdenum enriched in isotope ^{92}Mo is favoured over natural isotopic composition for utilization as inert matrix because of its advantageous behaviour during neutron irradiation. The main reason is to limit the build-up of ^{99}Tc ($T_{½}$ = 210000 a) which is regarded as one of the most problematic fission products. Additionally natural molybdenum has a much higher neutron capture cross section in the fast spectrum region compared to ^{92}Mo, especially the ^{95}Mo and ^{97}Mo isotopes. Neutron irradiation of ^{92}Mo will lead to ^{93}Mo which is only little radioactive (positron emission) and not radiotoxic and then to the stable ^{94}Mo.[46]

Table 4: Stable and the most important radioactive molybdenum isotopes together with their half-lives, decay modes and relative abundance.[97]

A	$T_{½}$	Decay mode (%)	Abundance (%)
92		stable	14.84
93	$4.0 \cdot 10^3$ a	β^- (100)	
93m	6.85 h	IT (99.88) ε, β^+ (0.12)	
94		stable	9.25
95		stable	15.92
96		stable	16.68
97		stable	9.56
98		stable	24.13
99	65.94 h	β^- (100)	
100	10^{19} a	primordial	9.67

Molybdenum is a transition metal and the electron configuration of its valence electrons is $4d^5$ $5s^1$. It occurs in the oxidation states -2, -1, 0, +1, +2, +3, +4, +5, and +6. The most important and stable compounds are those of the hexavalent molybdenum. The divalent and trivalent states are stable only under extreme oxygen exclusion.[73] Standard reduction potentials (V) for molybdenum at pH = 0 are displayed in Figure 8.

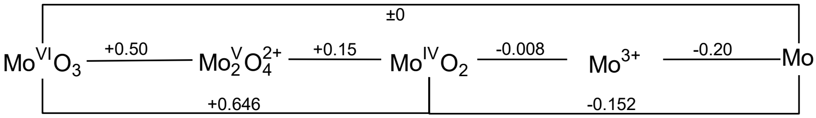

Figure 8: Standard reduction potentials (V) for molybdenum at pH = 0.[73]

1.8.3.1 Dissolution Chemistry of Molybdenum

Water has virtually no effect on molybdenum.[95] Molybdenum metal is relatively inert to acids such as hydrochloric acid at room temperature (RT). Molybdenum is sensitive against heated hydrochloric acid (110 °C); the attack of dilute HCl is much more aggressive than that of concentrated HCl (passivation).[95] An aqueous solution of sodium hydroxide and potassium ferricyanide dissolves molybdenum.[95]

The well-known PUREX process, which serves as a reference[59] is based on dissolution of the fuel in nitric acid as the head-end step. Therefore, nitric acid was used in all dissolution experiments in this work and will be considered in greater detail below.

Dissolution in Nitric Acid

The dissolution of molybdenum metal in nitric acid has been studied quite intensively in the late 1950s and early 1960s in the context of the reprocessing of uranium-molybdenum alloy nuclear fuels, which contain up to 10% Mo.[60-61, 98-99]

Molybdenum is attacked by cold nitric acid; however dilute acid has a stronger effect than concentrated acid. In the heat molybdenum is dissolved quickly independent of the concentration in a very vigorous reaction but the corrosion rate decreases with the contact time. [95] The attack of molybdenum by concentrated nitric acid solutions results from the oxidizing power of HNO_3. In the heat, the dissolution of Mo is quick and lively: the maximum speed was obtained for a nitric acid concentration of 36-38 wt.%, for which the sample shows a brown-black discoloration, probably due to MoO_2. At higher concentrations molybdenum remains clear and metallic.[96] The reaction in dilute acid is presumed to be

$$Mo + 2HNO_3 \rightleftharpoons H_2MoO_4 + 2NO \qquad \textbf{(34)}$$

or

$$Mo + 6HNO_3 \rightleftharpoons H_2MoO_4 + 6NO_2 + 2H_2O. \qquad \textbf{(35)}$$

$MoO_2(NO_3)_2$ or $[MoO_2{\cdot}MoO_3](NO_3)_2$ are formed in more concentrated nitric acid solutions. In concentrated nitric acid molybdenum dissolves according to

$$Mo + 2HNO_3 \rightarrow MoO_3 + 2NO + H_2O. \qquad \textbf{(36)}$$

However, the produced MoO_3 does not dissolve readily in nitric acid.[100] Therefore mixtures of acids have been used to improve the dissolution rates. The dissolution of molybdenum in nitric acid may be enhanced or inhibited by different additives.

The addition of **$NaNO_2$** stimulates dissolution which is autocatalytic, HNO_2 being the catalyst, and even eliminates the induction period.[100-101] During this period, the oxides (MoO_3 to MoO_2) form on the surface. Then, the dissolution is actually an electrolytic corrosion.[96]

The addition of **thiourea**, which acts as a HNO_2 scavenger, slows the dissolution and can inhibit it for several hours if the introduced concentration is sufficient, which actually corresponds to the time required for the total consumption of thiourea by HNO_2 formed.[102-103]

In (initially) 9 mol/L nitric acid containing 200 g/L **uranium** (introduced as a pellet of UO_2) molybdenum precipitates when its concentration exceeds 1 g/L. For 1.5 g/L Mo introduced precipitation of MoO_3 is slow and does not occur within the first 6 hours; no U^{VI}-Mo^{VI} is observed. In fact, molybdenum passes very quickly in solution up to 5 g/L and begins to precipitate during the dissolution of uranium; this is probably due to a more rapid initial dissolution of molybdenum. The influence of uranium is ambiguous since the final acidity varies according to the initial concentration of uranium. Molybdenum is less soluble in solutions with low uranium concentration and higher acidity. A precipitate, which appears from high initial concentrations of nitric acid (> 7 mol/L in this case), contains Mo and U when the final acidity is low (1.5 mol/L), while when it is high (9.7 mol/L) it would contain Mo. The reaction of the dissolution being exothermic, acid losses by formation of nitrous vapours are all the more important as the medium is acidic.[96]

When studying the influence of **plutonium** on the precipitation of molybdenum, using a sintered oxide $(U,Pu)O_2$ or crushed oxide leads to the same observations. In the presence of plutonium, the solubility of molybdenum seems to increase. Very fine rust coloured precipitates were observed. They contain Mo and Pu but no U. The authors note that extended contact of the mother solution and precipitate, the solid redissolves. Its solubility presents a negative temperature coefficient, probably due to solvation phenomena. A study of the interaction of molybdenum and plutonium was undertaken for the valences of plutonium IV and VI, introduced in solution in the form of nitrate. At low acidity and ambient temperature a precipitate between Pu^{IV} and Mo^{VI} is formed, but this is not observed at higher acidities (7 mol/L HNO_3). Species such as $Pu(MoO_4)_3H_2{\cdot}nH_2O$ or $Pu_2Mo_6O_{22}{\cdot}nH_2O$ were assumed. [96] A similar complex

($ZrMo_2O_7(OH)_2(H_2O)_2$) is known for the Mo-Zr system[104]. However, no precipitate is observed between Pu^{VI} and Mo^{VI} at RT. The introduction of iron(III) favours the formation of plutonium valency VI, and therefore its presence would reduce Pu losses.[96]

In nitric acid-**phosphoric acid** solutions uranium molybdenum alloys dissolve at high rates, with maximum rates at about 0.25 mol/L H_3PO_4. For example, the rate of the dissolution of uranium-3% molybdenum alloy in boiling 10 mol/L HNO_3 increases from 200 to about 290 mg/min·cm² when the phosphoric acid concentration is increased from 0 to 0.25 mol/L; a further increase in phosphoric acid concentration to 1 mol/L causes a decrease in rate to about 110 mg/min·cm². The rate increased with increasing nitric acid concentration in solutions of constant phosphoric acid concentration. The phosphate concentration did not change significantly during dissolution. Phosphate ions strongly complex molybdenum in dilute nitric acid solution by reaction similar to the following[61]

$$2PO_4^{3-} + 18MoO_3 \rightleftharpoons (P_2Mo_{18}O_{62})^{6-} \tag{37}$$

However, in solutions where the nitric acid concentration is greater than about 2 mol/L little benefit derives from the use of phosphoric acid as a complexing agent for molybdenum. Additionally, ferric ion is required to complex the phosphate in the subsequent solvent extraction step, which makes the use of phosphate impractical.[61, 105]

The dissolution of molybdenum in the presence of other **nitrates** also depends on the cations (Fe^{3+}, UO_2^{2+}, Al^{3+}, H^+).[101] **Iron(III)** nitrate is known to significantly increase the solubility of uranyl molybdate in nitric acid. Ferric ions strongly complex molybdenum in dilute nitric acid solution. Anion exchange resin studies indicate that a negatively charged iron-molybdenum complex ion is present in such solutions.[60] Heteropolymolybdate ions are formed by reactions similar to the following[61]:

$$2Fe^{3+} + 12MoO_3 + 6H_2O \rightleftharpoons (Fe_2Mo_{12}O_{42})^{6-} + 12H^+ \tag{38}$$

At each of the investigated acid concentration, uranium-molybdenum alloys dissolve in nitric acid-ferric nitrate solutions more rapidly than in nitric acid alone. For example, the initial rate of dissolution of U-Mo(3%) alloy in boiling 8 mol/L HNO_3 increases from 142 to about 200 mg/min·cm² as the ferric nitrate concentration increases from 0 to 1 mol/L. Off-gas analysis indicate that the gas mixture evolved during dissolution is about 70% NO and 25% NO_2. Less than 0.2% hydrogen is present in the gas. In most cases, the dissolution rate showed a first-order dependence on the ferric nitrate concentration regardless of the nitric acid concentration.[61, 99]

Other potential **complexing agents** for molybdenum such as Co(II), Cr(III), Ni(II), Al(III), Mg(II) and As(II) are less effective as Fe(III).[61]

Molybdenum probably reacts with undissociated nitric acid as follows[101]

$$HNO_3(\text{dissolved}) \rightarrow HNO_3(\text{adsorbed}) \rightarrow HNO_2(\text{dissolved}) + O(\text{adsorbed}) \tag{39}$$

$$2Mo + 3O(\text{adsorbed}) \rightarrow Mo_2O_3(\text{dissolved}) \tag{40}$$

The first adsorption step (equation (39)) is assumed to be rate determining, the other processes are fast. The dissolution rate r of molybdenum in nitric acid increases linearly with the concentration of undissociated acid, $c(1-\alpha)$ (α = degree of dissociation), and decreases more steeply with agitated samples because agitation partially removes the thin reaction layer on the sample. The reaction rate is no longer influenced by agitation for $2(1-\alpha) > \alpha$. The limit of $\alpha = 2/3$ shows a reaction between two dissociated molecules and one undissociated molecule, or such decomposition products having trapped oxygen to deliver to the metal surface.[96, 101]

1.8.3.2 Speciation of Molybdenum in Aqueous Solution

In aqueous solution the highest oxidation states of molybdenum (+4, +5, +6) are most stable. The lower oxidation states (-2, -1 and +1, 0) are found mainly in the form of organometallic complex compounds and ligands involving π-acceptors, which stabilize the oxidation states. Molybdenum shows a distinctive aqueous chemistry, primarily for the oxidation states +2 to +6. It occurs in the form of aqueous and oxoaqueous ions for these five states under acidic conditions (pH < 2). Due to the existence of rapid protonation, dimerization and polymerization equilibriums, the characterization of Mo(VI) species is complicated. The aqueous forms of oxidation states II to V have been identified and are summarized in Table 5. All of these species, except $Mo(H_2O)_6^{3+}$, are diamagnetic.[96]

Dimeric complexes, such as the acetate complex $Mo_2(O_2CMe)_4$ which, according to Cotton and Walton[106], exhibit quadruple intermetallic bonds dominate the chemistry of the oxidation state II. Covalent overlap is achieved through 4d orbitals of the metal.[107]

Molybdenum(III) is a relatively rare oxidation state and is easily oxidized by air and other oxidizing agents to more stable states. Several compounds of Mo^{III} exist in both aqueous and non-aqueous systems. However, the Mo^{3+} cation does not exist in the free state in aqueous solution, it hydrolyses, polymerizes or forms complexes.[108] By reduction of MoO_4^{2-} or $Mo_2O_4(H_2O)_6^{2+}$ in acidic solution, the green $Mo_2(OH)_2(H_2O)_8^{4+}$ is formed.

The coordination chemistry of Mo^{IV} is diverse and involves a number of important monomer and trimer systems. Although there are many examples of oxocomplex monomers, there is a similar proportion of non-oxocomplexes and Mo^{IV} has a great diversity in the coordination number with examples of 4 to 8. The core of the ion $Mo_3O_4(H_2O)_9^{4+}$, $Mo_3O_4^{4+}$, is very stable.

Table 5: Aqueous ions of molybdenum at pH < 2.

Description	Formula	Mo-Mo bond	Colour
Mo^{II}_2	$Mo_2(H_2O)_8^{4+}$	quadruple	red
Mo^{III}	$Mo(H_2O)_6^{3+}$	none	pale yellow
Mo^{III}_2	$Mo_2(OH)_2(H_2O)_8^{4+}$	triple	green
Mo^{IV}_3	$Mo_3O_4(H_2O)_9^{4+}$	single	red
Mo^{V}_2	$Mo_2O_4(H_2O)_6^{2+}$	single	yellow orange
Mo^{VI}_X	Different forms x = 1 or 2	none	colourless

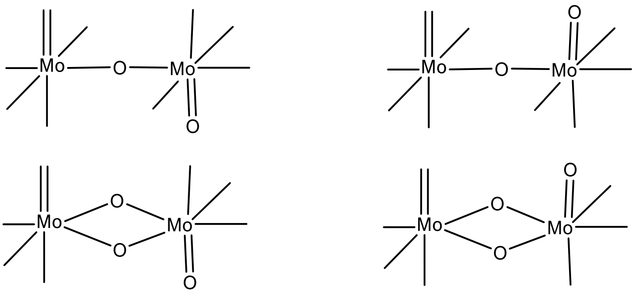

Figure 9: Different structures of Mo^{V}.

Molybdenum(V) is easily obtained by reduction of Mo^{VI} in the form of $Na_2[MoO_4]\cdot 2H_2O$ in acid solution as the binuclear yellow-orange ion $Mo_2O_4^{2+}$. The chemistry of Mo^{V} is dominated by mainly dimeric oxocomplexes. Nevertheless, monomeric species can be isolated from strongly acidic solutions. The best known monomeric species is the green chloro-complex isolated in solid form $(NH_4)_2[MoOCl_5]$. Figure 9 presents different structures of Mo^{V}. The diamagnetism of the aqueous ion of Mo^{V}, $Mo_2(=O)_2(\mu\text{-}O)_2(H_2O)_6^{2+}$, which contains two octahedral units $[MoO_6]$, has been rationalized by the proposal of a single Mo-Mo bond. The incorporation of Mo^{V} in species of mixed valence $Mo_2^{V}Mo_4^{VI}O_{18}^{2-}$ (blue), $Mo_3^{V}Mo_3^{VI}O_{18}H^{2-}$ (red) and $Mo_4^{V}Mo_2^{VI}O_{17}H^{-}$ (yellow) have been reported.[96]

The chemistry of the oxidation state VI is a much richer and more complex than the previous ones. Therefore, it will be described separately in the following section. Additionally, three mixed anionic Mo^{V}/Mo^{VI} species, which have been described in acid, are also reported.

1.8.3.3 The Chemistry of Mo(VI) in Solution

The speciation of molybdenum has been studied intensively in hydrochloric and perchloric acid medium, but little is known about the speciation in nitric acid medium, especially at high acidities, which are relevant for the dissolution of IMF. The chemistry of hexavalent molybdenum is dominated by the oxo ligand (O^{2-}) and its analogues. This oxidation state, the highest of Mo, requires the presence of ligands which are not only good π-donors but also good σ-donors for its stabilization. Such ligands should have filled p-orbitals not involved in bonds with other atoms. Formally, this leads to a situation in which a multiple bond is formed between the Mo and its ligand donor. The oxo ligand was considered as the only stabilizing ligand which complexes Mo^{VI}, but it is now recognized that the sulfido ligand (S^{2-}) can replace the oxo ligand in a significant number of cases.

Moreover, in some cases, selenido (Se^{2-}), peroxydo (O_2^{2-}), persulfido (S_2^{2-}), imido (NR^{2-}), nitrido (N^{3-}), ligands, and others, can form complexes analogous to oxo chemistry. The latter remains a benchmark from which the chemical structure of analogue ligands can be predicted[109]. Figure 10 summarizes the Mo(VI) speciation in aqueous phase as a function of pH.

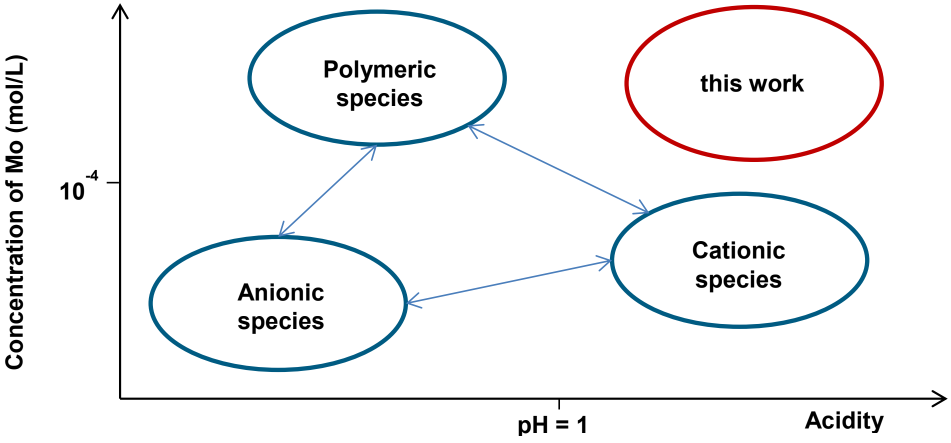

Figure 10: Summary of the Mo(VI) speciation in aqueous phase as a function of pH.[110]

The molybdate is well known to exist in alkaline solutions of pH > 7. With an increase in the molybdenum concentration molybdate ions polymerize to form isopolymolybdates, which were reported to exist in the region of molybdenum concentrations >10^{-4} mol/L.[110] Below this concentration, acidification of the molybdate proceeds to form mono protonated, diprotonated and finally cationic species. Cationic species exist in the region of pH below one. In the acidic region, the existence of dimeric cations has been suggested in the more concentrated solutions of molybdenum.[110]

Molybdate and Related Species

Examples of mononuclear species are abundant in the chemistry of simple coordination of Mo^{VI}. This is partly due to the absence of valence electrons in the complexes of Mo^{VI}, which excludes the formation of intermetallic Mo-Mo bonds. However, we must take into account the very large class of heterocyclic compounds (containing more metallic elements) and homo- (or iso-) polymolybdates. The overall equation for the formation of oxomolybdic(VI) species in aqueous solution can be written as:

$$pH^{+} + qMoO_4^{2-} \rightleftharpoons H_{p-2r}Mo_qO_{4q-r}^{(2q-p)-} + rH_2O \qquad \textbf{(41)}$$

r may be negative in the case of protonated monomer or polymer cations. Characteristic structures of oxo-complexes of Mo(VI) are given in Figure 11.

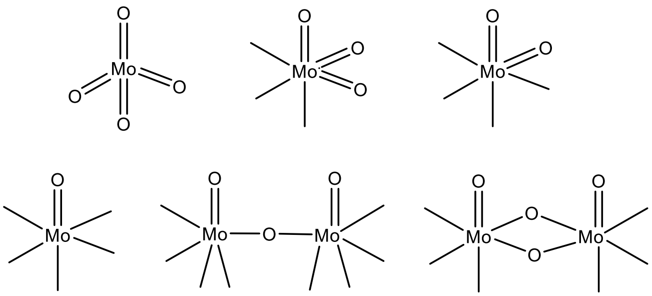

Figure 11: Structures of oxo complexes of molybdenum (VI).[111-112]

Terminal oxygen atoms are arranged in the cis position relative to each other. This structure allows the maximum utilization of the d-orbitals (dxz, dyz, dxy with ligands along x, y, and z axes) of the acceptor by strong-donor oxo-groups. Structural fragment characteristics of Mo(VI) complexes: cis-MoO_2^{2+} and fac-MoO_3 for mononuclear complexes and $Mo_2O_3^{6+}$ and $Mo_2O_5^{2+}$ for binuclear complexes have been described by various authors.[106, 113-115]

In the case where the species are not formed by protonation of MoO_4^{2-}, this equation must be considered only as a formal definition of p and q. This denotes the $H_{p-2r}MoO_{4q-r}^{(2q-p)-}$ case by the pair (p,q) notation used frequently in the literature.

The tetrahedral molybdate ion, MoO_4^{2-}, colourless, is the key precursor for many of the chemical compounds of Mo^{VI}. In moderately concentrated solutions, the mononuclear ion is only present in solutions of pH ≥ 7. For low concentrations of Mo ($< 10^{-4}$ mol/L), acidification of the solution to pH < 7 leads to the two protonated forms of the molybdate ion: $HMoO_4^-$ and H_2MoO_4 (assumed octahedral, although other geometries have been suggested). Cruywagen studied both protonations by spectrophotometry[116], respecting two essential conditions: (i) a low concentration of Mo to prevent any condensation reactions or polymerization; (ii) a low ionic strength to minimize the background of absorption and reduce the formation of polymeric species. The pH range for the study ranges from 2.5 to 6. The system can be described by the following equilibria:

$$HMoO_4^- \rightleftharpoons MoO_4^{2-} + H^+ \tag{42}$$

$$H_2MoO_4 \rightleftharpoons HMoO_4^- + H^+ \tag{43}$$

The reaction (42) is controlled by entropy while the reaction (43) is enthalpy controlled. For pH < 7 and moderate concentrations in aqueous solution, protonation initiates the polymerization. Equilibria (44) and (45) have significant effects and the heptamolybdate (or molybdate) ion predominates.

$$7MoO_4^{2-} + 8H^+ \rightleftharpoons Mo_7O_{24}^{6-} + 4H_2O \tag{44}$$

$$Mo_7O_{24}^{6-} + MoO_4^{2-} + 4H^+ \rightleftharpoons Mo_8O_{26}^{4-} + 2H_2O \tag{45}$$

These polymerized forms play an important role in the chemistry of Mo^{VI}, in the pH range between 2 and 7. For pH between 1 and 2 (depending on the concentration of the species) polymer degradation appears and leads to octahedral dimers and monomers. The polymerized forms are generated by converting the tetrahedral Mo^{VI} in an octahedral structure in which a corner, edge, or (occasionally) a face share the coordination of an O^{2-} ion between adjacent Mo atoms. The structures of the isopolymolybdate anions (as opposed to heteropolymolybdate) are based primarily on the Mo coordination number six. The isopolymolybdates are generally colourless.

The polymers obtained by lowering the pH below 7 have been extensively studied. For solutions with Mo^{VI} concentration above 10^{-3} mol/L and a pH between 3.0 and 5.5, the predominant form is the heptamolybdate(VI) ion: $Mo_7O_{24}^{6-}$, sometimes referred to as molybdate, which can be singly, doubly or triply protonated[100]. Despite numerous attempts, no intermediate was characterized unambiguously in the aqueous conversion of MoO_4^{2-} to $Mo_7O_{24}^{6-}$. At pH < 4.0, the octamolybdate β-$Mo_8O_{26}^{4-}$ was obtained according to equation (46).[117]

$$8MoO_4^{2-} + 12H^+ \rightleftharpoons Mo_8O_{26}^{4-} + 6H_2O \tag{46}$$

Heteropolymolybdates (polyoxometalates)

Molybdenum(VI) forms a large number of heteropolyanions, some of which have been known for over a century, but the actual polymerization mechanisms remain unclear. It can be assumed that the role of the counter ion differs depending on the ionic strength of the medium through the formation of ion pairs; even more important if the equilibrium involves polyanionic species.

Although new structures of polyanions continue to be discovered, it is possible to identify some general principles that control these structures. Many polyoxometalates are seen as arrangements of MoO_6 octahedra sharing their edges or their corners, each with one or two free vertices (terminal oxygen). In an alternative view of polyoxometalate structures, especially those incorporating non-metallic heteroatoms, they are presented as pseudo-clathrates. The compound $PMo_{12}O_{40}^{3-}$ is an example where the PO_4^{3-} groups are in a neutral layer ($Mo_{12}O_{36}$) consisting of square pyramidal MoO_5 sharing their edges and corners.

The reactions of molybdate ions with oxo/hydroxo/aquo species of the element X in acidic medium leads to the formation of heteropolymetalate ions in the overall equation:

$$\begin{gathered} pH^+ + qMoO_4^{2-} + rXO_u(OH)_v(H_2O)_w^{k\pm} \rightleftharpoons \\ X_rMo_qO_x(OH)_y(H2O)_z^{m-} + (4q+ru+rv+rw-x-y-z)H_2O \end{gathered} \tag{47}$$

with (m = 2q ± rk - p).

Many heteroatoms exist in diverse and often rare oxidation states in the heteropolyanions. Structures of heteropolymetalates depend on the heteroatom X (ionic radius, coordination number, oxidation state, etc.), the initial proportion $XO_u(OH)_v(H_2O)_w^{k\pm}/MoO_4^{2-}$ in solution, the pH and concentration of molybdate, time, temperature, the presence or absence of additional reagents, and catalytic effects.[118-120]

Cationic Mo^{VI} Species in Strongly Acidic Solution

Condensation of Mo^{VI}, in strongly acidic solution, in the absence of complexing ligands, results in the formation of cationic species dimers. Krumenacker[121-128] studied this phenomena and confirmed the presence of the species formed by electrophoresis on cellulose acetate strip and potentiometry. The degree of condensation of the cations was also determined by a study of diffusion coefficients. The existence of $HMo_2O_6^+$ cation, in perchloric acid, was postulated by Chauveau *et al.*[129] in 1955. Cruywagen *et al.*[130] proposed a system of descriptive equilibria in 3 mol/L perchloric medium in 1978:

$$HMoO_3^+ + H_2O \rightleftharpoons H_2MoO_4 + H^+ \tag{48}$$

$$2HMoO_3^+ \rightleftharpoons H_2Mo_2O_6^{2+} \tag{49}$$

$$H_2Mo_2O_6^{2+} \rightleftharpoons HMo_2O_6^+ + H^+ \tag{50}$$

$$H_3Mo_2O_6^{3+} \rightleftharpoons H_2Mo_2O_6^{2+} + H^+ \tag{51}$$

But this system does not take into account either the doubly charged cationic monomer species $Mo(OH)_4(H_2O)_2^{2+}$ or $H_2MoO_3^{2+}$ reported by Ojo *et al.*[131], considered negligible for a perchloric medium < 3 mol/L, or polycationic species over-condensation greater than two.

The formation of more species than the proposed monomeric and dimeric cationic species was proposed by two studies.[132-133] Light scattering techniques and Raman spectra revealed a decrease of aggregation of the Mo-entities during titration steps towards lower pH values, when the pH was lowered from 1.1 to 0.86 and then a rapid increase of the molecular weight of the species present in solution at a pH of 0.8.[133] Below the isoelectric point of molybdic acid there are different polymeric species present in solution, which are possibly positively charged. There is also strong evidence for the presence of larger oligomeric cationic species in their ^{95}Mo-NMR and Raman-spectroscopy data[132]. The data did not provide enough information for the determination of the structure of these species, but the Raman-spectra indicated an octahedral coordination of Mo and a presence of *cis*-dioxomolybdenum moieties in the oligomers.

1.8.3.4 Hydrates and Oxides of Molybdenum in the Solid State

Below 20 °C no reaction of Mo with air or oxygen can be observed, significant oxidation occurs at temperatures in the range of 400 °C (vigorous from about 600 °C). Metal powder reacts already at RT with the present humidity. Fine-grained powder is oxidized more easily than coarse-grained.[95] The molybdenum oxides are summarized in Table 6. In the heat molybdenum can be processed only under vacuum, hydrogen or an inert gas (e.g. argon). This applies especially to the operations sintering, preheating at shaping, intermediate annealing, etc.[95, 100, 108, 134]

MoO_3 is the main molybdenum oxide. The existence of oxides hydrated with one or two water molecules, $MoO_3{\cdot}H_2O$ and $MoO_3{\cdot}2H_2O$, has been established. Both hydrates can be obtained by acidification of a molybdate solution. Monohydrate is known to exist in diverse crystalline forms. There are no detailed studies on the range of existence of MoO_3 and the hydrates for acid system $MoO_3{\cdot}H_2O$. In acid solution at 20 °C, the solid phase in equilibrium with the solution is $MoO_3{\cdot}2H_2O$ in 2 to 6 mol/L HNO_3, while the monohydrate is the solid phase on both sides of this concentration range. For $T > 40$ °C, the monohydrate is the stable white solid phase in the acid system $MoO_3{\cdot}nH_2O$-H_2O. MoO_3 melts at 795 °C and can be sublimated at 800 °C in need vacuum. The vapour contains the molecules Mo_3O_9, Mo_4O_{12} und Mo_5O_{15}. From 1000 °C MoO_3 decomposes releasing oxygen.[135-136]

$MoO_3{\cdot}2H_2O$ is a transparent lemon yellow solid.[137] Dehydration in the air leads in the first stage (60 to 80 °C) to the yellow monohydrate, then in a second stage (110-125 °C) to the anhydrous trioxide. These two distinct stages result from the existence of two types of bonds to the water molecules in the structure. In an aqueous medium the water loss is continuous. According to Heyns *et al.*[138], the oxide easily loses a molecule of water of crystallization. Since the dihydrate is converted to monohydrate above 40 °C, the solubility of $MoO_3{\cdot}2H_2O$ results in metastable solutions[139]. The solubility in water at 25 °C is of the order of 0.012 mol/L. In a nitric medium, the maximum solubility is in the order of 0.125 mol/L for 3-4 mol/L HNO_3 at 26 °C. The decrease in solubility in concentrated solutions of perchloric acid is probably a variation of activity coefficients[124]. Surprisingly, according to Freedman [140] this decrease is due to the appearance of an anion.

Table 6: Solid molybdenum oxides/hydrates (OS = Oxidation state).[73, 100]

OS	Composition	Characteristics
II	MoO	black
III	$Mo(OH)_3$ or $Mo_2O_3 \cdot 3H_2O$	black
IV	$MoO_2 \cdot nH_2O$ n = 1; 2 or 2.5 or $MoO_{2\text{-}n}(OH)_{2n}$	brown
?	$MoO_{1.6}(OH)_{1.6}$ or $Mo_5O_8(OH)_8$ or $Mo_5O_7(OH)_{10}$	brown
V	$MoO(OH)_3$ and $MoO(OH)_3 \cdot 2H_2O$	brown amorphous
	$[Mo_2^VO_4(OH)_2(H_2O)_4] \cdot 6H_2O$	brown diamagnetic
V-VI	$MoO_{2.88} \cdot xH_2O$ x= 0.7 - 1.03	blue
	$MoO_{2.75} \cdot xH_2O$ to $MoO_{2.93} \cdot xH_2O$	amorphous, identification difficult
?	$MoO_2(OH)(OOH)$	yellow
V-VI	H_xMoO_3 ($0<x<2$) or $MoO_{3\text{-}x}(OH)_x$	4 intensely coloured phases
	$H_{0.5}MoO_3 \cdot xH_2O$ and $H_{-1.0}MoO_3 \cdot nH_2O$ n=1, 2	blue-black
VI	MoO_3	white
	$MoO_3 \cdot 2H_2O$	yellow

The monohydrate **$MoO_3 \cdot H_2O$** can be prepared by heating $MoO_3 \cdot 2H_2O$ in a molar solution of HNO_3 at 50 °C for 24 h. It crystalizes in the form of fine colourless needles. By acidification of ammonium, sodium or potassium molybdate solutions with nitric acid, monohydrates are obtained with the sodium compound in low concentration (0.4 mol/L) and an acid concentration of 2.5 mol/L at 40 °C (2 d) or 70 °C (20 h). For other molybdates, or more concentrated sodium molybdate solutions at higher temperatures, the precipitates obtained proved to be "Phase C" isopolymolybdate whose composition is very similar to that of $MoO_3 \cdot H_2O$.[96, 140] The solubility of the monohydrate in nitric acid medium has been studied by various authors. According to Shapiro[141], the degree of polymerization of isopolyanions increases with the increased acidity until the isoelectric point (pH 1.1-1.8), where the monohydrate precipitates. When the temperature increases from 20 to 100 °C, the solubility decreases significantly. Vorob'ev[142] attributed the decrease in solubility with temperature, for a given concentration of HNO_3, to the formation of lower soluble polymeric species of molybdenum at higher temperatures. The mechanism of dissolution in HNO_3 involves the oxygen vacancies on the surface of the solid, whereas in more oxidizing conditions these vacancies disappear (effect of acid concentration).[96, 143] In nitric acid solutions >4 mol/L, these defects can be removed by oxidation: At these high concentrations, the oxidation potential of nitric acid is sufficient to oxidise all of Mo^{III} to MoO_3 ($Mo^{III} \rightarrow Mo^{VI} + 3e^-$ E=0.5 V). The slow dissolution kinetics let surfaces becoming more ordered. And above 8 mol/L HNO_3, the solubility of monohydrate becomes zero[144]. Under certain conditions, the monohydrate tends to form colloidal solutions[145]. Vizsolyi[146] studied the precipitation of Mo^{VI}, adding an excess of reagent H_2MoO_4 to various solutions. In low concentrated nitric medium a $MoO_3 \cdot nH_2O$ precipitation is formed very slowly at RT. Heating the solution (50 - 60 °C), the precipitation becomes fast. The molybdic oxide obtained, characterized as the hemihydrate **$MoO_3 \cdot {}^1/_2H_2O$**, is not redissolved significantly when returned to RT after stirring for 24 hours.[142, 146-147]

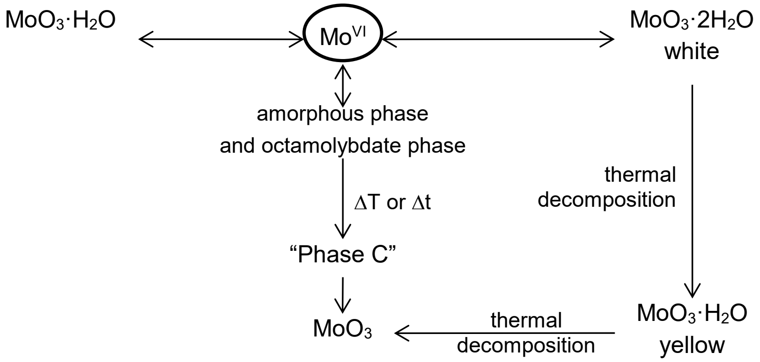

Figure 12: Precipitation of Mo^{VI} from concentrated acid solutions.[140]

The precipitation of Mo^{VI} from concentrated acid solutions is summarized in Figure 12. The compounds of the "Phase C" are predominant precipitates when the heated solutions have high concentrations of ammonium or alkali salts and acidity lower than 2.5 mol/L. Only the dihydrate crystallizes in a reversible manner, but the rate of crystallization is very slow for H^+ concentrations below 2.5 mol/L. The reactions that produce MoO_3 and "Phase C" are irreversible, which justifies the appearance of these compounds under conditions where hydrates are expected. Precipitation would therefore be under kinetic rather than thermodynamic control.[140]

1.8.3.5 Extraction Chemistry of Molybdenum

Various methods have been adopted for recovery of molybdenum from different solutions, including precipitation[148-150], adsorption with activated charcoal[151-152], ion exchange[153-155], and solvent extraction. Precipitation being the simplest method seldom yields high purity products. Small capacity and low selectivity and complexity of the process are the limiting factors in adsorption with activated carbon and ion exchange.[156]

From weakly acidic solutions Mo(VI) is effectively extracted by secondary or tertiary alkyl amines ($R=C_8$ - C_{15}), especially tri-n-octylamine, diluted in organic solvents (kerosene, benzene, dichlorpentane, etc.). The polymeric anion $Mo_8O_{26}^{4-}$ reacts according to

$$2(R_3NH)_2SO_4 + Mo_8O_{26}^{4-} \rightarrow (R_3NH)Mo_8O_{26} + 2SO_4^{2-} \qquad \textbf{(52)}$$

The re-extraction is carried out with sodium carbonate, ammonium carbonate or alkali metal hydroxide. Despite the very high degree of extraction of molybdenum by amines the low selectivity is disadvantageous. TBP dissolved in amounts up to 50% in diluents (kerosene, n-octane, n-heptane, benzene, xylene, isoamyl alcohol, CCl_4, etc.) is very suitable for the separation and extraction of Mo in hydrochloric acid solutions. For the back extraction ammonium hydroxide is used. In contrast to chloride media, from which it readily extracts into 1-10% TBP in the forms of molybdenyl chloride $MoO_2Cl_2(H_2O)_3{\cdot}(TBP)_2$ and the complex acid $HMoO_2Cl_3(H_2O)_3(TBP)_2$, molybdenum is poorly extracted with TBP from nitrate media. However, TBP is apparently capable to increase the capacity of other extractants under certain conditions, but the mechanism remains unclear.[157]

Di-2-ethylhexyl phosphate (D2EHPA) is particularly suitable for the separation of Mo-W and Mo-Re. The extraction is performed with 5 to 15% solutions of the alkyl phosphate preferably in kerosene. MoO_2^{2+} is extracted as $MoO_2(R_2PO_4)_2 \cdot 2H_2PO_4$ (R=ethyl hexyl radical). The most favourable is pH 1.5 - 2.5. Fe^{3+} has a strong inhibitory effect and must be removed by neutralization. The re-extraction is performed with sodium carbonate or ammonia.[158]

CYANEX® 600 is advertised as extracting agent for removing molybdate (Mo(VI), MoO_2^{2+}) from acidic solutions and was studied by Bremer *et al.*[159] to determine whether solutions of molybdenum based IMF in nitric acid could be decontaminated this way, i.e. by extracting molybdate while leaving actinide, fission product and corrosion product ions in the dissolution solution. The extraction of molybdate into solutions of CYANEX® 600 is promising for the purification of the molybdenum matrix material of CerMet fuels. The unwanted co-extraction of Zr(IV), Fe(III) and potentially Pd(II) can be suppressed by adding CDTA as a masking agent for these species.[159]

1.8.4 Actinides Oxides

The actinides (Ac), which contribute significantly to the radiotoxicity of spent fuel after nuclear reactor operation, are the 14 metals situated after the actinium (Z = 89) in the periodic table, from thorium (Z = 90) to lawrencium (Z = 103). The 5f level of the actinides is partly or completely filled with electrons, except the thorium. All of the about 200 known isotopes of the actinides are radioactive. Only actinium, protactinium, uranium and thorium occur naturally on earth in significant quantities. All transuranic are artificially produced and arise for example in the reactor. For transmutation the MA are preferred in their dioxide form of cubic fluorite structure, because of the large experience with UOX and MOX fuel which shows good stability under irradiation.[45] The dioxide has become the reactor fuel of choice for commercial LWR and many FR designs. Single and mixed element actinide dioxide fuels have been manufactured and irradiated. A variety of different fabrication routes were used, including chemical precipitation or mechanical blending followed by pelletisation and sintering. The material characteristics (grain size, surface area, porosity and density) are dependent on the fabrication routes. These material properties affect the process chemistry, particularly with regard to the dissolution behaviour.[160] The chemistry of the actinide oxides is complex, due to the wide range of oxidation states +II, +III, +IV, +V, and +VI, which can exist for the actinides. The actinide oxides mostly form dioxides and sesquioxides, and solid phases with different stoichiometries are summarized in Table 7.[73, 161] The +IV oxides of actinides have the general formula MO_2 and crystalize in the fluorite face centred cubic structure, their stability decreases with the atomic number. Americium dioxide can be prepared by heating a variety of americium compounds, e.g. hydroxides, carbonates, oxalate, or nitrate, in air or oxygen at temperatures of 600 - 800 °C. Due to radiation damage, which reversibly broadens the diffraction lines at low temperatures in both $^{241}AmO_2$ and $^{243}AmO_2$, it undergoes an expansion of its fcc lattice constant. AmO_2 contracts more strongly than the dioxides of the lower actinides upon cooling.[162] Plutonium dioxide (PuO_2) which is industrially prepared by the oxalate precipitation, calcination and sintering processes, is the only industrially relevant plutonium oxide.[21] The sintering conditions, notably increasing temperature, cause a decrease in surface area[20]. Some properties of PuO_2 are summarized in Table 8.

Table 7: Known stable phases of actinide oxides. The phases marked with * are considered as metastable phases. The most stable oxide of each element is printed in bold.[161, 163]

	Ac	**Th**	**Pa**	**U**	**Np**	**Pu**	**Am**	**Cm**	**Bk**	**Cf**	**Es**
+2		ThO*		UO*		PuO*					EsO
+3	Ac_2O_3					Pu_2O_3	Am_2O_3	**Cm_2O_3**	Bk_2O_3	**Cf_2O_3**	**Es_2O_3**
+4		**ThO_2**	PaO_2	UO_2	**NpO_2**	**PuO_2**	**AmO_2**	CmO_2	**BkO_2**	CfO_2	
+5			**Pa_2O_5**	U_4O_9 **U_3O_8**	Np_2O_5						
+6				UO_3	NpO_3						

Table 8: Properties of PuO_2.[164]

Property	**Value**	**Property**	**Value**
Molar mass	276.06 g/mol	**Crystal structure**	fluorite
Melting point	2400 °C	**Space group**	$Fm\bar{3}m$
Density (20 °C)	11.46 g/cm³	**Lattice parameter a**	5.3960(3) Å
Ionic radius	1.1 Å		

Table 9: Properties of CeO_2.[165-166]

Property	**Value**	**Property**	**Value**
Molar mass	172.12 g/mol	**Crystal structure**	fluorite
Melting point	2000 °C	**Space group**	$Fm\bar{3}m$
Density (20 °C)	7.3 g/cm³	**Lattice parameter a**	5.411 Å
Ionic radius	1.11 Å		

There are no major hindrances to forming a solid solution in a large composition range because the ionic radii of actinides are very similar and decrease with the atomic number. Therefore, minor actinides are generally introduced in the fuel in the form of a solid solution of $(U,Np,Pu,Am,Cm)O_{2-x}$ type, whenever it involves homogeneous recycling. $(Am,Cm)O_{2-x}$ type when it has to do with heterogeneous recycling on inert support, or $(U,Am,Cm)O_{2-x}$ type whenever it involves heterogeneous recycling in breeder blanket. Neptunium is generally not considered in heterogeneous recycling even though there are no disadvantages for transmutation. During the separation treatment, neptunium is easily extracted with uranium or with plutonium and therefore naturally follows the uranium or plutonium cycle rather than that of americium and/or curium. The compatibility of actinide oxides with the European R&D facilities of course made it easier to develop this type of fuel.[45]

The non-radioactive cerium dioxide (CeO_2) is commonly and accordingly in this work used as surrogate to simulate the behaviour of PuO_2[167-169], because of a very similar physico-chemical properties including ionic radii in octahedral and cubic coordination, melting points, standard enthalpy of formation and specific heat and chemical behaviour. Some properties of CeO_2 are summarized in Table 9, for PuO_2 compare Table 8.

1.8.4.1 Dissolution of Actinide Oxides in Nitric Acid

The dissolution of plutonium from fresh and spent PuO_2 or MOX is complex and depends on synthesis, microstructure, and thermal as well as irradiation history.[170-171] When sintered to temperatures greater than ~450 °C plutonium dioxide (PuO_2) is insoluble in nitric acid, because sintering to higher temperatures reduces the powder porosity and crystallinity[171-172]. According to Uriate and Rainey[171] the dissolution rates for PuO_2 in 2, 10 and 14 mol/L nitric acid are less than 10^{-2} mg/cm$^2\cdot$min. The dissolution rate is barely affected by the temperature and HNO_3 concentration[173]. However, complexants such as fluoride or oxidants such as Ag(II) and Ce(IV) accelerate the PuO_2 dissolution[170-171, 173].

Am and Cm oxides dissolve in hot concentrated nitric acid without producing insoluble residues. AmO_2 was irradiated and dissolved in 6 mol/L nitric acid at 75°C in an early study to identify Bk[174]. Due to high specific α-activity Am and Cm compounds are subject to significant lattice damage. The expansion of the lattice and introduction of defects into Am or Cm compounds[175] will make these materials susceptible to dissolution.

NpO_2 can be dissolved in nitric acid; however accelerants, such as fluoride or oxidants (Ce^{4+}/Ag(II)) are beneficial. The dissolution of the CerMet type fuel is also improved by the addition of small quantities of Hg as a catalyst, which also improves the dissolution of cladding materials[160]. More recently electrochemical dissolution techniques using Ag(II) as an oxidant has allowed complete recovery.[160]

In the hydrous, freshly precipitated form cerium dioxide redissolves quite easily in acids, but when prepared by ignition it is a rather inert material[176], which is not soluble in aqueous solutions of nitric acid, but can be attacked in an autoclave at 300 °C by nitric acid.[177]

1.9 *Electrospray Ionization Time-of-Flight Mass Spectrometry*

The electrospray ionization method, which can probe the stoichiometry and relative abundances of solution species, was developed by Dole *et al*.[178] to investigate macromolecules and coupled to a mass spectrometer(MS) for the first time in 1984 by Fenn and co-workers[179]. The method is mainly used for biomedical applications and the detection of large organic molecules. However, it is also widely used in studies on metal ions in aqueous solution that are mainly aimed at determining elemental speciation, the interaction of metals with organic ligands, and on the interaction of the metal ion with water or on hydrolysis. Electrospray ionization is a very gentle ionization method, making fragmentations less probable. The spectra reflect the distribution of charged molecules in the solution. With this method also minor species can be detected. Flight time analysis covers a wide mass range at the same time. An isobaric resolution is possible.

1.9.1 Electrospray Ionization Source

In electrospray ionization (ESI) an analyte solution is introduced through a metal capillary and a voltage is applied to the tip of the capillary. The voltage generates an electric field between the capillary and a counter electrode. The electric field penetrates the analyte solution and the ions move electrophoretically towards the counter electrode. A neutral carrier gas such as nitrogen is often used to support the nebulization of the solution and the evaporation of the solvent. Due to the evaporation of the solvent, the droplet size decreases, while the density of the electric field increases on the droplet surface. If the radius of the droplet becomes smaller than the so-called Rayleigh limit, the droplets decompose due to the repulsion of like charges (Coulomb explosions) via the formation of a Taylor cone to a fine aerosol (about 10 μm droplet size). A small portion of the ions pass through the skimmer orifice into the vacuum of the mass spectrometer. Figure 13 displays the schematic of an electrospray ionization source.[180]

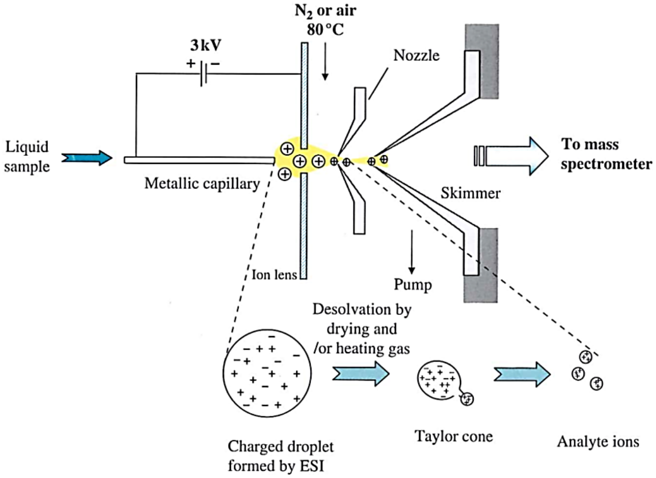

Figure 13: Schematic of electrospray ionization. Taken from Becker.[180]

1.9.2 Time-of-Flight Analyser

The time-of-flight (ToF) analyser utilizes the different masses of the ions which possess the same kinetic energy when entering the drift tube and therefore reach different velocities according to

$$E_{kin}=\frac{1}{2}m\cdot v^2. \tag{53}$$

With the kinetic energy E_{kin}, the mass m and the velocity v. The ions are accelerated at an acceleration voltage into a field-free drift region. Because of the relationship between energy, mass and velocity, the flight time of the ions is proportional to the square root of the mass. Light ions are faster than heavy ones and therefore reach the detector earlier than heavy ions, when flying through a field-free space. The principle of a linear ToF analyser is shown in Figure 14.[180]

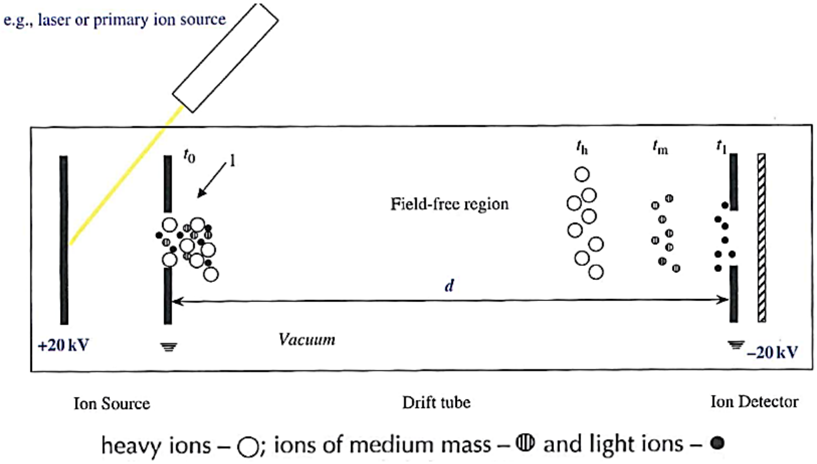

Figure 14: Principle of a linear time-of-flight (ToF) analyser. Taken from Becker[180].

The time resolution of the ions having different masses and the resulting resolution of the ToF analyser are proportional to length of the drift tube. Therefore, in practice devices with ion mirrors or reflectors in which the flight route is doubled by an additional electric field at the end of the original direction of flight have proven to be of value. Furthermore an additional focusing is achieved by this technique, since ions of the same mass, but with a higher starting energy, penetrate deeper into the opposite field, thus travel longer in the reflector and catch up again with the slower ions after the reversal of direction in the drift path and reach the detector at the same time. A diagram of a ToF analyser with reflector is displayed in Figure 15.[180]

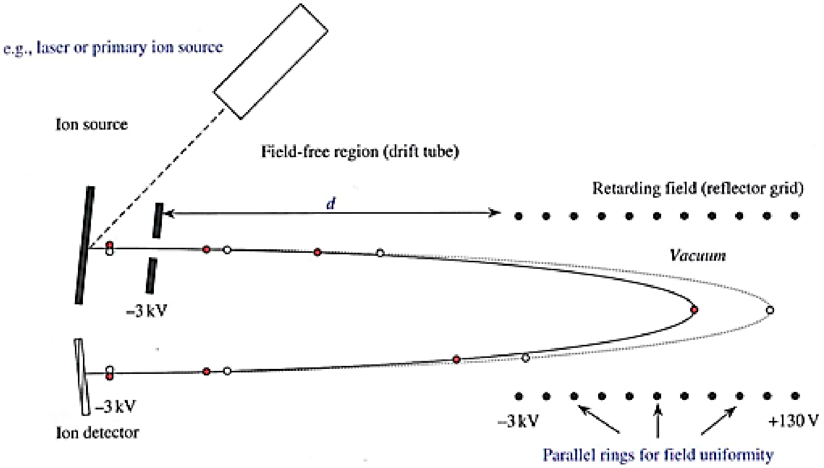

Figure 15: Diagram of a time-of-flight (ToF) analyser with reflector. ● mass m, lower starting energy, ○ mass m, higher starting energy. Taken from Becker[180].

2 Aim of this Work

This work aims to assess a feasible head-end process based upon the dissolution behaviour of MgO- and Mo-based inert matric fuels (IMF) dedicated to the recycling of minor actinides. The IMF fuel is devoted to the transmutation of minor actinides in accelerator driven systems within the partitioning and transmutation strategy (P&T) as future alternative for radioactive waste management. The oxide dissolution and separation strategy is a fairly mature process. New separation strategies have been tested on genuine spent fuel and the selected processes will be evaluated for industrial implementation. Whereas the above is valid for actinide oxide fuels, such as MOX and/or Minor Actinide containing MOX, the dissolution and separation issues for inert matrix fuels containing ceramic magnesium oxide (CerCer) or metallic molybdenum (CerMet) to improve the thermal properties of the fuel, has not been investigated systematically. The recovery of the matrix material is important to reduce the cost of the ^{92}Mo enrichment and to reserve the capacity of the vitrification. In this context the following main questions arise to evaluate the reprocessability of IMF:

- What are the optimal dissolution parameters for IMF and is it possible to achieve a separation of the matrix material and the actinides during the dissolution process?
- What are the solution species of molybdenum in concentrated nitric acid?
- How are well-established extraction processes influenced by the high content of matrix materials?
- Is there an alternative recycling process to the very complex dissolution of molybdenum in nitric acid?

Optimization of dissolution parameters – The dissolution of MgO has been studied intensively in hydrochloric acid. It is also well known that MgO can be dissolved easily in nitric acid, but the dissolution behaviour at conditions suitable for subsequent separation by established extraction processes has not been investigated. The dissolution behaviour of molybdenum in nitric acid has been studied in the 1960’s in the context of metallic uranium-molybdenum alloy reactor fuel. However, this type of fuel contains only 3 – 10% molybdenum (compared to at least 50% in the IMF) and uranium is known to improve the molybdenum solubility by complexation. The aim of this study is to determine conditions at which the matrix material can be selectively dissolved, allowing its separation, where the actinides remain undissolved.

Pure matrix pellets as well as pellets containing CeO_2, as surrogate for TRU oxide, were fabricated as reference samples. All fabricated pellets were thoroughly characterized by means of density measurements, micro hardness measurements, SEM investigation, and XRD. A systematic macroscopic study of dissolution kinetics was carried out using batch dissolution experiments. Besides the acid concentration and volume, temperature, stirring velocity, and pellet density dependence a more sophisticated microscopic approached was followed to investigate the evolution of the MgO pellet surface during the dissolution process. On the basis of this examination the total surface area of the pellet was estimated to establish a surface normalized dissolution rate. The influence of Fe(III) and NO_2^- ions on the dissolution behaviour of Mo was investigated. To get closer to a real fuel unirradiated Mo/PuO_2 pellets were utilized for further optimization of the dissolution parameters.

Solution species of molybdenum in concentrated nitric acid – A detailed knowledge of the speciation of molybdenum in nitric acid medium is crucial on the one hand to understand the dissolution process and on the other hand as a basis for the design of a tailored extraction process. The speciation of molybdenum has been studied intensively in hydrochloric and perchloric acid medium, but little is known about the speciation in nitric acid medium, especially at acidities related to reprocessing, which are relevant for the dissolution of IMF.

Therefore, electrospray ionization mass spectrometry, which can probe the stoichiometry and relative abundances of solution species, was applied in this work to extensively characterize and quantify the solution species of molybdenum in strongly acidic nitric acid medium. Moreover, the influence of macro amounts of Fe(III) on the speciation was investigated. To reduce the measurement times of the homemade nanospray ion source ALBATROS, a method was developed to analyse solutions of molybdenum with natural isotopic composition with a commercially available ESI/MS/MS instrument (QTrap) and implemented to investigate the acid and Fe(III) concentration dependence of the Mo speciation.

Impact of matrix materials on extraction process – Since Mg is not a constituent of conventional spent fuel its behaviour in established extraction systems has not been investigated hitherto. The extraction behaviour of molybdenum has been investigated in two different contexts. Molybdenum is a fission product of uranium and therefore a constituent of conventional spent fuel and was considered in previous studies. However, the molybdenum concentration in this kind of experiments is significantly lower, so that the problem of precipitation phenomena is extenuated. Extractability studies with highly concentrated molybdenum solutions have been performed in the context of separation of molybdenum from ores. However, ores are usually dissolved in hydrochloric acid and these solutions do not contain actinides.

The extractability of Mg and Mo as well as the influence of macro amounts of matrix material on the extraction of U(VI), Eu(III), and Am(III) were examined. Extraction studies with TBP were performed under PUREX conditions. The two well-known DIAMEX type extractants DMDOHEMA and TODGA were studied for actinide(III) and lanthanide(III) extraction.

Alternative to dissolution of molybdenum – As an alternative to the very complex dissolution of Mo based IMF the separation of the matrix from the fuel by thermal treatment was considered. This exploits the oxidation of molybdenum in air above 400 °C and sublimation of the resulting MoO_3 at 800 °C.

For this purpose an apparatus for exposure experiments was constructed and the investigation was completed by subsidiary TG-DSC experiments. Additionally, the residues and products were analysed by XRD. It is expected that the volatile components of the fuel are not deposited together with Mo and the remaining components of the fuel do not evaporate at these temperatures.

3 Experimental

3.1 Pellet Fabrication

To investigate the reprocessability of molybdenum and magnesia based inert matrix fuels reference samples containing different amounts of CeO_2 (0, 5, 10, 25, and 40 wt.%), which serves as surrogate for plutonium dioxide, have been prepared by powder metallurgy.

3.1.1 MgO Pellets

MgO powder (Merck, pro analysis) was calcined at 600 °C for 2 h and hand milled with an agate mortar. The powder (approximately 500 mg) was compacted into cylindrical pellets of 10 mm diameter by cold uniaxial pressing using a hydraulic press (Figure 16). The apparatus used here is an Oehlgass, Hahn & Kolb press.

The range of pressures used for the investigation of optimal pressing and sintering conditions varied from 130 to 765 MPa, the sintering temperatures varied from 1200 to 1600 °C. All MgO pellets were sintered for 5 h in air atmosphere in an electric resistance furnace (Linn HT 1800) with a heating rate of 2.8 to 3.8 K/min, depending on the holding temperature.

Figure 16: Hydraulic press for the fabrication of green bodies. The apparatus used here is an Oehlgass, Hahn & Kolb press.

3.1.2 MgO/CeO_2 Pellets

In addition to pure MgO, pellets with CeO_2 contents of 5, 10, 25 and 40 wt.% were synthesized. For this purpose, $Ce(OH)_4$ powder (Sigma Aldrich) was calcined at 600 °C to provide CeO_2, which was then hand milled using an agate mortar and mixed with magnesia. In order to provide a homogeneous distribution of the CeO_2 the mixing was carried out according to the following procedure. Both powders were given into a vial and shaken vigorously, the mixture was then hand milled for 10 min. The powder was then pressed with an uniaxial hydraulic press (Figure 16) at pressures between 190 and 700 MPa.

The resulting pellets were sintered at 1500 or 1600 °C for 5 h in air atmosphere. Mixed MgO/CeO_2 pellets used for dissolution experiments were pressed at 320 MPa pressure and sintered at 1600 °C.

3.1.3 Mo Pellets

The Mo pellets were produced under similar conditions as the pellets which were produced at NRG Petten[181]. For each pellet 1 g Mo was pressed with a pressing force of 50 kN (640 MPa) with a uniaxial hydraulic press (Ø = 10 mm, Figure 16). The pellets were then sintered under argon atmosphere. During a first heating period the pellets were heated to 500 °C within 2.5 h and this temperature was kept stable for 2 h. The pellets were then further heated to 1600 °C within 5.5 h and sintered at this temperature for additional 5 h.

For the speciation experiments with the ALBATROS ESI-ToF as well as on the separation of Mo by thermal treatment pellets with a mass of approximately 50-70 mg and a diameter of 2.7 mm were produced. Isotopically pure ^{98}Mo was utilized for the speciation experiments whereas molybdenum of natural isotopic composition was used for thermal treatments. The powder was pressed with a uniaxial hydraulic press at a pressing force of about 3.5 kN (610 MPa) and sintered according to the temperature program given above.

3.1.4 Mo/CeO_2 Pellets

According to the Mo/UO_2- and Mo/PuO_2 pellet production at NRG Petten[181] pellets with CeO_2 contents of 5, 10, 25 and 40 wt.% were synthesized. The preparation of CeO_2 and the mixing procedure was the same as for MgO/CeO_2 pellets. The resulting powder mixture was then pressed with an uniaxial hydraulic press (compare Figure 16) at a pressing force of 50 kN (640 MPa). The resulting pellets were sintered at the same conditions as the pure molybdenum pellets.

Additionally, those powder mixtures were pressed into pellets of about 20-50 mg weight and 2.7 mm diameter at a pressing force of about 3.5 kN (610 MPa) with an uniaxial hydraulic press and sintered at 1600 °C, at heating rate of 5 °C/min and 1 h holding time. These smaller pellets were used for investigations concerning the separation of molybdenum from the fuel by thermal treatment.

3.2 *Physical Properties and Microstructure of the Pellets*

The densities of the green bodies as well as the sintered pellets were measured by the geometrical or Archimedes method. For investigation of microstructure and mechanical properties, the surface of the pellets was polished and chemically etched. The micro hardness H_v, fracture toughness K_{1C}, and brittleness index B_i of the sintered pellets was studied by optical microscopy (Zeiss KS300). The grain size distribution, microstructure and morphological structures were investigated using a scanning electron microscope (SEM) with EDX. The later was used for determination of element composition.

3.2.1 Determination of the Compressibility and the Sinterability of the Powders

The green (ρ_G) and sintered (ρ_S) densities of the pellets were determined by the geometrical method. The mass m of the sample, its diameter D and its height h were measured and the density was calculated according to:

$$\rho_{geo}= \frac{4m}{\pi D^2 h} \tag{54}$$

For more accurate sintered density determination with Archimedes method the mass of the specimen is measured twice; once in air and once in a liquid of known density (water with $\rho(lig)=1\ g/cm^3$ was utilized in this work). The density is then calculated by equation (55)[182]:

$$\rho_A=\frac{m_L \cdot \rho(liq)}{m_L-m_{liq}} \tag{55}$$

with the density of the liquid $\rho(liq)$, the mass of the specimen in air m_L, and the mass of the pellet in solution m_{liq}.

3.2.2 Micro Hardness, Fracture Toughness and Brittleness

Prior to the investigation of the sintered pellets, they were carefully polished with abrasive paper of different sizes (BUEHLER abrasive paper CarbiMet 2: 1) 320/P400 PSA Back, 2) 400/P800 PSA Back, 3) 600/P1200 PSA Back) and finally with BUEHLER Polycrystalline Diamond Suspension Meta Di 1 µm until no more scratches were revealed under the optical microscope.

3.2.2.1 Micro Hardness H_V

The micro hardness (H_V) of sintered samples was measured by a diamond Vickers indenter (Anton Paar MHT 10). Indentation hardness measures the resistance of a sample to local material deformation due to a constant compression load from a sharp object[182-183]. The thoroughly polished and etched surface was indented using loads from 50 to 350 g. The full load was applied for 10 s. Five measurements were performed for each load for pure MgO pellets. Indentation was carried out 30 times for pure CeO_2 samples and 45 times for mixed pellets. Seven measurements at a load of 400 Pa were performed for each molybdenum containing pellet. The micro hardness (H_V (GPa)) was calculated by the following expression[183]:

$$H_V=1852\ \frac{F}{(2a)^2} \tag{56}$$

Where F (N) represents the load and 2a (µm) the average length of the diagonals of the Vickers indents. A typical indenter image is shown in Figure 17.

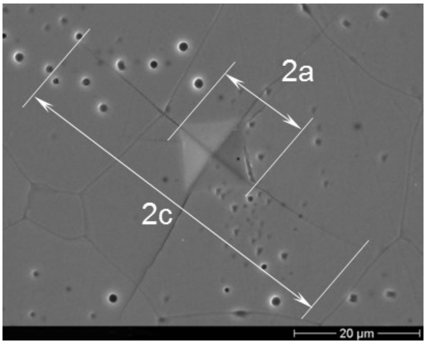

Figure 17: Typical indenter image with crack length (2c) and average indenter length (2a).

3.2.2.2 Fracture Toughness K_{1C} and Young's Modulus E

The amount of stress required to broaden an existing failure in the material (*e.g.* cracks or voids) is described by the fracture toughness of a material[183-184], which is calculated using different equations depending on the type of cracks (half-penny-shaped cracks or Palmqvist cracks (compare Figure 18)) produced by the indentation[184]. The fracture toughness of materials showing half-penny-shaped cracks is calculated by equation (57)[184]:

$$K_{1C} = 0.067 H_v \cdot \sqrt{a} \left(\frac{E}{H_v}\right)^{0.4} \left(\frac{c}{a}\right)^{-3/2} \quad \textbf{(57)}$$

While equation (58) is used in the case of Palmqvist cracks[184]:

$$K_{1C} = 0.018 H_v \cdot \sqrt{a} \left(\frac{E}{H_v}\right)^{0.4} \left(\frac{c}{a}\right)^{-1/2} \quad \textbf{(58)}$$

with the micro hardness H_v, the Young's modulus E, the crack length c, and half the average indenter diagonal a. The determination between half-penny-shaped and Palmqvist cracks is based on the quotient of the crack length c and the indentation diagonal a. Palmqvist cracks occur for $c/a < 3.5$ and half penny shaped cracks occur for $c/a > 2.5$[184].

The Young's modulus E is a measure of the elasticity of a material. Reference data is taken from the literature for the pure materials[185]; for the mixed MgO/CeO_2 pellets the young's modulus calculated as a function of CeO_2 content, assuming a linear dependence on the amount of CeO_2 X in vol.%:

$$E = (E_{CeO_2} - E_{MgO}) \cdot X + E_{MgO} \quad \textbf{(59)}$$

with Young's modulus of CeO_2 E_{CeO_2}: 317.7 GPa[186] and MgO E_{MgO}: 62.4 GPa[186].

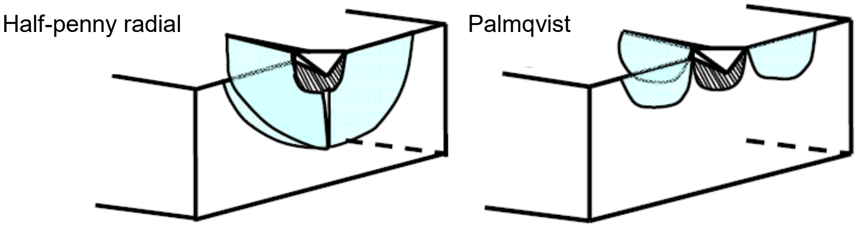

Figure 18: Comparison of half-penny crack and Palmqvist crack[187].

3.2.2.3 *Brittleness B_i*

The brittleness index B_i describes the degree of deformation a material undergoes under stress exposure before it breaks. The brittleness index resembles the quotient of micro hardness and fracture toughness K_{1C}[188]:

$$B_i = \frac{H_v}{K_{1c}} \tag{60}$$

3.2.3 Pellet Microstructure

For the investigation of the microstructure the polished MgO containing pellets were etched with a 5% NH_4NO_3 solution for 3 h. Therefore, the upper side of the pellet was completely covered with a droplet of the NH_4NO_3 solution (Figure 19). Sintered molybdenum containing pellets were etched with Murakami's reagent[189] (composition: 10 mg $K_3Fe(CN)_6$, 10 mg KOH, 100 mL distilled water) for 3 min. The pellets were then washed with suprapure water and dried at 90 °C.

Figure 19: Etching of a MgO pellet with 5% NH_4NO_3 solution.

3.2.3.1 *Scanning Electron Microscope*

The micro structure of the pellets was studied by scanning electron microscopy (SEM) utilizing a Quanta 200F SEM from FEI company with a field emission cathode. Measurements were carried out using low vacuum mode at 60 Pa and 10 mm working distance. The spot size was four. Element analyses were conducted by EDS measurements with a Genesis 4000 Silicon Drift Detector (SSD) from EDAX at 20 kV acceleration voltage. Samples were fixed on an aluminium specimen holder with a carbon patch for the measurements.

3.2.3.2 Powder X-ray Diffraction Analysis

Powder X-ray diffraction is a long-range order method used to define the structure of a crystalline sample. The XRD patterns typically show the intensity of the Bragg reflections versus 2θ (diffraction angle). X-ray diffraction analyses were performed in the range from 10 to 100° 2θ at RT with the D8 Advance (θ–2θ geometry) and the D4 Endeavour (θ–θ geometry) from Bruker AXS GmbH. Powders were analysed as obtained, pellets on the polished surface. Residues of exposure experiments were milled prior to measurements. Data analysis was carried out with the software “Match!” from Crystal Impact (version 1.9).

3.3 Dissolution Experiments

A dissolution set-up (Figure 20) has been installed in a fume hood and was used for all dissolution experiments. Dissolution experiments were conducted in a two-necked round-bottom flask equipped with a Liebig condenser. During dissolution, the liquor was stirred using a magnetic bar. An oil bath was used for temperature control.

The influence of temperature, acid concentration and volume, density, and agitation rate on the dissolution has been investigated. Nitric acid was used for all dissolution experiments. In the case of molybdenum also ferric nitrate ($Fe(NO_3)_3$; Sigma Aldrich, ACS reagent, ≥98%) was used as an additive in some cases. Typically 20 mL of acid were used per 1 g of pellet. For each dissolution experiment the acid (and additive) was provided in the flask and the temperature was adjusted, then the pellet was added.

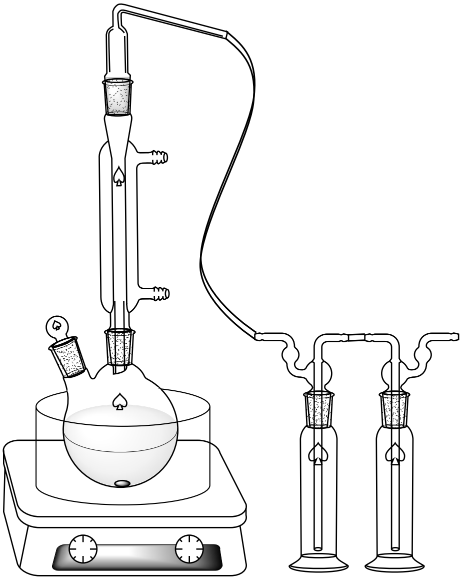

Figure 20: Experimental set-up for dissolution experiments.

During the dissolution process 50 µL samples were taken and measured in a calibration range of 0.1 to 100 µg/L with appropriate dilution of the analyte in 1% v/v HNO_3 (suprapure) solution. Molybdenum samples were centrifuged prior to dilution; for Magnesium samples filtration and centrifugation was proven to be unnecessary (compare section 4.1.2.1). The measurements were realized with the Elan 6100 DRC apparatus, developed by Perkin Elmer and SCIEX. The ICP-MS is a chemical analysis that counts the number of ions at a certain mass of the element. The sample is introduced in the nebulizer and is converted into small droplets, which are then carried through the spray chamber, the tube and finally into the plasma, which ionizes the elements present in the droplets. These ions pass through the interface, are focused by the ions lens, separated by their mass-to-charge ratio in the mass spectrometer and measured by the detector. The measured signal intensities are converted into concentrations of each element (by the computerized data system). A calibration curve is generated from the measurements of standards in order to compare them with the signals from unknown samples and to determine the concentration of each metal in the sample.

The concentrations of Mo and Pu in the solution of Mo/PuO_2 pellet dissolution were determined by ICP-MS (Perkin Elmer Elan 6100) after dilution in 2% HNO_3 suprapure by a factor of 10,000.

^{241}Am was determined by γ-counting (Packard Cobra Auto-Gamma 5003) in samples diluted by a factor of 100. Several samples were also measured on a HP-Ge gamma spectrometer to convert count rates from the gamma counter to activity concentrations.

The acid concentration of aqueous solutions was determined by potentiometric titration with a “798 MPT Titrino” from Metrohm. Titrations were carried out with 0.01 mol/L NaOH solutions.

3.4 *Speciation of Molybdenum in Nitric Acid*

3.4.1 ALBATROS ESI-ToF

The ALBATROS ESI-ToF was developed by T. Bergmann[190-193] and is located at the Institut für Radioökologie und Strahlenschutz (IRS) within the Leibniz Universität Hannover. Its set-up is displayed in Figure 21. The homemade nanospray ion source was operated with spray capillaries from New Objectives Inc. (Woburn, MA, USA) with an inner tip diameter of 2 μm to which a voltage of typically 2100 V is applied to generate the electrospray. The capillaries were filled with about 10 μL of the sample. To support a stable flow of the sample, a nitrogen pressure of < 0.5 bar was applied to the rear end of the needle. The flow rate was approximately 15 μL/min.

The charged particles enter the mass spectrometer through the orifice. Nitrogen with a flow rate of 0.5 L/min was used for the inverse flow. Between orifice and skimmer a voltage of 42 V was applied. After passing three differential pumping stages (about 10^{-3}, 10^{-5}, 10^{-7} mbar) the ions were injected orthogonally into the time-of-flight (ToF) analyser (10^{-7} mbar). The device was operated in positive ion mode. Mass resolutions of up to $m/\Delta m = 26000$ are possible.

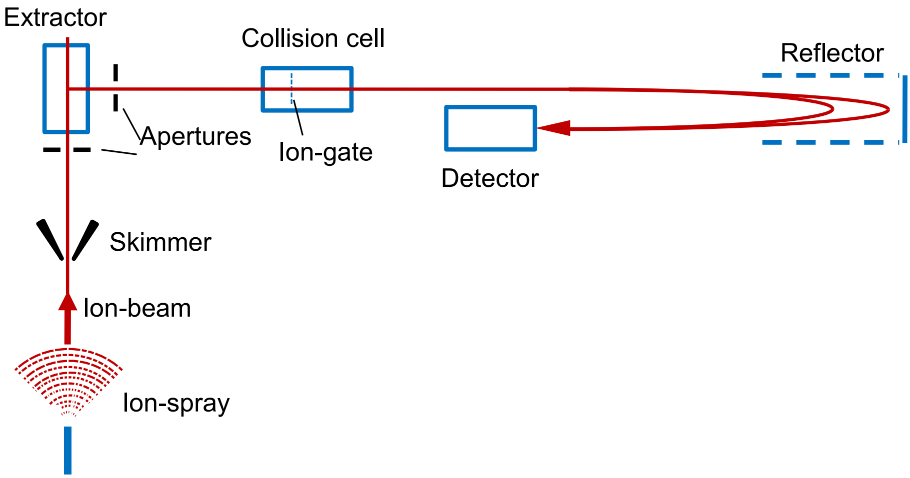

Figure 21: Schematic set-up of the ALBATROS ESI-ToF.[194]

3.4.1.1 *Sample Preparation*

Samples were prepared by dissolving isotopically pure ^{98}Mo metal-powder or pellets in nitric acid. The motivation for using isotopically pure molybdenum can be clearly seen in Figure 22. On the left a part of a mass spectrum of a solution containing natural molybdenum is shown. The right figure depicts a spectrum of isotopically pure molybdenum. Natural molybdenum has seven isotopes (compare section 1.8.3). Thus for each molybdenum molecule we can see several peaks (isotopic pattern) caused by the different isotopes.

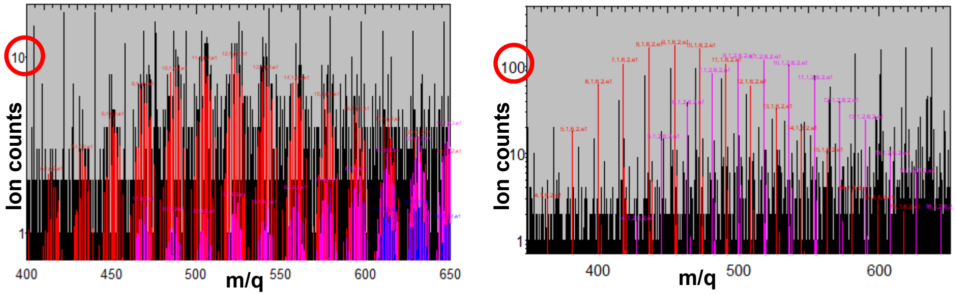

natural Mo

isotopically pure ^{98}Mo

Figure 22: Part of a mass spectrum of a solution containing natural molybdenum (left) and isotopically pure ^{98}Mo (right).

This means, that the ion counts of each species are distributed over several isotopic peaks. The effect of applying isotopically pure molybdenum is clearly visible in the spectrum on the right side. The whole signal intensity falls into one peak for each species. Consequently, for the same concentrations the signal intensity increases. In the mass spectra the ion counts are plotted as a function of the mass divided by charge ratio. The counts are plotted on a logarithmic scale to facilitate the visualization of minor species.

Two different acidic strengths (0.5 and 1 mol/L HNO_3) were used. During the dissolution of the Mo metal, taking about two weeks for complete dissolution, colour changes of the Mo solutions were observed. ESI-MS measurements on the solutions obtained during the dissolution of ^{98}Mo metal were performed. Additionally, a solution containing molybdenum and iron (ratio 1:1) was investigated. Therefore, a stock solution containing 1 mol/L $Fe(NO_3)_3 \cdot 9H_2O$ was prepared and added to the molybdenum sample. Moreover, the evolution of molybdenum speciation during the dissolution process was studied as a function of time. For this purpose, a ^{98}Mo pellet (38 mg) was dissolved in 1 mol/L HNO_3 at 60 °C and several spectra were recorded during the dissolution.

3.4.2 Commercially Available ESI/MS/MS Instrument (QTrap)

All experiments with the commercially available ESI/MS/MS instrument (QTrap) were performed at the Zentralinstitut für Engineering, Elektronik und Analytik (ZEA-3) within the Forschungszentrum Jülich GmbH. The aim of utilising a commercial instrument is to significantly shorten the measurement time and allow routine measurements.

3.4.2.1 Development of a Measurement Protocol

A measuring protocol to analyse solutions of molybdenum with natural isotopic composition with a commercially available ESI/MS/MS instrument (QTrap) was developed. Sodium molybdate dihydrate ($Na_2MoO_4 \cdot 2H_2O$) and ammonium molybdate (para) hydrate ($(NH_4)_6Mo_7O_{24}$) were dissolved in water and used as standard compounds; the molybdenum concentration was 10 mmol/L.

The stability of the detected polymolybdate anions was analysed with MS/MS experiments which were performed for the hexamolybdate (m/z 881.5) and the tetramolybdate (m/z 590).

Additionally, the influence of the solvent acetonitrile (AcN) on the relative abundance of polymolybdates in the molybdenum sample in 1 mol/L HNO_3 was systematically investigated. The Mo metal sample was diluted 1:100 with different AcN proportions in the solvent (0%, i.e. deionized water, to 99% acetonitrile). Acetonitrile is used to reduce the surface tension of the solution. The smaller the surface tension γ, the easier it is to generate finer charged droplets. Therefore, the addition of acetonitrile has the advantage of higher signal intensity. Measurement of the sample was performed by direct infusion, in the negative ion mode, Q1 scan, with an ions spray voltage (IS) of -4.5 kV or -5 kV. The measuring range was m/z 100 - 1500. Each sample was measured at three different declustering potentials (DP): -40 V, -100 V and -175 V. From the recorded spectra, a mean spectrum was calculated for each DP.

Analogous to the variation of the acetonitrile content at constant dilution factor, the influence of the variation of the dilution factor (1:200, 1:100, 1:50, 1:25, 1:10) was investigated for two solvents: water and 25% AcN. The dilutions were measured with the same measurement parameters as before. The peak areas were integrated analogue and the relative percentage for each polyoxomolybdate of the sum of the peak areas were determined.

For the simplified semi-quantitative estimation of the relative concentrations of the polymolybdates in the sample at this time only the peak area (in the selected double peak areas) can be used. It must be assumed that (i) the spectrum represents the real distribution of polymolybdates in the sample solution and (ii) all polymolybdates can be detected with the same sensitivity. Regarding assumption (i) systematic studies of various dilutions are required, to characterize the effect of Mo species concentration, HNO_3 concentration and the solvent (acetonitrile) on the relative molybdenum species distribution. With respect to assumption (ii) it is likely that the electrospray ionization efficiency depends on the degree of polymerization of the Mo species. Therefore, stable, well-characterized single standards of polymolybdates are required for calibration. Such standards are currently not available.

3.4.2.2 Measurement Conditions

Based on the studies of optimal measurement conditions, a protocol for the routine measurements was determined. Mo samples were diluted in water 1:100 and measured by direct infusion in the negative ion mode at a DP of -40 V. The quantitative evaluation was performed as before by determining the peak areas (integration) for the signals of the polyoxomolybdates. The relative abundance of polyoxomolybdates was calculated from the ratio of each peak area to the sum of all peak areas.

The speciation of molybdenum in nitric acid was investigated as a function of acid concentration for 0.1, 1, 2, 3, 4 and 7 mol/L HNO_3. Moreover, the influence of iron(III) on the speciation of molybdenum in nitric acid was investigated. For this purpose, samples of molybdenum in 1 mol/L HNO_3 with increasing iron concentration were measured analogous to the samples without iron in the negative mode.

3.4.3 Raman Spectroscopy

The speciation experiments during pellet dissolution were completed by subsidiary Raman measurements on equivalent solutions with molybdenum of natural isotopic composition. Raman spectroscopy is a short-range order method, which gives information about vibrational, rotational and other low frequency transitions between atoms. Raman spectra were recorded on the surface of liquids in the range of 800 – 1090 cm^{-1} with a HORIBA Jobin Yvon LabRam HR set up with a focal length of 800 mm, equipped with a Peltier-cooled CCD-detector. For the measurements a He-Ne laser (wavelength 632.8 nm), a grating with 1800 grooves per millimetre and an Olympus 100x-objective were used. Hole and slit were set to 1000 and 100 mm, respectively. The exposition time was set to 150 s, with an accumulation of 2. To obtain higher intensities in the interesting region additional spectra were recorded in the range of 800 – 1010 cm^{-1} with an exposition time of 1000 s; the remaining parameters were not changed.

3.5 Separation of Molybdenum by Thermal Treatment

As an alternative to the very complex dissolution of Mo-based IMF the separation of the matrix material from the fuel by thermal treatment was considered. This exploits the oxidation of molybdenum in air at temperatures from 400 °C and the sublimation of the resulting MoO_3 sublimes at 800 °C.

It is expected that the volatile components of the fuel (e.g. Cs, I) are not deposited together with the molybdenum and the remaining components of the fuel do not evaporate at these temperatures.

An apparatus was constructed substantially of a quartz tube 15 mm inner diameter and 50 cm length, which was placed in a horizontal SiC tube furnace. The sample (pellet or powder 10-150 mg) to be treated was placed in a quartz boat which was positioned in the middle of the furnace with a feed rod (Figure 23). The temperature control was performed with a thermocouple set into a quartz tube. The measurement site was located immediately adjacent to the sample boat. The apparatus was flushed with synthetic air, 1.3 L/h, to allow the oxidation of the molybdenum. The apparatus allowed for the connection of a washing bottle or a cold trap to catch any other components of the fuel.

The thermal behaviour of molybdenum was investigated from RT up to 1000 °C by thermogravimetry (TG) coupled with differential scanning calorimetry (DSC) in air at a heating rate of 10 K/min. The measurements were performed with an apparatus from the company Netzsch, model STA 449C Jupiter.

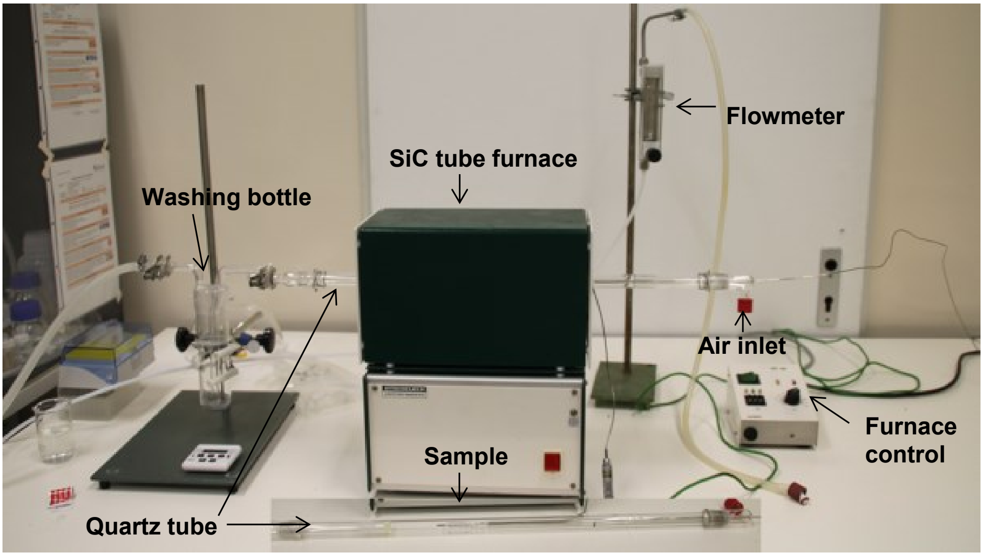

Figure 23: Set-up for thermal treatment of molybdenum, consisting of a quartz tube, which was placed in a horizontal SiC tube furnace. The sample is provided in a quartz boat in the centre of the oven.

3.6 Extraction Experiments

The extraction of Mo, Mg, U, Am, and Eu by three different solvents was tested. The used solvents were:

- 30% TBP in TPH (hydrogenated tetrapropene, industrial kerosene diluent), PUREX solvent
- 0.6 mol/L DMDOHEMA in Exxsol-d80 (industrial kerosene diluent), DIAMEX solvent
- 0.2 mol/L TODGA in Exxsol-d80 (industrial kerosene diluent), TODGA-like solvent

Equal volumes of 500 µL per phase were used in liquid-liquid extraction experiments. Aqueous solutions were spiked with trace amounts of ^{nat}U, ^{241}Am and ^{152}Eu, respectively.

Magnesium solutions (0.008-37.5 g/L) were prepared by dissolving a weighted amount of MgO in 3.09 mol/L HNO_3. Accordingly, the acid concentration decreased with increasing Mg concentration, due to partial neutralization of HNO_3, while the nitrate concentration was constant. An overview of the Mg concentrations and the corresponding acid and nitrate concentrations of aqueous solutions used for the extraction experiments is shown in Table 10.

Increasing weighted amounts of $(NH_4)_6Mo_7O_{24}\cdot 4\ H_2O$ were dissolved in 3.09 mol/L HNO_3 for preparation of Mo solutions, keeping the nitrate concentration constant. An overview of the Mo and the corresponding acid and nitrate concentrations is shown in Table 11.

The batch extraction experiments were performed in 2 mL glass vials in a thermostatted aluminium block at 22 °C and the extraction time was 15 minutes. The radioisotopes ^{241}Am and ^{152}Eu were directly analysed using a high-purity germanium spectrometer system (EG&G Ortec, Munich, Germany; equipped with the Gamma Vision software) without any additional sample preparation. The γ-lines at 59.5 keV and 121.8 keV were examined for intensities of ^{241}Am and ^{152}Eu, respectively. The results are reported as distribution ratios D ($D = [M_{org}]/[M_{aq.}]$), which have an uncertainty of ±5%, detection limits are 500 > D > 0.002.

Table 10: Magnesium solutions used for solvent extraction studies.

Mg concentration (g/L)	Acidity (mol/L)	$c(NO_3^-)$ (mol/L)
0.008	2.89	3.09
0.081	2.84	3.09
0.784	2.67	3.09
7.85	2.37	3.09
23.6	1.23	3.09
37.5	0.01	3.09

Table 11: Overview of the Mo concentrations and the corresponding acid concentrations.

Mo concentration (g/L)	Acidity(mol/L)	$c(NO_3^-)$ (mol/L)
0.010	3.09	3.09
0.102	3.09	3.09
1.02	3.08	3.09
9.57	3.02	3.09
43.4	2.74	3.09
106.2	2.23	3.09

Mg, Mo, and U were analysed using ICP-MS to determine the concentration of each element in the organic and aqueous phase. The aqueous phases were diluted with 1% HNO_3 (suprapure) to an appropriate concentration and measured directly. The organic phases were diluted with 1% HNO_3 (suprapure) containing 0.2% Triton-X 100 in order to disperse the organic phase in the sample homogenously. The results are given as distribution ratios D.

4 Results and Discussion

4.1 *Magnesium Oxide as CerCer Matrix Element*

Magnesium oxide pellets as well as pellets containing different amounts of CeO_2 (5, 10, 25, and 40 wt.%), which serves as surrogate for PuO_2, were synthesized by powder metallurgy.

4.1.1 Physical Properties and Microstructure

All fabricated pellets were thoroughly characterized by means of density measurements, micro hardness measurements, SEM investigation, and XRD. The micro hardness, fracture toughness and brittleness index of the different pellets were determined using a Vickers indenter.

4.1.1.1 Compactibility and Sinterability

MgO and mixed MgO/CeO_2 reference samples have been fabricated by powder metallurgy. Therefore, a detailed compactibility and sinterability study was performed. Compaction pressures between 130 and 765 MPa were applied and the pellets were sintered at 1200 to 1600 °C. The green densities (determined by geometrical method) of pure MgO and mixed MgO/CeO_2 pellets of all investigated compositions are displayed in Figure 24 as a function of the logarithm of the compaction pressure P_c. The relative green densities are plotted as a function of the logarithm of the applied pressure, as recommended in references[195-196]. The relative green densities linearly increase with the logarithm of the pressure. At 765 MPa ($\log(P_c)$ = 2.88) the density of the pure MgO pellet reaches 60% of the theoretical density (3.58 $g \cdot cm^{-3}$). The green densities of the mixed pellets show a similar dependence on the compaction pressure P_c. The green density of the pure CeO_2 pellet increases from 52%TD at P_c = 190 MPa ($\log(P_c)$ = 2.28 MPa) to 63%TD at a compaction pressure of P_c = 700 MPa ($\log(P_c)$ = 2.85 MPa).

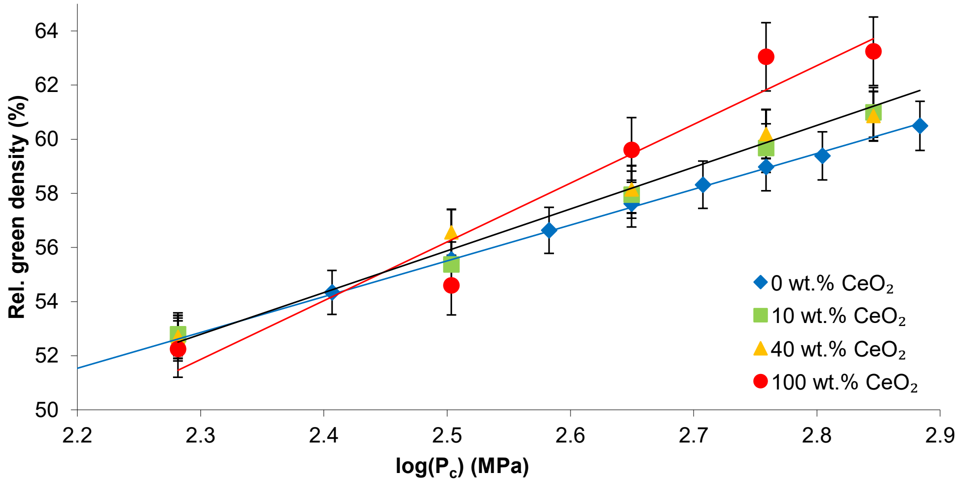

Figure 24: Relative green densities of various MgO/CeO_2 pellet compositions as a function of log(P).

After compaction the pure MgO pellets were sintered for 5 h in air atmosphere at different temperatures. The relative sintered density of the investigated pellets sintered at 1200, 1400, 1500 and 1600 °C was also plotted as a function of the logarithm of the compacting pressure and is displayed in Figure 25. The optimal compacting pressure P_{opt} corresponds to the pressure at the maximal value of sintered density ρ_S. The sinterability curve at a sintering temperature of 1200 °C shows a maximum at about 650 to 750 MPa ($\log(P_c) = 2.81 - 2.88$). In this region, pellets reach densities up to 97%TD. At a sintering temperature of 1400 °C the maximum (densities up to 98%TD) of the sinterability curve is shifted to about 460 to 560 MPa ($\log(P_c) = 2.66 - 2.75$). A maximum of the sintered density ρ_S occurs at about 220 to 320 MPa ($\log(P_c) = 2.34 - 2.51$) at a sintering temperature of 1500 °C. In this region, pellets reach densities up to 99%TD. The dependence of the sintered densities at a sintering temperature of 1600 °C shows a pronounced maximum at $P_c = 480$ MPa. The value of the maximal sintered density in dependence on the compaction pressure varies from 95 to 99%. At $P > P_{opt}$ crack formations take place in the pellets. The value of P_{opt} and the region of ρ_S strongly depend on the sintering temperature T_S (Figure 26). The highest densities are achieved at a sintering temperature of 1500 °C. Applying compaction pressures between 130 and 765 MPa and sintering temperatures between 1200 and 1600 °C sintered densities from 84 to 99%TD can be achieved.

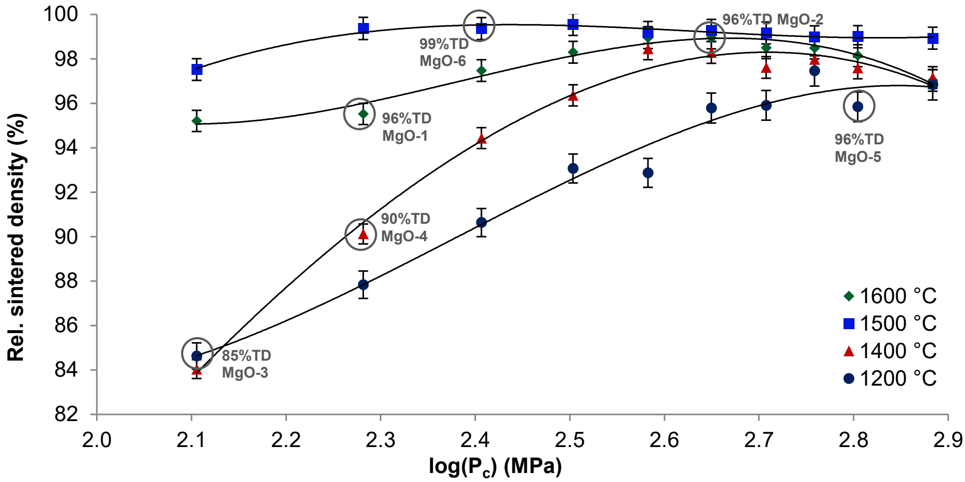

Figure 25: Sintered density of MgO pellets as a function of pressing load and sintering temperature.

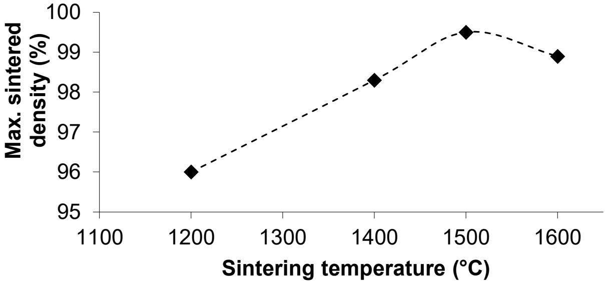

Figure 26: Maximal sintered density obtained as a function of the applied sintering temperature.

The relative sintered densities of various pellet compositions (T_S = 1500 °C) are displayed in Figure 27 as a function of the logarithm of the compaction pressure P_c. Pure MgO pellets show the highest sintered density, which decreases with increasing cerium dioxide content. The sintering densities of the pure MgO pellets and of mixed pellets with CeO_2 contents of 10 and 40 wt.% show distinct maxima at about 320 MPa P_c. The sintered density of pellets containing 25 wt.% CeO_2 is constant in the studied region and amounts to ~ 93%TD.

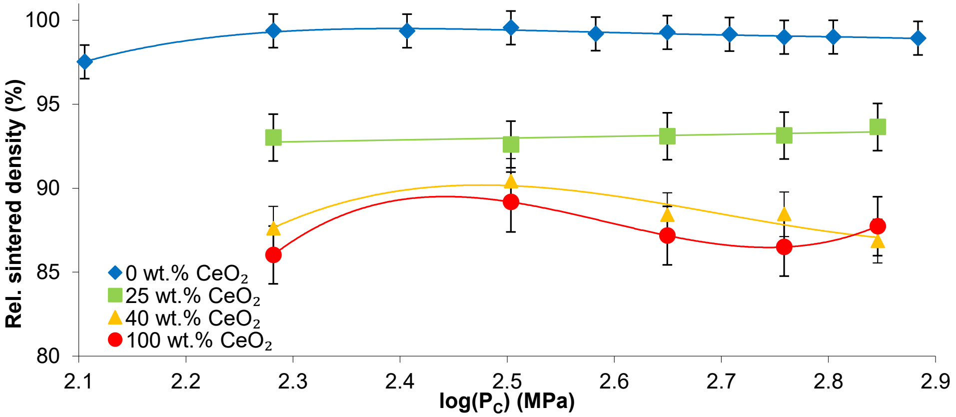

Figure 27: Relative sintered densities of various MgO/CeO_2 pellet compositions sintered at 1500 °C as a function of log(P_C).

The sintered densities of pure CeO_2 and mixed pellets are low compared to pure MgO pellets and do not meet the requirements for pellets representative of irradiated fuel. The production of CeO_2 pellets with higher sintering densities at sintering temperatures of T_s = 1600 °C has been reported by Bukaemskiy *et al.*[185] Since the highest densities were achieved at a compaction pressure of 320 MPa for pellets with 40 and 100 wt.% CeO_2 share, this pressure was selected for comparison of the sintering temperatures. By increasing the sintering temperature from 1500 to 1600 °C an increase in sintered density from about 90%TD to more than 95%TD could be achieved for all pellet compositions (compare Figure 28).

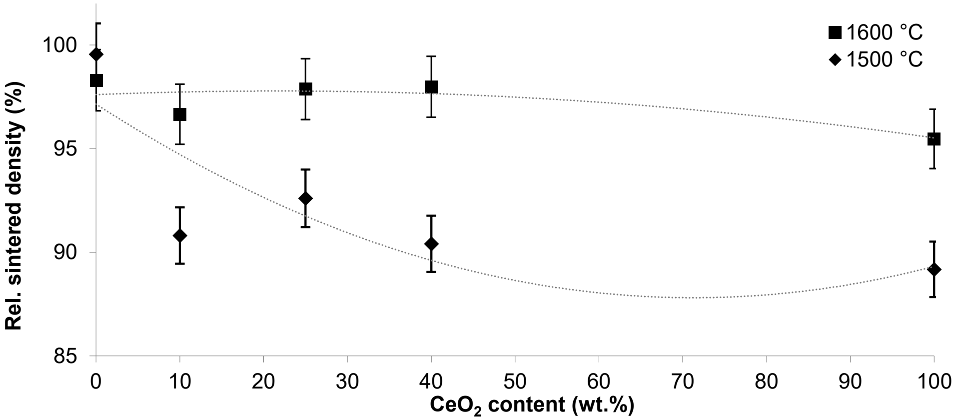

Figure 28: Comparison of the relative sintering densities (P_c = 320 MPa) of pure and mixed MgO pellets sintered at 1500 °C and 1600 °C as a function of the CeO_2 content.

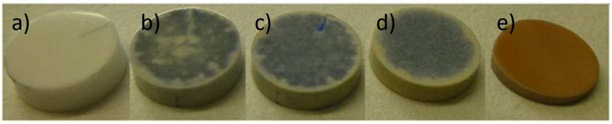

Figure 29: Photographs of pellets of different compositions: a) pure MgO, b) 90/10 wt.% MgO/CeO_2, c) 75/25 wt.% MgO/CeO_2, d) 60/40 wt.% MgO/CeO_2 and e) pure CeO_2.

Photographs of MgO, CeO_2 and mixed MgO/CeO_2 pellets are shown in Figure 29. All pellets were sintered at 1600 °C; the MgO pellet was pressed at 190 MPa and the pure CeO_2 pellet and the mixed pellets were pressed at 320 MPa. The pure MgO pellet exhibits a white, the pure CeO_2 pellet an orange-brown colour. All sintered mixed pellets are light yellow coloured; after polishing grey-green discolorations are revealed in the inner part of the pellet. The amount of discolorations, which increases with increasing CeO_2 content, might originate in the conversion of cerium (IV) to cerium (III), which is yellow-green in colour[197], during sintering. This could be excluded by XRD measurements, showing CeO_2 only (compare Figure 30). XRD measurements were performed for all pellet compositions, the XRD pattern of the pellet with the highest CeO_2 content is shown exemplarily. An overview of pellets used for dissolution experiments and the corresponding compacting and sintering parameters is given in Table 12.

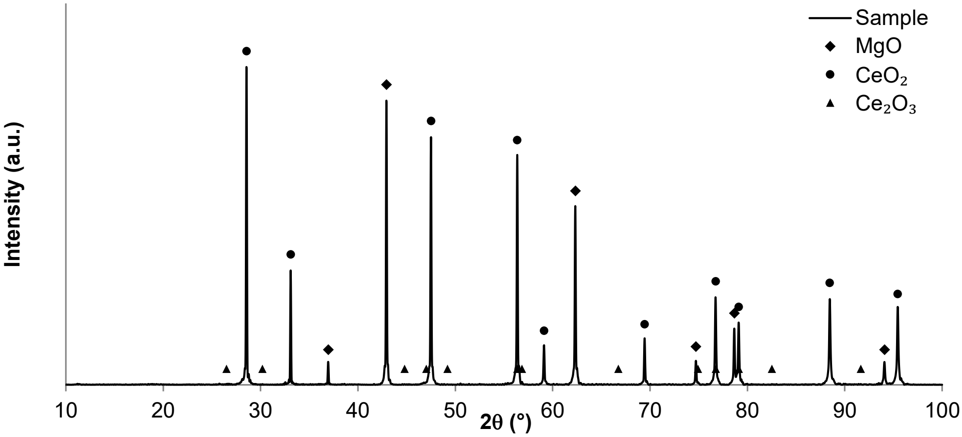

Figure 30: XRD pattern of a mixed MgO/CeO_2 pellets containing 40 wt.% CeO_2.

Table 12: Overview of pellets used for dissolution experiments and corresponding compacting and sintering parameters. The respective pellets are highlighted in Figure 25.

Pellet	Compaction pressure (MPa)	Sintering temperature (°C)	Density (%TD)	Mass (g)
MgO-1	190	1600	96	0.5
MgO-2	450	1600	99	0.7
MgO-3	130	1200	85	0.7
MgO-4	190	1400	90	0.7
MgO-5	640	1200	96	0.7
MgO-6	255	1500	99	0.7
MgO/CeO_2 (60/40 wt.%)	320	1600	98	0.5

4.1.1.2 Micro Hardness

The micro hardness H_V of two MgO pellets (MgO-1, $\rho_S = 96\%TD$, $T_S = 1600$ °C, P = 190 MPa and MgO-2, $\rho_S = 99\%TD$, $T_S = 1600$ °C, P = 450 MPa; compare Table 12) was analysed exemplarily by a diamond Vickers indenter. The micro hardness measures the resistance of a sample to material deformation due to a constant compression load from a sharp object. A typical Vickers indenter photograph is presented in Figure 31.

For the determination of the optimal load, the dependence of the micro hardness of the pellet MgO-2 ($\rho_S = 99\%TD$) as a function of the applied load was investigated. The values of H_V drastically decrease with increasing load from 50 to 200 g as depicted in Figure 32. At higher loads H_V slightly decreases but is nearly constant within the uncertainty range.

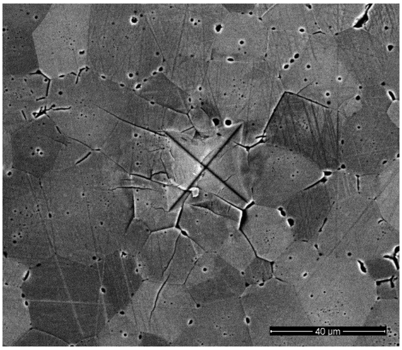

Figure 31: Photograph of a typical Vickers indent on magnesium oxide.

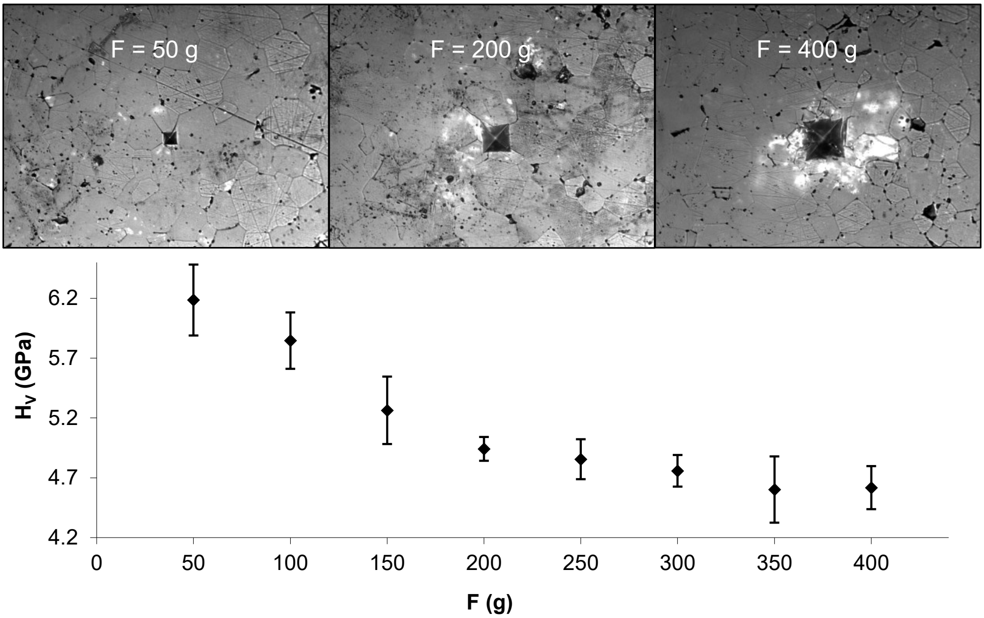

Figure 32: Micro hardness H_V (GPa) of MgO-2 pellet $\rho_S = 99\%TD$ ($T_S = 1600$ °C, $P_C = 450$ MPa) as a function of the load of the Vickers indenter. The pictures at the top show light microscope pictures of the Vickers indent at different loads (magnification x50).

At a load of 50 g the resulting indent is quite small which leads to a large uncertainty; at a load of 400 g the surrounding structure is damaged. As the value of the experimental uncertainty is minimal at F = 200 g this load was selected to measure the samples 15 times each, leading to the following results:

- MgO-1, $T_S = 1600$ °C, $P_C = 450$ MPa, $\rho_S = 96\%$TD: $H_V = 5.2 \pm 0.4$ GPa
- MgO-2, $T_S = 1600$ °C, $P_C = 450$ MPa, $\rho_S = 99\%$TD: $H_V = 5.3 \pm 0.4$ GPa

The micro hardness for both samples is consistent within the uncertainty range.

The dependence of the micro hardness H_v of mixed MgO/CeO_2 pellets ($T_S = 1500$ °C, $P_C = 320$ MPa) on the CeO_2 amount in vol.% is shown in Figure 33. The micro hardness linearly increases with increasing CeO_2 content. The experimental uncertainties of the micro hardness of the mixed pellets are larger compared to those of the pure pellets.

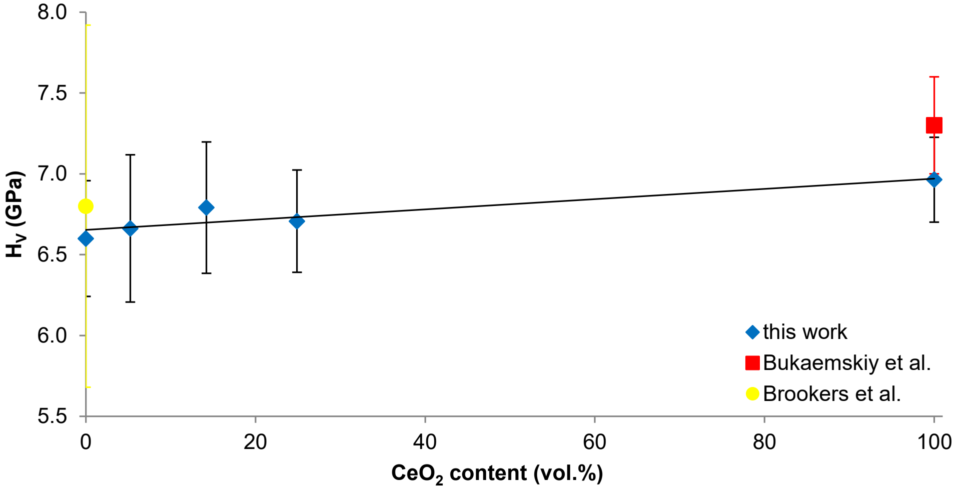

Figure 33: Micro hardness of mixed MgO/CeO_2 pellets ($T_S = 1500$ °C, $P_C = 320$ MPa) as a function of CeO_2 content. For comparison reference data is added for MgO[198] and CeO_2[185].

This phenomenon was investigated in detail on the basis of the micro hardness distribution of both pure and one mixed pellet. Figure 34 compares the micro hardness distribution of the investigated pellets. The H_v distribution reveals two maxima, which correspond to the pure oxides. The micro hardness of the pure MgO pellet is 6.61 ± 0.37 GPa and that of the pure CeO_2 pellet is 6.96 ± 0.26 GPa. The average micro hardness' of pure MgO (green vertical dashed line) and of pure CeO_2 (red vertical dashed line) are highlighted. For the mixed pellets the measured values are not symmetrically distributed. The distribution for the pellet with 10 wt.% CeO_2 share can be described as the sum of two symmetrical average distributions with maxima at ~ 6.5 GPa and ~ 7 GPa, which corresponds to the micro harnesses of pure MgO and pure CeO_2. Since the CeO_2 distribution in the pellets is inhomogeneous and MgO and CeO_2 rich regions exist in the pellet it can be assumed that one curve corresponds to the indentation of a magnesia rich region and one to the indentation of a ceria rich region. The expression of the maxima corresponds to the ratio of magnesia rich to ceria rich regions.

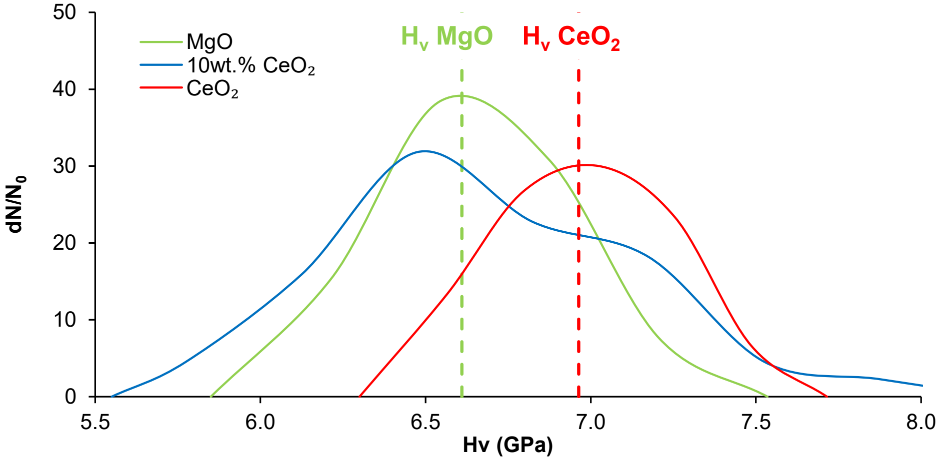

Figure 34: Comparison of the micro hardness distribution of pellets containing different amounts of CeO_2.

For the pellet containing 40 wt.% CeO_2 the first maximum decreases while the second maximum increases; this corresponds to the MgO-CeO_2 ratio. This existence of two separate curves increases the experimental uncertainties for the mixed pellets. The described distribution is not reflected by the plot of the pellet containing 25 wt.% CeO_2. The second maximum is much higher than the first, although the major part of the pellet consists of MgO which may be due to poor statistics or insufficient mixing. Table 13 summarizes the determined micro hardness for the pellets under investigation and the experimental uncertainties.

Table 13: Micro hardness and experimental uncertainties for different pellet compositions.

MgO/CeO_2 (wt.%)	H_v (GPa)	Experimental uncertainty (GPa)
100/0	6.6	±0.36
90/10	6.66	±0.46
75/25	6.79	±0.41
60/40	6.71	±0.32
0/100	6.96	±0.26

4.1.1.3 Fracture Toughness and Brittleness Index

Depending on the type of crack the fracture toughness is calculated by two different equations (compare chapter 3.2.2). Therefore, c/a ratios for the different pellets were calculated and are summarized in Table 14.

Table 14: c/a ratio (c: crack length, a: indentation diagonal) of indentation zones of the different investigated pellets. c/a ratios < 3.5 indicate a Palmqvist type crack.

MgO/CeO_2 (wt.%)	c/a	Crack type
90/10	0.975	Palmqvist
75/25	0.808	Palmqvist
60/40	0.842	Palmqvist
0/100	1.603	Palmqvist

All cracks are of the Palmqvist type which is confirmed by the SEM images of the polished samples (Figure 35). As illustrated by the schematic drawing, the pellet surface is raised at the rim of the indenter zone during the indentation procedure and this elevation is removed by the polishing. Therefore, the crack cannot be observed any longer in the near surrounding of the indentation zone. This effect is visible on the investigated pellets (compare Figure 35).

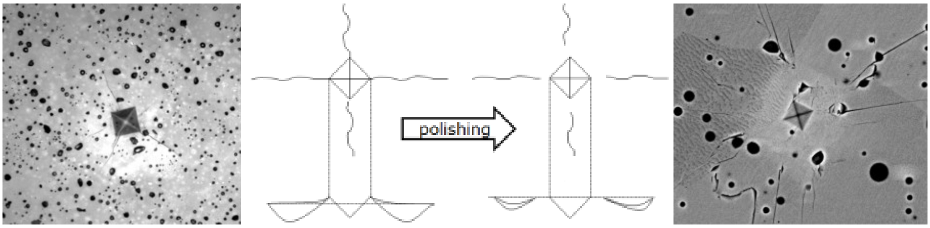

Figure 35: Comparison of indenter zone and cracks before (optical microscope) and after polishing (SEM). CeO_2, P_C = 320 MPa, T_S = 1600 °C.

The fracture toughness K_{1C} of mixed MgO/CeO_2 pellets is displayed in Figure 36 as a function of the CeO_2 share. Both pure materials are brittle materials with low fracture toughness (MgO: 1.38 $MPa \cdot m^{0.5}$ and CeO_2: 1.02 $MPa \cdot m^{0.5}$). The mixed materials show higher fracture toughness. The cause might be that the small CeO_2 grains lead to the inhibition of the cracks and prevent their proliferation. The determined values for the pure materials are in good agreement with the literature[185, 199]. Reference data for mixed samples was not available.

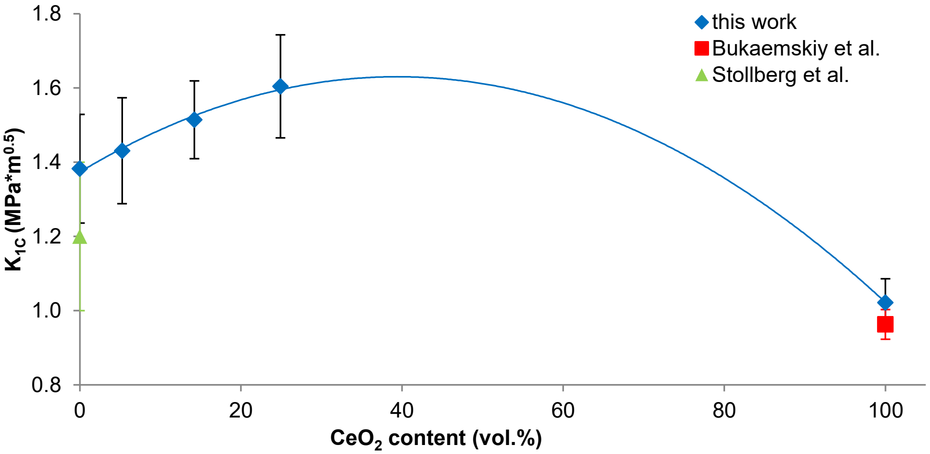

Figure 36: Fracture toughness K_{1C} of mixed MgO/CeO_2 pellets (T_S = 1500 °C, P_C = 320 MPa) as a function of CeO_2 content in vol.%. Reference data is added for MgO[199] and CeO_2[185].

The **brittleness indices** were calculated using equation (60) and are shown in Figure 37 as a function of the CeO_2 content. In correlation with the results for the fracture toughness; starting from pure MgO (B_i: 4.8 $mm^{-0.5}$) the brittleness index decreases with increasing CeO_2, the brittleness index of CeO_2 is significantly higher (B_i: 6.8 $mm^{-0.5}$). The value determined for CeO_2 is in good agreement with the literature.[185] Overall the pure oxides are more brittle than the mixed oxides.

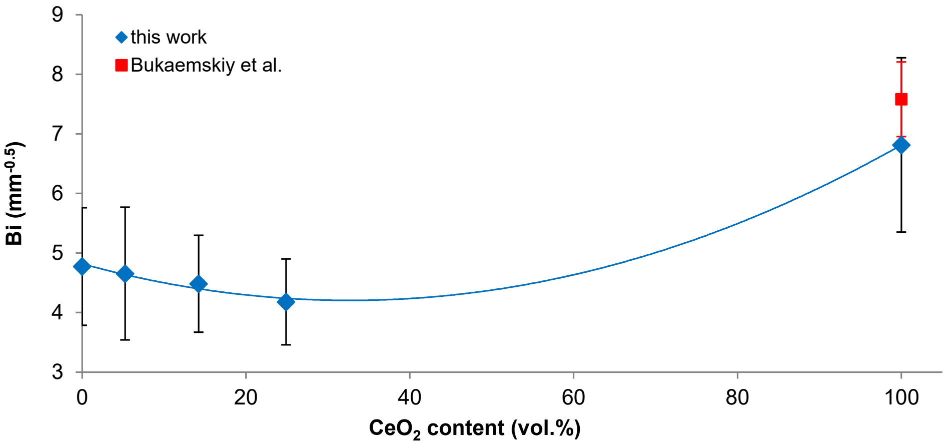

Figure 37: Pellet brittleness indices B_i of mixed MgO/CeO$_2$ pellets (T_S = 1500 °C, P_C = 320 MPa) as a function of the CeO$_2$ content in vol.%. Reference data is added for CeO$_2$[185].

4.1.1.4 Scanning Electron Microscopy Investigation

The microstructure of two pure MgO pellets ρ_S = 96%TD (MgO-1, T_S = 1600 °C, P = 190 MPa) and ρ_S = 99%TD (MgO-2, T_S = 1600 °C, P = 450 MPa) was analysed using SEM. The less dense pellet (MgO-1) shows high porosity (Figure 38, a): inter and intra granular porosity (diameter of pores $d_p \leq 1\mu$m), pores at grain boundaries and at triple points. The denser pellet (MgO-2, Figure 38, b) shows well-formed grains and grain boundaries. The quantity of pores is insignificant compared to the less dense pellet. The denser pellet (MgO-2) shows a lower quantity of intra granular porosity and the pores are smaller, the porosity is concentrated at the grain boundaries and triple points. The grains show different shades (grey, dark grey & white) but EDX analyses just show pure MgO (compare Figure 39, Table 15). As shown in Table 15 there is no significant chemical differences between the different shades of white, grey and dark grey. The different shades of the grains are caused by different crystal orientations.

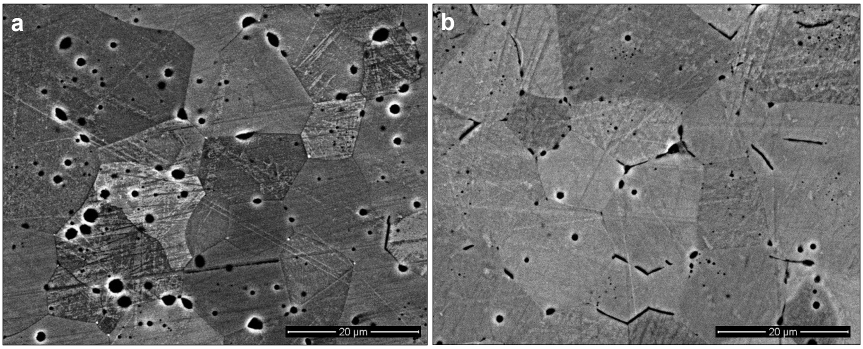

Figure 38: Comparison of the microstructure of samples less dense pellet (MgO-1, 96%TD, a) and a denser pellet (MgO-2, 99%TD, b).

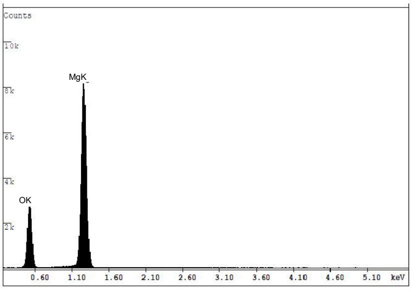

Figure 39: EDX analysis of the magnesium oxide pellet surface.

Table 15: EDX analysis on of grains of the MgO pellet with different colour.

	O (at.%)	**Mg (at.%)**
white	52.82	47.18
dark grey	52.89	47.11
grey	52.65	47.35
Σ	52.78	47.22

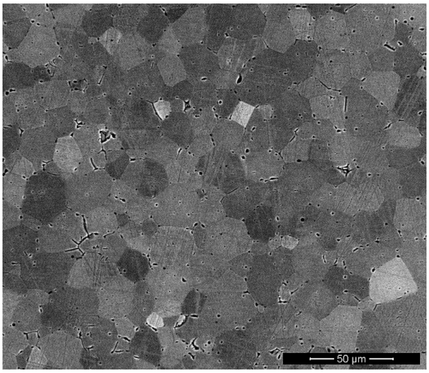

Figure 40: Representative surface of a MgO pellet $\rho_S = 99\%$TD (MgO-2, $T_S = 1600$ °C, P = 450 MPa).

The average grain size was determined for the denser pellet (ρ_S = 98.9%TD). Minimal and maximal size were measured for 217 grains (Figure 40). The grain size distribution is displayed in Figure 41 (left). The average grain size D_{av} amounts to 15.3 ± 6.0 µm, the rate of sphere D_{max}/D_{min} to 1.4 ± 0.4 µm. The number of sides of the grains n was determined for 120 grains. The number of sides' distribution is displayed in Figure 41 (right). The mean number of sides equals 5.

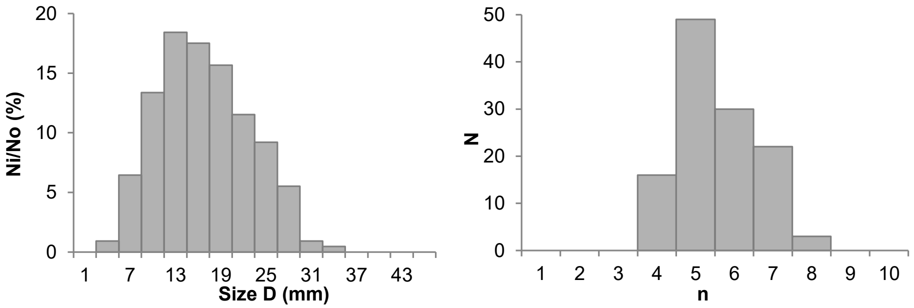

Figure 41: Grain size distribution (left) and grain morphology distribution (right) of a MgO pellet ρ_S = 98.9%TD (T_s = 1600 °C, P_C = 450 MPa).

The representative SEM images of pellet surface of MgO pellets containing different amounts of CeO_2 are presented in Figure 42 after polishing and chemical etching. Well-developed grains and grain boundaries are visible in the case of pure CeO_2 pellets, but the porosity is very high and the size of the pores is larger compared to the pure MgO pellets (Figure 40), pores are located inside the grains as well as at the grain boundaries and the triple points. The different levels of grey are due to different crystal orientations as described above.

All mixed pellets show well-formed grains and well defined grain boundaries as well as a small amount of pores including few spherical pores. The pellets consist of lighter and darker regions on which EDS measurements were performed (Figure 43). The EDS spectrum of the darker grain shows only magnesium peaks (Magnesium K-Lines), whereas the spectrum of the lighter grain shows mainly the L-lines of CeO_2. However, the magnesium K-lines also appear in the spectrum, because the depth of the measuring range of the EDS is higher than the depth of the CeO_2 grain, MgO which is located below the CeO_2 grain is also detected as demonstrated in Figure 44. The distribution of the two phases in the pellet is similar as for the CerCer pellets fabricated at ITU, in which actinides in yttria-stabilized zirconia particles are dispersed in a MgO matrix.[8]

The sizes of the CeO_2 grains in the mixed pellets range from 1 µm to 100 µm similar to the MgO grains. The mixed pellets show three distinct regions: 1) CeO_2 rich regions, 2) MgO rich regions and 3) mixed regions with small homogeneously distributed CeO_2 and MgO particles. The amount of CeO_2 in the mixed regions increases with increasing CeO_2 content but pure MgO regions do also exist in pellets containing 40 wt.% CeO_2 (Figure 42). All pellet compositions were investigated in detail, but the results for pellets containing 10 wt.% are presented here exemplarily.

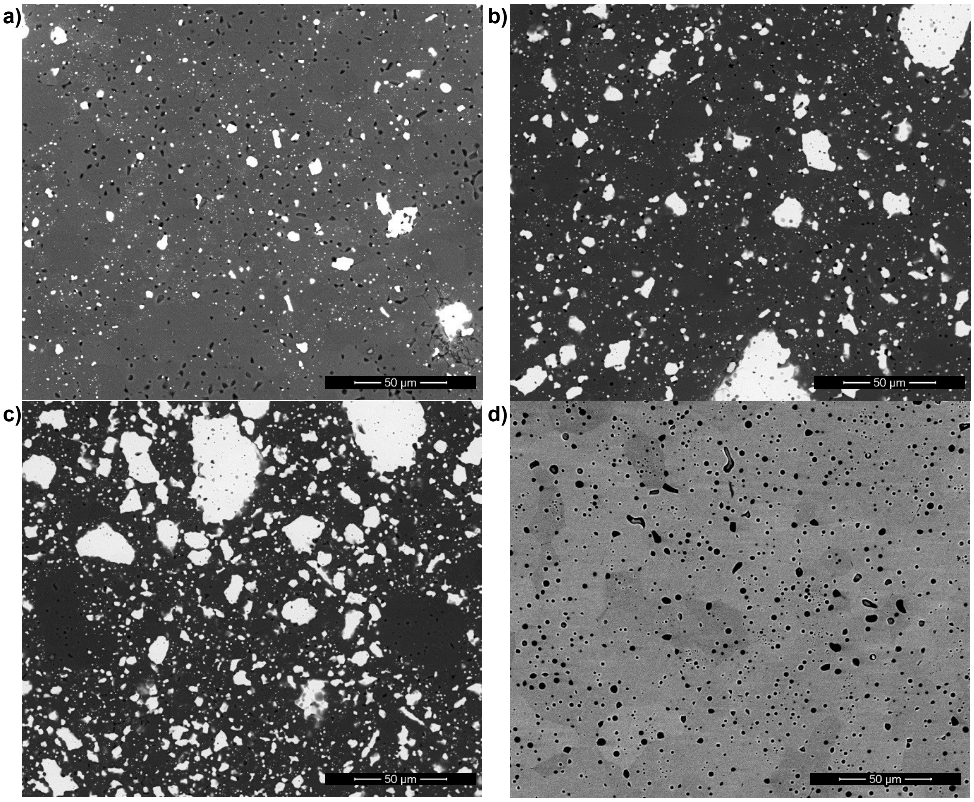

Figure 42: SEM images of pellet surfaces MgO containing: a) 10 wt.% CeO_2, b) 25 wt.% CeO_2, c) 40 wt.% CeO_2, and d) pure CeO_2. All pellets were polished and etched with ammonium nitrate solution for 3 h.

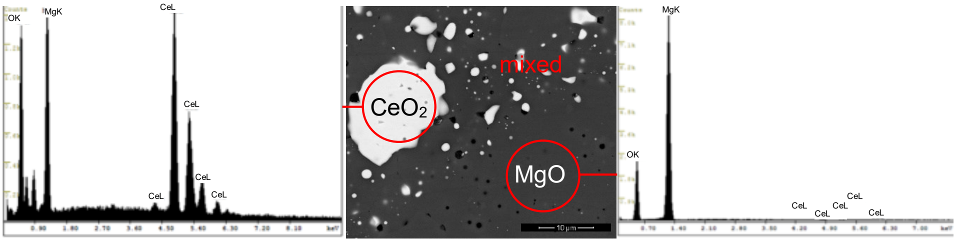

Figure 43: EDS measurement of MgO and CeO_2 rich regions.

The CeO_2 rich regions mainly consist of large pure CeO_2 grains, which were formed from large CeO_2 particles during sintering. The small CeO_2 grains (~ 1 µm) are located mainly distributed alongside the MgO grains with a characteristic size of ~ 10 µm. Presumably the calcined and hand milled MgO powder consists of some amount of porous agglomerate with a characteristic pore-size of 1 µm into which small CeO_2 particles penetrated in the process of mixing. The pellets consist mainly of well mixed regions and the amount of CeO_2 and MgO rich regions is low as evident from Figure 42. This is the consequence of an appropriate powder mixing procedure. It should be especially noted that the two phases (MgO and CeO_2) are well connected (Figure 45).

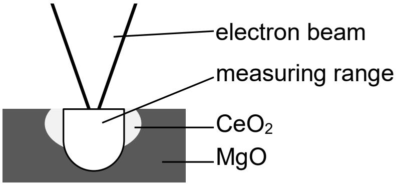

Figure 44: Comparison of measuring range of the EDS and a CeO_2 grain.

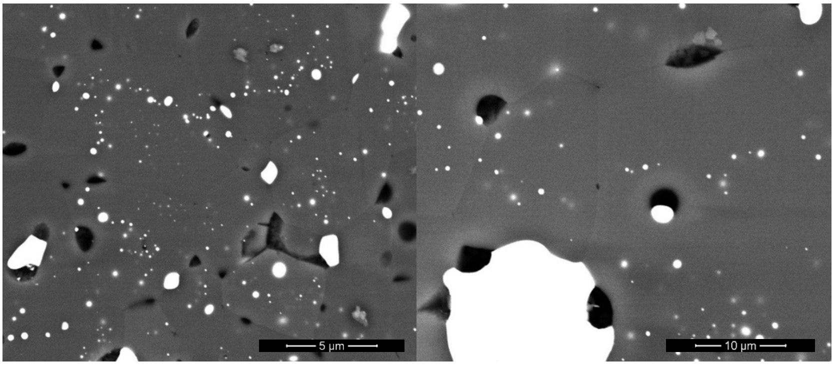

Figure 45: Etched surface of pellet with 10 wt.% CeO_2 share at two different magnifications.

4.1.2 Dissolution Behaviour

The dissolution behaviour of these pellets was studied in macroscopic experiments as a function of acid concentration and volume, temperature and stirring velocity. Additionally, the dissolution process of MgO was investigated following a microscopic approach on the basis of SEM.

4.1.2.1 Mechanism of MgO Dissolution

The chemical dissolution mechanism of six MgO pellets was investigated by reaction with 2.5 mol/L HNO_3 at 30 °C with reaction times of 0, 0.5, 2, 3.5, 8 and 15 h respectively. The remaining solid was carefully washed with water and 2-propanol and dried at 90 °C for SEM investigation. Figure 46 displays the magnesium ion concentration as a function of the reaction time in 2.5 mol/L HNO_3 at 30 °C. In order to avoid particles that may have been removed during sampling, the solution was filtered with a PVDF syringe filter unit (0.22 µm, Millex-GV). Each solution was measured once with and once without filtration. At the beginning of the experiment the concentration of the Mg^{2+} strongly increases and then levels off after about five hours reaction time. The measurements show no systematic difference between the filtered and the unfiltered samples.

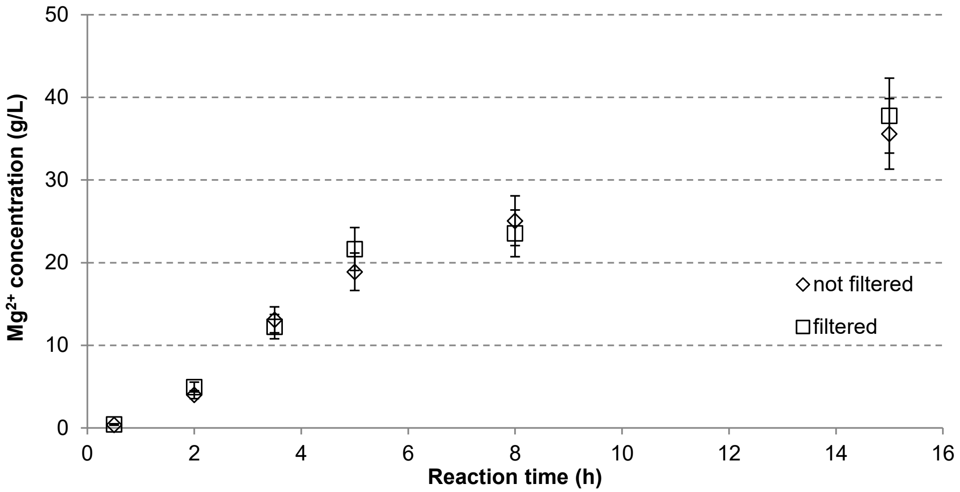

Figure 46: Mg^{2+} concentration as a function of the reaction time for dissolution of MgO pellets in 10 mL of 2.5 mol/L HNO_3 at 30 °C.

According to the literature the dissolution of magnesium oxide may be described by the following reaction[94]:

$$MgO + 2H^+ \rightarrow Mg^{2+} + H_2O \tag{61}$$

Assuming that this equation describes the dissolution reaction correctly, the theoretically required proton consumption for the dissolution of MgO at the different reaction times can be calculated from the results of the ICP-MS measurements:

$$n(H^+)_t=2\cdot n(Mg^{2+})_t \tag{62}$$

with the proton concentration $n(H^+)_t$ at the time t and the Mg^{2+} concentration $n(Mg^{2+})_t$ at the time t. Two protons are required to dissolve one equivalent of MgO. Figure 47 shows the measured release rate of Mg^{2+} in mol/h (squared symbols) as a function of the reaction time. Additionally, the calculated amount of protons required for the dissolution of the MgO (open circles) is displayed. For comparison the proton release rate measured by titration is shown as filled circles. The comparison of the calculated and the measured proton consumption rates show good agreement. At the beginning of the experiment the consumption rate of protons increases until a reaction time of 5 h. For longer reaction times a decrease of the proton consumption rate is observed. In correlation, Mg^{2+} release rate increases for short reaction times and then decreases. At the investigated conditions (2.5 mol/L HNO_3, 30 °C) an MgO pellet dissolved completely within about 20 h.

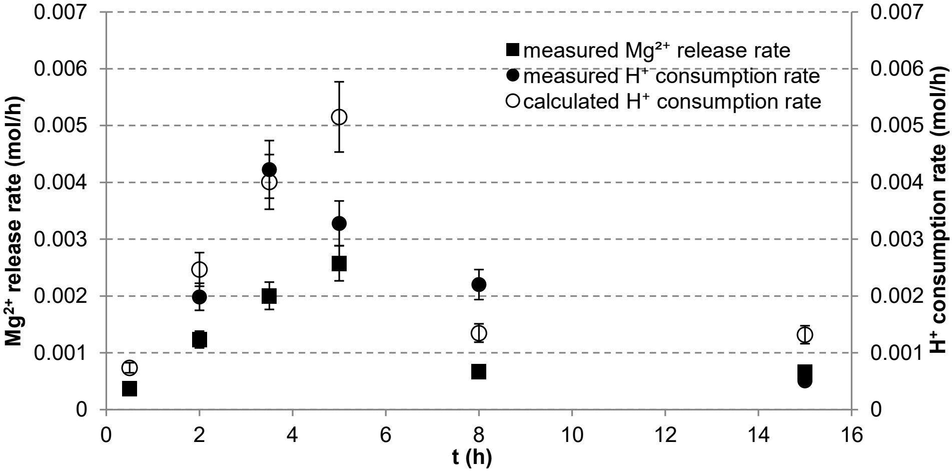

Figure 47: Temporal evolution of the Mg^{2+} release rate during dissolution of a MgO pellet (MgO-1, 500 mg, 10 mL 2.5 mol/L HNO_3, 30 °C) compared to the calculated and the measured H^+ consumption rates.

However, a literature review has pointed out a brucite-like ($Mg(OH)_2$) layer formation at the periclase (MgO) surface during the dissolution. The dissolution of MgO has been investigated by various authors[89-90, 92-94], including determination of dissolution rates, morphology evaluation and chemical reaction. In the majority of these studies MgO powder was used. According to Segall *et al.*[89] the important factors for the determination of the dissolution kinetics of MgO are atomic surface detail, surface morphology, and bond strength for the solid and diffusion, pH, and electrolyte concentration for the solution. At low pH (2-5) MgO (periclase) dissolves in HNO_3 by first forming a brucite-like ($Mg(OH)_2$) layer on the surface.[90, 92] A two-step protonation of periclase is introduced by Wogelius *et al.*[92] and Fedorocková *et al.*[94]. Vermilyea *et al.*[90], Wogelius *et al.*[92], Segall *et al.*[200], and Fedorocková *et al.*[94] propose the second protonation step is rate determining.

An XRD analysis of sintered MgO powder (compare Figure 48) after reaction with 2 mol/L HNO_3 for 2 h, which was washed with 2-propanol and dried, also shows the presence of a brucite phase in addition to the periclase at these conditions (pH_{ini} = 0.3).

Based on these results as well as the preceding studies the dissolution of MgO in nitric acid should be more precisely described by

$$MgO + H^+ \rightarrow Mg^+\text{-}OH \tag{63}$$

$$Mg^+\text{-}OH + H^+ \rightarrow Mg^{2+} + H_2O \tag{64}$$

In a first fast step, surface oxygen is protonated whereby a brucite-like layer is formed (equation (63)) followed by a second slower, rate-limiting step of detachment of Mg from this brucite-like structure (equation (64)). The formation of a brucite or brucite-like layer on the periclase surface during dissolution explains why the dissolution rates of brucite and periclase are identical in the acidic pH region.[92]

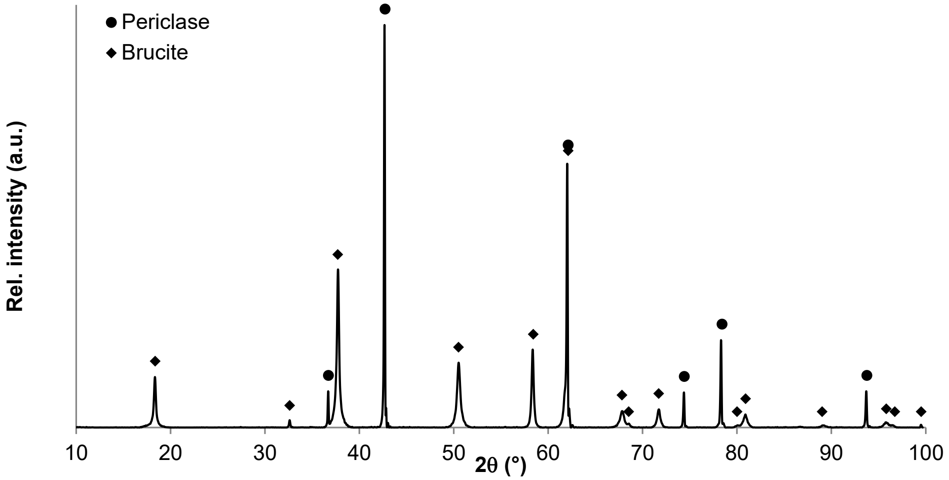

Figure 48: XRD pattern of MgO powder residue after reaction with 2 mol/L HNO_3 (pH_{ini} = 0.3) at RT for 2 h, which was washed with 2-propanol and dried.

4.1.2.2 Temperature Dependence

At PUREX conditions UO_2 is dissolved in 7 mol/L nitric acid under reflux. At these conditions MA and plutonium contained in conventional spent fuel also dissolve.

Since the aim of this work is to evaluate conditions at which the matrix material can be selectively dissolved, the temperature dependence of the dissolution rate of MgO pellets (MgO-1, compare Table 12) in 7 mol/L nitric acid was investigated. The dissolution velocity of MgO in 7 mol/L HNO_3 is strongly dependent on the temperature as demonstrated in Figure 49.

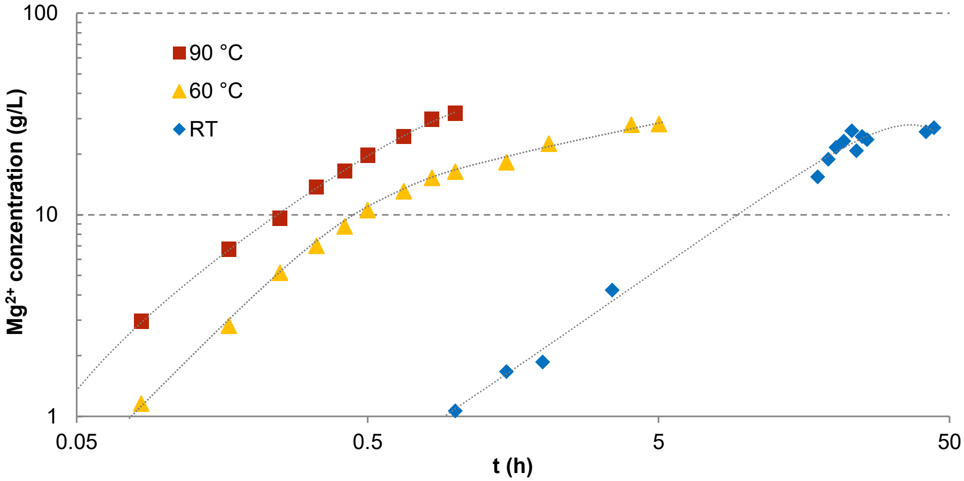

Figure 49: Dissolution of MgO pellets (0.5 g) in 7 mol/L HNO_3 (10 mL) at various temperatures.

The dissolution experiments were compared by plotting average dissolution rate (mg·min^{-1}). Typically dissolution rates are compared by plotting as a function of time. However, since the examined conditions lead to very diverse dissolution velocities the amount of pellet dissolved (%) is plotted instead for a clearer visualization of the results[175]. The average dissolution rate was calculated by equation (65) and percentage dissolution by equation (66).

$$a_{Mg}=\frac{[Mg]V_t}{t} \tag{65}$$

$$P=\frac{100[Mg]V_t}{m} \tag{66}$$

Where a_{Mg} is the average dissolution rate of magnesium (mg/min), [Mg] is the magnesium concentration (g/L), V_t is the volume at the time of sampling (mL), t is time (min), P is the percentage of pellet dissolved (%) and m is the mass of magnesium in the pellet (mg). The dissolution rates a_{Mg} of MgO pellets in 7 mol/L nitric acid at different temperatures are illustrated in Figure 50. In addition to the calculation of the dissolution rates as described above, dissolution rates were derived by the initial rate method. Therefore, the mass of the dissolved magnesium is plotted as a function of time. The slope of the fit to the linear first part of the dissolution curve (compare Figure 51) is equal to the dissolution rate.

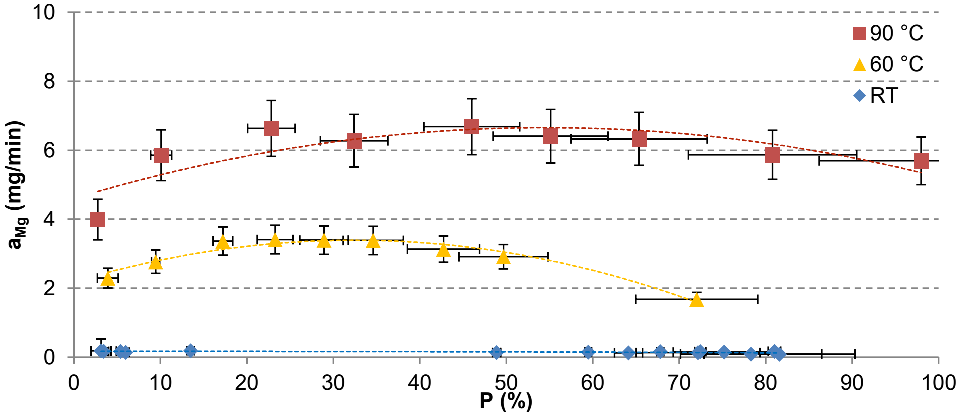

Figure 50: Average dissolution rates a_{Mg} of MgO pellets (0.5 g) in 7 mol/L HNO_3 (10 mL) at various temperatures. P is percentage of pellet dissolved (%).

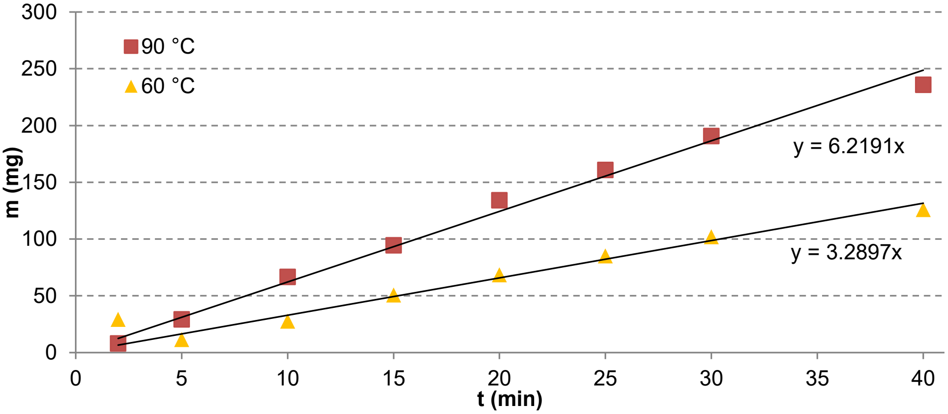

Figure 51: Dissolution of MgO (0.5 g) in 7 mol/L HNO_3 at different temperatures.

The temperature dependence of dissolution rates is typically expressed using Arrhenius law (compare section 1.7, page 15, equation (11)). The label "apparent" is used to distinguish it from the classical activation energy of an elemental reaction, because several elemental reactions might be involved in determining E_{app}.[201] The activation energy can be determined by plotting the rate constant as a function of 1/T. Here, ln (rate) (instead of ln (rate constant)) is plotted versus 1/T. The Arrhenius plot of dissolution rates of MgO in pure MgO pellets in nitric acid of different concentrations is displayed in Figure 52.

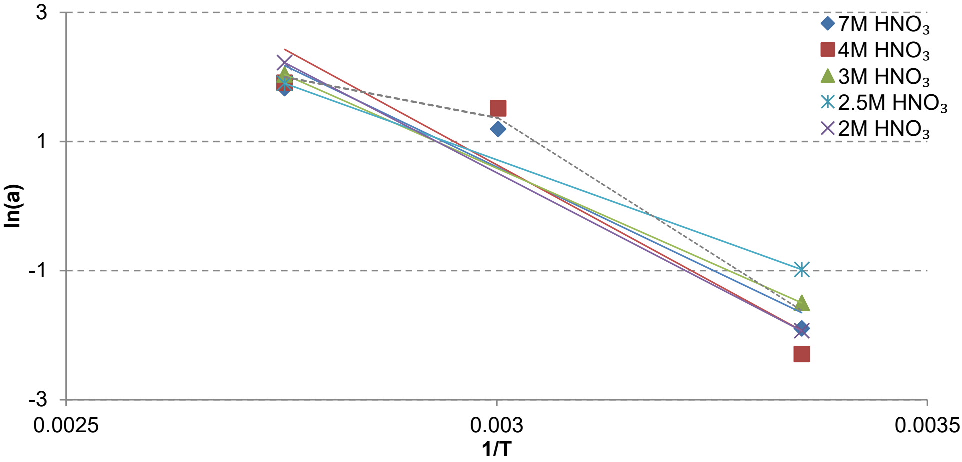

Figure 52: Arrhenius plot of dissolution rates of MgO pellets in nitric acid of different concentrations. The dashed line represents an alternative interpretation of the Arrhenius involving a change of dissolution mechanism with temperature.

In case of transport controlled dissolution, the activation energy would be equal to diffusion.[202] In aqueous medium activation energies of about 20 kJ/mol should be expected. A surface controlled dissolution is indicated by appreciably higher activation energies.[203] An activation energy of 60 ± 12 kJ/mol has been reported for brucite ($Mg(OH)_2$)[203]. The obtained activation energies for dissolution of magnesia in nitric acid of different concentration show no clear trend but vary in the range from 40 to 60 kJ/mol. However, the activation energies indicate a surface controlled dissolution and are in agreement with activation energy of brucite reported by Jordan and Ramsey.[203] An alternative interpretation of the Arrhenius plot based on the outliers at 60 °C suggests a change of dissolution mechanism with temperature as indicated by the grey dotted lines which correspond to a surface controlled dissolution at room temperature and a transport controlled dissolution at elevated temperatures. The amount of data is insufficient to determine the temperature at which the mechanism changes.

Table 16: Activation energies of MgO dissolution at different HNO_3 concentrations.

c(HNO_3) (mol/L)	**$E_{A\ app}$ (kJ/mol)**
2	57.6
2.5	40.0
3	49.0
4	60.4
7	53.0

4.1.2.3 Acid Concentration Dependence

The acid concentration dependence of the MgO dissolution was investigated in the range of 2 to 7 mol/L nitric acid. The comparison of the dissolution rates as a function of acid concentration at different temperatures (Figure 53) shows that the dissolution rate of magnesium oxide is strongly dependent on the dissolution temperature as discussed above, while the acid concentration has hardly any effect in the range of 2 to 7 mol/L. The calculated average dissolution rates (triangles) and the dissolution rates derived from the initial rate method (diamonds) agree within the error limits. These results are in agreement with preceding studies on acid-induced MgO dissolution. For instance, Suárez and Compton[93] found that at concentrations of HCl between 0.01 and 0.1 mol/L changes little, while Guspiel and Riesenkampf[204] found that the dissolution of MgO was constant at concentrations of H_2SO_4 between 0.1 and 2 mol/L, and Jones *et al.*[205-206] report the dissolution of (100) MgO surfaces was independent of pH in the range 2.0-3.5. Although these pH ranges do not correspond to the range investigated here, the trends are in agreement. The dissolution rates of magnesia as a function of the acid volume are depicted in Figure 54 for two different temperatures. The acid volume does not influence the dissolution rate despite the proton consumption. This is in agreement with the observation that the dissolution rate is independent of the acid concentration.

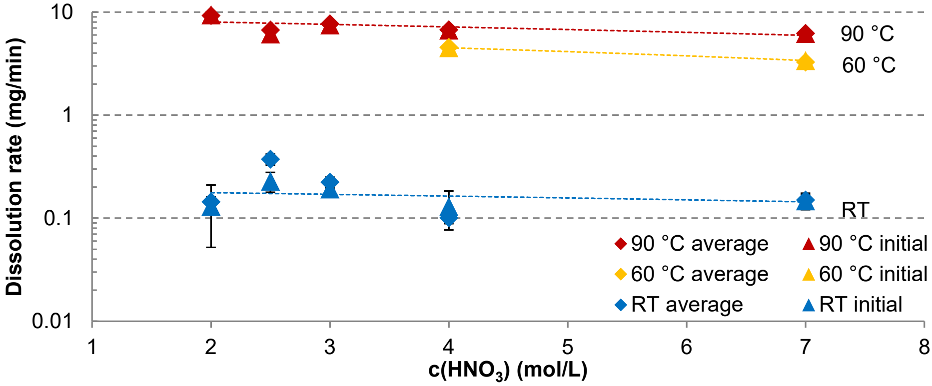

Figure 53: Comparison of the dissolution rates of MgO at different temperatures as a function of acid concentration. Dissolution rates were determined by the initial rate method (triangle symbols) or correspond to the average dissolution rate (diamond symbols).

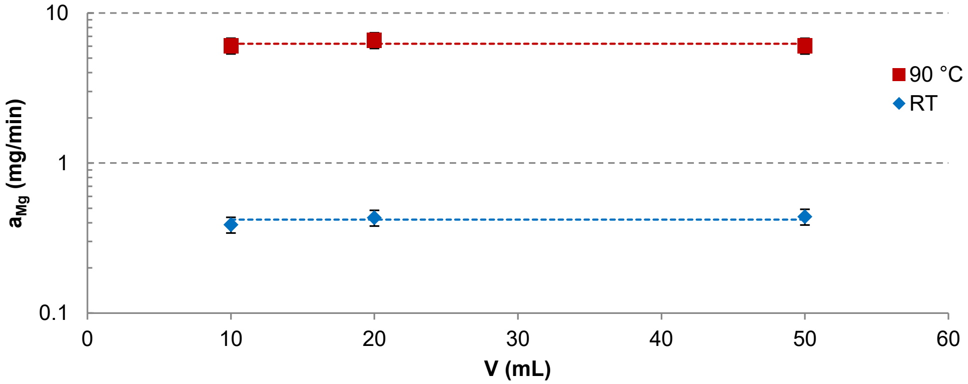

Figure 54: Dissolution rates of MgO in 7 mol/L HNO_3 as a function of the acid volume for different temperatures.

4.1.2.4 Influence of Agitation Velocity

To further investigate whether the MgO dissolution is controlled by surface reaction or by transport the dissolution experiments were performed at varying agitation rates. Figure 55 displays the average dissolution rate of magnesia as a function of the agitation velocity for three different temperatures. The dissolution rate is independent of the agitation velocity within the uncertainty range, which indicates a surface controlled dissolution mechanism. The diffusion of protons to the pellet boundary layer and the diffusion of the dissolved magnesium ions out of this layer is fast compared to the dissolution reaction. These observations are in accordance with the observations from literature [90, 93, 200] and are further supported by the etch pits which were observed at the pellet surface during dissolution. According to Brantley *et al.*[65] etch pit formation at the pellet surface indicates a surface controlled mechanism.

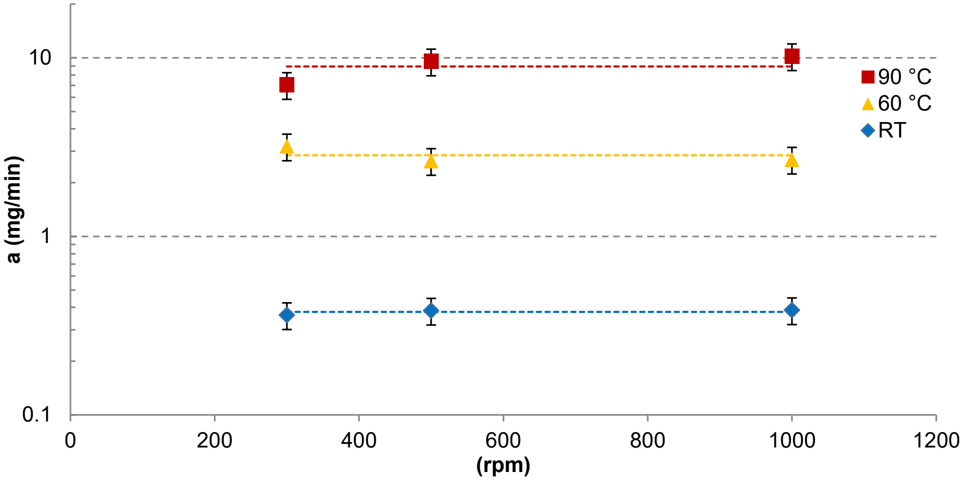

Figure 55: Dissolution rates of MgO in 7 mol/L HNO_3 as a function of the agitation velocity for different temperatures.

4.1.2.5 Density Dependence

The density dependence of the dissolution is relevant for the dissolution of irradiated transmutation targets because a higher burn-up results in higher target porosity due to the helium generation. Helium is mostly produced from the α-decay of TRU. Additionally, helium can be produced as a direct fission product in ternary fission.[19] The decisive role of helium on swelling of composite targets was demonstrated in the EFTTRA-T4, T4bis, and Ecrix-H experiments.[45] The impact of fast neutron irradiation on thermophysical properties of inert materials were investigated in the context of the MATINA experiment.[207] During irradiation the density of MgO pellets decreased from 96.6%TD to 93.6%TD due to the formation and segregation of loops. The dissolution rates of four pellets with different densities (MgO-3 to MgO-6, 85, 90, 96, and 99%TD; compare Table 12) are compared in Figure 56. The dissolution rates of the pellets with densities below 96%TD are very similar whereas the dissolution velocity at a pellet density of 99% is significantly smaller.

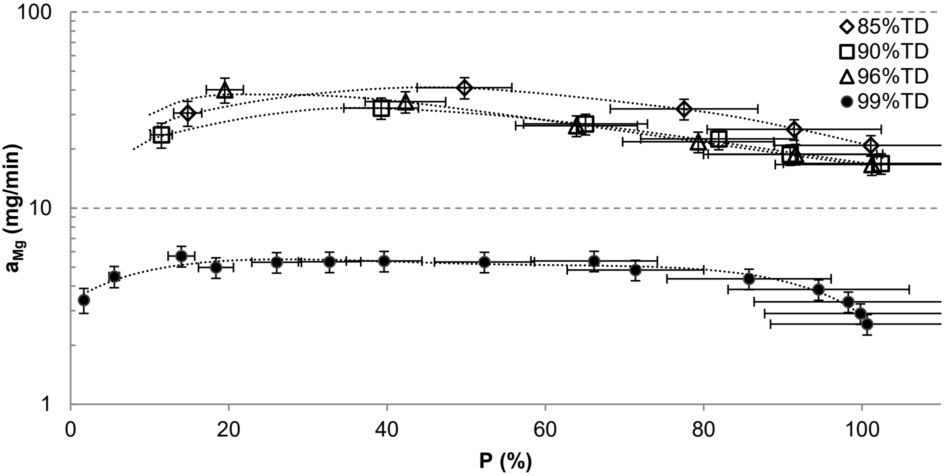

Figure 56: Average dissolution rates a_{Mg} of MgO pellets (MgO-3 to MgO-6, 0.7 g) of different densities (84 – 99%TD) in 4 mol/L nitric acid (14 mL) at 90 °C as a function of the amount of pellet dissolved (%).

This difference in dissolution rate is caused by the different microstructures of pellets with different densities. The microstructure of two pellets (96 and 99%TD) was analysed in detail by SEM and is shown in Figure 38, section 4.1.1.4, page 65. Both pellets were sintered at 1600 °C. The less dense pellet was pressed at 190 MPa and has a density of 96%TD, and shows a lot of pores (Figure 38, left): inter and intra granular porosity (diameter of pores $d_p \leq$ 1 µm), pores at grain boundaries and at triple points. The denser pellet (Figure 38, right) was compacted at 450 MPa and its density amounts to 99%TD. The quantity of intra granular porosity is less and the pores are smaller, the porosity is concentrated at the grain boundaries and triple points. The decreased porosity is equivalent to a smaller surface, which leads to a slower dissolution.

4.1.2.6 Evolution of the Pellet Surface

The surface or microstructure plays a key role in dissolution[63, 208] and hence, the dissolution rate is usually normalized to the surface area to allow comparability with other samples with different microstructure or geometry. Therefore, the changes of the surface during dissolution are important to calculate the dissolution rate of a solid in a certain solvent. Changes in surface area depend on the solute and the dissolution conditions (*e.g.* temperature or pH). The dissolution rate is defined as change of dissolved solute concentration dc per time normalized to the surface area A and is given by equation (7) (compare page 15)[63].

In situ microscopic observation of the dissolution would be necessary to derive the true reactive surface area, but is beyond the scope this study. However, the evolution of the pellet surface during dissolution in 2.5 mol/L HNO_3 at 30 °C was investigated with scanning electron microscopy (SEM) in detail. The microstructure of the original (not polished, not etched and not reacted with acid) pellet is depicted in Figure 57. Because the surface of the pellet was not polished or etched the grain boundaries appear deep and no statements can be made about porosity and connection of grains, but this has been examined in section 4.1.1.

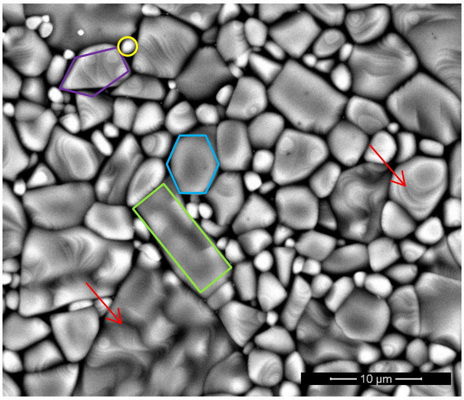

Figure 57: SEM image of the starting MgO pellet, pressed at 190 MPa and sintered at 1600 °C. The different colours represent different shapes of the grains round (yellow), rectangular (green), pentagonal (purple), and hexagonal (blue).

The grains are different in size (1-15 µm) and shape. They are e.g. mainly round (yellow), rectangular (green), pentagonal (purple), or hexagonal (blue). During sintering the larger grains grow at the expense of the smaller ones. Dihedral angles of 120° are formed at the contact point of three grains, since, in equilibrium, the grain boundary energies are the same and the balance is maintained. Planar interfaces can therefore only arise if the grains have six sides in the cross-section, but this depends in turn on the number of the next neighbors. If the number of sides is less than six, convexly curved grain boundaries form. If it is larger, concave grain boundaries are formed, as viewed from the interior of the grain. But since concave surfaces have a higher interfacial energy than convex ones and the state of lowest energy is always aspired, the grain boundaries will move in the direction of the centers of the radii of curvature, and thus to the centers of the smaller grains. Terrace and spiral structures are found on some of the grain surfaces (red arrows). During the first sintering stage an approximation to the energetically most favorable state takes place on a free surface by surface diffusion as well as evaporation and condensation. On the one hand, the grain strives to form a round shape under the surface tension when the grain boundary is narrowed in, on the other hand, a crystallographic boundary surface is formed by selective evaporation and deposition. Spiral growth is made possible by a screw displacement, which again and again generates new semi-crystal layers and thus stimulates continuous growth through continuous step formation. Crystalline growth is described in the framework of the Kossel-Stranski theory by electrostatic interactions at the surface. The core statement of the theory is that ions are deposited on a crystal surface exactly where the highest energy gain is to be expected.[209]

The structure of the pellet (grains and grain boundaries) can still be identified after reaction with 2.5 mol/L HNO_3 at 30 °C for 0.5 h (compare Figure 58), but a heterogeneous surface was found, which can be divided into three parts: smooth areas (1), rough areas (2), and holes (3). Smooth and rough areas are present in similar quantity. Circular and triangular etch pits are observed in the smooth areas. Moreover, the smooth areas contain steps. The diverse development of the surface of different grains can probably be attributed to heterogeneous crystal orientations. This is in agreement with the observation by Suárez and Compton[93] within an atomic force microscopy study, where the different surfaces of MgO crystal (100), (110), and (111) dissolve in hydrochloric acid via heterogeneous etch patterns. There the (100) plane shows circular and square shaped etch pits, the (110) plane evolves ridges and the (111) plane triangular etch pits. The (100) plane is postulated to be the most stable.[93] In our study, the holes are located mainly at the triple points, have five to six corners, and are approximately equal in diameter. These observations indicate a dissolution starting at the triple points, where the density of defect is the largest[210-211]. The rough areas of the surface contain crenulations which stick out of the surface with different orientations *e.g.* perpendicular, horizontal or skewed. The tips of the crenulations appear brighter than the rest of the surface, which may be due either to surface charging or to another elementary composition. This might be the $Mg(OH)_2$, which forms on the surface during the dissolution (compare section 4.1.2.1). The crenulations may result from the formation of innumerable triangular etch pits as described by Suárez and Compton for the (111) surface.[93]

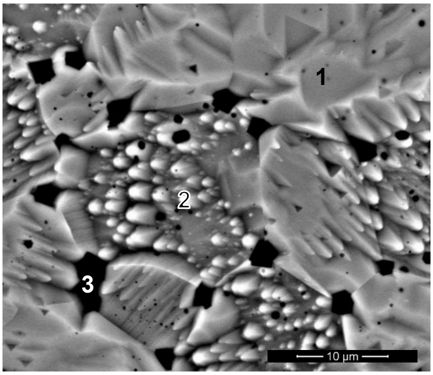

Figure 58: Surface topography of a MgO pellet after 0.5 h reaction in 10 mL of 2.5 mol/L HNO_3 at 30 °C.

After a reaction time of 2 h (compare Figure 59) the amount of grains with crenulations has decreased dramatically. In contrast, more smooth grains and grains with ridges are observed. According to Suárez and Compton the parallel ridges can be attributed to the (110) surface[93], while the smooth grains probably correspond to the (100) surface since it is known to be most stable.[93, 212-213] The size of the holes increased and circular etch pits can be observed in all grains.

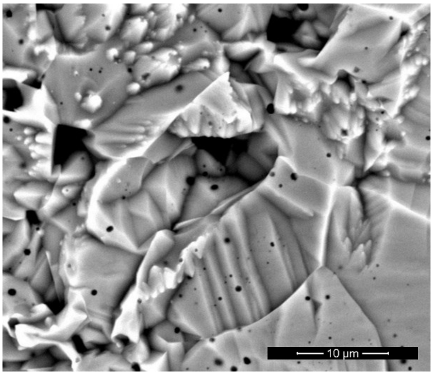

Figure 59: Surface topography of a MgO pellet after 2 h reaction in 10 mL of 2.5 mol/L HNO_3 at 30 °C.

The further microstructural investigations of MgO pellets showed a heterogeneous development of the pellet surface. Figure 60 shows the Surface topography of a MgO pellet after 3.5 h reaction in 10 mL 2.5 mol/L nitric acid at 30 °C. Significant differences between the outer and the inner part of the pellet can be observed. The amount of the rough areas decreased extremely and the amount and size of the holes increased. The outer part reveals a considerably higher amount of holes than the inner part. At the edge the surface is exposed to the acid at two instead of one side which might lead to a faster dissolution of the MgO. Moreover, a higher pressure is applied to the pellet centre during the pressing procedure, which leads to a higher density in the inner part of the pellet.[214] While grains and grain boundaries are still visible in the inner part of the pellet, the amount of holes and solid parts are approximately equal in the outer region and therefore, the original microstructure is not visible any longer. Mainly smooth areas of the pellet surface can be observed. Some residual rough parts can also be seen. This indicates that the rough areas dissolve faster than the smooth areas. The smooth areas still show steps in the inner part (Figure 60, right), but no clear statement can be made about the outer part (Figure 60, left). At none of the grains crenulations are observed anymore, but a zigzag structure appeared in the inner part (Figure 60, right). In both parts of the pellet circular etch pits can be identified. The remaining solid parts in the outer region of the pellet are connected by “bridges”, which could explain that the pellet structure is retained and does not fall apart during dissolution. Different levels of height in the pellet can be identified, indicating that the dissolution has proceeded into the pellet. The pellet dissolves inhomogeneously but a pellet structure remains until complete dissolution, as opposed to a pulverization.

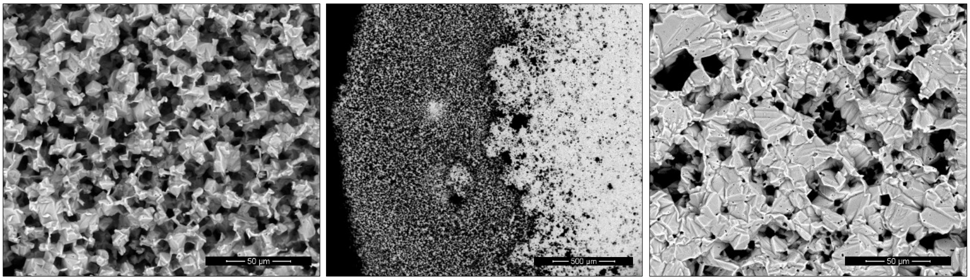

Figure 60: Surface topography of a MgO pellet after 3.5 h reaction in 10 mL 2.5 mol/L nitric acid at 30 °C (middle); zoom to the outer (left) and the inner (right) part of the pellet.

4.1.2.7 Surface Normalization of the Dissolution Rate

Based on the SEM images a model to describe the changes in pellet surface area in the progress of dissolution was developed. The geometrical surface area of the pellets was calculated from the diameter and height of the remaining pellets, which were determined from photographs taken with a camera containing a benchmark using the program ImageJ 1.47v. With this program, the number of pixels in a certain distance can be determined and related to the actual length with the help of the benchmark. Each parameter was averaged over ten values.

Considering the macroscopic shape of the pellets a significant change cannot be observed within the first 0.5 h of the dissolution. The pellet surface is rough after a reaction time of 5 h and the outer part of the pellet is thinner than the inner. At a reaction time of 8 h one of the dents developed to a u-like opening at the rim. Nevertheless, the macroscopic decrease of the pellet during dissolution can be described in a first approach by a model assuming that the pellets dissolve homogeneously in all directions and retain a cylindrical geometry during the entire dissolution process. The geometrical surface of the pellets A_{geom} was calculated by:

$$A_{geom} = 2\pi r(r+h) \tag{67}$$

with the radius r and the height h of the pellet. Table 17 summarizes the radius and height, the geometrical surface, and the mass of the remaining pellets. The development of the geometrical surface area as a function of the reaction time is displayed in Figure 61.

Table 17: Evolution of the pellet surface with increasing reaction time.

Reaction time (h)	Diameter (cm)	Height (cm)	Geometrical surface (cm²)	Pellet mass (g)
0	0.81	0.37	1.98	0.487
0.5	0.82	0.31	1.86	0.482
2	0.79	0.28	1.68	0.414
3.5	0.8	0.21	1.53	0.290
5	0.7	0.19	1.19	0.195
8	0.6	0.09	0.74	0.0526
15	0.38	0.04	0.27	0.0045

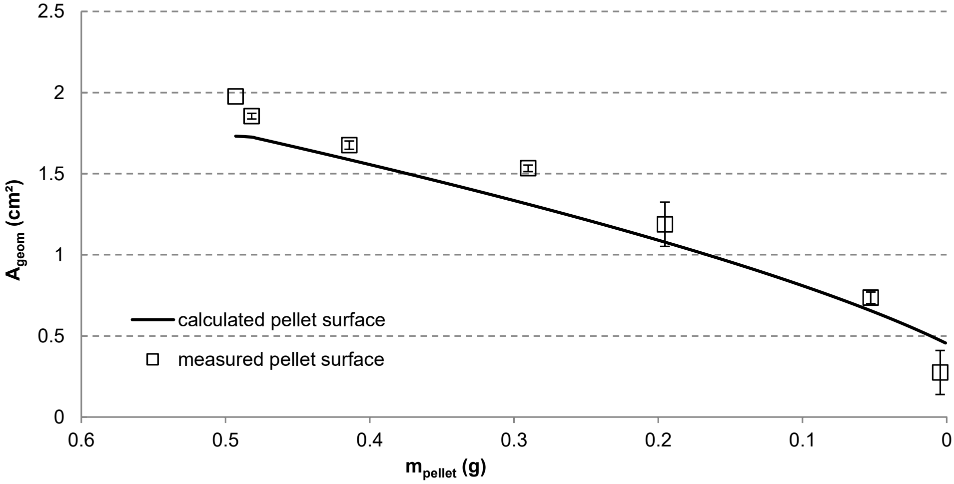

Figure 61: Change of the geometrical pellet surface as a function of the pellet mass. Experimental values were obtained by evaluation of photographs of pellet dissolved in 2.5 mol/L HNO_3 at 30 °C utilizing the program ImageJ.

The developed model is confirmed by comparing the calculated geometrical surface areas to a theoretical calculation, which assumes a uniform decrease of the height and the diameter in 10 µm intervals:

$$m_{pellet}=h\rho\pi r^2 \tag{68}$$

with the mass of the pellet m_{pellet}, the height of the pellets h, the density of MgO ρ and the radius of the pellet r. The surface of the pellets was calculated with equation (67) the initial values were obtained by measurement of an unreacted MgO pellet. Figure 61 compares the calculated and measured surface areas as a function of the pellet mass, which are good agreement, although the measured values are slightly higher. This is caused by the fact, that the model does not consider the increasing porosity of the pellet.

The geometrical surface-normalized dissolution rates of MgO were calculated using equation (7) with the geometrical surface areas obtained by the model calculation and the Mg^{2+} concentrations measured by ICP-MS. The results are depicted in Figure 62 in diamond symbols. The geometrical surface area normalized dissolution rate increases in the beginning of the experiment an reaches a constant value of about $1.2 \cdot 10^7$ mg/m$^2 \cdot$d.

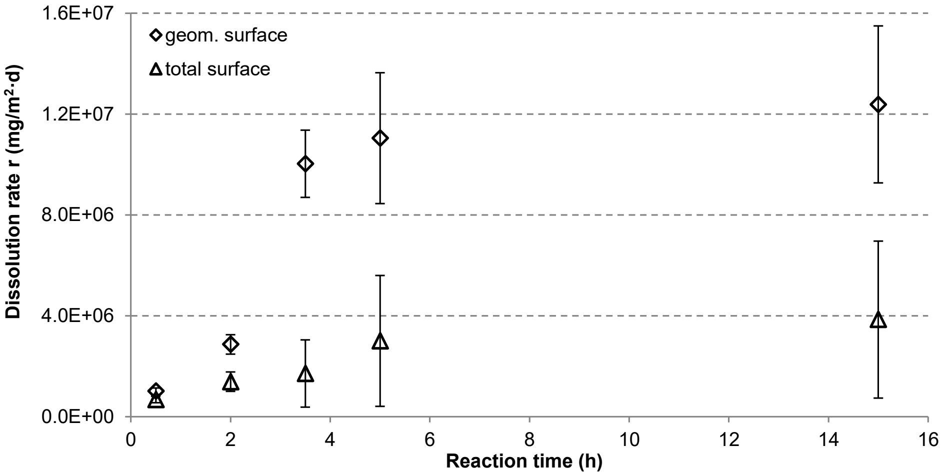

Figure 62: Comparison of the dissolution rates normalized to the geometrical and the total pellet surface area for MgO dissolution in 2.5 mol/L HNO_3 at 30 °C.

The calculated geometrical surface does not reflect the true surface of the pellets, because on the one hand the pellets do not show a perfect cylindrical geometry and on the other hand the roughness of the surface was not considered. Therefore, the developed model was further improved by considering the roughness of the pellet surface. The SEM investigations have shown that the pellet surface increases during dissolution due to the formation of crenulations, etch pits and holes. A second model to describe the microscopic surface changes was developed. The additional surface area caused by the holes was considered by assuming that they are cylindrical with a diameter equal to the height.[215-216] The diameter of the holes was measured from the SEM images with the program ImageJ as described above. The amount of holes in the pellet at the different reaction times was determined with the function “Analyse Particles” of the program. The obtained cylinder surfaces were summed up and added to the geometrical surface. These new total pellet surfaces were used to recalculate the dissolution rates, which are shown in Figure 62 (triangular symbols). The recalculated dissolution rates are found to be between $7 \cdot 10^5$ and $4 \cdot 10^6$ mg/m$^2 \cdot$d. Indeed, these surface normalized dissolution rates describe the dissolution of MgO more precisely as the pellet surface increases during the dissolution due to the augmented formation of holes.

The roughness factors of the pellets were calculated according to equation (69) and reported in Table 18. After an initial increase the maximal roughness factor was determined after 3.5 h.

During further dissolution the roughness factor decreases, this might result from the limitations of the applied model, which can only consider the near geometrical surface are; holes which develop to the inside of the pellet cannot be considered. It is likely that the amount of holes which extent to the inner part of the pellet increase with proceeding dissolution.

$$\lambda = \frac{A_{total}}{A_{geom}} \tag{69}$$

Table 18: Calculated geometrical and total surface area of the pellets and respective roughness factors after different reaction times.

Reaction time (h)	Geometrical surface (cm^2)	Total surface (cm^2)	Roughness factor
0.5	1.9	2.9	1.6
2	1.7	1.9	2.2
3.5	1.5	6.1	6.7
5	1.2	5.0	4.2
15	0.3	1.0	3.7

The studied MgO pellets are polycrystalline and not all regions of the pellets dissolve equally as described above. Therefore, it is questionable if an overall dissolution rate for the whole pellet is sufficient to describe the dissolution of MgO. Lüttge *et al.*[63] state, that an overall rate does not describe the dissolution sufficiently, but individual dissolution rates need to be considered for different surface sites. Consequently, it is even more controversial for a polycrystalline system to determine an overall dissolution rate for the entire system.

4.1.2.8 Dissolution of Mixed MgO/CeO$_2$ Pellets

The influence of the HNO$_3$ concentration and the temperature on the dissolution behaviour of mixed MgO/CeO$_2$ Pellets (60/40 wt.%) was investigated in batch experiments (1, 2, 4, and 7 mol/L HNO$_3$; RT, 60 and 90 °C). The magnesium ion concentrations relative to the total amount of Mg in the pellet (diamond symbols) and the relative cerium ion concentrations (square symbols) are depicted in Figure 63 as a function of the reaction time for dissolution in 4 mol/L HNO$_3$ at RT. Complete dissolution of the metal ions is indicated by the thick line. While MgO is also soluble at mild conditions, no more than 1% of CeO$_2$ was dissolved at any of the investigated conditions.

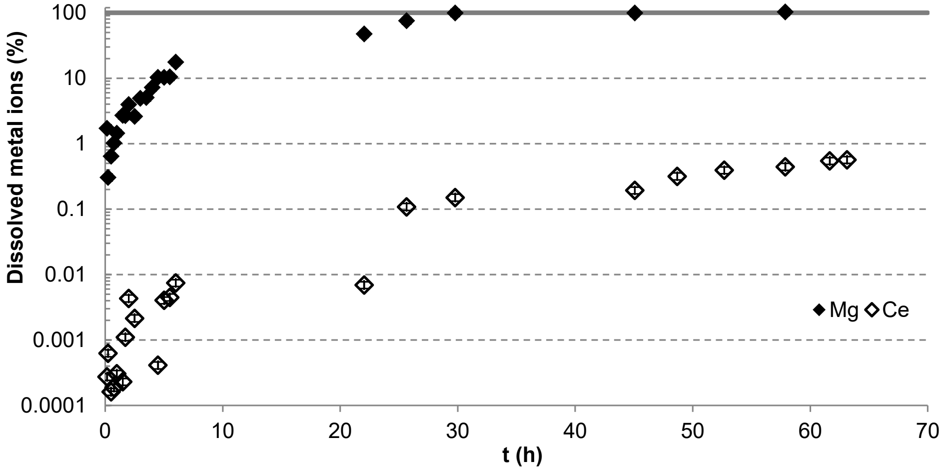

Figure 63: Dissolution curves of MgO (filled symbols) and CeO_2 (open symbols) in 4 mol/L HNO_3 at RT.

The dissolution rates of Mg (filled symbols) and Ce (open symbols) as a function of acid concentrations at different temperatures are compared in Figure 64. The dissolution rates of MgO are about three orders of magnitude higher than those for CeO_2 under equal conditions. For MgO an increase in temperature results in faster dissolution, while the acid concentration has nearly no effect on the dissolution rate. The dissolution rates of CeO_2 also show a strong dependence on the temperature. Moreover, the dissolution rate of CeO_2 slightly increases with increasing acid concentration. Therefore, an optimized separation of magnesium and cerium can be achieved at low acid concentrations, where no dissolution of the plutonium dioxide is expected as well. However, the PUREX process utilizes 6-8 mol/L HNO_3.[174] Accordingly, the separation processes would have to be adapted to the acid concentration. PuO_2 is not expected to dissolve at any of the investigated conditions, because it is insoluble in nitric acid when sintered at temperatures greater than ~450 °C, due to reduced powder porosity and crystallinity[171-172]. According to Uriarte and Rainey[171] the dissolution rates for PuO_2 in boiling 2, 10 and 14 mol/L nitric acid are less than 10^5 mg/m^{2}d, which is one order of magnitude lower than the dissolution rate of MgO at RT determine in this work. The dissolution rate of PuO_2 is barely affected by the temperature and HNO_3 concentration[173]. However, complexants such as fluoride or oxidants such as Ag(II) and Ce(IV) accelerate the PuO_2 dissolution[170-171, 173].

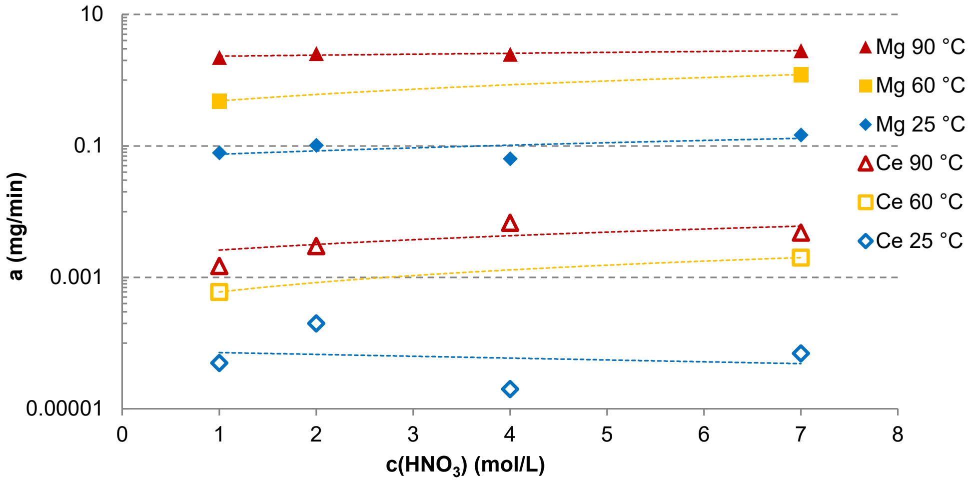

Figure 64: Comparison of dissolution rates a as a function of acid concentrations at different temperatures for Mg (filled symbols) and Ce (open symbols).

The Arrhenius plots of dissolution rates of MgO and CeO_2 in mixed MgO/CeO_2 pellets in nitric acid of different concentrations are depicted in Figure 65 and Figure 66 respectively. The activation energies were determined as described above and are summarized in Table 19. The calculated values for the activation energy of MgO are in total a little lower than those calculated from the dissolution of the pure MgO pellets and the values vary less. The activation energies calculated for CeO_2 for the different acid concentrations vary greatly and no clear trend is visible. However, the determined activation energies correspond to the range expected range for a surface controlled dissolution of the ceria.

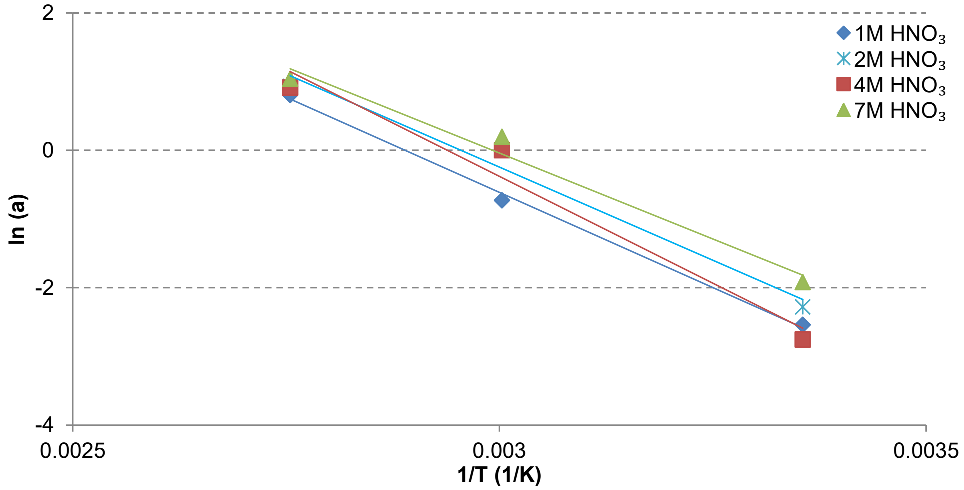

Figure 65: Arrhenius plot of dissolution rates of MgO in mixed MgO/CeO_2 pellets in nitric acid of different concentrations.

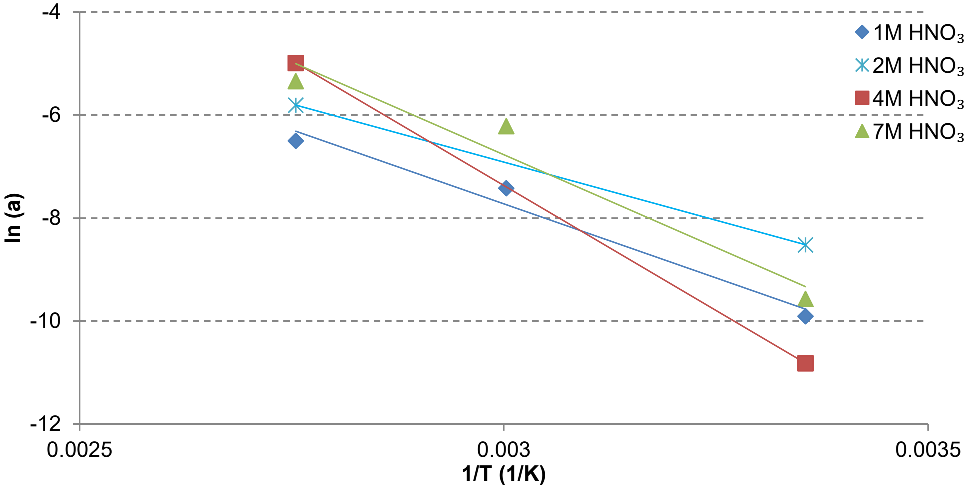

Figure 66: Arrhenius plot of dissolution rates of CeO_2 in mixed MgO/CeO_2 pellets in nitric acid of different concentrations.

Table 19: Activation energies of MgO and CeO_2 for different acid concentrations.

Acid concentration (mol/L)	Activation energy (kJ/mol)	
	MgO	CeO_2
1	46.0	47.8
2	45.1	37.5
4	51.7	80.7
7	41.5	60.0

The dissolution of mixed MgO/CeO_2 was also investigated in more detail by SEM in a study comparable to that of the pure MgO pellets. The structure of the pellet (grains and grain boundaries) can still be identified after reaction with 2.5 mol/L HNO_3 at 30 °C for 0.5 h (compare Figure 67), but a heterogeneous surface was found, which can be divided into two parts: CeO_2 rich regions and MgO rich regions. The CeO_2 rich regions (Figure 67, left) apparently dissolve homogeneously. The original microstructure of the CeO_2 rich regions (Figure 67, left), especially the grain boundaries can still be identified. The dissolution apparently proceeds homogeneously via circular etch pits. In the MgO rich regions (Figure 67, right) the same heterogeneous surface was found, as was observed on the pure MgO pellets, and can be divided into three parts: smooth areas, rough areas, and holes. Predominantly circular etch pits are observed.

After a reaction time of 2.5 h (Figure 68) the MgO rich regions are not visible any longer and the outer part of the pellet consists solely of CeO_2. In addition to the large CeO_2 agglomerates, countless small particles are visible, which could either originate from disintegration due to weakening of the grain boundaries or be a precipitate.

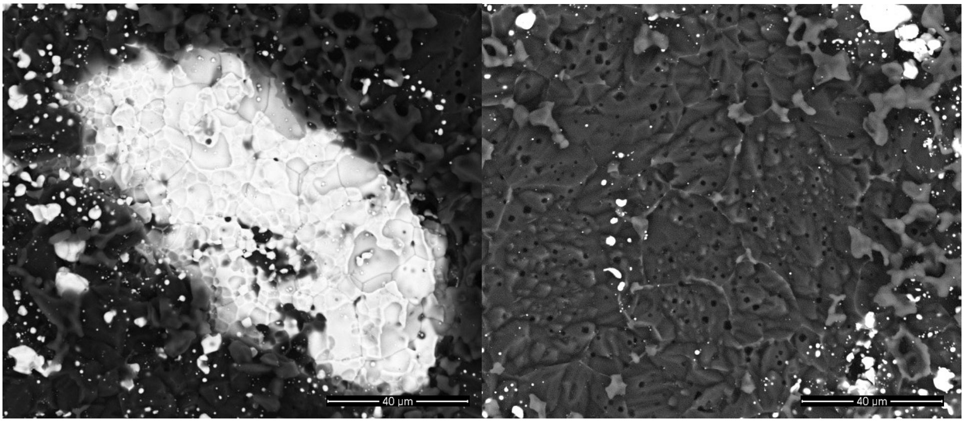

Figure 67: Surface topography of a MgO/CeO_2 pellet after 0.5 h reaction in 10 mL of 2.5 mol/L HNO_3 at 30 °C; left: CeO_2 rich region, right: MgO rich region.

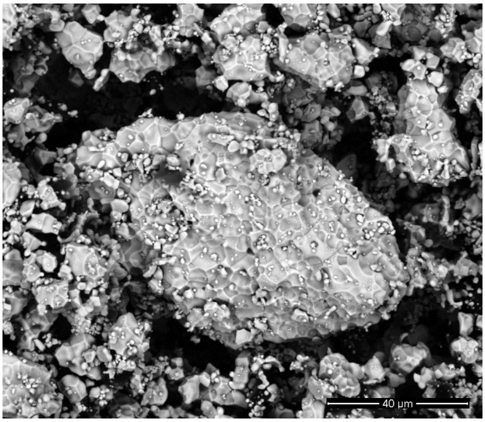

Figure 68: Surface topography of a MgO/CeO_2 pellet after 2.5 h reaction in 10 mL of 2.5 mol/L HNO_3 at 30 °C.

4.1.2.9 Comparison of the Dissolution of MgO from Pure and Mixed Pellets

The dissolution rates of MgO from pure (filled symbols) and mixed (open symbols) pellets at different temperatures are compared in Figure 69. The observed trends are similar for pure and mixed pellets. However, the dissolution rates for the mixed pellets are systematically lower. This is caused on the one hand by the smaller reactive surface area of the MgO and on the other hand by the different fabrication conditions and resulting higher density of 98%TD of the mixed pellets compared to 96%TD of the pure MgO pellets.

To complete the analysis of the dissolution behaviour of MgO the previous results are to be confirmed by experiments with mixed MgO/UO_2 and MgO/PuO_2 pellets. Vertical scanning interferometry could be utilized for further investigation of the surface topography of the pellets.

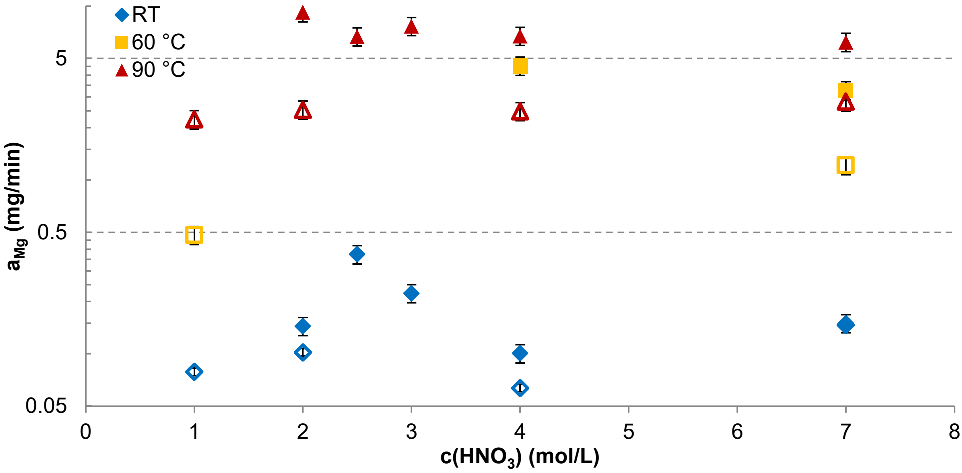

Figure 69: Comparison of dissolution rates a as a function of acid concentrations at different temperatures for pure MgO pellets (filled symbols) and mixed MgO/CeO_2 pellets (open symbols).

4.2 Molybdenum as CerMet Matrix Element

According to the Mo/UO_2- and Mo/PuO_2 pellet production procedure at NRG[181], Mo pellets with CeO_2 contents of 0, 5, 10, 25 and 40% were synthesized.

4.2.1 Physical Properties and Microstructure

The pellets were characterized by means of density measurements, micro hardness measurements, SEM investigation, and XRD.

4.2.1.1 Densities of the Pellets

The geometrical density of the pellets was calculated from measurements of pellets height and diameter. Bulk density was determined by Archimedes method (immersion in water). Bulk and geometric densities of the Mo/CeO_2 pellets are compared with Mo/UO_2 pellets produced in Petten by NRG in Figure 70. The geometrical densities of mixed pellets containing CeO_2 are considerably lower compared to those containing UO_2. This might be caused by a slight deformation of the pellet during the sintering process, since the geometrical density determination is based on a cylindrical shape of the pellets. However, the bulk densities agree very well. Altogether, the density of the pellets increases with increasing molybdenum content.

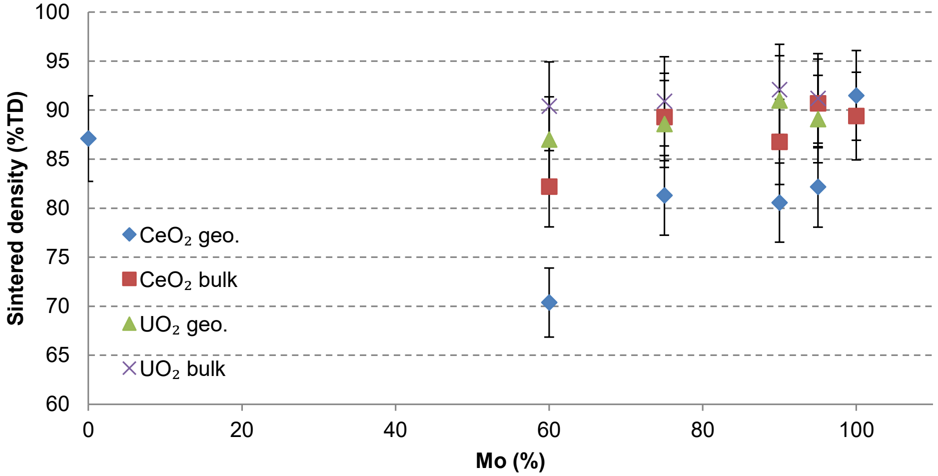

Figure 70: Densities of CeO_2/Mo pellets (Jülich) compared to UO_2/Mo pellets (NRG[181]) as a function of Mo content.

Optical microscope pictures of mixed Mo/CeO_2 and Mo/UO_2 (NRG[181]) pellets are shown in Table 20. CeO_2 and UO_2 respectively are homogeneously distributed in the molybdenum matrix.

Table 20: Optical microscope pictures of mixed Mo/CeO_2 (magnification x20) and Mo/UO_2[181] (magnification x10) pellets.

	CeO_2	**UO_2 (NRG[181])**
95% Mo	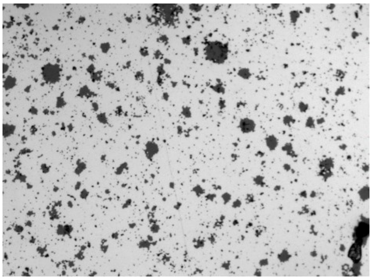	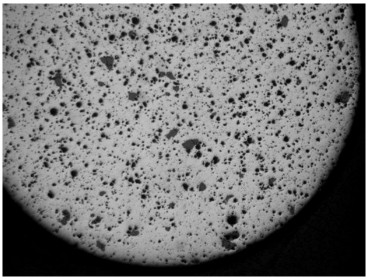
90% Mo	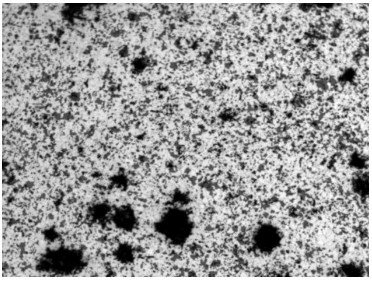	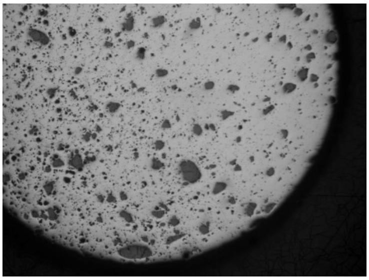
75% Mo	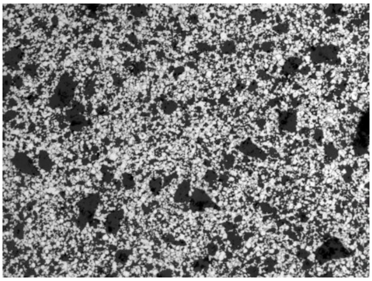	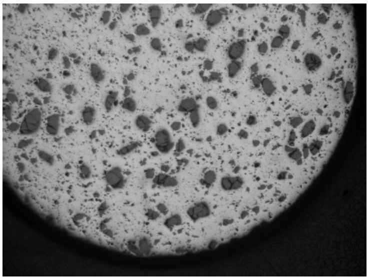
60% Mo	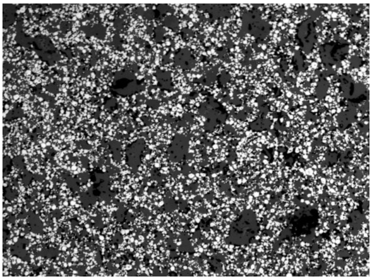	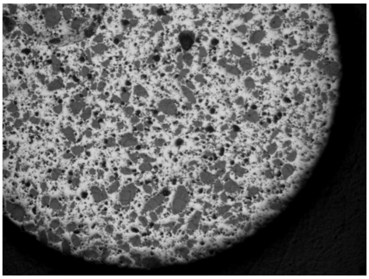

4.2.1.2 Investigation of Micro Hardness

The micro hardness (H_V) of sintered samples was measured by a diamond Vickers indenter (Anton Paar MHT 10). The thoroughly polished and etched surface was indented using a load of 400 Pa. The full load was applied for 10 s. Seven measurements were performed for each pellet. The micro hardness (H_V (GPa)) of the pellets was calculated by equation (56) (page 43) and is depicted in Figure 71 as a function of the ceria content. The curve shows a linear dependence, the discrepancies at 10 and 40 wt.% ceria content are caused by a bad sample quality and high sample porosity respectively.

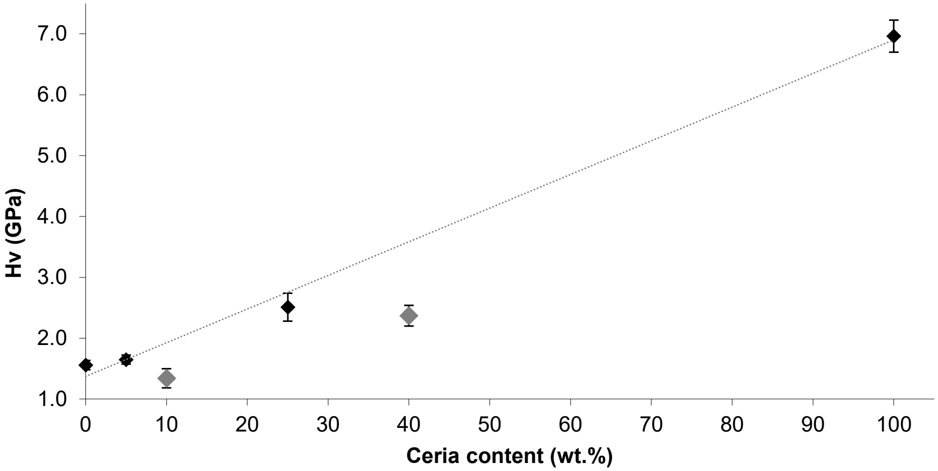

Figure 71: Micro hardness H_V (GPa) of mixed Mo/CeO_2 pellets as a function of ceria content.

4.2.1.3 Scanning Electron Microscopy Investigations

Sintered pellets were carefully polished with abrasive paper and diamond paste (1 µm) and etched with Murakami's reagent[189] (composition: 10 mg $K_3Fe(CN)_6$, 10 mg KOH, 100 mL distilled water) for 3 min for the investigation of the microstructure. The micro structure of the pellets was studied by SEM. The optical microscope and SEM pictures of the mixed Mo/CeO_2 pellets and pure Mo and CeO_2 pellets are depicted in Figure 72. In all mixed pellets the cerium dioxide is distributed quite homogenously in the Mo matrix. The CeO_2 pellet (Figure 72, f) is significantly more porous compared to the Mo pellet (Figure 72, a). Therefore, the pellet porosity increases with increasing ceria content. The Mo pellet shows well developed grains and grain boundaries. The amount of inner grain porosity is low; the pores are concentrated at the triple points. The pellets consist of two different regions; one shows a more distinct microstructure than the other; EDS measurements were performed on both regions.

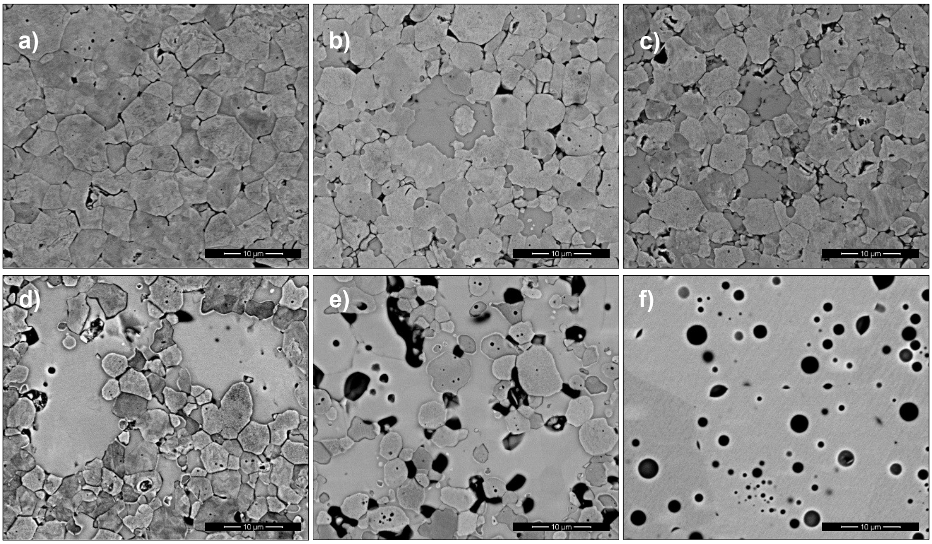

Figure 72: SEM pictures of mixed Mo/CeO_2 pellets with a) 0 wt.%, b) 5 wt.%, c) 10 wt.%, d) 25 wt.%, e) 40 wt.%, and f) 100 wt.% CeO_2.

All pellet compositions were investigated in detail, but the results for pellets containing 25wt.% CeO_2 are presented here in detail (Figure 73). The EDS spectrum of the region with less distinct microstructure (n1) shows mainly the L-lines of CeO_2. However, the molybdenum L-lines also appear in the spectrum, because the depth of the measuring range of the EDS is higher than the depth of the CeO_2 grain and Mo which is located below the CeO_2 grain is also detected (compare section 4.1.1.4, Figure 44, page 69). The EDS spectrum of the region with more distinct microstructure (n2) shows mainly the L-lines of Mo. The microstructure is more visible for the molybdenum grains, because the etching procedure was optimized for the metal phase.

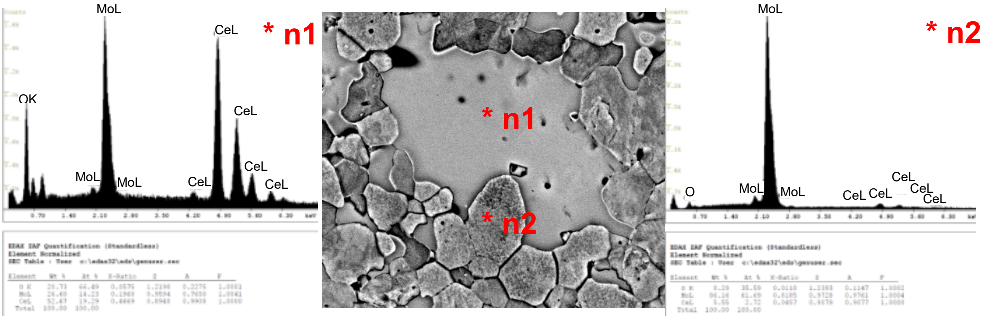

Figure 73: EDS measurement of different regions on the surface of mixed Mo/CeO_2 pellet containing 25 wt.% CeO_2.

The mixed pellets were analysed by XRD and the achieved data was standardized to an intensity of 1,000. The diffractogram of a mixed Mo/CeO_2 pellet with 25 wt.% CeO_2 is exemplarily shown in Figure 74. The diffraction pattern shows two phases, body-centred cubic molybdenum and the fluorite structure of CeO_2; no additional mixed phase is observed.

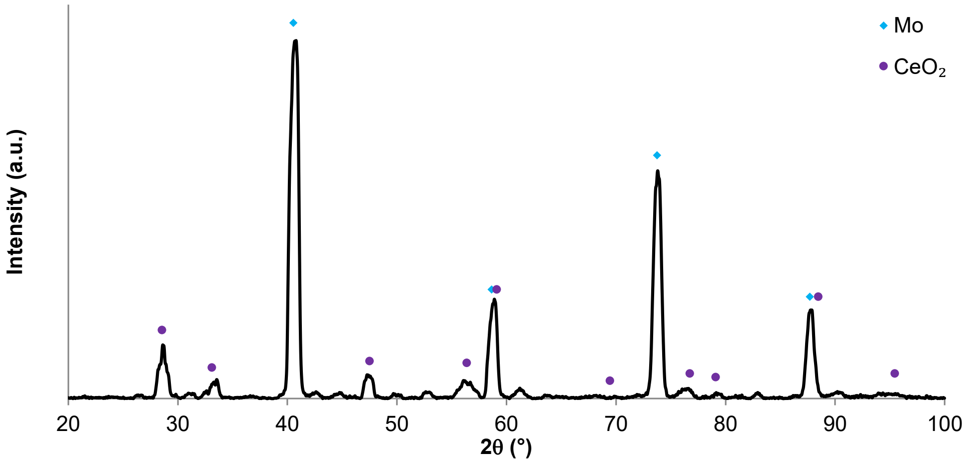

Figure 74: X-ray powder diffraction pattern of a mixed Mo/CeO_2 pellet with 25 wt.% CeO_2 share.

4.2.2 Dissolution Behaviour

The dissolution behaviour of molybdenum has been investigated as a function of the acid concentration and the temperature. Moreover, the influence of Fe(III) as additive on the dissolution was considered.

4.2.2.1 Dissolution in Nitric Acid

The dissolution of molybdenum in nitric acid produces an s-shaped curve, as the surface area initially increases, then the surface area decreases until pellet dissolution is complete as can be seen in Figure 75. This profile is also typical for autocatalytic mechanisms, due to generation of the catalytic species nitrous acid, which initiates the dissolution.[217-218] The dissolution velocity of Mo pellets is strongly dependent on the acid concentration. Higher acid concentrations result in higher dissolution velocities but also in more precipitation. Molybdenum is oxidized to Mo(VI) (compare section 1.8.3) which then precipitates as MoO_3. This is in agreement with the observation of Shapiro[141], who found an increasing degree of polymerization of isopolyanions with the concentration of protons until the isoelectric point (pH 1.1-1.8), where the monohydrate precipitates. During dissolution of a molybdenum pellet in 2 mol/L nitric acid at RT first precipitation occurs after 48 h, while in the case of 4 mol/L nitric acid first precipitations occur already after about 24 h. During dissolution of a molybdenum pellet in 7 mol/L nitric acid first precipitation occurs after only 25 min.

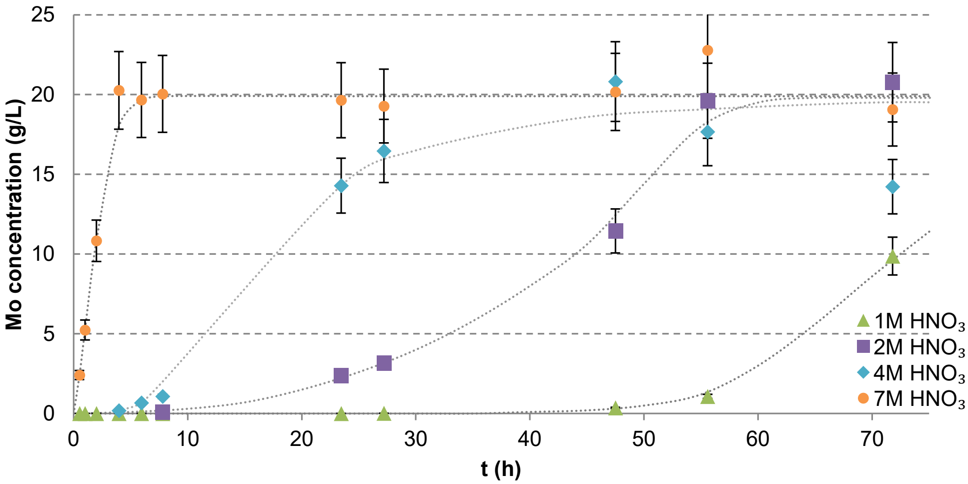

Figure 75: Dissolution of Mo pellets (1 g) in nitric acid (50 mL) of different concentrations at RT.

The existence of oxides hydrated with one or two water molecules, $MoO_3 \cdot H_2O$ and $MoO_3 \cdot 2H_2O$, has been established. Both hydrates can be obtained by acidification of a molybdate solution. Monohydrate is known to exist in diverse crystalline forms. There are no detailed studies on the range of existence of MoO_3 and the hydrates for acid system. In acid solution at 20 °C, the solid phase in equilibrium with the solution is $MoO_3 \cdot 2H_2O$ in 2 to 6 mol/L HNO_3, while the monohydrate is the solid phase on both sides of this concentration range. For $T > 40$ °C, the monohydrate is the stable white solid phase in the acid system $MoO_3 \cdot nH_2O$-H_2O.[73, 100] The precipitates were identified as MoO_3 (molybdite) by XRD measurement. The diffractogram of the precipitate in 1 mol/L HNO_3 at RT is shown in Figure 77. The ratio of molybdenum in solution and precipitated Mo was determined by ICP-MS. For this purpose the MoO_3 was dissolved in NaOH solution. The results are depicted in Figure 76. In 1 mol/L HNO_3 about 5% of the molybdenum precipitate while only 50% dissolve in 4 mol/L HNO_3, and in 7 mol/L HNO_3 less than 30% of the molybdenum dissolves.

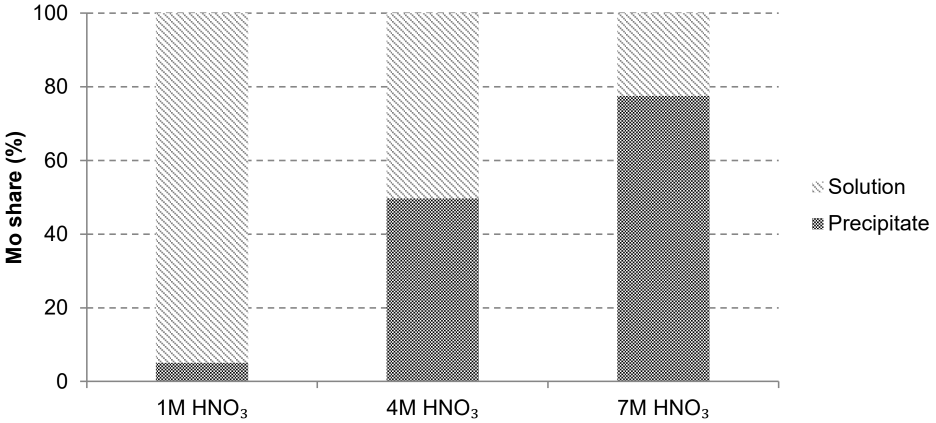

Figure 76: Distribution of Mo (1 g) between solution and precipitate for different dissolver solutions (20 mL) at RT.

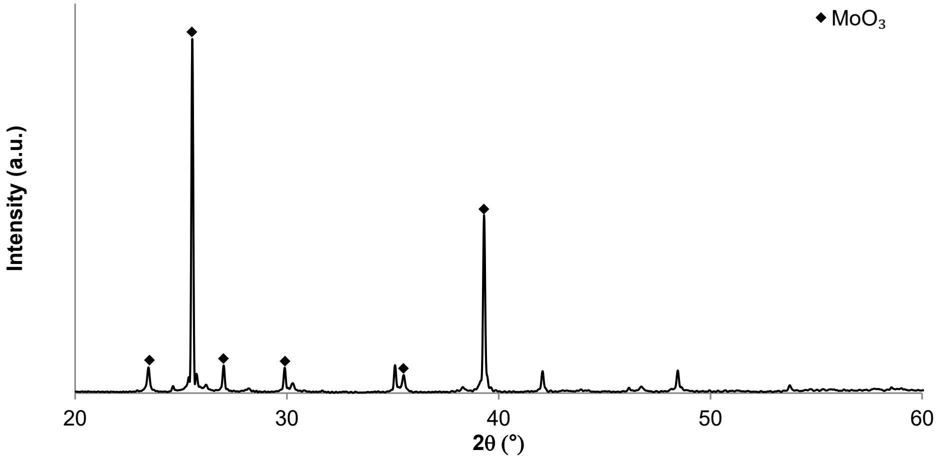

Figure 77: XRD of the precipitate occurring during dissolution of Mo in 1 mol/L HNO_3 at RT.

An increase in temperature results in faster dissolution velocities but also greater amount of precipitation (Figure 78). During dissolution of a molybdenum pellet in 7 mol/L nitric acid at 60 °C first precipitations occur already after about 90 min. During the first 30 min of dissolution of a molybdenum pellet in 7 mol/L nitric acid a huge amount of precipitation occurs at 90 °C (Figure 79), whereas at RT only a few flakes are visible. At temperatures above RT the molybdenum concentration in the solution increases during the first phase of the dissolution, but then decreases at the onset of the precipitation. The decrease in solubility of molybdenum oxide with temperature, for a given concentration of HNO_3, was attributed by Vorob'ev[142] to the formation of different polymeric species of molybdenum according to the temperature and which are less soluble at higher temperatures.

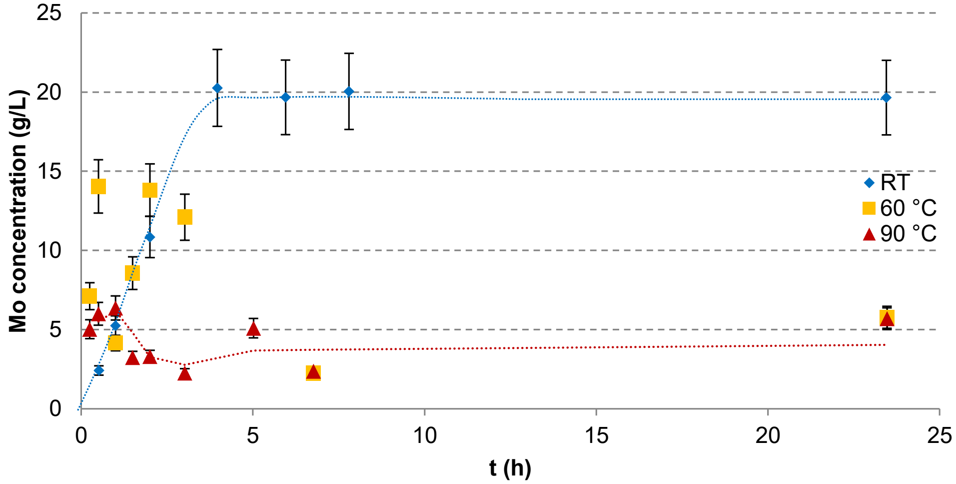

Figure 78: Dissolution of Mo pellets (1 g) in 7 mol/L nitric acid (50 mL) at different temperatures.

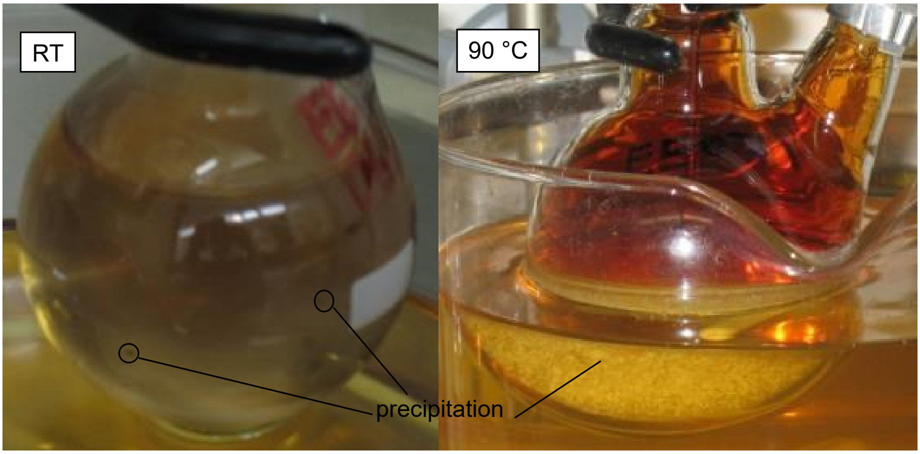

Figure 79: Dissolution of a Mo pellet in 7 mol/L nitric acid after 30 min at RT (left) and at 90 °C (right).

The dissolution rates of Mo were derived by the initial rate method and are displayed in Figure 80 as a function of nitric acid concentration at RT and at 90 °C. For that purpose, the mass of the dissolved molybdenum was plotted as a function of time. The slope of the fit to the linear first part of the dissolution curve is equal to the dissolution rate, as described in more detail in section 4.1.2.2. However, this method is based exclusively on the molybdenum concentration in solution and does not consider the precipitate. Accordingly, it provides only an approximation whose quality depends on the amount of the precipitate. The dissolution rates increase with increasing acid concentration at both temperatures. Moreover, an elevated temperature leads to a significant increase in dissolution rate at a given nitric acid concentration. However, this simultaneously results in augmented precipitation of molybdenum oxide, as reported before and is attributed to the formation of lower soluble polymeric species of molybdenum at higher temperatures.[142]

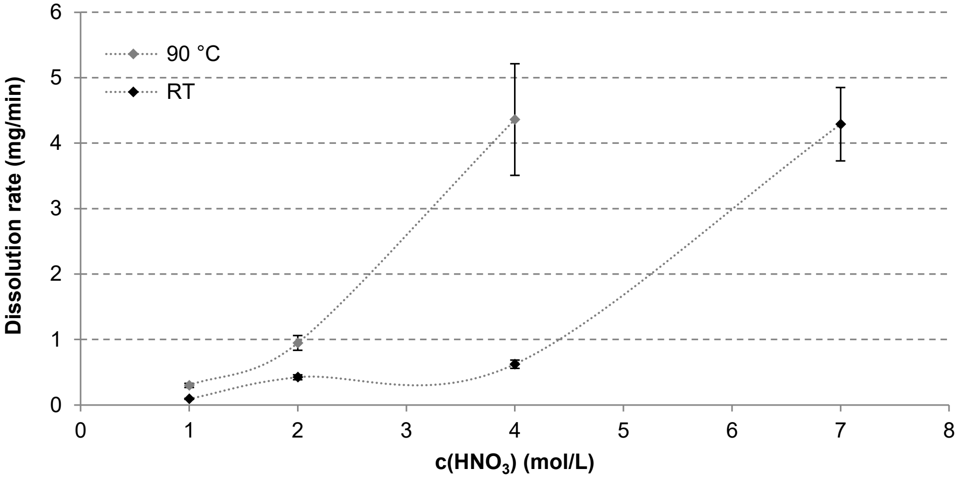

Figure 80: Initial dissolution rates of Mo as a function of nitric acid concentration at RT and at 90 °C.

The temperature dependence of dissolution rates is typically expressed using Arrhenius law (compare section 1.7, equation (11)). The activation energy can be determined by plotting the rate constant as a function of 1/T and was calculated for the dissolution of Mo in HNO_3 using equation (11) from the slopes of the linear fits (not shown here). The obtained activation energy was 18 ± 8 kJ/mol, which indicates a diffusion controlled dissolution[202].

4.2.2.2 Dissolution in Nitric Acid with Ferric Nitrate as Additive

Iron(III) is known to significantly increase the solubilities of both MoO_3 and $MoO_3 \cdot 2H_2O$ in dilute HNO_3.[61] Anion exchange resin studies indicate that a negatively charged iron-molybdenum complex ion is present in such solutions[60]. The addition of ferric nitrate to the acid increases the dissolution velocity of the Mo pellet as shown in Figure 81. The pellet can be completely dissolved in 1 mol/L HNO_3 containing at least 1 mol/L Fe(III). In 1 mol/L HNO_3 without the addition of Fe(III) only about 40% of the pellet are dissolved after 3 days, whereas in 1 mol/L HNO_3 containing 1 mol/L $Fe(NO_3)_3$ the pellet completely dissolves within about one day. The addition of 1 mol/L ferric nitrate to the solvent prevents the precipitations at low acid concentrations (compare Figure 82). The Mo pellet can be completely dissolved in 1 or 2 mol/L nitric acid with the addition of 1 mol/L ferric nitrate and these solutions are stable. However, at the higher acid concentrations (4 and 7 mol/L HNO_3) precipitates occur. Nevertheless, the large amount of iron in the solution might interfere and disturb the extraction process (compare section 1.8.3.5) and will add substantially to waste volumes unless the iron solution can be reused after Mo extraction.

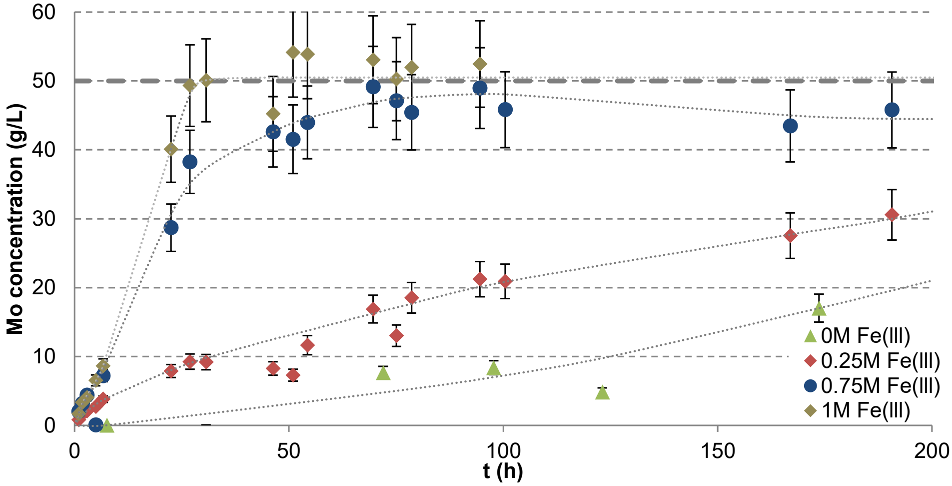

Figure 81: Dissolution of Mo pellets (1 g) in 1 mol/L HNO_3 (20 mL) with the addition of different amounts of $Fe(NO_3)_3$ at RT. The dashed line corresponds to the concentration expected for complete dissolution.

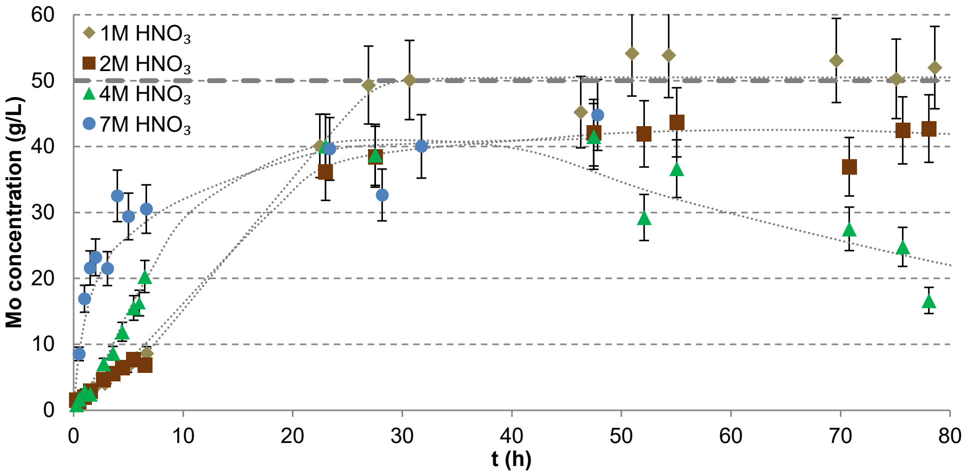

Figure 82: Dissolution of Mo pellets (1 g) in nitric acid (20 mL) of different concentrations + 1 mol/L $Fe(NO_3)_3$ at RT. The dashed line corresponds to the concentration expected for complete dissolution.

The addition of ferric nitrate to the nitric acid increases the dissolution rate of Mo as is shown in Figure 83, where the dissolution rate is plotted against the Fe(III) content in 1 and 7 mol/L nitric acid. In 1 mol/L HNO_3 the dissolution rate linearly increases with Fe(III) content. The dissolution rate in the presence of 1 mol/L Fe(III) is a factor of six higher compared to the dissolution without iron. In the case of 7 mol/L HNO_3 no clear trend can be identified due to the scattering of the values. The dissolution rates are significantly higher in 7 mol/L nitric acid compared to 1 mol/L nitric acid. For comparison, the initial rate of dissolution of U-3% Mo alloy in boiling 8 mol/LHNO_3 increases from 142 to about 200 mg/cm^2·min (factor of 1.4) as the ferric nitrate concentration increases from 0 to 1 mol/L.

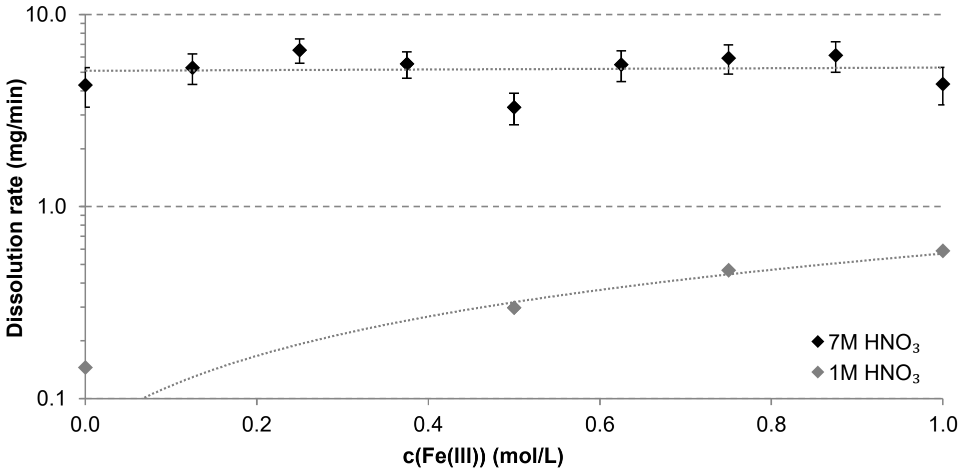

Figure 83: Initial dissolution rates of Mo pellets (1 g) as a function of Fe(III) addition to 1 and 7 mol/L nitric acid (20 mL) at RT.

However, the overall solubility is lower in 7 mol/L nitric acid as discussed above. Iron(III) is well known to oxidize Mo(V) complexes, in acidic aqueous solution.[112] The hydrolysed Fe(III) cation $[Fe(OH)]^{2+}$ is considered as the reactive species. The concentration of this cation decreases with increasing acid concentration, decelerating the oxidation[112], which could explain the smaller effect of the Fe(III) addition in 7 mol/L HNO_3 compared to 1 mol/L HNO_3. On the other hand, molybdate is known to accelerate the oxidation of iron(II) by nitric acid (brown ring test).[219-220] However, no information on the catalytic mechanism could be found.

As reported before, in the presence of iron an increase of temperature results in faster dissolution kinetics as shown in Figure 84 but at temperatures above RT precipitations occur during the dissolution of the pellet. Due to the formation of precipitates the determination of dissolution rates is difficult.

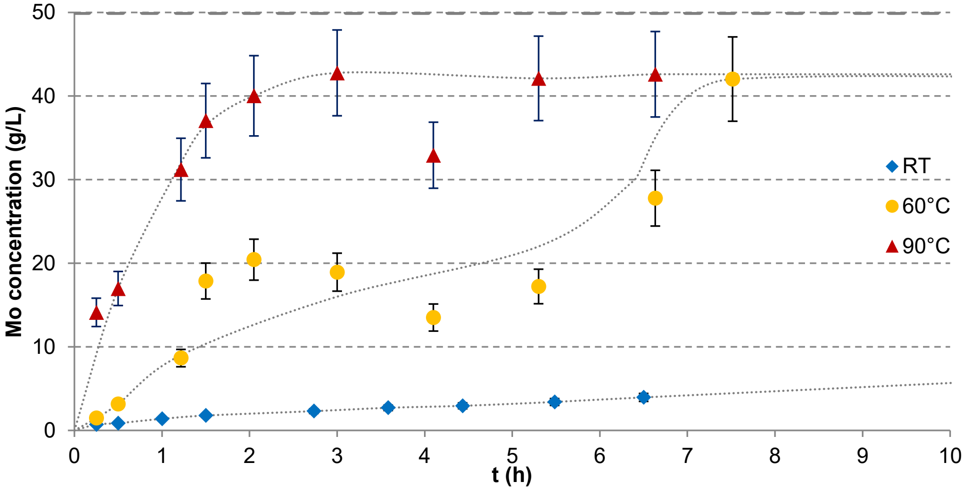

Figure 84: Dissolution of Mo pellets in 1 mol/L HNO_3 with the addition of 1 mol/L $Fe(NO_3)_3$ at different temperatures. The dashed line corresponds to the concentration expected for complete dissolution.

The dissolution rates of Mo are strongly dependent on the temperature as depicted in Figure 85 for 1 and 2 mol/L nitric acid containing 1 mol/L $Fe(NO_3)_3$. In nitric acid solutions which do not contain iron an increase in dissolution temperature results in an increased degree of precipitation, making the determination of dissolution rates impossible.

The activation energy of the dissolution of molybdenum in nitric acid containing iron(III) as an additive was determined as described above and is 42 ± 11 kJ/mol, which suggests a surface controlled dissolution.[203]

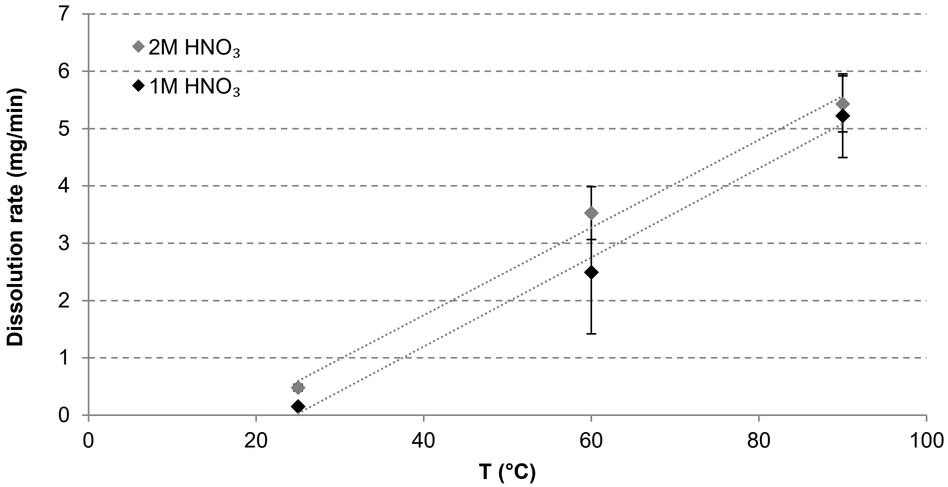

Figure 85: Initial dissolution rates of Mo as a function of temperature in 1 and 2 mol/L nitric acid containing 1 mol/L $Fe(NO_3)_3$.

4.2.2.3 *Dissolution Experiments on Mixed Mo/CeO₂ Pellets*

Since mild conditions are most suitable for molybdenum dissolution, experiments on mixed Mo/CeO_2 (60/40wt.%) pellets have been performed in 20 and 100 mL 1 mol/L HNO_3 without Fe(III) or containing 1 equivalent of Fe(III) per equivalent of Mo at RT. The dissolution of Mo/CeO_2 (60/40wt.%) pellets (1 g) in 20 mL 1 mol/L HNO_3 with and without Fe(III) is displayed in Figure 86 as a function of time. In the absence of Fe(III) the dissolution of molybdenum is slower compared to cerium in the induction period and then speeds up. In the presence of Fe(III) the induction period of the molybdenum dissolution is shortened and the dissolution of molybdenum is faster compared to cerium during the entire experiment. Overall the dissolution velocity of molybdenum increases in the presence of iron, while the dissolution velocity of cerium is unaffected.

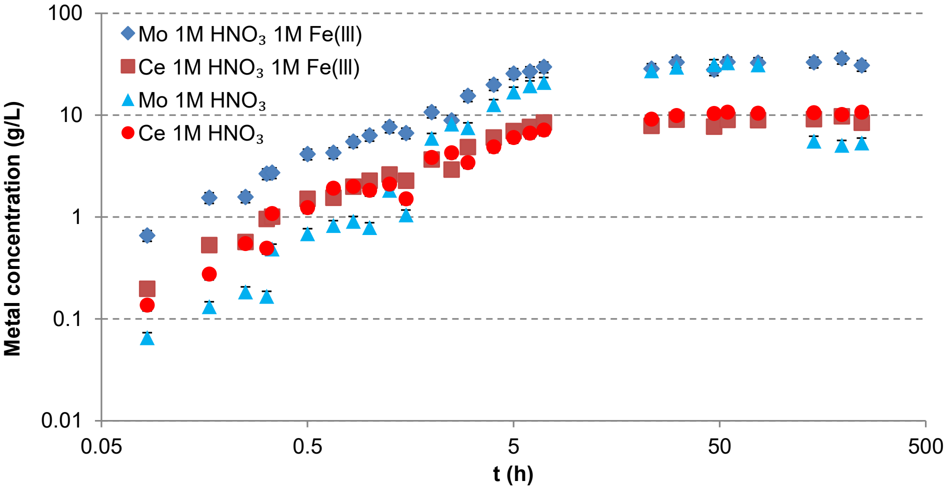

Figure 86: Dissolution of molybdenum and cerium from mixed Mo/CeO_2 (60/40 wt.%) pellets (1 g) in 20 mL 1 mol/L HNO_3 without Fe(III) or containing 1 eq. of Fe(III) per eq. of Mo at RT.

In the absence of Fe(III) a pale precipitate appears after about 100 h, which corresponds to a dramatic drop of Mo concentration. This precipitate was identified by XRD as MoO_3. The overall picture for the dissolution in 100 mL dissolver solution is quite similar; however the dissolution is overall slower. The XRD pattern of the residue of the dissolution of a Mo/CeO_2 (60/40 wt.%) pellet in 100 mL 1 mol/L HNO_3 is displayed in Figure 87. The diffractogram shows one phase, which can be identified as CeO_2, although the reflexes are slightly shifted. The MoO_3 precipitate which was also visible in the flask is below the detection limit.

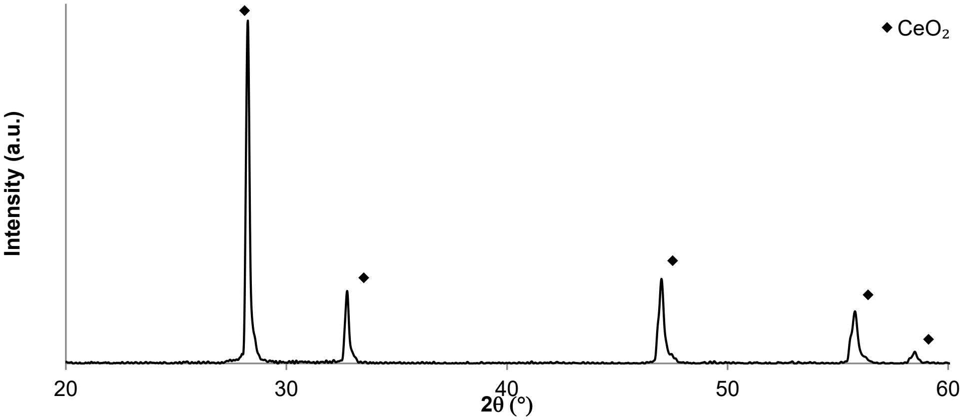

Figure 87: XRD pattern of the residue of the dissolution of a Mo/CeO_2 60/40wt.% pellet in 100 mL 1 mol/L HNO_3.

The average dissolution rates (mg/min) (derived from equation (4)) of molybdenum and cerium from mixed Mo/CeO_2 (60/40 wt.%) pellets for the different dissolver solutions are compared in Figure 88. The dissolution rate of molybdenum is higher in 20 mL compared to 100 mL acid and also increases in the presence of iron. The dissolution rate of cerium is barely influenced by the composition of the dissolver solution. In all cases the solutions in equilibrium (prior to the molybdenum precipitation) contain about 1 mmol cerium and 7 mmol molybdenum.

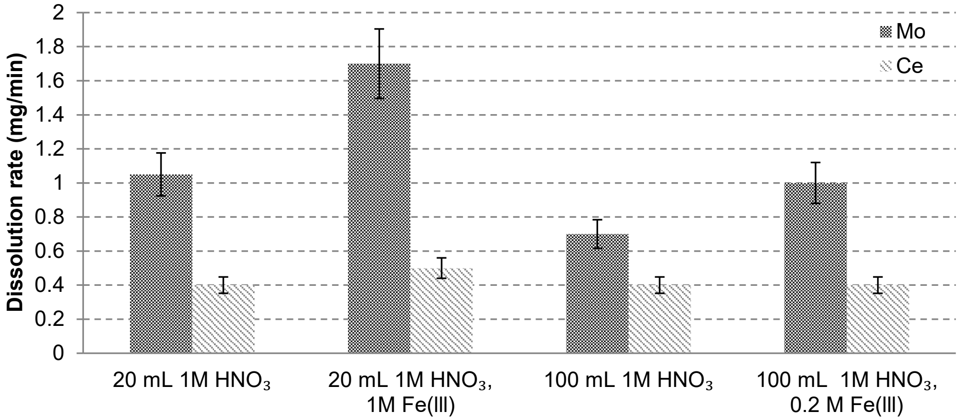

Figure 88: Comparison of average dissolution rates (mg/min) of molybdenum and cerium from mixed Mo/CeO_2 (60/40 wt.%) pellets in 20 and 100 mL 1 mol/L HNO_3 without Fe(III) or containing 1 equivalent of Fe(III) per equivalent of Mo at RT.

Comparing the dissolution behaviour of both matrix materials molybdenum and magnesium a systematic difference is observed. The dissolution of CeO_2 from Mo/CeO_2 pellets is significantly faster and a larger amount of CeO_2 is dissolved compared to MgO/CeO_2 pellets. It is probable that this is due to enhanced reductive dissolution, involving the reduction of Ce(IV) by Mo(V) as described by Chappelle *et al.*[221] The occurrence of Mo(V) as intermediate in the dissolution of molybdenum metal in nitric acid will be discussed later on, in the context of speciation of Mo in HNO_3 (compare section 4.2.3.1).

4.2.2.4 Mechanism and Kinetics

The difference in dissolution rate of molybdenum in 20 and 100 mL is caused by the dissolution mechanism of metals (e.g. Cu, Fe, Ni, Zn, Co) in nitric acid[75-83] (compare section 1.8.3.1), which involves autocatalysis by nitrous acid. The undissociated HNO_3 but not the dissociated $NO_3{\cdot}H_3O$ acts oxidizing to metals.[75] The first step in metal dissolution by nitric acid is an adsorption desorption step.[75, 79, 82]

$$\text{Mo} + HNO_3 + 2H^+ \rightleftharpoons \text{Mo}{:}HNO_3 + 2H^+ \rightarrow \text{Mo}^{2+} + HNO_2 + H_2O \qquad \textbf{(70)}$$

The first adsorption-desorption step (71) is considered to be rate determining for the dissolution[79]; a slow induction period followed by a more rapid dissolution was observed. The adsorption-desorption of the intermediate HNO_2 on the metal surface is much faster than that of HNO_3. The first step (equation (71)) plays an important role in the initial formation of HNO_2 by reduction of the absorbed HNO_3 on the metal surface. At the time of a measurable decrease in HNO_3 concentration relatively faster step starts to be predominant. This step involves the reduction of HNO_2 to NO on the metal surface:[79]

$$\text{Mo}^{n+} + HNO_2 + H^+ \rightleftharpoons \text{Mo}^{(n+1)+} + NO + H_2O \quad n = 0 - 5 \qquad \textbf{(71)}$$

The adsorption-desorption of the intermediate HNO_2 on the metal surface is much faster than that of HNO_3. Nitric oxide formed in reaction (72) reacts rapidly with HNO_3 forming HNO_2.

$$2NO + HNO_3 + H_2O \rightarrow 3HNO_2 \qquad \textbf{(72)}$$

This reaction takes place at the metal surface as well as in the bulk solution[79]. In 20 mL acid the nitrous acid is diluted less, which leads to a shortened induction period, as can be seen in Figure 89. Comparing dissolution rates in 20 and 100 mL the nitrous acid concentration is lower in 100 mL acid; therefore the induction period is longer and concentrations are lower at the surface and in the bulk solution.

Additionally, the induction period is further shortened by the addition of iron. The dissolution rate after the induction period is similar for all dissolver solutions. As described above the activation energy of the dissolution of molybdenum in nitric acid indicates a diffusion control, which is in agreement with the autocatalytic mechanism. In the presence of iron the activation energy is suggests a surface controlled. The presence of iron(III) not only increases the solubility, but also influences the dissolution mechanism of molybdenum in nitric acid.

The obtained activation energy of the dissolution of molybdenum in nitric acid was 21 ± 10 kJ/mol, whereas the activation energy of the dissolution of molybdenum in nitric acid containing iron(III) as an additive was significantly higher (42 ± 11 kJ/mol). A similar effect was observed for the dissolution of uranium dioxide by various authors, an activation energy of 37 kJ/mol was found for the ’nitrous acid route’, while the activation energy of the ‘nitric acid route’ was 80 kJ/mol.[217, 222-224]

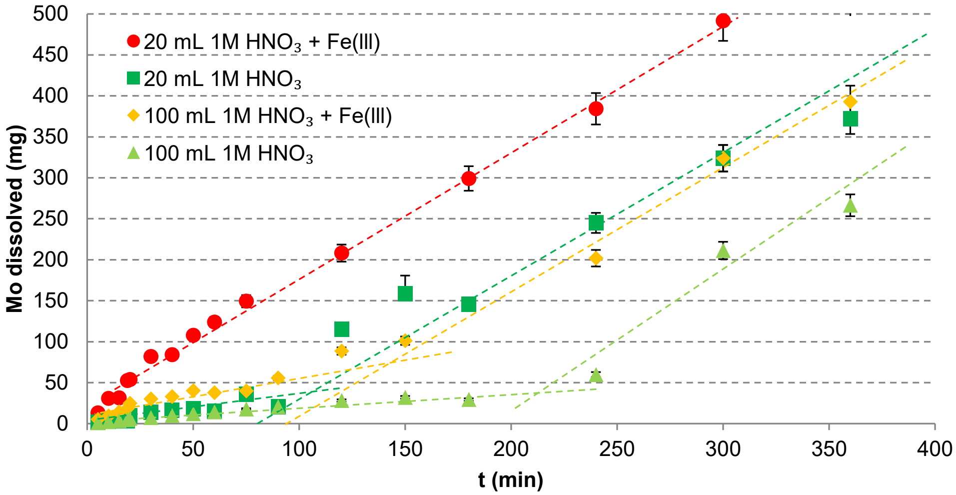

Figure 89: Dissolution of molybdenum from mixed Mo/CeO_2 60/40 pellets (1 g) in 20 and 100 mL 1 mol/L HNO_3 without Fe(III) or containing 1 eq. of Fe(III) per equivalent of Mo at RT.

This is further confirmed by experiments where $NaNO_2$ is added to the nitric acid. In 1 mol/L HNO_3 the addition of $NaNO_2$ stimulates dissolution which is autocatalytic, HNO_2 being the catalyst, and even eliminates the induction period as depicted in Figure 90. During this period, the oxides (MoO_3 to MoO_2) form on the surface. Then, the dissolution is actually an electrolytic corrosion.[96, 101] On the contrary, in the presence of iron the addition of nitrite has no effect as shown in Figure 91.

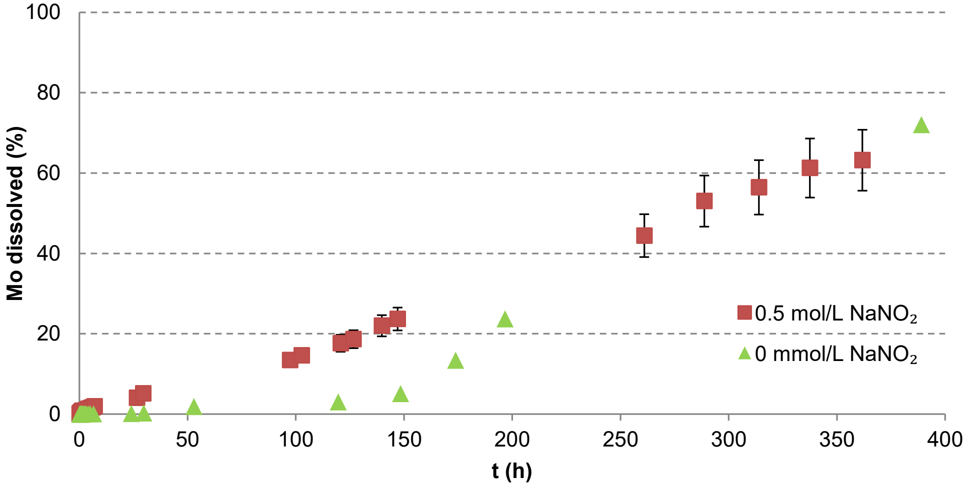

Figure 90: Dissolution of Mo pellets in 1 mol/L HNO_3 with and without the addition of $NaNO_2$ at RT.

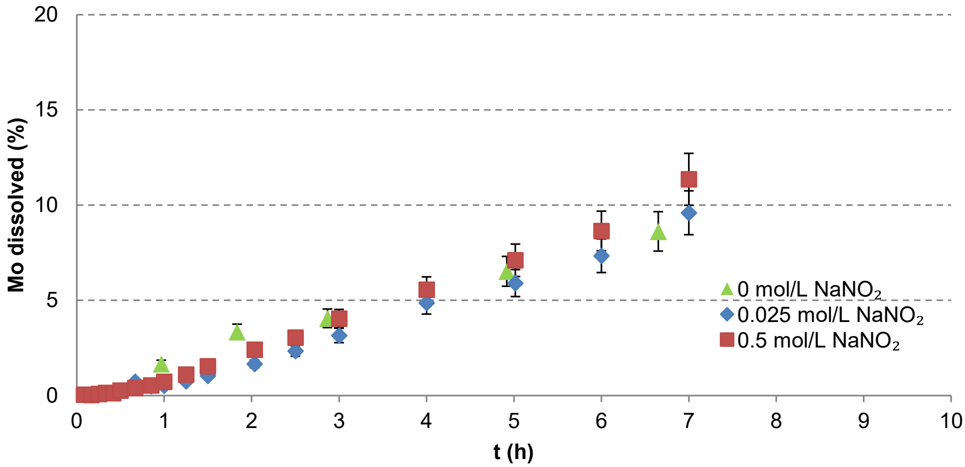

Figure 91: Dissolution of Mo pellets in 1 mol/L HNO_3/1 mol/L $Fe(NO_3)_3$ with the addition of different amounts of $NaNO_2$ at RT.

4.2.2.5 Mo/PuO_2 Pellets

All dissolution tests with unirradiated pellets containing PuO_2 were performed at the Institute für Nukleare Entsorgung (INE) within the Karlsruher Institut fürTechnologie (KIT). The dissolution of mixed Mo/PuO_2 pellets is carried out at RT in an acid volume of 100 mL. The larger acid volume was chosen to minimize Mo precipitation.

Pre-tests

The dissolution parameters which were chosen for the dissolution experiments on unirradiated Mo/PuO_2 pellets were pretested with Mo powder. 1 mol/L HNO_3, 1 mol/L HNO_3/0.2 mol/L $Fe(NO_3)_3$, and 7 mol/L HNO_3 were chosen as solvent. In the case of 7 mol/L HNO_3 15 mL of acid were used initially and later on (after 7 d) diluted to reach a HNO_3 concentration of 1 mol/L. This method was chosen because the dissolution kinetic in 7 mol/L HNO_3 is faster, but the solubility of Mo is lower compared to 1 mol/L HNO_3. The concentrations of molybdenum in solution are displayed in Figure 92 as a function of time. Molybdenum can be completely dissolved in 1 mol/L HNO_3 in the presence of iron(III). Although the Mo concentrations in 1 mol/L HNO_3 without Fe(III) are similar a precipitate is visible. Contrary to expectation the Mo concentration in 7 mol/L HNO_3 declines upon dilution, a complete dissolution cannot be achieved. Therefore, an additional test in 3 mol/L HNO_3 was performed, because this condition was successfully tested at NRG Petten. However, the results were very similar to the 1 mol/L HNO_3 (compare Figure 92 and Figure 93). The ratio of Molybdenum in solution and precipitated Mo for the different dissolver solutions is shown in Figure 93. Mo is completely dissolved in 1 mol/L HNO_3/0.2 mol/L $Fe(NO_3)_3$; in the case of 1 and 3 mol/L HNO_3 about 5% of the molybdenum precipitate. In 7 mol/L HNO_3 which is diluted to 1 mol/L HNO_3 less than 50% of the molybdenum dissolves. PuO_2 is not expected to dissolve at the chosen conditions. The residue would afterwards be washed in NaOH to dissolve possible MoO_3 precipitates, and then dissolved at suitable conditions, such as boiling concentrated nitric acid (5-7 mol/L). Complexants such as fluoride or oxidants such as Ag(II) and Ce(IV) accelerate the PuO_2 dissolution[170-171, 173].

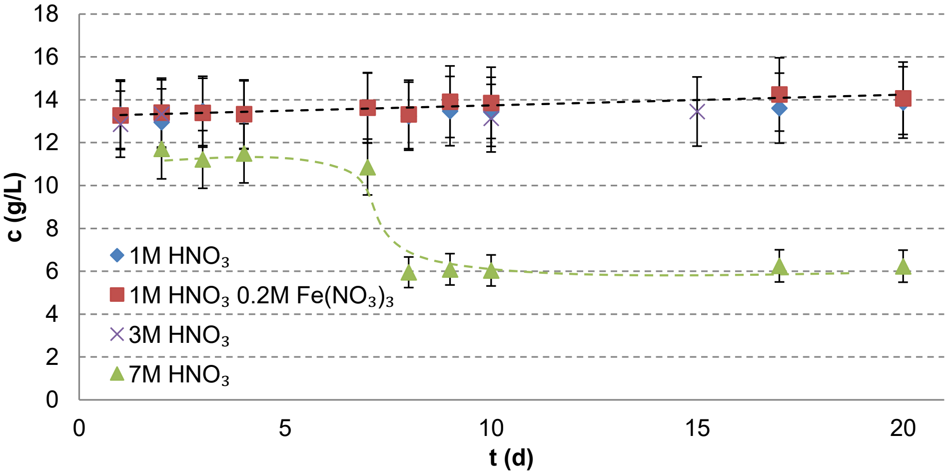

Figure 92: Dissolution of Mo powder (1 g) in various solvents (100 mL; 7 mol/L HNO_3: 15 mL, after 7 d dilution to 100 mL) at RT.

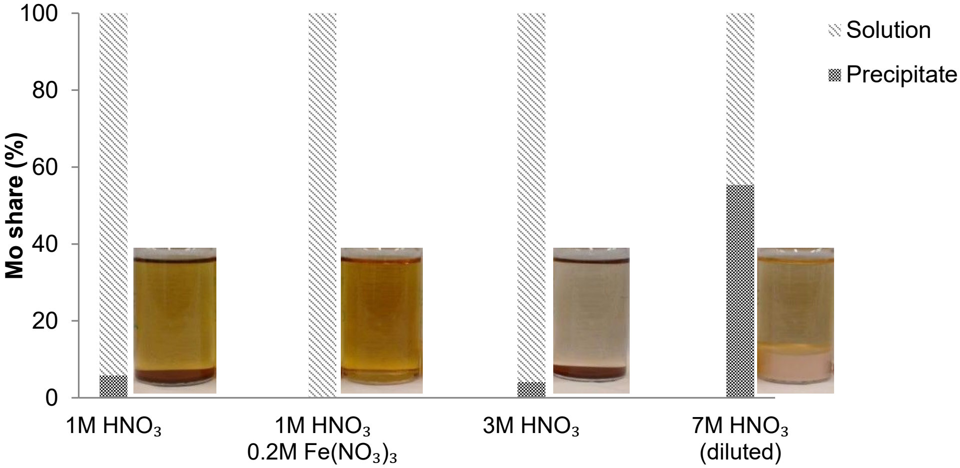

Figure 93: Distribution of Mo (1 g) between solution and precipitate for different dissolver solutions (100 mL; 7 mol/L HNO_3: 15 mL, after 7 d dilution to 100 mL).

Tests with Unirradiated PuO_2 Pellets

Pellets with PuO_2 contents of 5, 25, and 40 wt.% were dissolved in 100 mL solution. The dissolution media were 1 and 3 mol/L HNO_3 and 1 mol/L HNO_3/0.2 mol/L $Fe(NO_3)_3$. All dissolution experiments were performed at RT. The concentrations of Mo and Pu in the solution are determined by ICP-MS, and ^{241}Am by γ-counting. The plutonium dioxide fraction of the pellet contains 0.67 wt.% ^{241}Am, which is a decay product of ^{241}Pu. The residues are still to be investigated by XRD and SEM. The results of the dissolution experiments in 3 mol/L HNO_3 are displayed in Figure 94 for molybdenum and Figure 95 for plutonium.

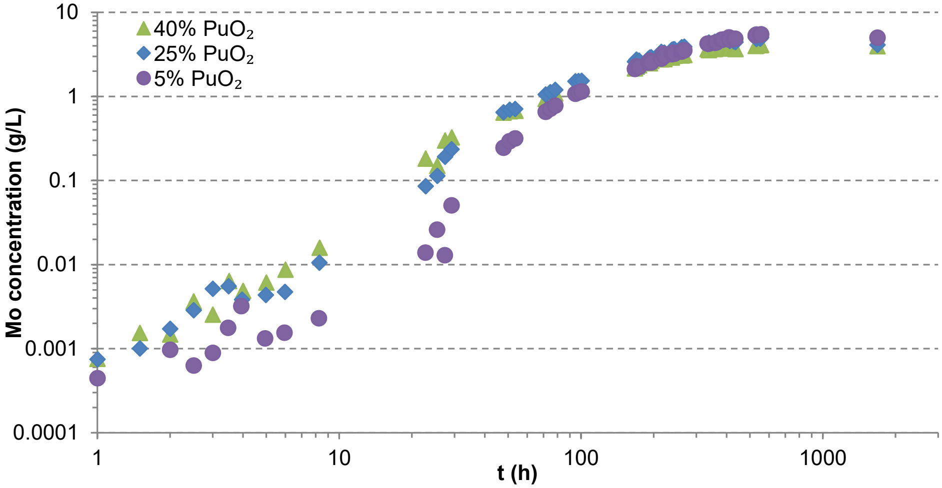

Figure 94: Dissolution of molybdenum from mixed Mo/PuO_2 pellets (0.8 g) with different Plutonium shares in 100 mL 3 mol/L HNO_3 at RT as a function of time.

The dissolution velocity of molybdenum is similar for all pellet compositions (Figure 94), whereas the dissolution of plutonium (Figure 95) and americium (not shown) is significantly slower for the pellet with the lowest plutonium content. This can be assigned to the difference in PuO_2 surface area. No voluminous white MoO_3 precipitate was observed. Equilibrium in Mo dissolution is reached after about 20 days, at this time the Mo concentration in solution is about 4 g/L, which corresponds to 85% of the molybdenum, the Pu concentration is 0.08 g/L (3%) and the Am concentration is 0.001 g/L (5%). At the end of the experiments a black powder, which is expected to be PuO_2, remains as a residue.

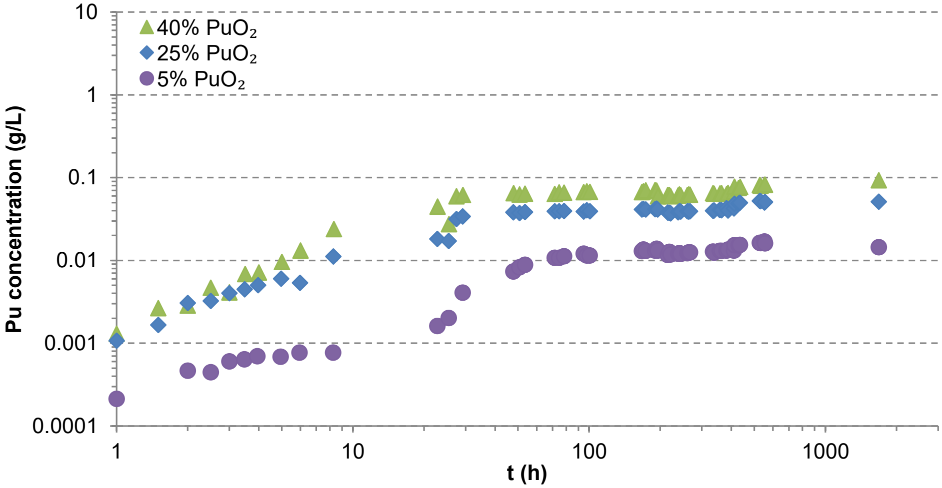

Figure 95: Dissolution of plutonium from mixed Mo/PuO_2 pellets (0.8 g) with different Plutonium shares in 100 mL 3 mol/L HNO_3 at RT as a function of time.

The dissolution of molybdenum, plutonium and americium from mixed Mo/PuO_2 pellets in 3 mol/L HNO_3 and 1 mol/L HNO_3 containing 0.2 mol/L $Fe(NO_3)_3$ is compared in Figure 96 and Figure 97 respectively. The pellet with 25 wt.% PuO_2 share is most suitable to represent all three pellet compositions and is therefore considered exemplarily. In 3 mol/L HNO_3 the initial concentration of molybdenum is similar to that of plutonium, but shows a greater increase with time. The concentration of Am is about two orders of magnitude lower compared to Pu at all times. When the equilibrium in Mo dissolution is reached the Mo concentration is about two orders of magnitude higher than the Pu concentration and four orders of magnitude higher than that of Am. In 1 mol/L HNO_3/0.2 mol/L $Fe(NO_3)_3$ the dissolution rate of molybdenum is significantly increased, while the dissolution rates of the actinides are decreased, as described above. The concentrations of Mo and Pu in 1 mol/L HNO_3/0.2 mol/L $Fe(NO_3)_3$ differ by four orders of magnitude, the concentrations of Mo an Am by five orders of magnitude. The same applies to the overall solubility.

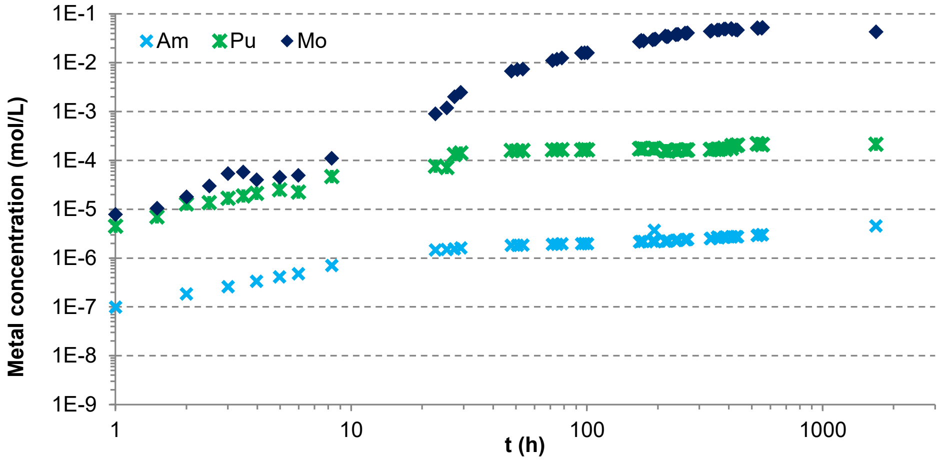

Figure 96: Dissolution of Mo, Am, and Pu from mixed Mo/PuO_2 pellets (0.8 g) with 25 wt.% PuO_2 share in 100 mL 3 mol/L HNO_3 at RT as a function of time.

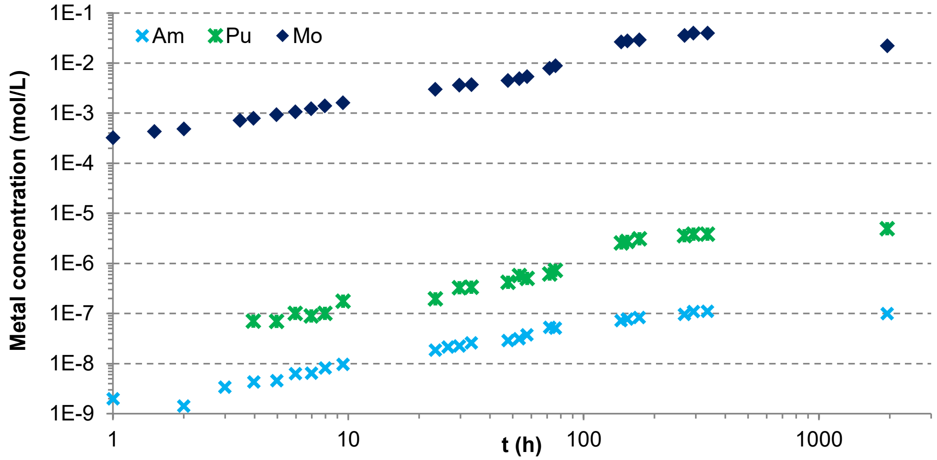

Figure 97: Dissolution of Mo, Am, and Pu from mixed Mo/PuO_2 pellets (0.8 g) with 25 wt.% PuO_2 share in 100 mL 1 mol/L HNO_3/0.2 mol/L $Fe(NO_3)_3$ at RT as a function of time.

The influence of the dissolver solution on the dissolution of Mo, Pu, and Am is highlighted in Figure 98, Figure 99 and Figure 100 respectively. Again the pellet with 25 wt.% PuO_2 content is considered exemplarily. Molybdenum (Figure 98) initially dissolves significantly faster in 1 mol/L HNO_3 containing 0.2 mol/L $Fe(NO_3)_3$ compared to 3 mol/L HNO_3, but the concentrations align after about 80 h; in 1 mol/L HNO_3 molybdenum dissolution is significantly slower. The dissolution of plutonium (Figure 99) as well as americium (Figure 100) is similar in 1 and 3 mol/L HNO_3, but is significantly slower in the presence of iron. Moreover, the overall solubility of both elements is reduced. The overall solubility of both actinides is slightly lower in 1 mol/L HNO_3 compared to 3 mol/L HNO_3. The increase in molybdenum solubility in the presence of iron(III) is caused by complexation as discussed above. In the case of the actinides different approaches may be considered concerning the influence of Fe(III) on the dissolution. The solution chemistry of Pu is very complex, because it undergoes disproportionation reactions and can exist simultaneously as Pu(IV), Pu(V), and Pu(VI) under oxidizing conditions. Plutonium is expected to be present in oxidation state +4 due to the solution being loaded with nitric acid and reduction products (HNO_2) from molybdenum dissolution.

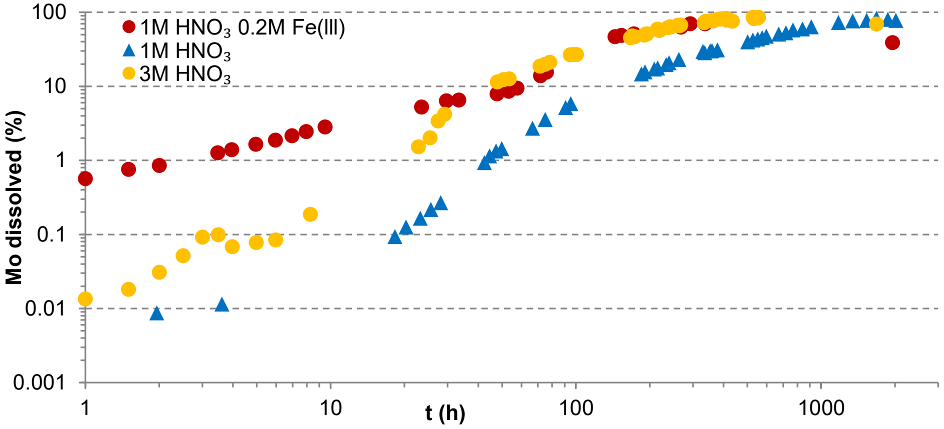

Figure 98: Dissolution of Mo from mixed Mo/PuO_2 pellets (0.8 g) with 25 wt.% PuO_2 share in 100 mL of different dissolver solutions at RT as a function of time.

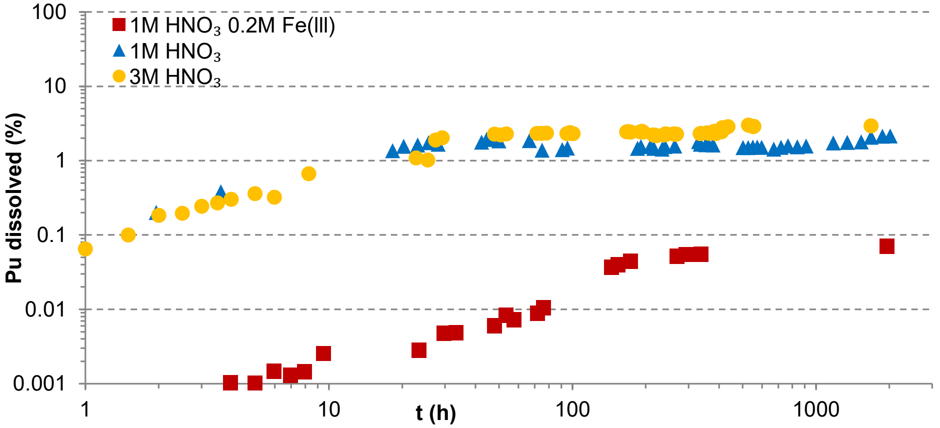

Figure 99: Dissolution of Pu from mixed Mo/PuO_2 pellets (0.8 g) with 25 wt.% PuO_2 share in 100 mL of different dissolver solutions at RT as a function of time.

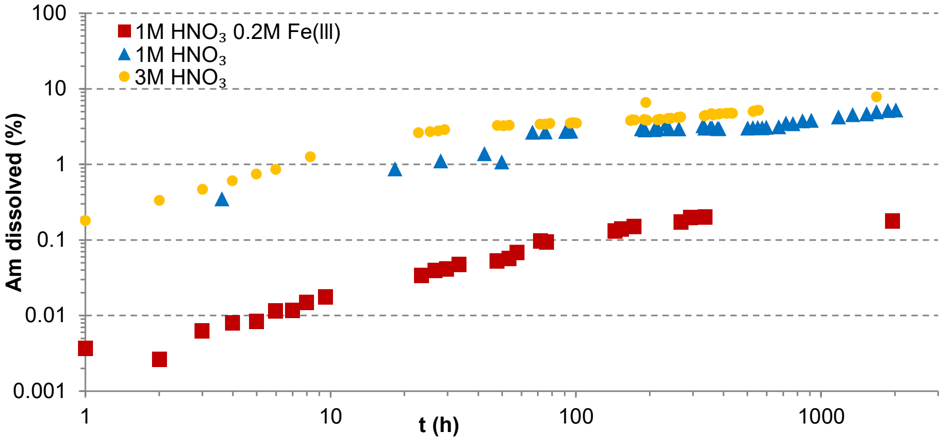

Figure 100: Dissolution of Am from mixed Mo/PuO_2 pellets (0.8 g) with 25 wt.% PuO_2 share in 100 mL of different dissolver solutions at RT as a function of time.

Kulyako *et al.*[225] studied the dissolution of UO_2, U_3O_8 and solid solutions of actinides in UO_2 in aqueous solution of ferric nitrate as a new approach to reprocessing of oxide nuclear fuel. In the process; Fe(III) oxidizes U(IV) to U(VI) the compounds of which are more soluble than those of U(IV). However, Pu occurs in these solutions in the form of Pu(III), because the Pu(IV) initially present in the MOX fuel was reduced in the course of the dissolution to Pu(III) with Fe(II) originating from the oxidation of U(IV) to U(VI) with Fe(III). Am present in the crystal lattice of UO_2-AmO_2 as Am(IV) is likewise reduced to Am(III).[225] Since there is no U present in the system investigated in this work and there is no other clear evidence for the presence of Fe(II), this approach can be excluded. The influence of the presence of metal cations, among them Zr(IV), Al(III) and Fe(III) on the dissolution of actinide oxides in HNO_3-HF solution was investigated by various authors[226-228]. A decrease in dissolution rate was observed. However, this effect is attributed to the complexation of fluoride by the cations, which cannot be the case here. According to Esbelin[96] the presence of plutonium seems to increase the solubility of molybdenum due to the mixed species such as $Pu(MoO_4)_3H_2 \cdot nH_2O$ or $Pu_2Mo_6O_{22} \cdot nH_2O$. This could also explain the relatively high solubility of plutonium. The solubility of plutonium could also be promoted by molybdate surface complexation of PuO_2, favouring dissolution. The introduction of Fe(III) favours the formation of plutonium valency VI, and therefore its presence would further reduce Pu losses.[96] However, the large excess of iron present in the solutions investigated here could displace the Pu from the complexes, thereby reducing the solubility of plutonium. Iron(III) and many of the actinide elements, especially plutonium(IV), share many chemical properties. They are hard Lewis acids, behave similar in water and are bound by basic ligands that can provide electrical charge, such as negatively charged oxygen donor ligands.[229-230] The formation of mixed iron molybdenum complexes was verified by ESI-MS measurements as discussed in section 4.2.3.1.

4.2.3 Speciation of Molybdenum in Nitric Acid Medium

The solution species of Mo in strongly acidic media were characterized and quantified comprehensively. For this purpose electrospray ionization mass spectrometry (ESI-MS), which can probe the stoichiometry and relative abundances of solution species, was applied. The speciation of molybdenum in nitric acid was studied with the homemade ALBATROS ESI-ToF and with a commercially available QTrap instrument. The ALBATROS is located at the Institut für Radioökologie und Strahlenschutz (IRS) within the Leibniz Universität Hannover. This allows the direct measurement of the sample, even in concentrated nitric acid, without dilution or other alteration of the sample. However, the acquisition of one spectrum takes about two days. With the QTrap instrument, which is located at the Zentralinstitut für Engineering, Elektronik und Analytik (ZEA-3) within the Forschungszentrum Jülich GmbH, on the other hand, the measurement time is reduced to a few minutes, making routine measurements possible. But due to potential corrosion problems the samples need to be diluted prior to measurements, which may influence the speciation. A method to analyse solutions of molybdenum with natural isotopic composition with a commercially available ESI/MS/MS instrument (QTrap) was developed. The stability of the detected polymolybdate anions was analysed with MS/MS experiments. Additionally, the influence of the solvent (acetonitrile) and the dilution on the relative abundance of polymolybdates was systematically investigated. Based on this investigation a measuring protocol was defined and implemented to study the speciation of molybdenum in nitric acid at low pH.

4.2.3.1 ALBATROS ESI-ToF

The mass spectrum of a solution of [^{98}Mo] < 10 mmol/L in 0.5 mol/L HNO_3 is shown in Figure 101. The spectra are plotted on a logarithmic scale to facilitate the visualization of minor species. The measured data are plotted in black, the coloured lines are fits to the data taking into account varying number of water molecules n, which causes the appearance of a peak cluster in the spectra, of each detected molecule ($[Mo_xO_y(OH)_a(NO_3)_b(N_2)_c]^+ \cdot nH_2O$). This means that the species assigned as $[MoO_2OH]^+$ represents ions with the general formula $[MoO_2OH(H_2O)_n]^+$ with n = 10 - 40 for instance. Only singly charged species are observed. The evaluation of the spectra was carried out as follows: All possible combinations

$$\begin{gathered}[Mo_xO_y(OH)_a(NO_3)_b(N_2)_c]^+ \cdot nH_2O,\\ x = 1 - 10;\ y = 1 - 29;\ a = 0, 1;\ b = 0, 1;\ c = 0, 1;\ n = 0 - 40\end{gathered} \qquad \textbf{(73)}$$

are fit to the data by a C++ based fitting routine. When a set of data fits the data simultaneously, the relative abundances are calculated. The peak areas of all different numbers of water molecules are summed up for each species $[Mo_xO_y(OH)_a(NO_3)_b(N_2)_c]^+ \cdot nH_2O$, resulting in the total number of ions N

$$N([Mo_xO_y(OH)_a(NO_3)_b(N_2)_c]^+) = \sum_n N([Mo_xO_y(OH)_a(NO_3)_b(N_2)_c]^+ \cdot nH_2O) \qquad \textbf{(74)}$$

The water molecules are omitted in the following for the sake of simplicity. The mass spectrum reveals the following Mo(VI) hydroxide complexes: monomeric $[MoO_2OH]^+$, dimeric $[Mo_2O_5OH]^+$, trimeric $[Mo_3O_8OH]^+$, tetrameric $[Mo_4O_{11}OH]^+$, and pentameric $[Mo_5O_{14}OH]^+$. Additionally, a dimeric nitrate complex is detected $[Mo_2O_5NO_3]^+$. No hexamere is detected, as in previous measurements of MoO_3 at the same measurement parameters[231]. Besides the presence of Mo(VI) species the spectrum shows that two Mo(V) species ($[Mo^VOOHNO_3]^+$ and

$[Mo^VO_2]^+$) are present in solution in spite of the oxidizing condition in strong nitric acid. Since the conditions in the electrospray (positive mode) are also oxidizing, experimental artefacts are unlikely. There are a few peaks in the spectrum (in the range of m/q 450-600) which could not be assigned yet but they account to a proportion of only 4-5%.

The mass spectrum of a solution of $[^{98}Mo] < 10$ mmol/L in 1 mol/L HNO_3 is depicted in Figure 102. Like in the first sample monomeric $[MoO_2OH]^+$, dimeric $[Mo_2O_5OH]^+$ and $[Mo_2O_5NO_3]^+$, trimeric $[Mo_3O_8OH]^+$, tetrameric $[Mo_4O_{11}OH]^+$, and pentameric $[Mo_5O_{14}OH]^+$ are detected. Additionally, one pentavalent Mo species ($[Mo^VOOHNO_3]^+$) is present in solution. The relative abundances of the molybdenum species are compared in Figure 103. The tendency towards polymerization is lower in 1 mol/L HNO_3 compared to 0.5 mol/L HNO_3.

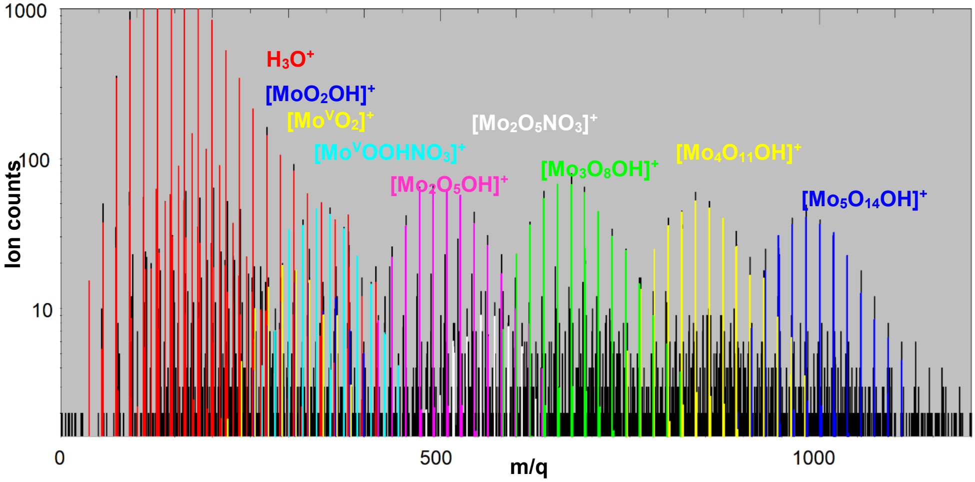

Figure 101: Mass spectrum of a solution of $[^{98}Mo] < 10$ mmol/L (metal powder) in 0.5 mol/L HNO_3 aged for about 2 weeks.

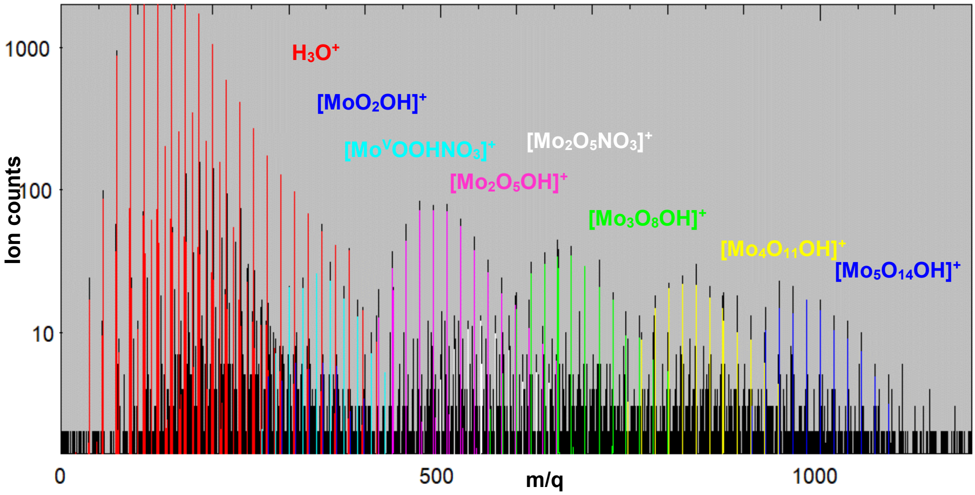

Figure 102: Mass spectrum of a solution of $[^{98}Mo] < 10$ mmol/L (metal powder) in 1 mol/L HNO_3 aged for about 2 weeks.

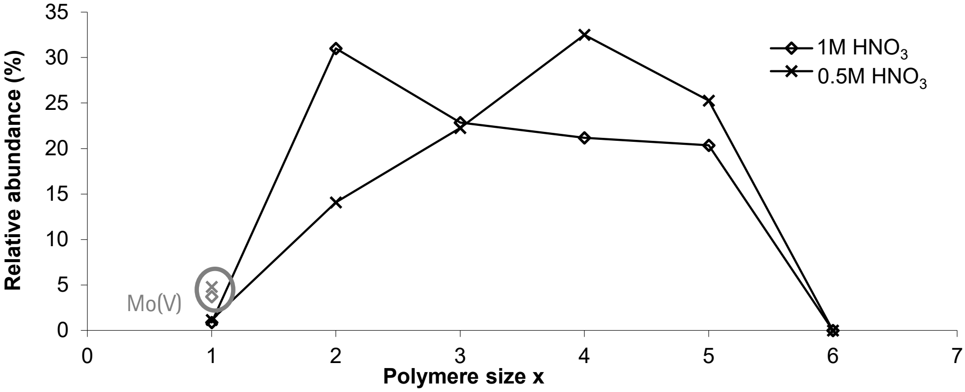

Figure 103: Relative abundances of Mo-polymers in 0.5 and 1 mol/L HNO_3.

Speciation of Molybdenum during Pellet Dissolution

A molybdenum pellet synthesized with isotopically pure ^{98}Mo metal-powder at similar conditions as the pellets mentioned before but with a diameter of 2.5 mm, a height of 0.7 mm and a mass of 38 mg was dissolved in 1 mol/L nitric acid at 60 °C. Samples were taken after 3, 5, 6 and 10 days as well as after 6 month. Figure 104 shows the MS spectrum of the dissolution of Mo pellets in 1 mol/L HNO_3, at 60 °C after 3 days. The mass spectrum reveals the following hexavalent molybdenum (Mo(VI)) complexes: dimeric $[Mo_2O_5OH]^+$ and $[Mo_2O_5NO_3]^+$ the latter is known as solution species of molybdenum in concentrated nitric acid solution (compare section 1.8.3.1); trimeric $[Mo_3O_8OH]^+$ and $[Mo_3O_8NO_3]^+$; tetrameric $[Mo_4O_{11}OH]^+$; and pentameric $[Mo_5O_{14}OH]^+$. No hexamere is detected, which is agreement with previous measurements of MoO_3 at the same measurement parameters [231]. Besides the presence of hexavalent Mo species the spectrum shows that two pentavalent Mo species ($[Mo^VOOHNO_3]^+$ and $[Mo^VO_2OH]^+$) are present in solution in spite of the oxidizing condition in strong nitric acid. Since the conditions in the electrospray (positive mode) are also oxidizing, experimental artefacts are unlikely.

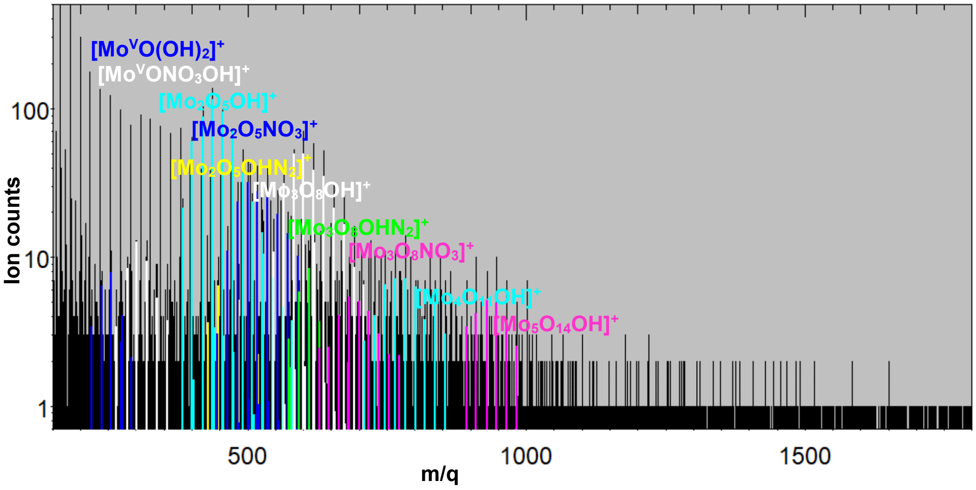

Figure 104: Speciation during dissolution of Mo pellets in 1 mol/L HNO_3, at 60 °C after 3 days.

With the progress of time even larger polymers appear in the spectrum (compare Figure 105). The mass spectrum of the dissolution of Mo pellets in 1 mol/L HNO_3, at 60 °C after 12 month additionally shows hexavalent molybdenum hydroxide ($[Mo_7O_{20}OH]^+$, $[Mo_8O_{23}OH]^+$, $[Mo_9O_{26}OH]^+$, and $[Mo_{10}O_{29}OH]^+$) and nitrate ($[Mo_4O_{11}NO_3]^+$, $[Mo_5O_{14}NO_3]^+$, and $[Mo_7O_{20}NO_3]^+$) complexes.

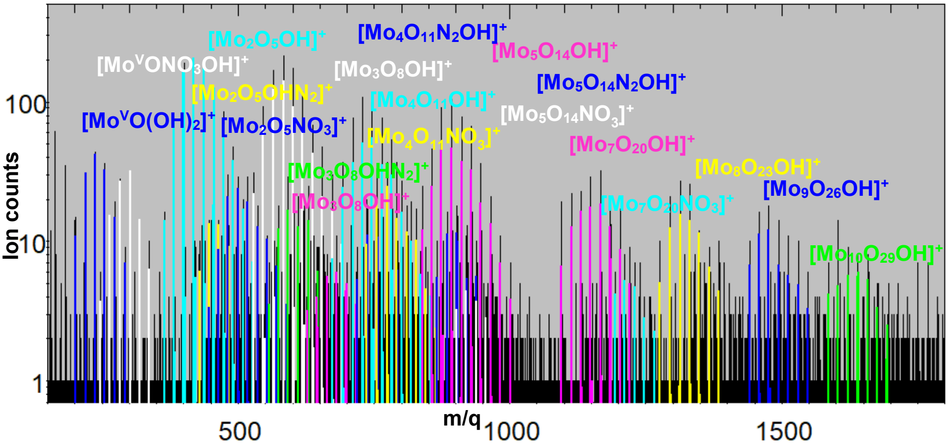

Figure 105: Speciation during dissolution of Mo pellets in 1 mol/L HNO3, at 60 °C after 6 month.

The abundances of Mo polymers upon dissolution in 1 mol/L HNO_3, at 60 °C for different times or rather concentrations are depicted in Figure 106. Larger Mo polymers form with increasing molybdenum concentration or time. First the dimer is the dominant species. The relative abundance of the trimeric species $[Mo_3O_8OH]^+$ increased with time. After more than 5 days, at Mo concentrations above 8 mmol/L the trimer becomes the dominant species. Whether the polymerization is dependent on the concentration or the time or both cannot be distinguished on the basis of this investigation. A remeasuring of the first sample would be necessary to check whether the speciation has changed over time. As in all previous measurements no hexamer is detected.

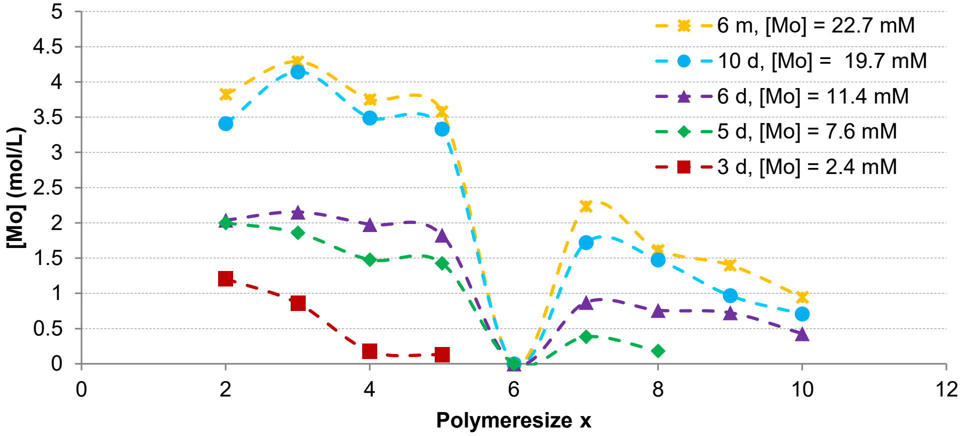

Figure 106: Abundances of Mo polymers upon dissolution in 1 mol/L HNO_3, at 60 °C for different times or rather concentrations.

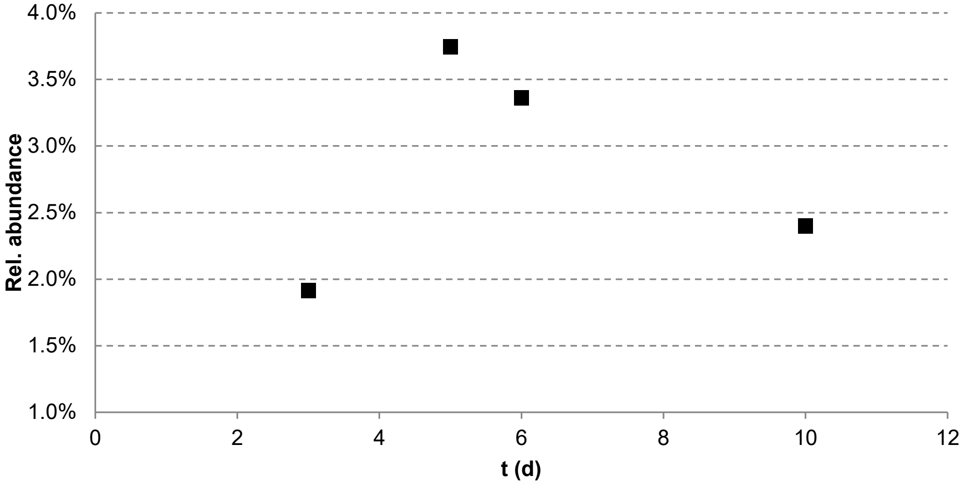

Figure 107: Relative abundance of Mo(V) in solution obtained by dissolution of Mo pellets in 1 mol/L HNO_3 at 60 °C as a function of time.

In all samples a portion of the Mo is present in the oxidation state +V ($Mo^{V}O(NO_3)(OH)^+$ and $Mo^{V}O(OH)_2^+$). These species seem to form as intermediate species in the dissolution process. The relative abundance of Mo(V) decreases with time (compare Figure 107), which is in agreement with the expected progressing oxidation by nitric acid. The initial increase in Mo(V) abundance is probably due to a molybdenum(VI) oxide layer which had been formed on the surface of the pellet prior to the start of the dissolution experiment and dissolves at first.

Raman spectra were recorded on the surface of equivalent solutions with molybdenum of natural isotopic composition. Figure 108 shows the Raman spectra of the solution of a Mo pellet in 1 mol/L HNO_3, at 60 °C after different amounts of time. Intensities of the spectra were normalized based on the nitrate band at 1048 cm^{-1}. The most intense band at 955 cm^{-1} can be assigned to the symmetrical stretching vibration of a Mo=O group, assigned by Himeno and Hasegawa[232]. The two other bands at 922 and 860 cm^{-1} are assigned to the asymmetric stretching vibrations of a M=O group and a linear mono-oxobridge. The intensity of the band assigned symmetrical stretching vibration of terminal Mo=O groups increases with the Mo concentration within the first 6 days and then stays constant while the intensity of the band assigned to the asymmetric stretching vibrations of mono-oxobridges appears, which is in agreement with the observation of increasing relative abundance of the larger polymers after 6 days.

The relatively complicated distribution of species might have implications on the actual reprocessing steps of the Mo-IMF, because different species can exhibit a different behaviour during liquid-liquid extraction steps.

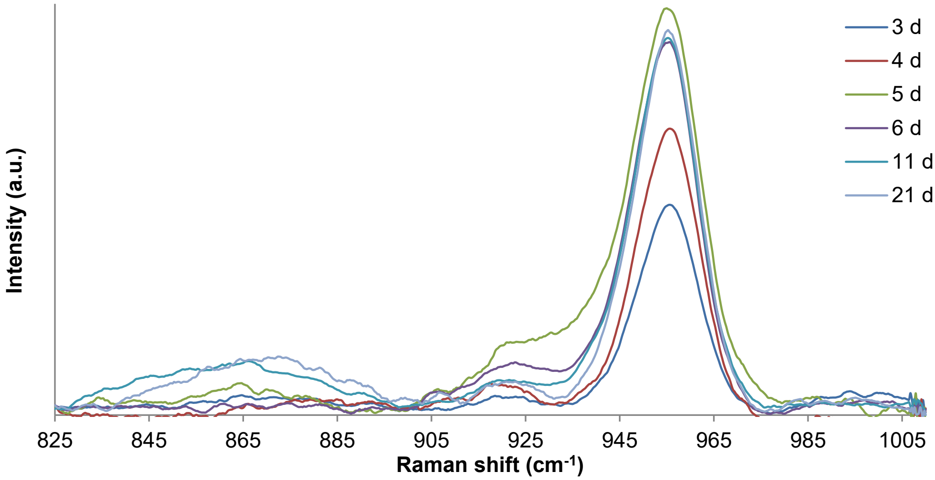

Figure 108: Raman spectra of solutions obtained by dissolving a Mo pellet in 1 mol/L HNO_3, at 60 °C after different amounts of time. Intensities of the spectra were normalized based on the nitrate band.

Mixes Molybdenum Iron Species

Additionally, a solution containing molybdenum and iron (ratio 1:1) was investigated. For this purpose, a stock solution containing 1 mol/L $Fe(NO_3)_3 \cdot 9H_2O$ was prepared and added to a molybdenum sample. The sample was measured after a few days as well as after 14 month. The spectrum of the fresh solution shows the presence of pentavalent and hexavalent Mo species in the solution (compare Figure 109). One monomeric pentavalent molybdenum species ($[Mo^{V}OOHNO_3]^+$) and two dimeric and one trimeric hexavalent Mo species ($[Mo_2O_5OH]^+$, $[Mo_2O_5NO_3]^+$, and $[Mo_3O_8OH]^+$) are detected. Additionally, the spectrum shows mixed iron molybdenum species: $[Mo^{VI}O_2Fe^{III}(NO_3)_2(OH)_2]^+$ (rel. abundance about 7% of the Mo solution species), $[Mo^{VI}_2O_5Fe^{III}NO_3(OH)_3]^+$ (rel. abundance about 13% of the Mo solution species) and $[Mo^{V}_2O_3Fe^{III}(NO_3)_5(OH)]^+$. This is however merely a chemical formula and each species contains water molecules. So it might be in the case of $[Mo^{VI}_2O_5Fe^{III}NO_3(OH)_3]^+$ species that this is actually $[Mo^{VI}_2O_6Fe^{III}NO_3OH \cdot H_2O]^+$. However the $[Mo_2O_5]^{2+}$ ion is known from the literature.[111, 233] The same applies to the $[Mo^{VI}O_2Fe^{III}NO_3OH \cdot H_2O]^+$ species. This cannot be distinguished on the basis of the chemical formula. However, these are clearly mixed iron-molybdenum species. Concentration artefacts are unlikely as the mixed species do not consist simply of the corresponding main species. Besides the presence of Fe(III) the spectrum shows that Fe(II) is present in solution in spite of the oxidizing condition in strong nitric acid. Since the conditions in the electrospray (positive mode) are also oxidizing, experimental artefacts are unlikely. Iron(III) is well known to oxidize Mo(V) complexes, in acidic aqueous solution.[112]

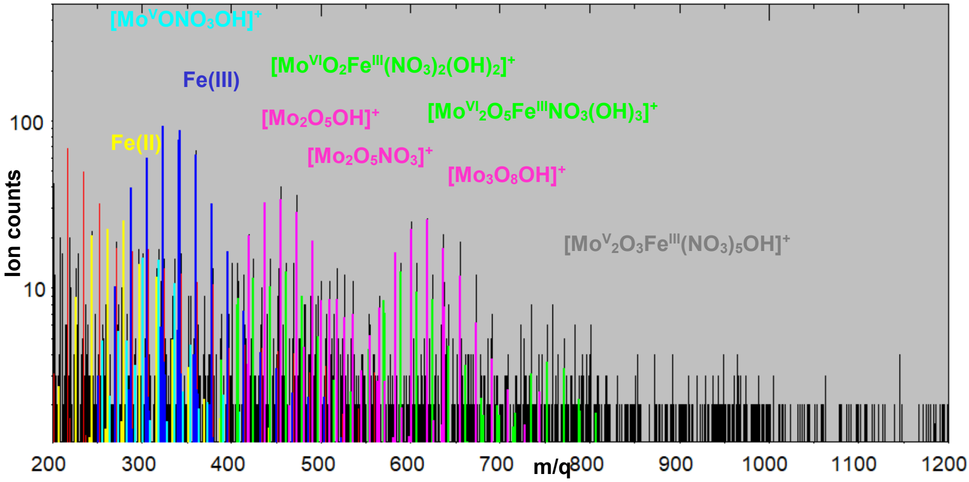

Figure 109: MS spectrum of a fresh solution containing ^{98}Mo and Fe(III) 1:1, $[^{98}Mo]$ = 10 mmol/L, [Fe] = 10 mmol/L in 1 mol/L HNO_3.

After the sample has been aged for 14 month the spectrum (Figure 110) additionally shows two hexavalent molybdenum hydroxide complexes (tetrameric $Mo_4O_{11}(OH)^+$ and pentameric $Mo_5O_{14}(OH)^+$) and two mixed iron molybdenum species ($Mo^{VI}{}_3O_8Fe^{III}(NO_3)(OH)_3{}^+$ and $Mo^{VI}{}_4O_{11}Fe^{III}(NO_3)(OH)_3{}^+$). The mixed iron molybdenum species might be responsible for faster dissolution and for not forming precipitates. However, further methods are necessary to confirm these species. Identical samples as well as Mo metal samples for insitu investigations during dissolution were prepared for Mo K-edge X-ray absorption spectroscopy (XAS) at the ANKA facility at Karlsruhe. However, the intensity was insufficient for appropriate data evaluation.

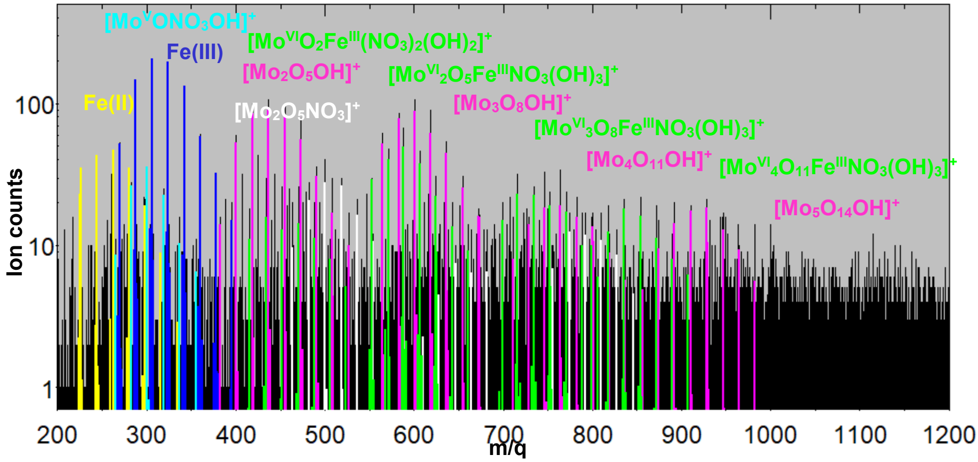

Figure 110: MS spectrum of a solution containing ^{98}Mo and Fe(III) 1:1, $[^{98}Mo]$ = 10 mmol/L, [Fe] = 10 mmol/L in 1 mol/L HNO_3, which was aged for 14 month**.**

The relative abundances in relation to all molybdenum species of molybdenum polymers in the fresh or aged solution are compared in Figure 111. The sum of molybdenum polymers (Figure 111) and mixed iron molybdenum complexes (Figure 112) corresponds to the molybdenum species as a whole. In agreement with the observations on samples containing no iron, larger polymers form with increasing time. In the fresh solution the dimer is the dominant species, whereas the trimer is dominant in the aged solution. In accordence with the molybdenum polymers, larger mixed iron molybdenum species are formed over time as can be seen from Figure 112. However, only complexes containing a single iron atom are detected. The shares of molybdenum, which occur in mixed iron molybdenum or pure molybdenum species are compared in Figure 113. Over time more mixed species form, while the percentage of pure molybdenum species decreases. The formation of these mixed iron molybdenum complexes is probably the reason for the increased dissolution rate and the higher solubility of molybdenum in nitric acid in the presence of iron.

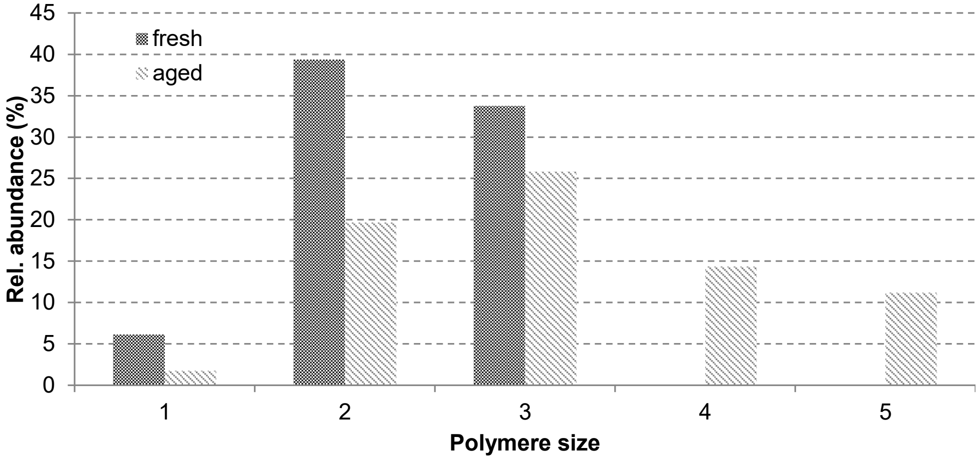

Figure 111: Relative abundances of Mo polymers in a fresh or aged solution (^{98}Mo:Fe(III) 1:1, [^{98}Mo] = 10 mmol/L, [Fe] = 10 mmol/L in 1 mol/L HNO_3) in relation to all Mo species.

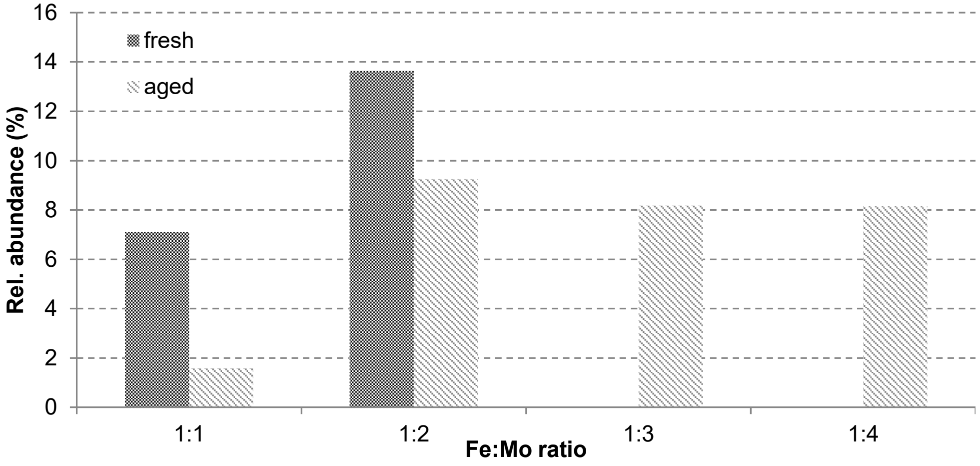

Figure 112: Relative abundances of mixed iron Mo complexes in a fresh or aged solution (^{98}Mo:Fe(III) 1:1, [^{98}Mo] = 10 mmol/L, [Fe] = 10 mmol/L in 1 mol/L HNO_3) in relation to all Mo species.

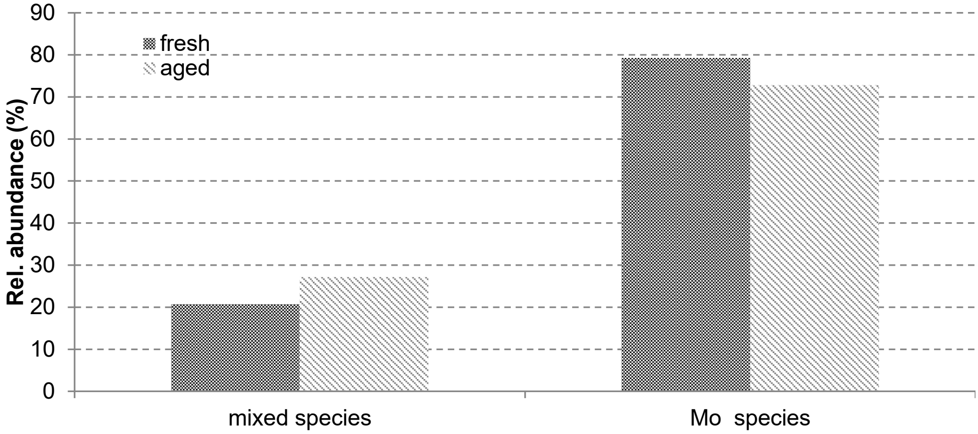

Figure 113: Rel. abundances of Mo in mixed Fe-Mo complexes and pure Mo species in a fresh or aged solution (^{98}Mo:Fe(III) 1:1, [^{98}Mo] = 10 mmol/L, [Fe] = 10 mmol/L in 1 mol/L HNO_3).

4.2.3.2 *Commercially Available ESI/MS/MS Instrument (QTrap)*

Analogous solutions of molybdenum with natural isotopic composition were analysed with a commercially available ESI/MS/MS instrument (QTrap). With the QTrap instrument the measurement time is reduced to a few minutes, making routine measurements possible. However, due to potential corrosion problems the samples need to be diluted prior to measurements, which might influence the speciation.

Development of a Measuring Protocol

The spectrum of the sodium molybdate (Na_2MoO_4) stock solution is shown in Figure 114. Monomeric molybdate can be assigned in the spectrum; the isotope pattern in the spectrum is consistent with the calculated pattern. In contrast to measurements with the ALBATROS, anionic species were detected with the commercial device, which is due to the dilution of the samples. This change in speciation is attributed to changes in the outer coordination sphere, because the polymerization of molybdenum was found to be slow.

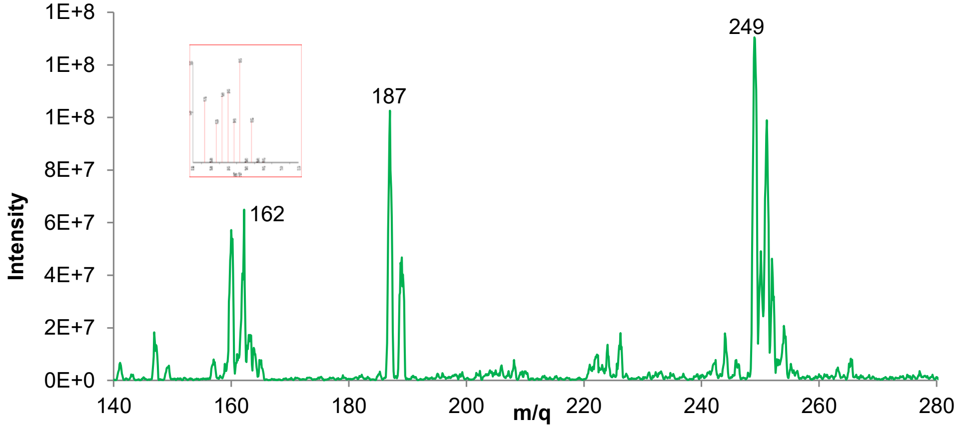

Figure 114: Sodium molybdate stock solution 10 mmol/L Mo in water, dilution 1:100 in water, then 1:10 in 50% AcN, measurement parameters: Q1 Scan, negative ion mode, MCA, IS -4.5 kV, DP -40 V.

The spectrum of the ammonium molybdate (para) hydrate ($(NH_4)_6Mo_7O_{24}\cdot 4H_2O$) stock solution is shown in Figure 115. According to Gmelin[108], the composition of ammonium para molybdate is usually not known precisely and the compound decomposes easily to form the tetra- and trimolybdate. Therefore, the compound is not useful as a single standard for the heptamolybdate. However, it can be used as mixed standard to optimize ESI conditions and to study the solvent effect on the polyoxomolybdates. The mass spectrum obtained matches the literature. On the basis of the m/z values and the isotope pattern (compare with the calculated pattern shown in red) singly charged anions of tri-, tetra -, penta-, hexa- and heptamolybdate are assigned. When considering the peak width it is noticeable that m/z 407, 480, 563, and 624 are smaller in width (15 u) then those already identified as the singly charged anions. This indicates doubly charged anions, which is confirmed by the occurrence of intervals of 0.5 u within the isotope pattern.

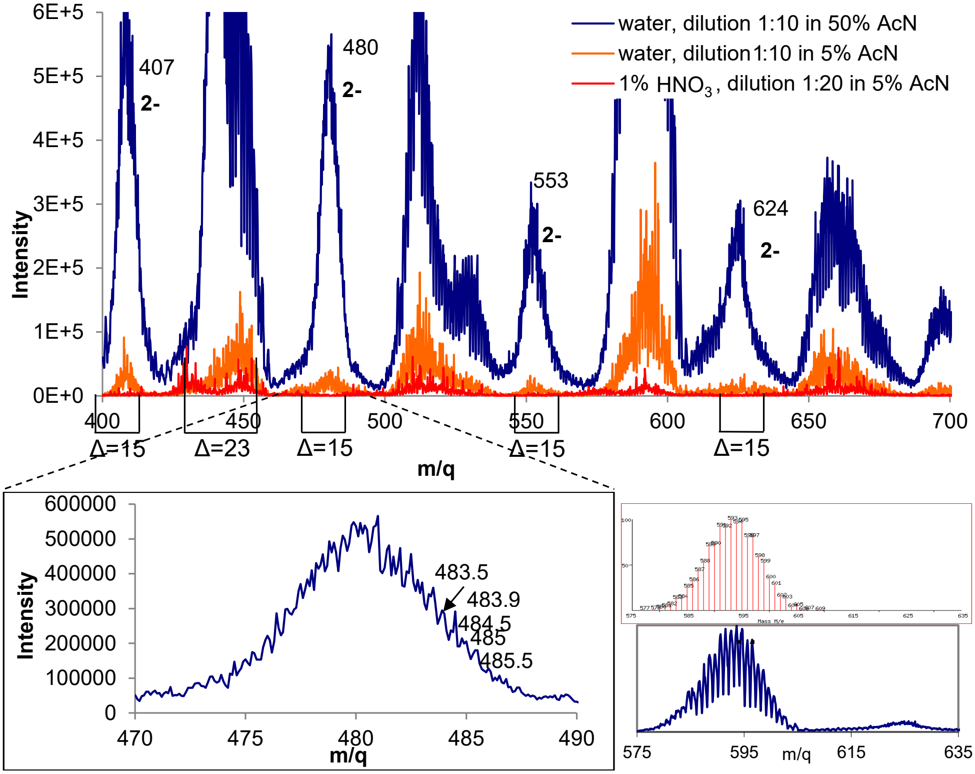

Figure 115: Ammonium molybdate (para) hydrate stock solution 10 mmol/L in water, dilution 1:10 in 50% and 5% AcN, and in 1% HNO_3 dilution 1:20 in 5% AcN; measurement parameters: Q1 Scan, negative ion mode, IS -4 kV, DP -175 V.

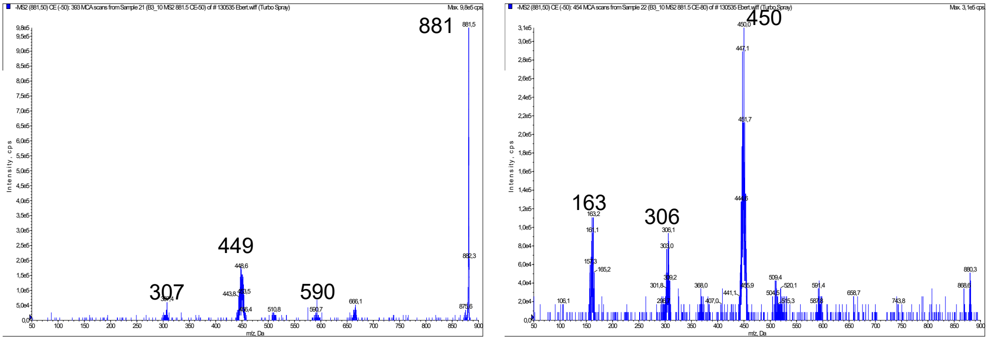

Figure 116: Para molybdate, MS/MS of 881.5, CE -50 eV (left); CE -80 eV (right).

For further characterization and study of the stability of the detected polymolybdate anions MS/MS experiments were performed for the hexamolybdate (m/z 881.5) and the tetramolybdate (m/z 590). Di-, tri-and tetramolybdate were detected as fragment ions at the fragmentation of the hexamolybdate with 50 eV collision energy (CE, compare Figure 116). At higher CE (80 eV) the monomeric molybdate (m/z 1623 is also detected. At 50 eV only partially fragmentation of the ion at hexamolybdate occurs. This indicates a relatively high stability of the molecule, so that artefacts are unlikely due to fragmentation in the ESI source. In fragmentation of the tetramolybdate the product ions are of the monomeric molybdate and the dimolybdate. Also here, a collision energy of at least 40 eV is required to achieve substantial fragmentation.

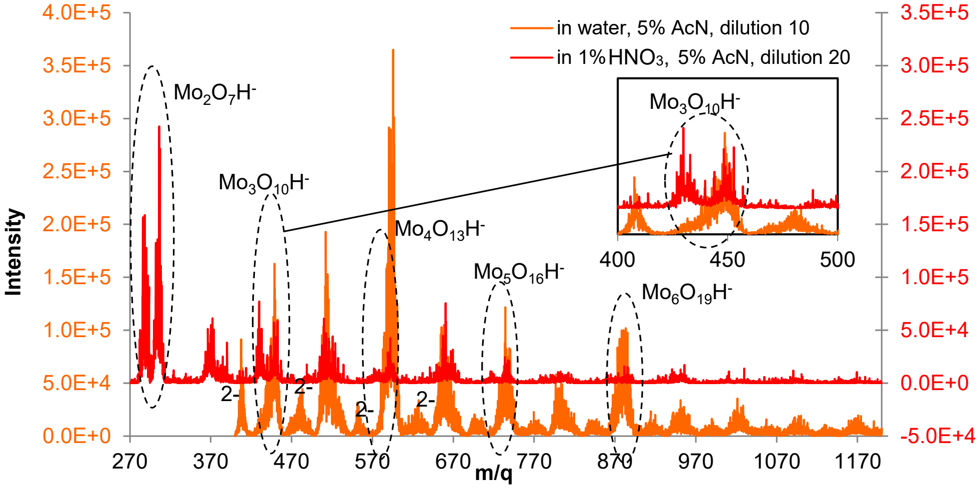

Figure 117: Comparison of the spectra of para molybdate from aqueous stock solution (orange) and 1% HNO_3 (red) diluted in 5% AcN.

In addition, a stock solution of para molybdate in 1% HNO_3 was prepared. When measuring the dilution of this stock solution, no doubly charged anions are detected. This is apparently due to the lower pH in this standard solution. The further comparison of the spectra of para-molybdate from aqueous stock solution and 1% HNO_3 shows a splitting of the signals of the singly charged molybdate anions (compare Figure 117). The enlargement shows distances of 17 or 18 u, which can be explained by elimination of water from the molecule. In addition, a series of signals occur which have the same spacing to each other as the singly charged polymolybdate anions (about 150 u, corresponding to MoO_3 in the assigned series): 372, 515, 662 and 807. These signals occur approximately in the middle between the polymolybdate anion. These Signals are not yet identified. The spectrum of a molybdenum solution in 0.1 mol/L HNO_3 is displayed in Figure 118. Signals with isotopic pattern of Mo were detected only in the m/z range < 300 u. The magnification shows monomeric molybdate (m/z 162). The isotope pattern is slightly modified in comparison with the calculated patterns. This may possibly be an effect of the spectra accumulation. The signal at m/z 249 has almost the same isotope pattern as molybdate, and is therefore probably also a Mo compound with one Mo atom. Due to the low HNO_3 concentration in this sample, a formation of polymolybdates is not expected. Therefore, the spectrum obtained is reasonable.

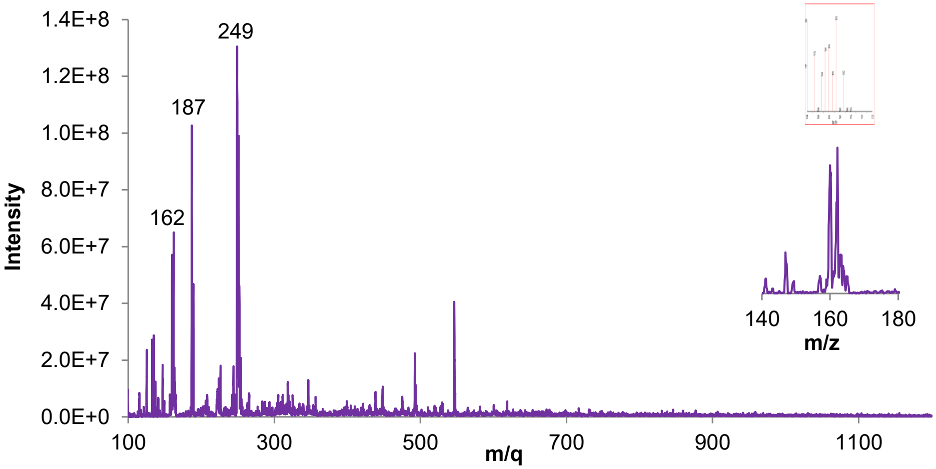

Figure 118: 0.1 mol/L HNO_3, 20.5 g/L Mo, dilution 1:100 in deionized water, then 1:10 in 50% AcN, measurement parameters: Q1 scan, negative ion mode, MCA, IS -4.5 kV, DP -40 V.

In short measurement time (5 min), a mean spectrum was obtained for molybdenum in 1 mol/L HNO_3 (Figure 119), which shows a similar structure as the spectrum of para molybdate in 1% HNO_3. Therefore, the split signals of the singly charged anions polymolybdate were assigned analogously to the para molybdate. Despite 100-fold dilution of the sample, the signal intensities of the polymolybdates are in the range from 10,000 to 100,000 cps.

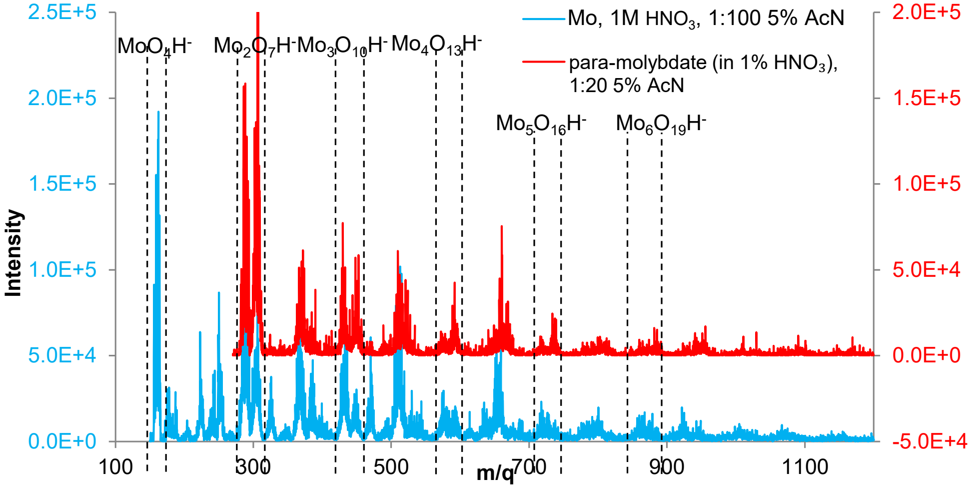

Figure 119: 1 mol/L HNO_3, ca. 20 g/L Mo, dilution: 1:100 in 5% AcN, measurement parameters: Q1 scan, negative ion mode, IS -4 kV, DP -175 V (blue) compared to para molybdate in 1% HNO_3 (red).

For the simplified semi-quantitative estimation of the relative concentrations of the polymolybdates in the sample at this time only the peak area (in the selected double peak areas) can be used. It must be assumed that the spectrum represents the real distribution of polymolybdates in the sample solution and all polymolybdates can be detected with the same sensitivity as discussed in detail in section 3.4.2.1. The relative abundance was calculated from the peak area relative to the sum of all polymolybdates. The comparison of relative abundances obtained for Mo in 1 mol/L with the QTrap and the ALBATROS ESI-ToF (Figure 120), shows in both cases dimolybdate as the most common Mo species. In measurements with the QTrap the monomeric molybdate and the hexamolybdate show higher abundances and the tetra- and pentamolybdate lower abundances compared to measurements with the ALBATROS ESI-ToF.

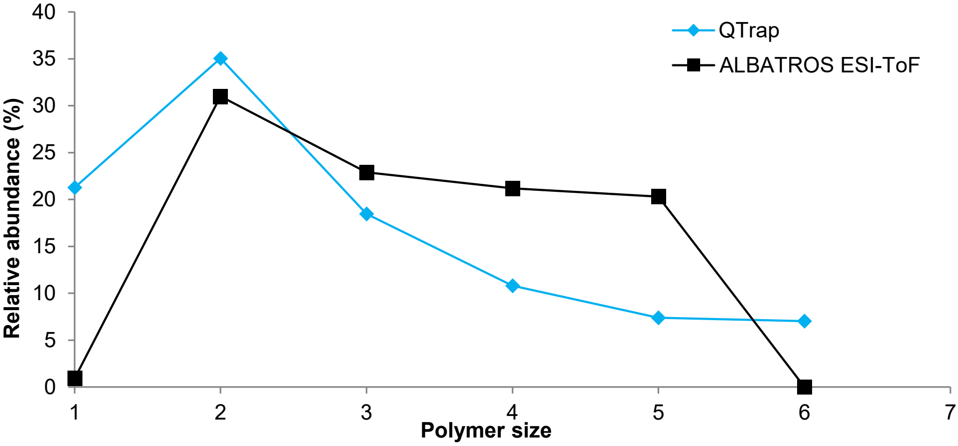

Figure 120: Comparison of relative abundances obtained for Mo in 1 mol/L with the QTrap and the ALBATROS ESI-ToF.

However, the distribution obtained with the commercial instrument is similar overall and therefore a further development of this method is promising with the potential to shorten the measurement time as well as to perform alternative, independent measurements. The complexity of the spectra is much lower despite the use of natural Mo with the total isotope pattern compared to the spectra of ALBATROS ESI-ToF of the undiluted ^{98}Mo samples with a high degree of solvent adducts and signal overlap. Nevertheless, one has to bear in mind that dilution of samples is necessary for measurement with the Qtrap and the spectra might not represent the true speciation of Mo in solution.

A comparison of the relative abundance from the peak area for dilution of aqueous stock solution of para molybdate in 50% AcN and 5% AcN and the dilution of stock solution in 1% HNO_3 with 5% AcN is displayed in Figure 121. The relative proportions of penta- and hepta- molybdate are very similar, whereas the heptamolybdate was not detected in the dilute HNO_3 stock solution. The influence of the acetonitrile concentration is low, a significant difference is for the hexamolybdate. The stock solution in 1% HNO_3 in comparison to the stock solution in water shows mainly differences for the tri- and tetramolybdate.

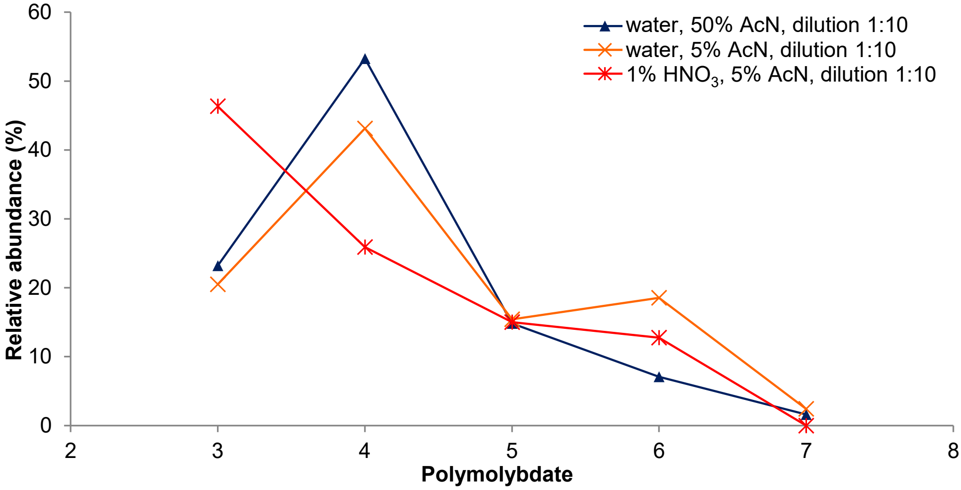

Figure 121: Comparison of the relative abundance from the peak area for dilution of aqueous stock solution of para molybdate in 50% AcN and 5% AcN and the dilution of stock solution in 1% HNO_3 with 5% AcN.

The comparison of the relative abundance of polymolybdates (stock solution in 1% HNO_3) with the molybdenum metal sample (in 1 mol/L HNO_3) shows almost the same distribution (Figure 122). Either the low-molecular polymolybdates exist in the sample in a higher proportion than the larger polymers or the ionization efficiency decreases significantly with increasing degree of polymerization.

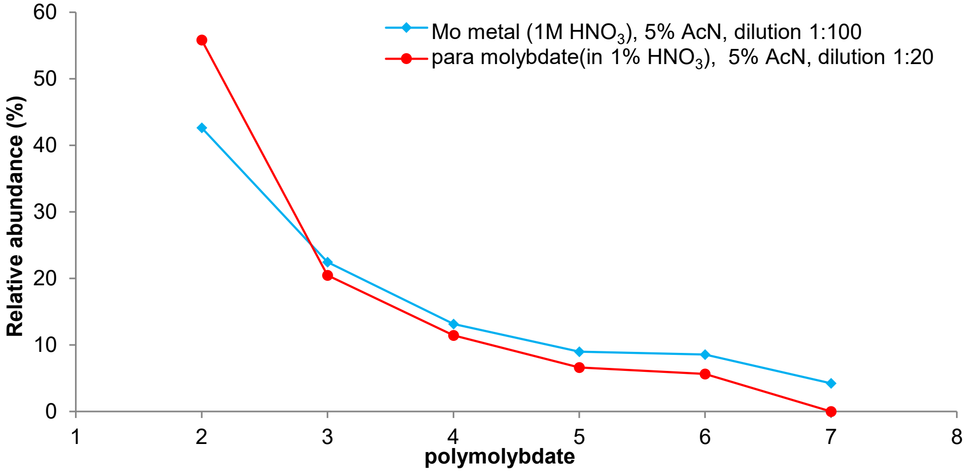

Figure 122: Comparison of the relative abundance of polymolybdates (stock solution in 1% HNO$_3$) with the molybdenum metal (in 1 mol/L HNO$_3$) sample.

As a next step, the influence of the solvent (AcN) on the relative abundance of polymolybdates in the molybdenum sample in 1 mol/L HNO$_3$ was systematically investigated. The spectra of the 1:100 dilution in 5% AcN at the beginning and at the end of the measurement series are in good agreement, so that direct comparison of the signals of the measured sample series is possible without drift correction. Each sample was measured at three different DP (declustering potential): -40 V, -100 V and -175 V. A comparison of the obtained spectra is displayed in Figure 123.

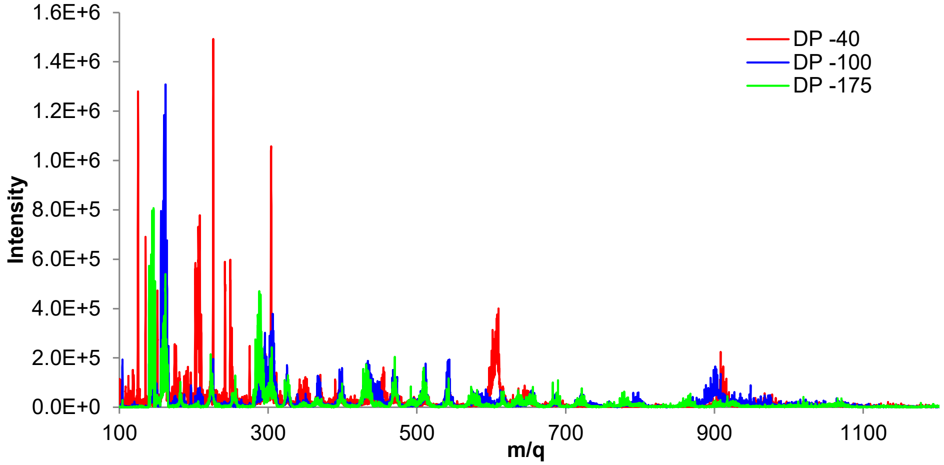

Figure 123: Comparison of the obtained spectra measured at three different DP (declustering potential): -40, -100 and -175 V.

The Mo metal sample was diluted 1:100 with different acetonitrile proportions in the solvent (0%, i.e. deionized water, to 99 % acetonitrile, Figure 124). The superposition of the obtained spectra for DP -100 V shows increasing signal intensity with increasing AcN content. At high AcN concentrations (> 50%) additional signals occur (highlighted in Figure 124).

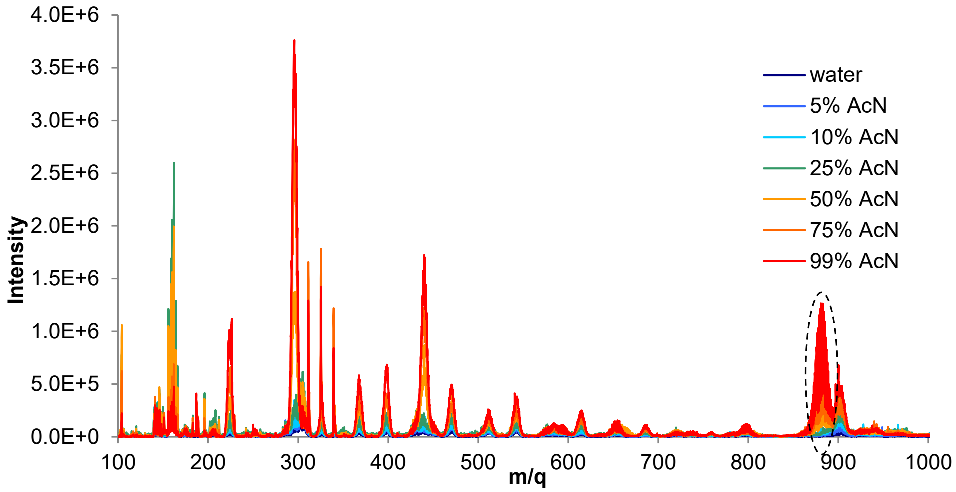

Figure 124: Superposition of spectra for DP -100 V with different AcN in the solvent.

The quantitative analysis was based on the peak areas. According to the integration limits in the example shown above (Figure 119), the signals of the Polyoxomolybdates 1 - 6 were integrated. The following illustration compares the abundance of the polymolybdates with different acetonitrile proportions in the solvent for different declustering potentials. Figure 125 shows significant differences between the individual samples for DP -40 V. This is partly due to the adducts in the spectra. For DP -100 V and -175 V no significant dependence of the relative signal intensities of the polyoxomolybdates of the solvent composition is noted for 0 to 25% AcN. In AcN content > 50% occur light differences occur for DP -100 V and clear differences occur for DP -175 V. Thus, when using 25% AcN (or less) no formation of artefacts by the solvent appear in comparison to deionized water at the same dilution.

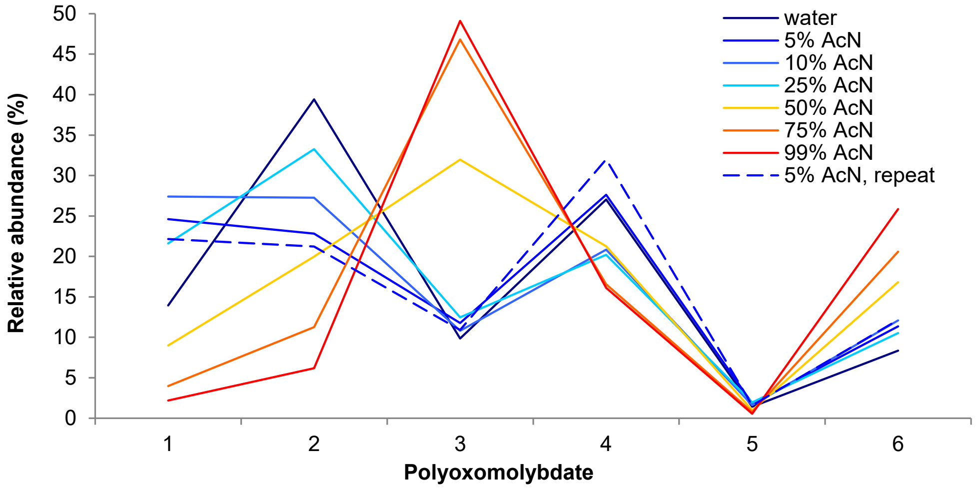

Figure 125: Relative abundances of polyoxomolybdates with different acetonitrile proportions in the solvent at DP -40 V.

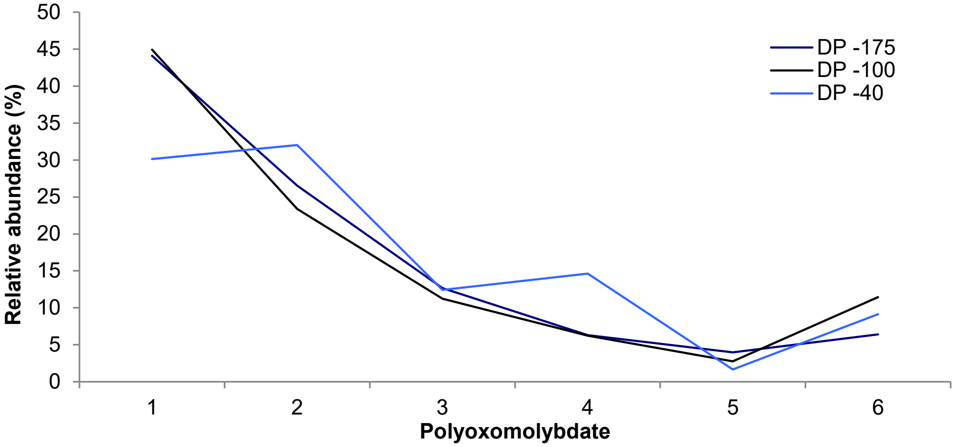

Figure 126: Comparison of different declustering potentials for the same sample (dilution 1:100, 25% acetonitrile).

The comparison of different declustering potentials for the same sample (dilution 1:100, 25% AcN) (Figure 126) shows good agreement for DP -100 V and DP -175 V. For DP -40 V differences occur for the mono-, di-, and the tetraoxomolybdate, probably due to fragmentation of the polymolybdates at higher declustering potentials.

Analogous to the variation of the acetonitrile content at constant dilution factor, the influence of the variation of the dilution factor was investigated for two solvents: water and 25% AcN. The peak areas were integrated analogue and the relative percentage for each polyoxomolybdate of the sum of the peak areas were determined. First, the results for water as a solvent are shown. The spectra of the Mo metal sample in 1 mol/L HNO_3, dilution 1:100 in water at the beginning of the measurement series and at the end are in good agreement, so that no drift correction is required. The superposition of the spectra of different dilutions shows the same peak distribution. The intensity at lower dilution is somewhat larger, but the increase in the intensity is not proportional to the reciprocal value of the dilution factor. The higher concentration of matrix, particularly HNO_3, at a lower dilution appears to have a reduction in the ionization or a signal suppressing the effect. The relative abundances of the polymolybdates for diverse dilutions in water and with 25% acetonitrile were determined for three different declustering potentials and are shown in water for a declustering potential of -40 V in Figure 127. The influence of the dilution factor on the relative abundances of the polymolybdates is low. Therefore, dilution 1:100 appears well suited to hold matrix effects in the ionization low for water as solvent. The potential to improve the detection sensitivity by reducing the dilution factor is low (possibly a factor of 2).

The comparison of different declustering potentials for the same sample (dilution 1:100, water) (Figure 128) shows good agreement for DP -100 V and DP -175 V. For DP -40 V differences occur for the mono- and the tetraoxomolybdate, probably by formation of adducts that dissociate at higher DP, so that more stable results are obtained.

Variation of the dilution in the range 1:200 to 1:10 appears unproblematic in terms of stability of the polyoxomolybdates (Figure 129).

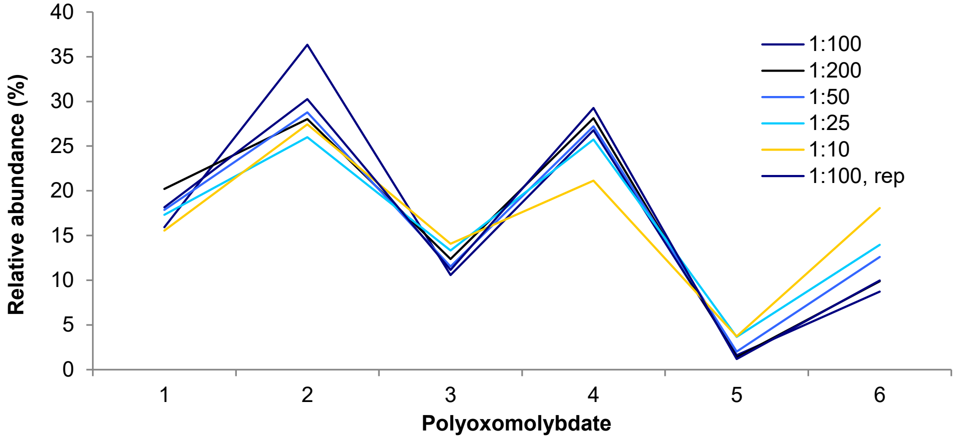

Figure 127: Rel. abundances of the polymolybdates for diverse dilutions in water, DP -40 V.

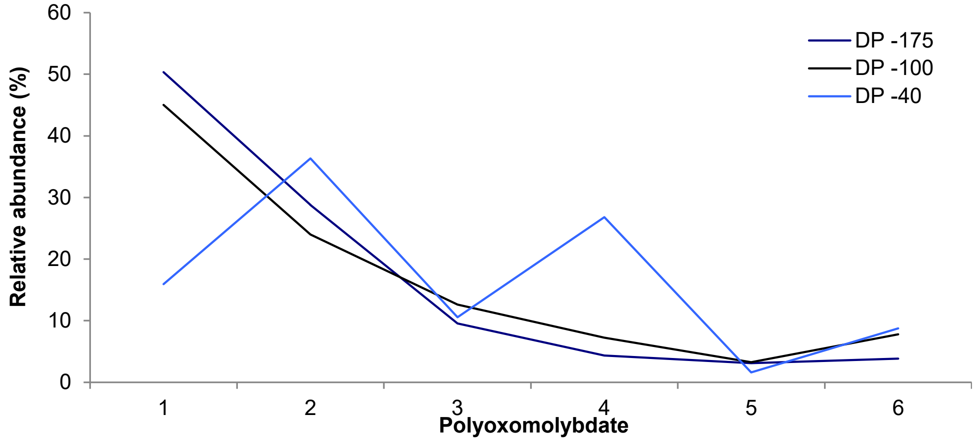

Figure 128: Comparison of different DP for the same sample (dilution 1:100, water).

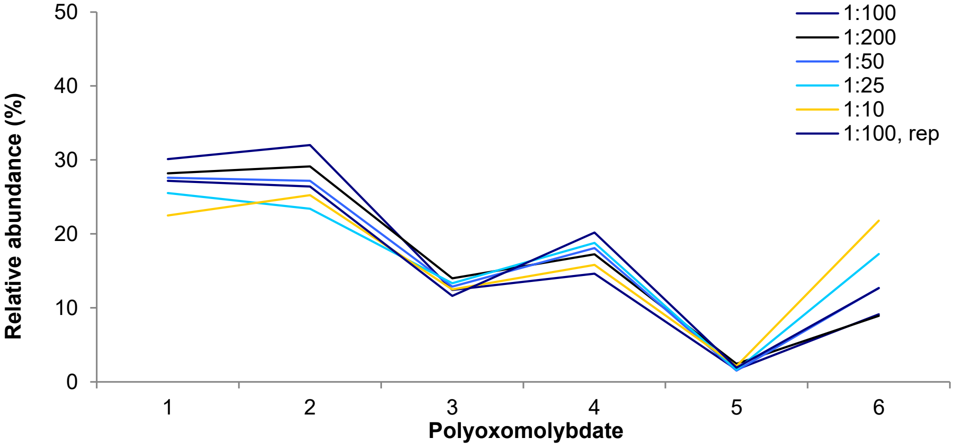

Figure 129: Relative abundances of the polymolybdates for diverse dilutions in 25% AcN, DP -40 V.

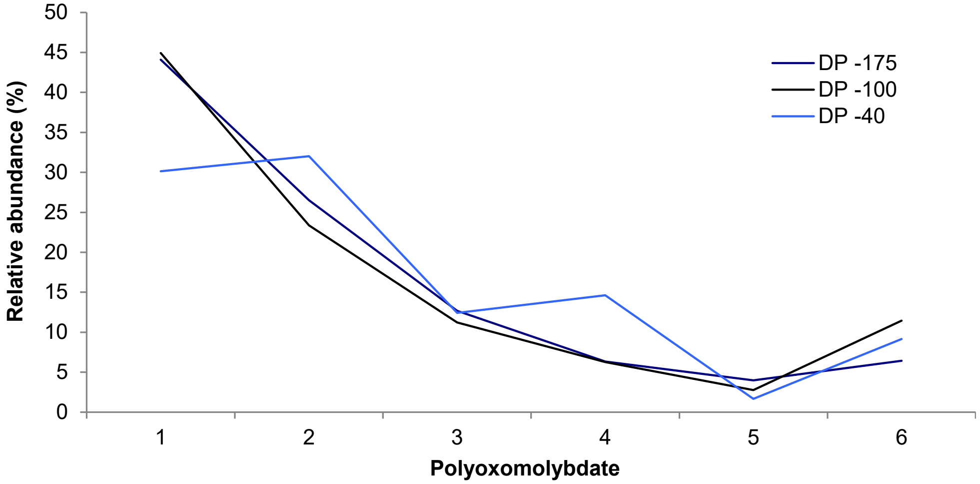

Figure 130: Comparison of different DP for the same sample (dilution 1:100, 25% AcN).

The comparison of different declustering potentials for the same sample in 25% AcN (dilution 1:100, Figure 130) provides similar results as in water. Declustering potentials of -100 V and -175 V show good agreement, for -40 V differences occur for the mono- and the tetraoxomolybdate.

In summary it can be said, that an acetonitrile content up to 25% does not significantly alter the detected frequency distribution polyoxomolybdates in the samples. Addition of acetonitrile has the advantage of higher signal intensity. Fragmentations occur at higher declustering potentials (DP -100 V and DP -175 V). Suitable conditions are 1:100 dilution (if necessary 1:200 to 1:50), as well as on the one hand deionized water as the solvent and on the other hand 25% AcN. Nevertheless, each dilution of the sample represents a dramatic intervention to the system and might influence the speciation of molybdenum. It is absolutely necessary to ensure that the detected species correspond to those which exist in the sample. Therefore the kinetics of the transformation of species upon dilution should be investigated. The validation of the quantitative determination remains problematic due to lack of stable individual standards of polyoxomolybdates species, i.e. the species dependent ionization efficiency cannot be corrected.

Speciation of Molybdenum as a Function of Acid Concentration

Mo samples in 0.1, 1, 2, 3, 4 and 7 mol/L HNO_3 were diluted in water 1:100 and measured by direct infusion in the negative ion mode at a declustering potential of -40 V. The quantitative evaluation was performed as before by determining the peak areas (integration) for the signals of the polyoxometalates. The relative abundance of polyoxomolybdates was calculated from the ratio of each peak area to the sum of all peak areas. The relative abundances of polyoxomolybdates in nitric acid of different concentrations is depicted in Figure 131. In 0.1 mol/L HNO_3 (blue diamonds) the monomere is the dominant species. The relative abundance of the polymeres decreases with increasing size. With incresing acid concentration the relative abundance of the monomeric species decreases. In ≥ 1 mol/L HNO_3 the dimere is the dominant species, whereas the abundances of the remaining polymers are similar. This is most pronounced in 7 mol/L HNO_3 (orange circles). A strong tendency of molybdenum to dimerize at high acid concentrations especially in perchloric acid medium has been reported before[121-124, 130-131, 234-235] and is also in agreement with former investigations on the solution species of MoO_3 in nitric acid medium[231].

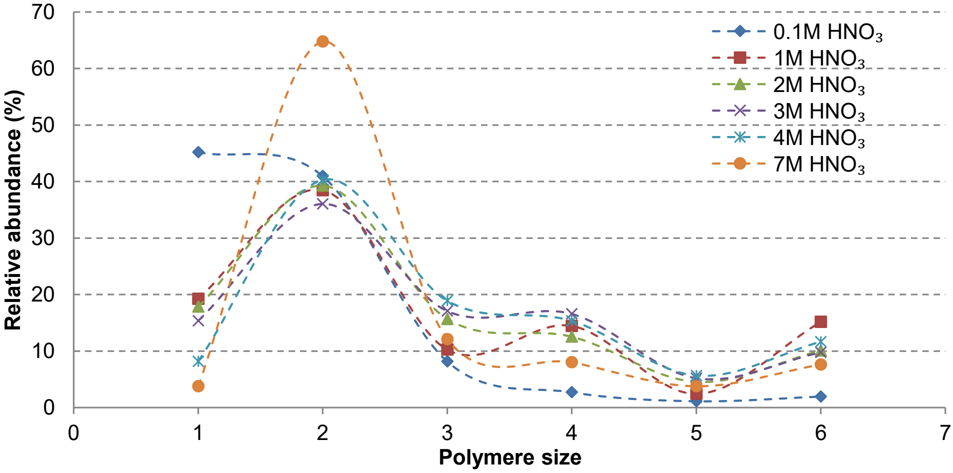

Figure 131: Relative abundances of polyoxomolybdates in nitric acid of different concentrations (dilution 1:100 in water, DP -40 V).

The relative abundances of the different Mo polymers in nitric acid as a function of the acid concentration of the initial sample are depicted in Figure 132 for the range from 0.1 to 7 mol/L HNO_3. With increasing acid concentration the relative abundance of the monomer decreases, whereas the relative abundance of the dimer is constant in the concentration range from 0.1 to 4 mol/L and significantly increases at a higher concentration. The relative abundances of the larger polymers are similar in the considered concentration range.

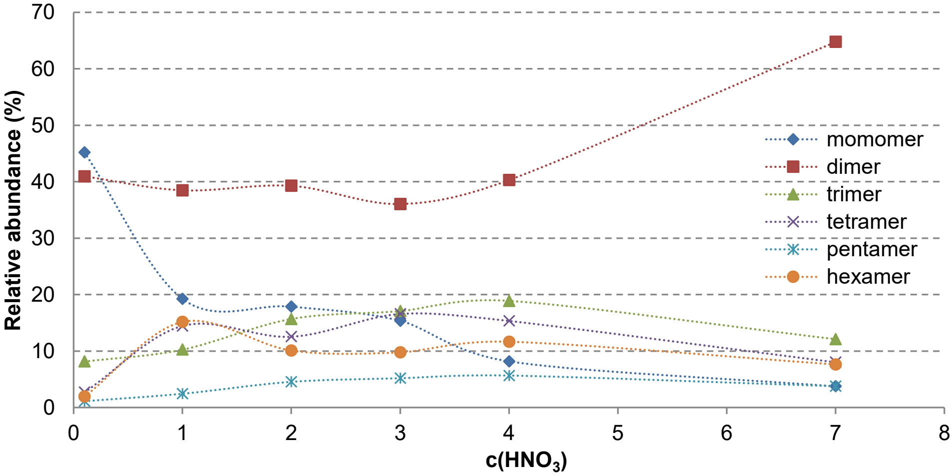

Figure 132: Relative abundances of the different Mo-polymers in nitric acid as a function of the pH of the initial sample (dilution 1:100 in water, DP -40 V).

Speciation of Molybdenum as a Function of Fe(III) Concentration

Samples with increasing iron concentration were measured analogous to the samples without iron in the negative mode. The superposition of spectra of molybdenum in 1 mol/L HNO_3 without iron and containing 1 mol/L $Fe(NO_3)_3$ is displayed in Figure 133. Numerous small-width signals occur corresponding to the isotope pattern of a mono-Fe compound, while the pure molybdenum species cannot be identified.

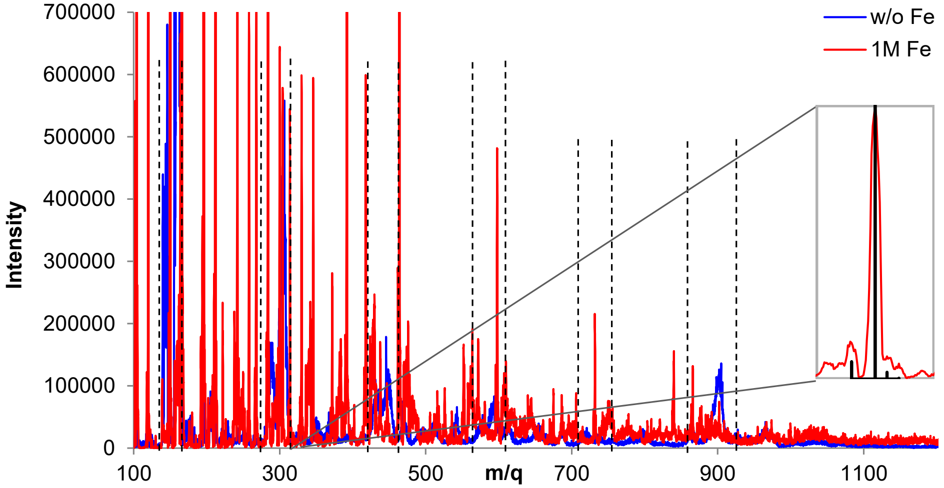

Figure 133: Superposition of spectra of molybdenum in 1 mol/L HNO_3 without iron and containing 1 mol/L $Fe(NO_3)_3$ for DP -100 V, dilution 1:100 in water.

A selected region of the section of the mass spectra of molybdenum in 1 mol/L HNO_3 without iron(III) and containing different amounts of iron(III) is compared in Figure 134. Three signals appear at m/z 314, m/z 330, and m/z 346, which can be assigned to mono-Fe spieces. The intensity of these signals increases with the iron concentration. Aditionally, a series of signals m/z 335 – 345 is detected, which reveals the isotopic pattern of a mono Mo-species. Based on the m/z this species can be assigned to $MoO_4Fe(NO_3)_2$.

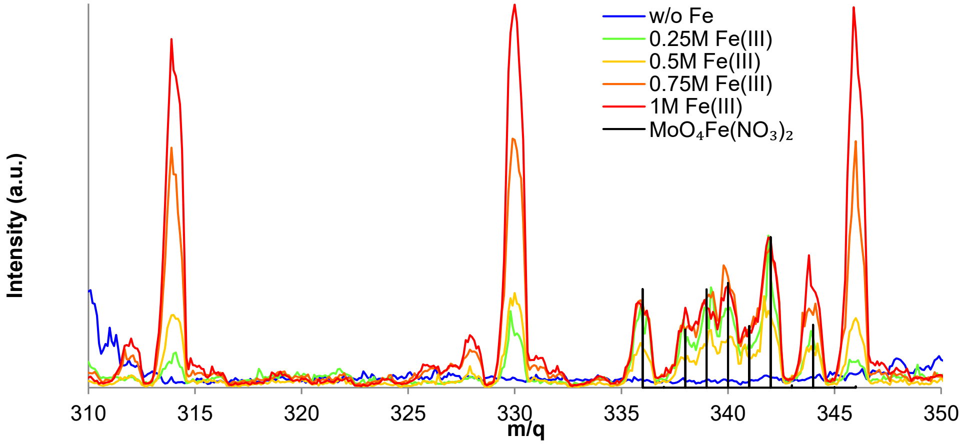

Figure 134: Superposition of spectra of molybdenum in 1 mol/L HNO_3 without iron and containing different amounts of $Fe(NO_3)_3$ for DP -100 V, dilution 1:100 in water.

Figure 135 and 137 compare the spectra of Mo in 1 mol/L HNO_3 containing 0.25 mol/L $Fe(NO_3)_3$ and without iron. Between m/z 280 and 310 a dimolybdate signal appears for the reference sample without Fe(III) (blue), for the sample with 0.25 mol/L Fe(III) (green) a signal is detected with low intensity; for higher iron contents (not depicted for the sense of clearness) no signal is detected. The same trend is observed for other molybdate signals. On closer inspection, additional signals are identified which are attributed to mixed Fe-Mo-species and are labelled accordingly in the diagram. The mixed species are composed according to the same system from the pure molybdenum species and one or two iron atoms and hydroxide or nitrate as found with the ALBATROS ESI-ToF. The relative abundances were calculated as described above. However, due to the overlap of some species in the mass spectra and because not all peaks could be assigned the abundances should be regarded as approximate only. Besides pure molybdenum species (27.6%), species containing one (39.7%) or two (32.7%) iron atoms were detected. If all species with the same number of Mo atoms but different number of iron atoms are considered together, the abundances of the polymers in 1 mol/L HNO_3 with or without iron are similar.

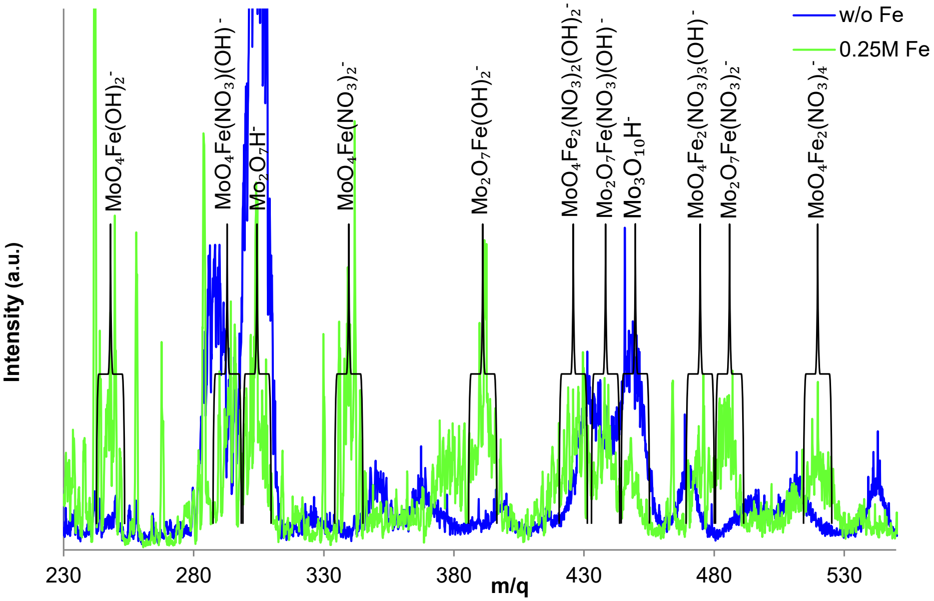

Figure 135: Superposition of spectra of molybdenum in 1 mol/L HNO_3 without iron and containing 0.25 mol/L $Fe(NO_3)_3$ for DP -100 V, dilution 1:100 in water.

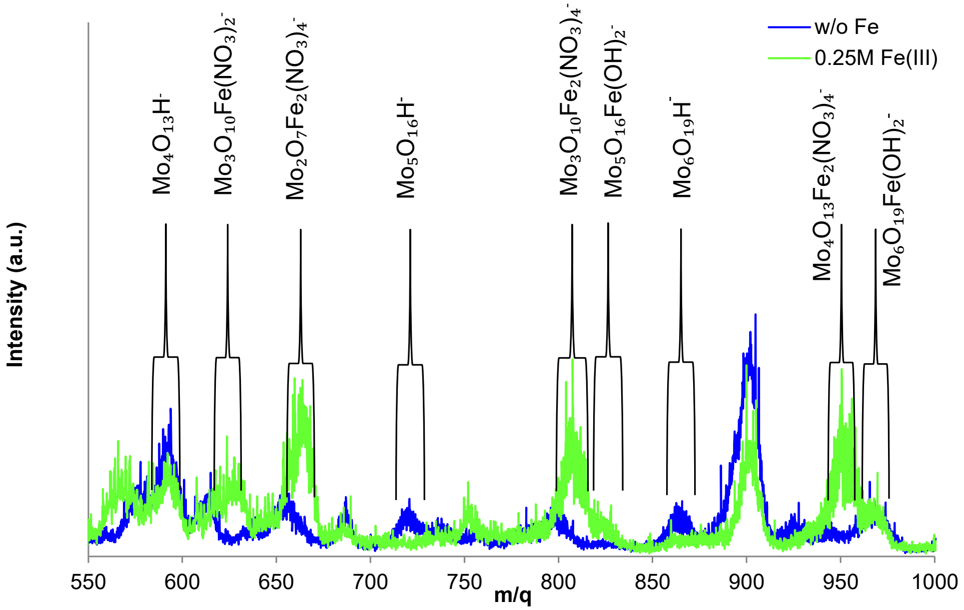

Figure 136: Superposition of spectra of molybdenum in 1 mol/L HNO_3 without iron and containing 0.25 mol/L $Fe(NO_3)_3$ for DP -100 V, dilution 1:100 in water.

4.3 Extraction Studies

Extraction studies with tri-n-butyl-phosphate (TBP) were performed under PUREX conditions. The extractability of Mg and Mo as well as the influence of macro amounts of matrix material on the extraction of U(VI), Eu(III), and Am(III) were examined. The two well-known DIAMEX type extractants N,N'-dimethyl-N,N'-dioctylhexylethoxymalonamide (DMDOHEMA) and N,N,N',N'-tetraoctyldiglocylamide (TODGA) were studied for actinide(III) and lanthanide(III) extraction.

First, the extractability of Mg^{2+} and Mo^{6+} was investigated by the PUREX solvent 30% TBP in TPH. Additionally, the influence of increasing Mg and Mo concentration on uranium, americium and europium extraction was studied. For this purpose the solutions were spiked with trace amounts of ^{nat}U, ^{241}Am and ^{152}Eu, although Mo(VI) is a known complexing agent for U(VI).[236]

With the PUREX solvent Mg was not extracted (D<0.1). Uranium was well extracted with distribution ratios of ~ 25 (Figure 137, left). Americium and europium were poorly extracted with D-ratios < 0.1, although at the highest initial Mg concentration an increase in the Am/Eu distribution ratios was observed. This was caused by the decreasing acid concentration as shown in Table 10 and Table 11 for the Mg and the Mo system, while the nitrate concentration was constant. It is well known that TBP extracts also nitric acid at high acidity by solvation mechanism. Thus at low acitity the free TBP concentration in the organic phase is higher, resulting in increased uranium, americium and europium distribution ratios. Molybdenum was also not extracted (D < 0.1). Uranium was well extracted in the presence of molybdenum with distribution ratios of ~ 22 (Figure 137, right). Americium and europium were poorly extracted with D-ratios ~ 0.1. No 3rd phase formation or precipitation was observed in both cases.

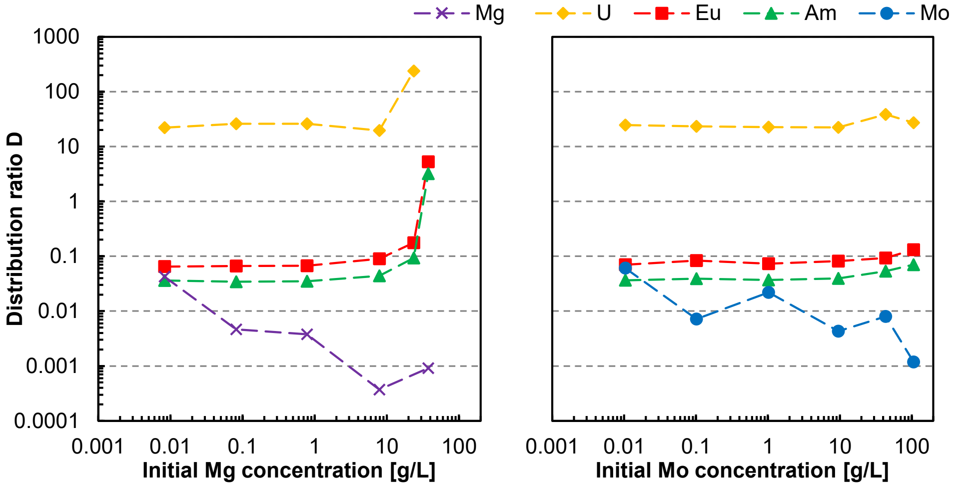

Figure 137: Distribution ratios of Mg(II), Eu(III), Am(III), U(VI), and Mo(VI) using TBP in the organic phase and nitric acid solutions with increasing Mg or Mo concentrations in the aqueous phase. Lines are a guide to the eye. Org: 30% TBP in TPH, Aq: left: increasing amount of Mg (8 mg/L – 38 g/L) in initially 3 mol/L HNO_3, right: increasing amount of Mo (10 mg/L – 90 g/L) in initially 3 mol/L HNO_3.

Magnesium as well as molybdenum were not extracted by the PUREX solvent 30% TBP in TPH, but remained in the aqueous phase together with the lanthanides and minor actinides. Therefore, the extractability of MgO and Mo by DIAMEX type solvents as well as their influence on the extraction of actinides and lanthanides is explored in the next step.

With the DIAMEX solvent, a fine precipitation was observed at $c_{ini}(Mg) = 38$ g/L. Magnesium was not extracted with D-ratios ~ 0.01 at the lower initial Mg concentrations. However, an increasing extraction of Mg was observed at the highest initial Mg concentrations. The increasing extraction of Mg with DMDOHEMA was surprising and needs to be further investigated. However, the behaviour of the actinides (U, Am) and Eu is in line with literature data. Uranium was highly extracted (D ~ 100), and Am (D ~ 5) and Eu (D ~ 3) were well extracted (Figure 138, left). Third phase formation was also observed in the Mo system at $c_{ini}(Mo) = 43$ g/L and a precipitation occurred at $c_{ini}(Mo) = 90$ g/L. This was due to the good extraction of Mo by DMDOHEMA, with D-ratios reaching a maximum of 4 (Figure 138, right). Uranium was very well extracted (D > 100), and Am (D ~ 4) and Eu (D ~ 2) were well extracted.

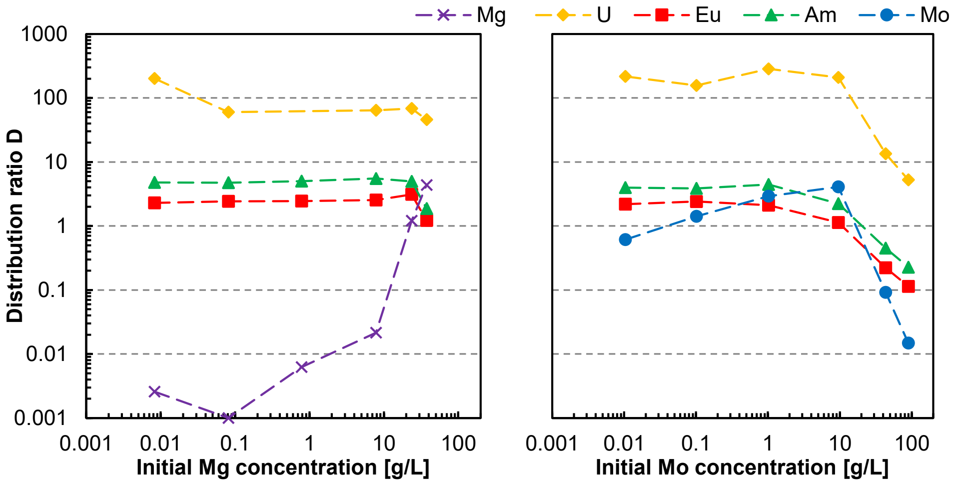

Figure 138: Distribution ratios of Mg(II), Eu(III), Am(III), U(VI), and Mo(VI) using DMDOHEMA in the organic phase and nitric acid solutions with increasing Mg or Mo concentrations in the aqueous phase. Lines are a guide to the eye. Org: 0.6 mol/L DMDOHEMA in Exxsol-d80, Aq: left: increasing amount of Mg (8 mg/L – 38 g/L) in initially 3 mol/L HNO_3, right: increasing amount of Mo (10 mg/L – 90 g/L) in initially 3 mol/L HNO_3.

In the presence of macro amounts Mg, no 3rd phase formation or precipitation was observed with TODGA. Magnesium was not extracted with D-ratios ~ 0.01. Uranium was well extracted with D-ratios ~ 10 and Am and Eu were very well extracted with D-ratios > 100 (Figure 139, left). In the case of molybdenum a fine precipitate was observed at $c_{ini}(Mo) = 90$ g/L. Molybdenum was moderately extracted with D-ratios of 2.5 at low initial Mo concentration, while decreasing Mo distribution ratios are observed at higher Mo concentrations (Figure 139, right). Uranium was well extracted with D-ratios ~ 10 and Am and Eu were very well extracted with D-ratios >100.

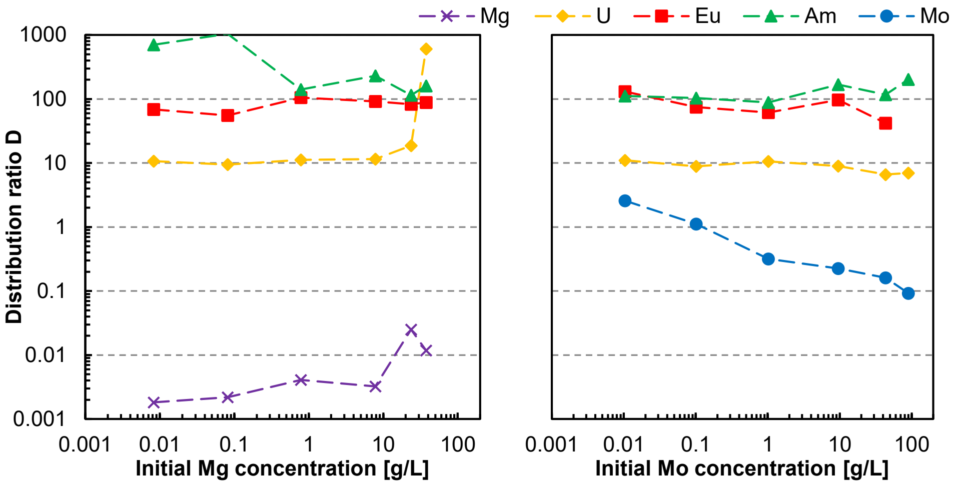

Figure 139: Distribution ratios of Mg(II), Eu(III), Am(III), U(VI), and Mo(VI) using TODGA in the organic phase and nitric acid solutions with increasing Mg or Mo concentrations in the aqueous phase. Lines are a guide to the eye. Org: 0.2 mol/L TODGA in Exxsol-d80, Aq: left: increasing amount of Mg (8 mg/L – 38 g/L) in initially 3 mol/L HNO_3, right: increasing amount of Mo (10 mg/L – 90 g/L) in initially 3 mol/L HNO_3.

The extraction results show that Mo is partly extracted by DMDOHEMA and TODGA, causing 3rd phase formation or precipitation problems at the highest initial Mo-concentrations. The behaviour of the actinides (U, Am) and Eu is in line with literature data.[237-240]

4.4 Separation of Molybdenum by Thermal Treatment

Due to the complexity of the molybdenum dissolution the separation of the matrix material from the fuel by thermal treatment was considered as an alternative. The option to separate the molybdenum from the remaining fuel by sublimation has been studied through TG-DSC and furnace experiments. The residues were analysed by powder XRD.

4.4.1 Pure Molybdenum

The feasibility of the distillation of molybdenum was first verified with pure molybdenum powder in the furnace set-up displayed in Figure 23 (page 53). A sample of pure molybdenum was quantitatively evaporated and recovered at the end of the oven as pale yellow crystals at the inside of the quartz tube (compare Figure 140). The crystals were dissolved in sodium hydroxide solution for quantification by ICP-MS. The TG-DSC diagram (Figure 141) reveals the oxidation of molybdenum at 543 °C with a mass increase of 50%, which corresponds to the oxidation to MoO_3. This is also confirmed by the XRD pattern of the product which is displayed in Figure 142. The evaporation of the MoO_3 at 804 °C can also be observed in the TG-DSC diagram.

Figure 140: Photograph of the quartz tube after the experiment with pale yellow crystals at the end of the oven and empty quartz boat.

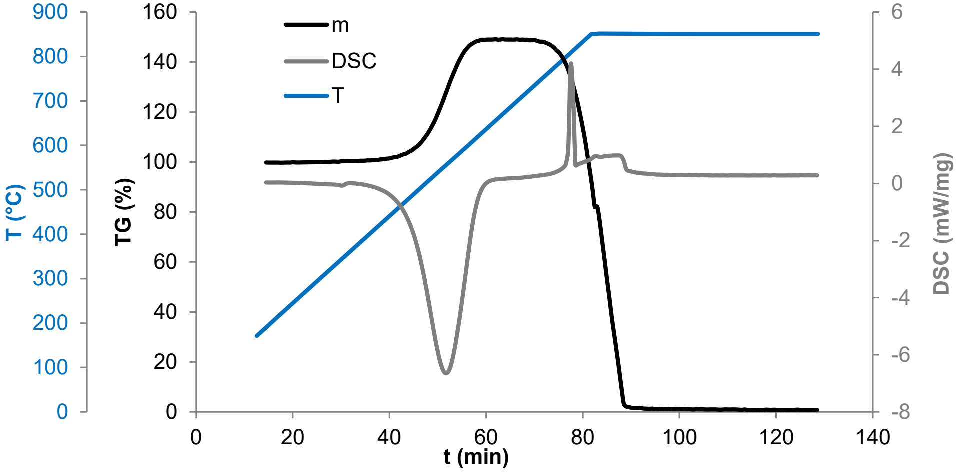

Figure 141: TG-DSC measurement on molybdenum powder (app. 10 mg) with a heating rate of 10 °C/min up to 850 °C, holding time 1 h, synthetic air.

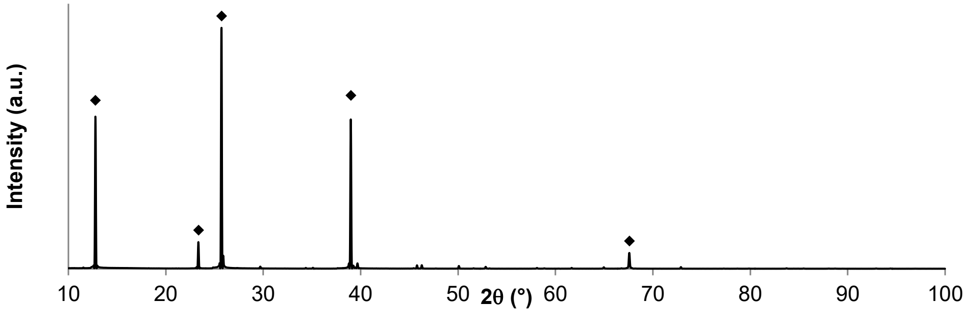

Figure 142: XRD pattern of the product of thermally treated molybdenum powder.

4.4.2 Mo/CeO_2 Powder Mixtures (TG-DSC)

The TG-DSC diagram of a Mo/CeO_2 (60/40 wt.%) powder mixture (Figure 143) reveals the oxidation of molybdenum at 552 °C with a corresponding mass increase of 25%, which corresponds to the oxidation to MoO_3. The peak at 674 °C corresponds to a solid state reaction of MoO_3 and CeO_2, which has been described in the literature.[241-242] The phase diagram of the MoO_3-CeO_2 system is displayed in Figure 144, the region corresponding to the sample composition is marked in green in the diagram. An alternative progression of the melting curve, which is better described by the data, is drawn in blue. Nevertheless, after the initial mass gain due to the oxidation, a continuous mass reduction due to the evaporation of MoO_3 is observed. At 785 °C the decomposition of the mixed oxide $Ce_2Mo_4O_{15}$, in which $Ce_2(MoO_4)_3$ and MoO_3 are generated[242], takes place in parallel. However, the MoO_3 could not be quantitatively evaporated during the experiment. A mass decrease to 40% of the initial mass was expected. Nevertheless, an additional holding time is expected to enhance the mass loss, because the mass still decreases at the end of the experiment. A further increase in temperature is not considered because it might lead to the evaporation of other components of the actual fuel.

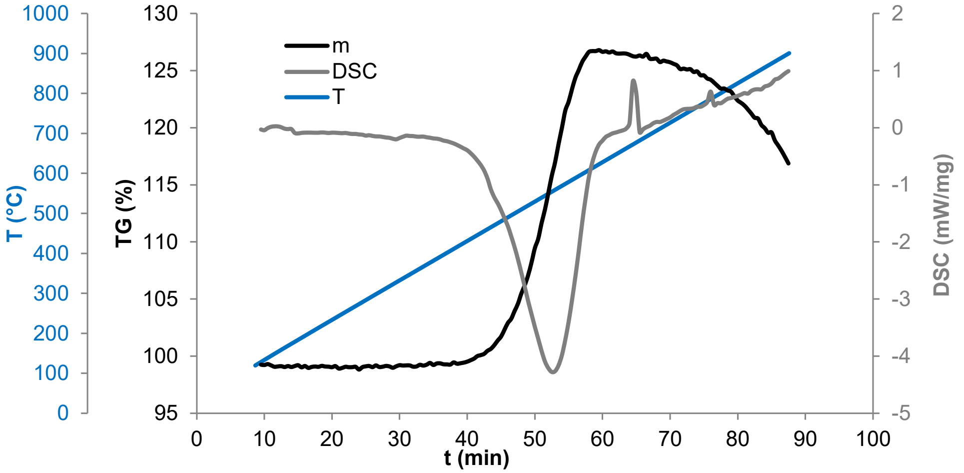

Figure 143: TG-DSC measurement on Mo/CeO_2 (60/40 wt.%) powder with a heating rate of 10 °C/min up to 1000 °C.

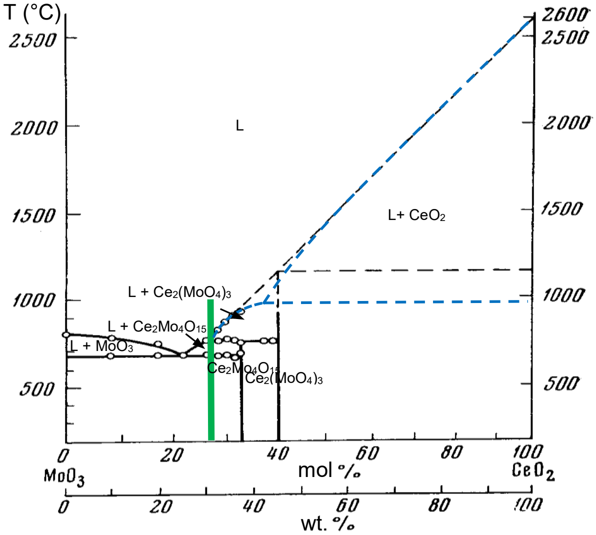

Figure 144: Phase diagram of the MoO_3-CeO_2 system. Taken from Ustinov *et al.*[243] The region corresponding to the sample composition is marked in green. An alternative progression of the melting curve is drawn in blue. L: liquid.

4.4.3 Mo/CeO_2 Powder Mixtures (Furnace Experiments)

For the constant temperature `furnace´ experiments with the tube furnace a powder mixture containing 60 wt.% Mo and 40 wt.% CeO_2 was used. The same batch of powder was used for all experiments. First the furnace was heated to the desired temperature, and then the powder mixture (about 120 mg) in a quartz boat was positioned in the middle of the furnace with a feed rod. Temperatures between 650 and 900 °C were investigated. The solid state reaction of MoO_3 and CeO_2 is expected to occur from temperatures around 670 °C as observed in the phase diagram of the MoO_3-CeO_3 system (Figure 144) and was also confirmed by TG-DSC measurements, as described above. Therefore, a lower temperature was studied. Temperatures above 900 °C were not investigated, because fission products are expected to vaporise at elevated temperatures. The amount of molybdenum recovered (as MoO_3) from Mo/CeO_2 (60/40 wt.%) powder mixtures as function of time for different temperature is displayed in Figure 145. Four or five experiments with different holding times were performed for each temperature. The molybdenum was recovered at the end of the furnace in the cold zone (compare Figure 140), dissolved in 5 mol/L NaOH solution and quantified by ICP-MS. The recovery of molybdenum increases with heating time and temperature, but is rather similar for temperatures between 650 and 800 °C. A temperature of 900 °C is needed to significantly improve the recovery. However, under the investigated conditions only up to 25% of the molybdenum could be retrieved.

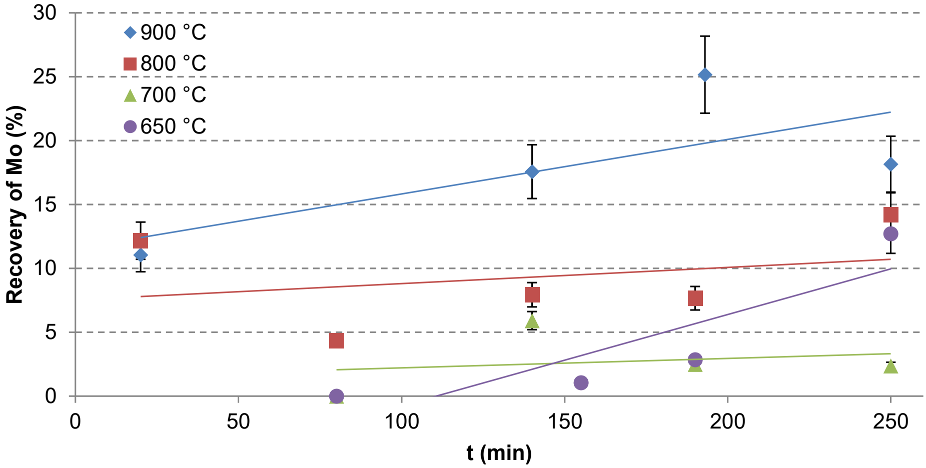

Figure 145: Recovery of molybdenum (MoO_3) from Mo/CeO_2 (60/40 wt.%) powder mixtures at the end of the oven as function of time for different temperatures.

The chemical compositions of the residues of thermally treated Mo/CeO_2 (60/40 wt.%) powder mixtures at 650 and 800 °C for 250 min were determined by XRD and are displayed in Figure 146 and Figure 147 respectively. The 2θ range was limited to 22-36 ° as reference data was available for this range. The XRD pattern of the residue after treatment at 650 °C is dominated by MoO_3. This temperature is sufficient for oxidation of the molybdenum, but higher temperatures are needed to evaporate the oxide. Additionally, $Ce_8Mo_{12}O_{49}$ and $Ce_2Mo_4O_{15}$ are detected as expected. As reported by Wu *et al.*[241] both phases form at temperatures above 500 °C depending on the Mo-Ce ratio. At 800 °C the bulk MoO_3 is evaporated. In addition to the two molybdenum cerium oxides also formed at 650 °C a third oxide $CeMo_5O_8$ is detected. This phase is formed only at significantly higher temperatures.[244] Additionally, the thermal behaviour of Mo metal and MoO_3 was compared. Therefore, an additional powder mixture which contains MoO_3, was prepared, to investigate the influence of the molybdenum oxidation on the recovery yield. To keep the molybdenum to cerium ratio equivalent to the other powder, this mixture contains 69 wt.% MoO_3 and 31 wt.% CeO_2. Five experiments with different holding times were performed for each powder mixture. The comparison between molybdenum metal and molybdenum oxide as a starting material is shown in Figure 148. The necessary oxidation of the molybdenum metal has no significant effect on the yield.

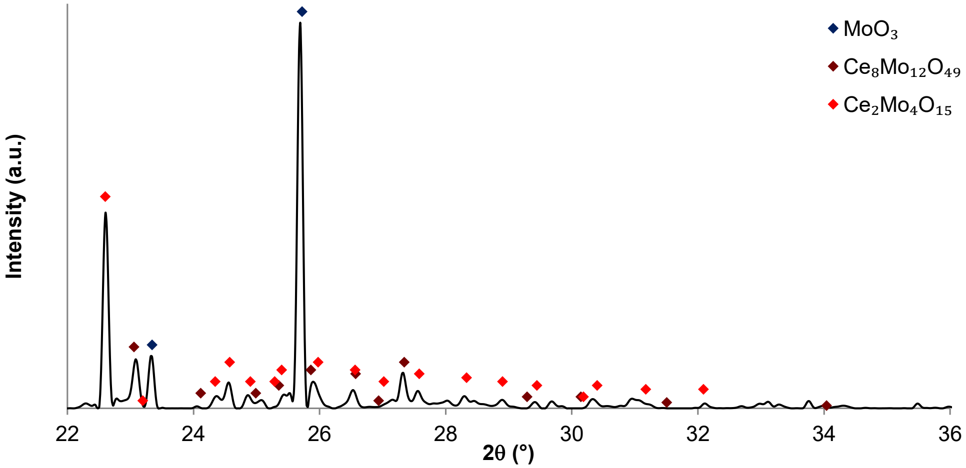

Figure 146: XRD pattern of the residue of a thermally treated Mo/CeO2 (60/40 wt.%) powder mixture at 650 °C for 250 min.

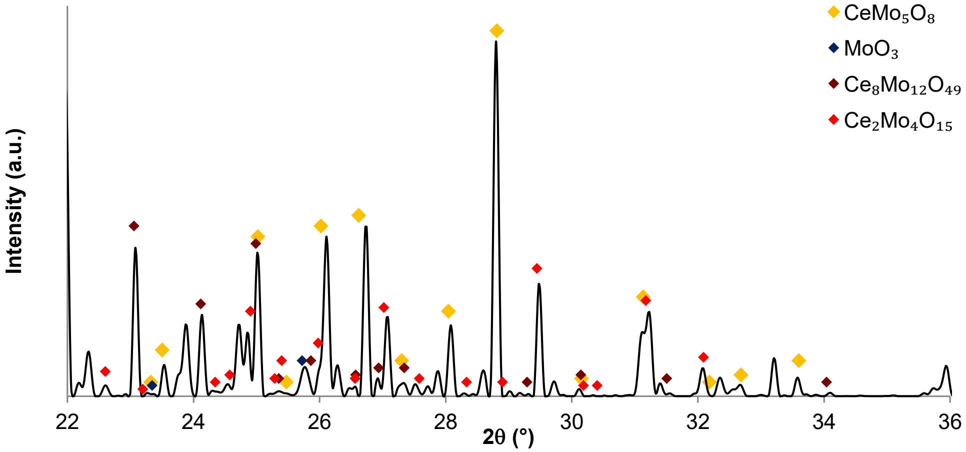

Figure 147: XRD pattern of the residue of a thermally treated Mo/CeO2 (60/40 wt.%) powder mixture at 800 °C for 250 min.

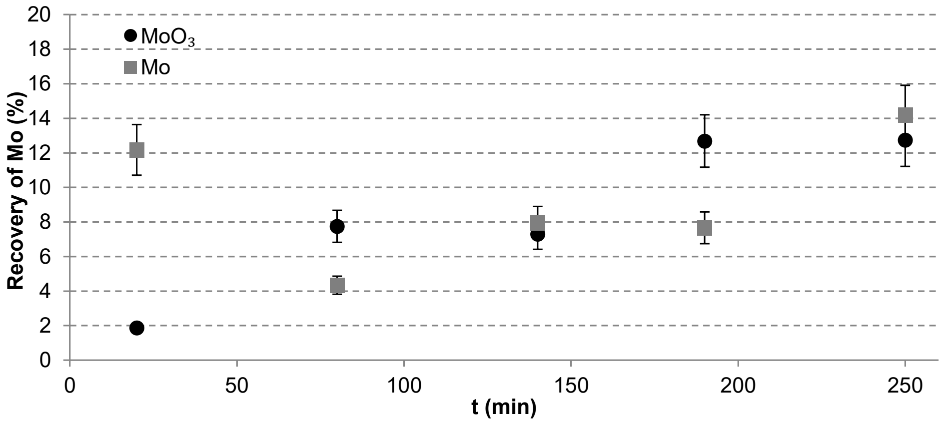

Figure 148: Recovery of Mo (MoO3) from Mo/CeO2 (60/40wt.%, Mo) and MoO3/CeO2 (69/31 wt.%, MoO3) powder mixtures at the end of the oven as function of time at 800 °C.

4.4.4 Mo/CeO_2 Pellets (Furnace Experiments)

Additionally experiments have been performed with pellets. Mixed Mo/CeO_2 pellets have been prepared after the same procedure as the pellets used for dissolution experiments. However, due to the limited volume of the furnace, smaller pellets were prepared. The mass of these pellets amounts to about 40 mg (compare section 3.1.4). The recovery of molybdenum (as MoO_3) from Mo/CeO_2 (60/40 wt.%) powder mixtures and pellets as function of time at 900 °C is compared in Figure 149.

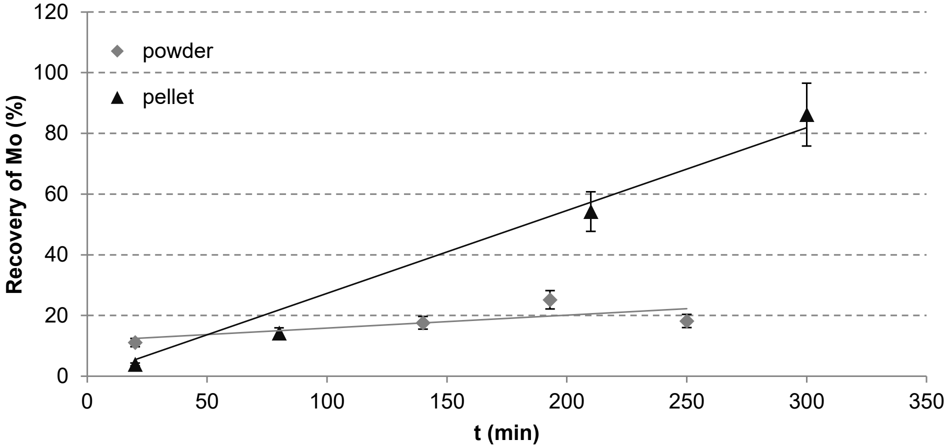

Figure 149: Recovery of molybdenum (as MoO_3) from Mo/CeO_2 (60/40 wt.%) powder mixtures and pellets at the end of the oven as function of time at 900 °C.

The recovery of molybdenum from pellets is much more effective. This is probably caused by the formation of agglomerates during sintering of the pellets, which reduces the area of contact of the MoO_3 and CeO_2 phases and therefore hinders the solid state reaction. A optical microscope image is displayed in Figure 150. Up to 86% of the molybdenum could be recovered upon thermal treatment at 900 °C in 5 h. If the recovery of molybdenum as a function of time followed the linear behaviour, a complete recovery would be achieved after 6 h.

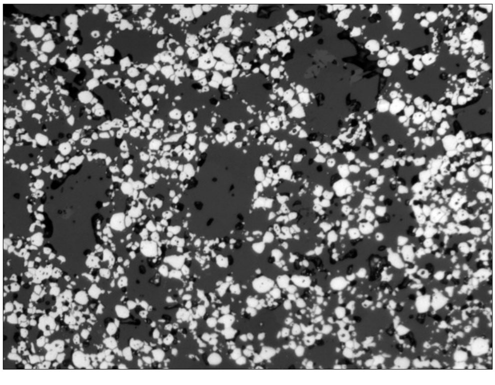

Figure 150: Optical microscope picture of a Mo/CeO_2 60/40 wt.% pellet (magnification 50x).

The XRD pattern of the residue of a Mo/CeO_2 (60/40 wt.%) pellet after thermal treatment at 900 °C for 210 min (Figure 151) shows $Ce_8Mo_{12}O_{49}$, $Ce_2Mo_4O_{15}$, and $CeMo_5O_8$. In addition remaining Molybdenum is detected. This is probably the case because the oxygen cannot gain access to some of the molybdenum grains and the molybdenum is not oxidized. No MoO_3 is found, which means that all molybdenum which was oxidized also evaporated.

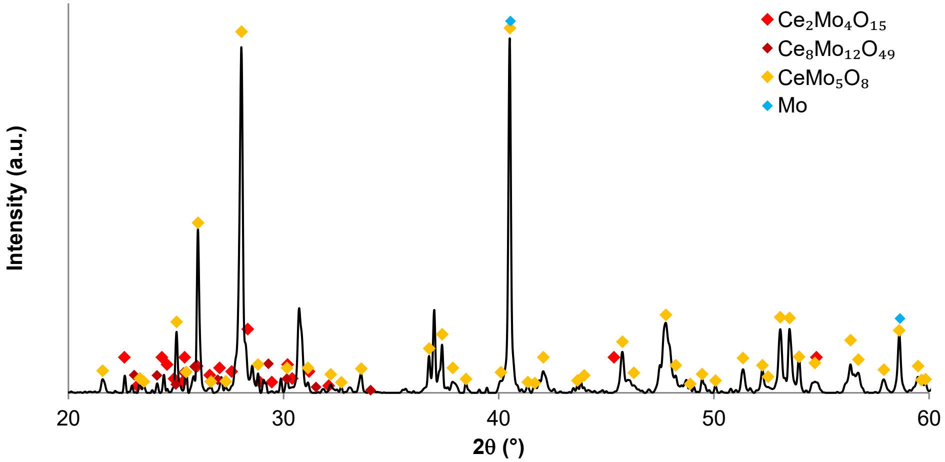

Figure 151: XRD pattern of the residue of a thermally treated Mo/CeO_2 (60/40wt.%) pellet at 900 °C for 210 min.

Figure 152 compares the recovery of molybdenum (as MoO_3) from Mo/CeO_2 pellets of different compositions within 20 min as function of temperature. In the case of pellets with 90 wt.% Mo share the yield at 900 °C is significantly higher, which is probably due to the higher amount of molybdenum accessible at the surface.

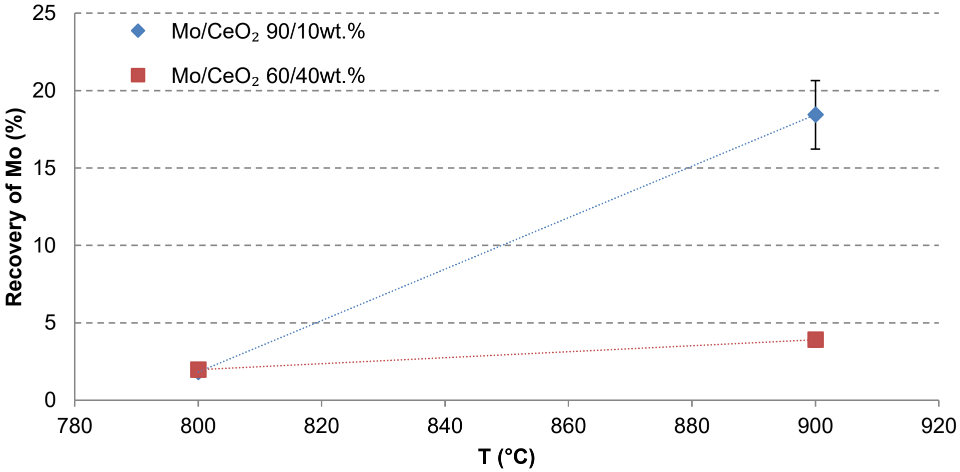

Figure 152: Recovery of molybdenum (MoO_3) from Mo/CeO_2 pellets of different compositions at the end of the oven within 20 min as function of temperature.

4.4.5 Mo/CeO_2 Pellets (TG-DSC)

These findings are confirmed by the TG-DSC measurements of powder and a pellet, which are depicted in Figure 153. For the pellet a lower weight gain and significantly faster mass loss are observed compared to the powder. Additionally the total mass loss at the end of the measurement is significantly higher for the pellet although equilibrium has not been reached in both cases. In the case of a powder the molybdenum loss amounts to 33% in relation to the molybdenum content, whereas 75% of the molybdenum in the pellet could be evaporated. For a final assessment of the feasibility of the separation of molybdenum and cerium dioxide thermodynamic modelling of the system would be an asset, but thermodynamic data on the Mo-Ce-O system is sparse.

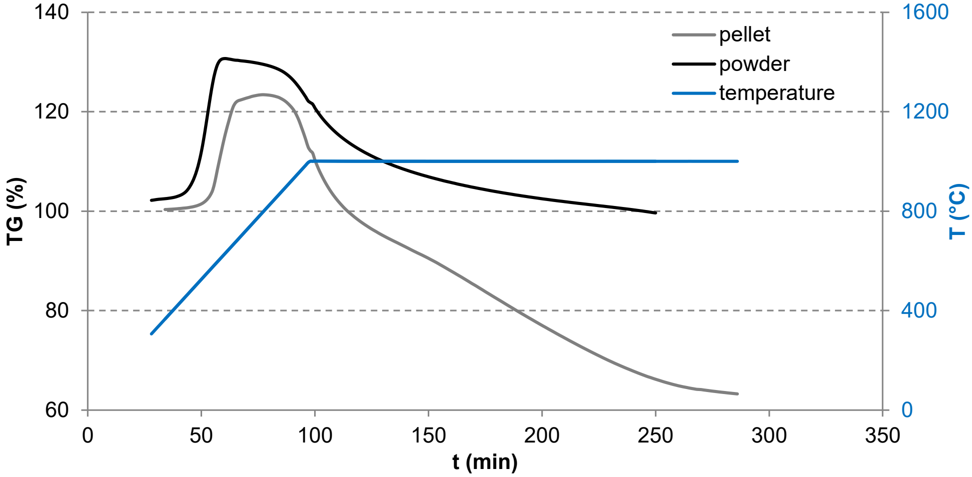

Figure 153: TG-DSC measurement on Mo/CeO_2 (60/40wt.%) pellet with a haeting rate of 10 °C/min up to 1000 °C compared to an equivalent experiment with powder.

4.4.6 Mo/PuO_2 Mixtures (Considerations)

An experimental study on the thermal treatment of Mo/PuO_2 mixtures was not possible, however some theoretical considerations were undertaken on the basis of the foregoing experiments with Mo/CeO_2 mixtures and the phase diagram of the MoO_3 – PuO_2 system, which has been described in a Russian publication by Porokoshin *et al.*[245] In the case of thermal treatment of Mo/PuO_2 mixtures at equivalent conditions a mixed oxide $PuMo_2O_8$ is expected to form, as can be seen from the phase diagram (compare Figure 154). This reaction will affect the evaporation in a way similar to the MoO_3 and CeO_2 solid state reaction. However, the bulk of the Mo should be evaporated and the mixed oxide $PuMo_2O_8$ could be dissolved as it is soluble in nitric acid.[245] The thermal treatment of the fuel is a promising method for the separation of the bulk molybdenum to simplify the dissolution and minimize the effect on the liquid-liquid extraction.

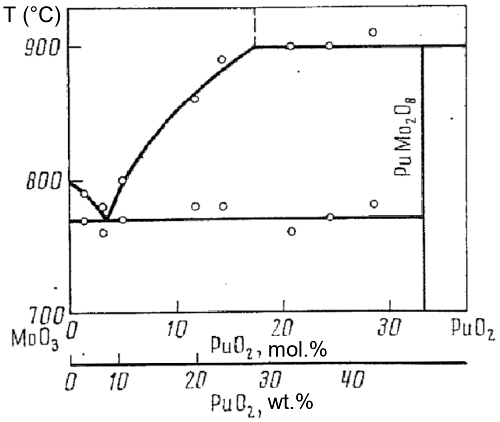

Figure 154: Phase diagram of the MoO_3-PuO_3 system. Taken from Porokoshin *et al*.[245]

5 Conclusions and Outlook

The minor actinides (MA) and plutonium are the main contributors to long term radiotoxicity, heat load and proliferation risk of radiotoxic waste generated during nuclear reactor operation. A large amount of research at recent times is performed on the partitioning and transmutation of these nuclides. One of the methods under consideration to reduce the long term radiotoxicity of the remaining waste is burning the actinides in uranium free fuels in accelerator driven systems (ADS). The dissolution and separation issues for inert matrix fuels containing ceramic magnesium oxide (CerCer) or metallic molybdenum (CerMet) has been investigated because, except for the manufacturing, the handling of the inert component could be of a major concern in a recycling process. In this context some major aspects have been considered to evaluate the reprocessability of IMF: (1) optimal dissolution parameters and feasibility of a separation during the dissolution process, (2) solution species of molybdenum in concentrated nitric acid, (3) influence of the high contents of matrix on well-established extraction processes, and (4) an alternative to dissolution of molybdenum in nitric acid.

Optimization of Dissolution Parameters – Pure matrix reference samples as well as samples containing CeO_2, as surrogate for TRU oxide, were fabricated and thoroughly characterized. Batch dissolution experiments were used for a systematic macroscopic study of dissolution kinetics. Additionally, the evolution of the MgO pellet surface during the dissolution process was investigated with a more sophisticated microscopic approach which allowed an estimation of the total surface area of the pellet and establishment of a surface normalized dissolution rate. The influence of Fe(III) and NO_2^- ions on the dissolution behaviour of Mo was investigated. To get closer to a real fuel Mo/PuO_2 pellets were dissolved to understand differences between CeO_2 and PuO_2 using the conditions optimized during inactive studies.

MgO dissolves via a two-stage mechanism including the intermediate formation of a brucite-like surface layer. The microstructural investigations showed a heterogeneous evolution of the pellet surface, which is attributed to the dissolution of different surfaces of a MgO crystal via heterogeneous etch patterns and to an inhomogeneous density of the pellets. Accordingly, some regions of the pellet dissolve fast, but a pellet structure remains until complete dissolution. Apart from the surface evolution additional evidence for a surface controlled dissolution were obtained, such as an activation energy of 52 ± 8 kJ/mol. The dissolution of MgO is possible even under mild conditions (2.5 mol/L HNO_3, RT). The average dissolution rates of MgO in HNO_3 of different concentrations are similar, and the dissolution rate is strongly dependent on the dissolution temperature. The dissolution rate was normalized to the total surface area, which was obtained by considering the additional surface area due to the formation of holes and resulted in a dissolution rate of approximately $1.2 \cdot 10^7$ $mg/m^2 \cdot d$. The dissolution of the MgO/CeO_2 pellets shows that during dissolution of MgO, the bulk CeO_2 remains undissolved allowing a rough separation of MgO and CeO_2. In all of the experiments less than 1% of CeO_2 was dissolved. A dissolution behaviour similar to that of CeO_2 is expected for PuO_2 so that MgO could be separated in a first dissolution step at mild conditions, while the PuO_2 would be dissolved in an additional step utilizing e.g. HNO_3 with Ag(II) as catalyst.

The dissolution rate of Mo was strongly dependent on the acid concentration as well as the temperature. Molybdenum dissolves in nitric acid according to an autocatalytic mechanism involving the formation of nitrous acid. The dissolution of Mo pellets in HNO_3 was complex due to its specific aqueous redox chemistry (Mo -II - +VI) and precipitation phenomena due to Mo polymerization at high acid and Mo concentrations. The addition of 1 mol/L ferric nitrate to the acid mitigates precipitation at low nitric acid concentrations and accelerates the dissolution. However, it is unclear whether adding high concentrations of Fe^{3+} to the dissolver solution could influence the subsequent extraction process. The trends of the dissolution kinetics of molybdenum in nitric acid without Fe(III) or containing 1 equivalent of Fe(III) per equivalent of Mo has been confirmed with mixed Mo/CeO_2 (60/40 wt.%) pellets at RT. The dissolution of cerium dioxide is not influenced by Fe(III). Dissolution tests on unirradiated PuO_2 pellets revealed that while the solubility of molybdenum in nitric acid increases in the presence of iron, the solubility of the actinides is further decreased. In 1 and 3 mol/L HNO_3 without the addition of iron about 2 and 3% of the plutonium dissolved respectively, while less than 0.1% of the Pu dissolved in the presence of iron. Therefore, it seems that the matrix can be dissolved selectively; the remaining residue is expected to be PuO_2.

Solution Species of Molybdenum in Strongly Acidic Nitric Acid – the stoichiometry and relative abundances of solution species in concentrated nitric acid medium was extensively characterized and quantified by electrospray ionization mass spectrometry. The influence of macro amounts of Fe(III) on the speciation was also investigated. A method was developed to analyse solutions of molybdenum with natural isotopic composition with a commercially available ESI/MS/MS instrument (QTrap) to reduce the measurement times of the homemade nanospray ion source ALBATROS and implemented to investigate the pH and Fe(III) concentration dependence of the Mo speciation.

Mo pellets dissolve rather slowly in 1 mol/L nitric acid at RT. Within the first 3 days, only about 10 %of the Mo pellet dissolves. However, the low concentrations and low timespan leads to a rather simple species distribution: the largest oligomers that form are pentameric Mo species, the dimers have by far the largest relative abundance. With further dissolution of Mo, larger oligomers are formed with up to 10 Mo moieties. Hexameric species are absent in all samples measured with the ALBATROS. Besides the Mo(VI) species, a small fraction of Mo(V) is observed in all the spectra. These species seem to form as intermediate species in the dissolution process. After some time, the Mo(V) fraction is oxidized to Mo(VI) in the solution and these species disappear in the spectra of aged solutions.

In contrast to measurements with the ALBATROS, anionic species were detected with the commercial device, which is due to the dilution of the samples. This change in speciation is attributed to changes in the outer coordination sphere, as the polymerization of molybdenum was found to be slow and the relative abundances of the polymers measured with the ALBATROS and the QTrap were similar. The dissolution behaviour might have implications for the actual reprocessing steps of the Mo matrix fuel. When the molybdenum is completely dissolved, the species distribution is rather complicated. Each of the many different species can exhibit a different behaviour during liquid-liquid extraction steps. The dissolution of molybdenum metal in nitric acid is enhanced by the addition of $Fe(NO_3)_3$ to the solution. Besides the expected molybdenum species a variety of mixed Mo-Fe species containing one or two Fe-atoms were detected. Furthermore, a part of the Fe(III) added to the solution was detected in its reduced form Fe(II), in spite of the oxidizing conditions in both, strong nitric acid and the ESI needle tip. This hints to an involvement of the Fe(III) as a redox partner in the dissolution processes of Mo metal, although the detected mixed species contain only Fe(III). The mixed Mo-Fe species in solution could explain the enhanced dissolution kinetics of Mo-metal in the presence of Fe(III). Furthermore, redox reactions between molybdenum and iron seem to play a role.

Impact of Matrix Materials on Extraction Process – The extractability of Mg and Mo as well as the influence of macro amounts of matrix material on the extraction of U(VI), Eu(III), and Am(III) were examined.

The matrix elements Mg and Mo were not extracted using the PUREX solvent. In the DIAMEX solvent Mg was extracted at low acidity, while Mo was extracted with moderate distribution ratios. The TODGA solvent did not extract Mg, but Mo was slightly extracted at low Mo concentrations. However, both the DMDOHEMA and the TODGA system suffer from 3rd phase formation and precipitation issues, which will have to be resolved.

Alternative to Dissolution of Molybdenum – The separation of the matrix from the fuel by thermal treatment was considered as an alternative to the very complex dissolution of Mo based IMF. For this purpose an apparatus was constructed and the investigation was completed by subsidiary TG-DSC experiments. Additionally, the residues and products were analysed by powder XRD.

Molybdenum was quantitatively recovered as pale yellow crystals, which were identified as MoO_3 by XRD. During thermal treatment of Mo/CeO_2 mixtures $Ce_8Mo_{12}O_{49}$, $Ce_2Mo_4O_{15}$, and $CeMo_5O_8$ were detected as expected due to a solid state reaction which was reported before. Up to 86% of the molybdenum could be recovered upon thermal treatment at 900 °C for 5 h and a further improvement is expected for longer treatments. In the case of thermal treatment of Mo/PuO_2 mixtures at equivalent conditions a mixed oxide $PuMo_2O_8$ is expected to form, which will hinder the separation. However, $PuMo_2O_8$ is well soluble in nitric acid**.** The thermal treatment of the fuel is a promising method for the separation of the bulk molybdenum to simplify the dissolution and minimize the effect on the liquid-liquid extraction.

Outlook – This work has shown that MgO- and Mo-based IMF can be dissolved in nitric acid at mild conditions, where a separation of the matrix material from the actinides during the dissolution is possible in principle. The PuO_2 residues from the Mo/PuO_2 pellet dissolutions ought to be isolated and investigated by XRD and microscopy. However, an overall evaluation of the dissolution behaviour of IMF can be given only if the effect of irradiation (burn-up) is considered. Therefore, dissolution experiments with irradiated targets are necessary. The surface evolution of the MgO pellets could be further investigated using vertical scanning interferometry to obtain more precise results.

Following the ^{98}Mo-metal pellet dissolution in presence of Fe(III) with ESI-MS will enable a more profound understanding of the enhancement of Mo dissolution kinetics by iron. In order to allow absolute quantification of the Mo-species by ESI-MS, stable, well-characterized single standards of polymolybdates are required for calibration. Such standards are currently not available. An alternative would be the quantification based on the Mo content possible by coupling a separation system such as HPLC with an element-selective detector (e.g. ICP-MS). For this, it would need to be examined whether a chromatographic separation of the polymolybdates is possible without changing the relative contents of each Mo species

Methods have to be developed to separate Mg and Mo to improve the final conditioning of the remaining fission products before vitrification. One the one hand commercial extracting agents used in extraction from ore leach liquors could be tested in nitric acid medium, and on the other hand supplementary established extracting agents for the partitioning of fuels could be tested with macro amounts of molybdenum, including the influence of complexing agents (oxalic acid, CDTA etc.).

With respect to the separation of molybdenum by thermal treatment the thermodynamic modelling of the behaviour of all fuel components, especially the fission products, at the relevant conditions would be an asset, but thermodynamic data is sparse.

6 References

[1] S. Bilgen, Structure and environmental impact of global energy consumption*, Renew. Sust. Energ. Rev.* **2014**, *38*, 890-902.

[2] IEA, World Energy Outlook **2012** (Released on 12 November 2012).

[3] DERA, Deutsche Rohstoffinformationen, Energiestudie 2012, Reserven, Ressourcen und Verfügbarkeit von Energierohstoffen, ISSN 2193-5319, Available from: http://www.bgr.bund.de.

[4] IAEA, *Status of monor actinide fuel developement*, Vienna, **2009**.

[5] A. Fernandez*, et al.*, Design and fabrication of specific ceramic–metallic fuels and targets*, J. Nucl. Mater.* **2003**, *319*, 44.

[6] W. D. Loveland*, et al.*, *Modern nuclear chemistry* Wiley, New York, NY, **2006**.

[7] G. F. Thomas, G. Till, The dissolution of unirradiated UO_2 fuel pellets under simulated disposal conditions*, Nucl. Chem. Waste Man.* **1984**, *5*, 141-147.

[8] B. Rabu*, et al.*, *State-of-the-art of the transmutation fuels and fuel fabrication facilities*, **2008**.

[9] D. C. Barrier, *Characterisation and fabrication of zirconia and thoria based ceramics for nuclear applications,* Berichte des Forschungszentrums Jülich, Institurt für Sicherheitsforschung und Reaktortechnik Jül-4188, Forschungszentrum, Zentralbibliothek, Jülich, **2005**.

[10] D. Bosbach, L. Duro, SPECIAL ISSUE: Radiogeochemical Aspects of Nuclear Waste Disposal Preface*, J. Contam. Hydrol.* **2008**, *102*, 173-173.

[11] J.-M. Montel, Minerals and design of new waste forms for conditioning nuclear waste*, Comptes Rendus Geoscience* **2011**, *343*, 230-236.

[12] G. Modolo*, et al.*, A review of the demonstration of innovative solvent extraction processes for the recovery of trivalent minor actinides from PUREX raffinate*, Radiochim. Acta* **2012**, *100*, 715-725.

[13] G. Modolo, *Untersuchungen zur Abtrennung, Konversion und Transmutation von langlebigen Radionukliden: ein Beitrag zur fortschrittlichen Entsorgung von hochradioaktiven Abfällen,* Schriften des Forschungszentrums Jülich, Reihe Energie & Umwelt Band 235, Forschungszentrum Jülich GmbH, Zentralbibliothek, Jülich, **2014**.

[14] C. Poinssot*, et al.*, Main results of the French program on Partitioning of Minor Actinides, a significant improvement towards nuclear waste reduction*, Atalante 2012 International Conference on Nuclear Chemistry for Sustainable Fuel Cycles* **2012**, *7*, 358-366.

[15] J. B. Starks, The PUREX Process*,* (Ed.: S. T. Department), E. I. du Pont de Nemours & Company Savanah River Plant, **1977**.

[16] J. E. Birkett*, et al.*, Recent developments in the purex process for nuclear fuel reprocessing: Complexant based stripping for uranium/plutonium separation*, Chimia* **2005**, *59*, 898-904.

[17] B. J. Mincher*, et al.*, Review article: The effects of radiation chemistry on solvent extraction: 1. Conditions in acidic solution and a review of TBP radiolysis*, Solvent Extr. Ion Exch.* **2009**, *27*, 1-25.

[18] B. J. Mincher*, et al.*, Review article: the effects of radiation chemistry on solvent extraction: 3*, Solvent Extr. Ion Exch.* **2009**, *27*, 579-606.

[19] O. Courson*, et al.*, Partitioning of minor actinides from HLLW using the DIAMEX process. Part 1 - Demonstration of extraction performances and hydraulic behaviour of the solvent in a continuous process*, Radiochim. Acta* **2000**, *88*, 857-863.

[20] D. Serrano-Purroy*, et al.*, Towards a DIAMEX process using high active concentrate. Production of genuine solutions*, Radiochim. Acta* **2005**, *93*, 357-361.

[21] D. Serrano-Purroy*, et al.*, Recovery of minor actinides from HLLW using the DIAMEX process*, Radiochim. Acta* **2005**, *93*, 351-355.

[22] P. Baron*, et al.*, Separation of the Minor Actinides: the DIAMEX-SANEX Concept*,* in proceedings of *GLOBAL 2001*, Paris, France, **2001**.

[23] Y. I. Sasaki, G. R. Choppin, Solvent extraction of Eu, Th, U, Np and Am with N,N'-dimethyl-N,N'-dihexyl-3-oxapentanediamide and its analogous compounds*, Anal. Sci.* **1996**, *12*, 225-230.

[24] Y. Sasaki, G. R. Choppin, Extraction of Np(V) by N,N'-dimethyl-N,N'-dihexyl-3-oxapentanediamide*, Radiochim. Acta* **1998**, *80*, 85-88.

[25] Y. Sasaki*, et al.*, The novel extractants, diglycolamides, for the extraction of lanthanides and actinides in HNO_3-n-dodecane system*, Solvent Extr. Ion Exc.* **2001**, *19*, 91-103.

[26] G. Modolo*, et al.*, TODGA Process Developement for Partitioning of Actinides (III) from PUREX Raffinate*,* in proceedings of *GLOBAL 2003*, New Orleans, Louisiana, USA, **2003**, 1926–1930.

[27] A. Geist, G. Modolo, TODGA Process Development: an Improved Solvent Formulation*,* in proceedings of *GLOBAL 2009*, Paris, **2009**, 1022-1026, paper 9193.

[28] D. Magnusson*, et al.*, Demonstration of a TODGA based Extraction Process for the Partitioning of Minor Actinides from a PUREX Raffinate Part III: Centrifugal Contactor Run using Genuine Fuel Solution*, Solvent Extr. Ion Exch.* **2009**, *27*, 26-35.

[29] G. Modolo*, et al.*, Development of a TODGA based Process for Partitioning of Actinides from a PUREX Raffinate Part I: Batch Extraction Optimization Studies and Stability Tests*, Solvent Extr. Ion Exch.* **2007**, *25*, 703-721.

[30] J. Chandler, N. Hertel, Choosing a reprocessing technology requires focusing on what we value*, Progress in Nuclear Energy* **2009**, *51*, 701-708.

[31] J.-M. Adnet*, et al.*, Development of New Hydrometallurgical Processes for Actinide Recovery: GANEX concept*,* in proceedings of *GLOBAL 2005*, Tsukuba, Japan, **2005**.

[32] G. Modolo*, et al.*, Minor actinide separations in the reprocessing of spent nuclear fuels: recent advances in Europe*,* in *Reprocessing and Recycling of Spent Nuclear Fuel* (Ed.: R. Taylor), Woodhead Publishing, Oxford, **2015**.

[33] M. Salvatores, G. Palmiotti, Radioactive waste partitioning and transmutation within advanced fuel cycles: Achivements and challenges*, Prog. Part. Nucl. Phys.* **2011**, *66*, 144-166.

[34] C. D. Bowman, Accelerator-driven systems for nuclear waste transmutation*, Annual Review of Nuclear and Particle Science* **1998**, *48*, 505-556.

[35] F. Delage*, et al.*, Minor actinide transmutation in an accelerator-driven system prototype: Results from fuel developments within the European programme EUROTRANS*,* in proceedings of *Actinide and Fission Product Partitioning and Transmutation - Eleventh Information exchange meeting*, San Francisco, **2010**, 177-186.

[36] P. A. Gokhale*, et al.*, Accelerator driven systems (ADS) for energy production and waste transmutation: International trends in R&D*, Progress in Nuclear Energy* **2006**, *48*, 91-102.

[37] P. Liu*, et al.*, Accelerator Driven Systems for Transmutation: Safety Considerations and Analyses of EFIT Type Cores*,* in *Challenges of Power Engineering and Environment* (Eds.: K. Cen, Y. Chi, F. Wang), Springer Berlin Heidelberg, **2007**, 1127-1133.

[38] W. Maschek*, et al.*, Accelerator driven systems for transmutation: Fuel development, design and safety*, Progress in Nuclear Energy* **2008**, *50*, 333-340.

[39] M. Salvatores, G. Palmiotti, Radioactive waste partitioning and transmutation within advanced fuel cycles: Achievements and challenges*, Prog. Part. Nucl. Phys.* **2011**, *66*, 144-166.

[40] S. Taczanowski, Transmutations of nuclear waste in accelerator-driven subcritical systems*, Applied Energy* **2003**, *75*, 97-117.

[41] X.-N. Chen*, et al.*, Comparative studies of CERCER and CERMET fuels for EFIT from the viewpoint of core performance and safety*, Progress in Nuclear Energy* **2011**, *53*, 855-861.

[42] J. O. Denschlag, Technical Application of Nuclear Fission*,* in *Handbook of Nuclear Chemistry*, 2 ed. (Eds.: A. Vértes, R. G. Lovas, S. Nagy, F. Rösch, Z. Klencsár), Springer, Heidelberg, **2011**.

[43] J. Wallenius*, et al.*, *Selection of the preliminary fuel candidate for DM1*, EUROTRANS, **2006**.

[44] M. Becker, *et al.*, Partitionierung und Transmutation: Forschung – Entwicklung – Gesellschaftliche Implikationen, *acatech STUDIE* **2013**.

[45] S. Pillon, Actinide-Bearing Fuels and Transmutation Targets, in *Comprehensive Nuclear Materials* (Ed.: R. J. M. Konings), Elsevier, Oxford, **2012**, 109-141.

[46] D. Haas, *et al.*, Properties of cermet fuels for minor actinides transmutation in ADS, *Energy Conversion and Management* **2006**, *47*, 2724-2731.

[47] D. Haas, *et al.*, CERMET fuel behavior and properties in ADS reactors, *Energ. Convers. Manage.* **2008**, *49*, 1928-1933.

[48] T. Ogawa, *Fuels and Materials for Transmutation, A Status Report*, **2005**.

[49] L. Donnet, *et al.*, The FUTURA-FTA Experiment in PHENIX, in proceedings of *GLOBAL 2005*, Japan, **2005**.

[50] M. Jolkkonen, *et al.*, Thermo-chemical modelling of uranium-free nitride fuels, *J. Nucl. Sci. Technol.* **2004**, *41*, 457-465.

[51] R. W. Margevicius, *et al.*, *AFC fuels development update*, Los Alamos National Laboratory, **2003**.

[52] H. Z. Zhang, *et al.*, Melting behaviour of oxide systems for heterogeneous transmutation of actinides. III. The system Am-Mg-O, *J. Nucl. Mater.* **1997**, *250*, 88-95.

[53] H. Kleykamp, Selection of materials as diluents for burning of plutonium fuels in nuclear reactors, *J. Nucl. Mater.* **1999**, *275*, 1-11.

[54] M. Fromont, *et al.*, Behaviour of Uranium-Plutonium Mixed Nitride and Carbide Fuels Irradiated in Phenix, in proceedings of *GLOBAL 2005*, Japan, **2005**.

[55] H. Matzke, Radiation-damage in crystalline insulators, oxides and ceramic nuclear-fuels, *Radiat. Eff. Defect. S.* **1982**, *64*, 3-33.

[56] L. Zaboudko, *In minutes of the ISTC CEG meeting in Brussels, January 2006*, **2006**.

[57] C. Ekberg, *et al.*, ASGARD, in proceedings of *Sustainable Nuclear Energy Conference SNEC*, Manchester, **2014**.

[58] N. Ouvrier, H. Boussier, Recycling of MgO, Mo & ZrO_2 based Actinide-Bearing Matrices: Assessment of Reprocessing Feasibility & Waste Production, *Procedia Chemistry* **2012**, *7*, 322-327.

[59] G. Skarnemark, Solvent extraction and ion exchange in Radiochemistry, in *Handbook of nuclear chemistry* (Eds.: A. N. Sandor, Z. Klencsar, R. G. Lovas, F. Rösch), **2011**, 2403-2428.

[60] W. W. Schulz, E. M. Duke, *Reprocessing of low-enrichment uranium-molybdenum alloy fuels*, Richland, **1959**.

[61] L. M. Ferris, J. F. Land, *Aqueous Processes for Dissolution of Uranium-Molybdenum Alloy Reactor Fuel Elements*, **1961**.

[62] G. Modolo, *et al.*, Development of a TODGA based process for partitioning of actinides from a PUREX raffinate part I: Batch extraction optimization studies and stability tests, *Solvent Extr. Ion Exc.* **2007**, *25*, 703-721.

[63] A. Lüttge, *et al.*, A Stochastic Treatment of Crystal Dissolution Kinetics, *Elements* **2013**, *9*, 183-188.

[64] M. A. Blesa, *et al.*, *Chemical Dissolution of Metal Oxides*, CRC Press, Boca Raton, Florida, **1994**.

[65] S. L. Brantley, *et al.*, *Kinetics of Water-Rock Interaction*, Springer, Berlin, **2008**.

[66] A. C. Lasaga, Fundamental Approaches In Describing Mineral Dissolution And Precipitation Rates, in *Chemical Weathering Rates Of Silicate Minerals, Vol. 31*, Mineralogical Soc. America, Washington, Dc, **1995**, 23-86.

[67] C. Anbeek, Surface roughness of minerals and implications for dissolution studies, *Geochim. Cosmochim. Ac.* **1992**, *56*, 1461-1469.

[68] H. C. Helgeson, *et al.*, Thermodynamic and kinetic constraints on reaction rates among minerals and aqueous solutions. II. Rate constants, effective surface area, and the hydrolysis of feldspar, *Geochim. Cosmochim. Ac.* **1984**, *48*, 2405-2432.

[69] S. Brunauer, *et al.*, Adsorption of Gases in Multimolecular Layers, *J. Am. Chem. Soc.* **1938**, *60*, 309-319.

[70] C. Fischer, *et al.*, How predictable are dissolution rates of crystalline material?, *Geochim. Cosmochim. Ac.* **2012**, *98*, 177-185.

[71] G. Jordan, W. Rammensee, Dissolution rates and activation energy for dissolution of brucite (001) : A new method based on the microtopography of crystal surfaces*, Geochim. Cosmochim. Ac.* **1996**, *60*, 5055-5062.

[72] R. A. Berner, Rate Control Of Mineral Dissolution Under Earth Surface Conditions*, Am. J. Sci.* **1978**, *278*, 1235-1252.

[73] N. Wiberg*, et al.*, *Lehrbuch der Anorganischen Chemie [E-Book],* 102nd compl. rev. ed., De Gruyter, Berlin.

[74] F. T. Shadid, D. Handley, Nitrous acid formation and decomposition during the absorption of nitrogen oxides*, Chem. Eng. J.* **1990**, *43*, 75-88.

[75] T. G. O. Berg, Über die Lösung von Kupfer in Salpetersäure. II*, Z. anorg. allg. Chem.* **1951**, *266*, 118-129.

[76] T. G. O. Berg, Über die Lösung von Kupfer in Salpetersäure. III*, Z. anorg. allg. Chem.* **1951**, *266*, 130-139.

[77] T. G. O. Berg, Le Mechanisme de Dissolution des Metaux dans l'Acide Nitrique*, J. Chim. Phys. PCB* **1954**, *31*, 169-181.

[78] T. G. Owe Berg, Über die Dissoziation der Salpetersäure. I. Die Lösungsgeschwindigkeit des Kupfers in Salpetersäure*, Z. anorg. allg. Chem.* **1951**, *265*, 332-337.

[79] F. M. Elcheikh*, et al.*, The role of intermediates in the kinetics of copper dissolution in nitric-acid*, Annali di chimica* **1983**, *73*, 75-89.

[80] C. Delwaulle*, et al.*, Development of a new method for investigating the mechanisms of solid particle dissolution in nitric acid media: Millifluidic study using fluorescent indicators*, Chem. Eng. J.* **2011**, *174*, 383-389.

[81] T. P. Kravtchenko*, et al.*, A novel method for determining the dissolution kinetics of hydrocolloid powders*, Food Hydrocolloids* **1999**, *13*, 219-225.

[82] S. A. Khalil, M. A. Elmanguch, The kinetics of zinc dissolution in nitric acid*, Monathefte für Chemie* **1987**, *118*, 453-462.

[83] S. M. A. E. Haleem, E. E. A. E. Aal, Thermometric behavior of cobalt in HNO_3 solutions*, J. Mater. Process. Tech.* **2008**, *204*, 139-146.

[84] E. Pietsch, H. Gehlen, *Magnesium Teil B. Die Verbindungen des Magnesiums. System-Nummer 27. ,* Gmelins-Handbuch der anorganischen Chemie, Verlag Chemie, Berlin, **1939**.

[85] Yang Xiao*, et al.*, Novel Mg-Zr-A-H (A=Li, Na) hydrides synthesized by a high pressure technique and their hydrogen storage properties*, J. Alloy. Compd.* **2011**, *509*, p1211-p1246.

[86] G. Brauer, M. Baudler, *Handbuch der präparativen anorganischen Chemie. 3., umgearb. Aufl,* Handbuch der präparativen anorganischen Chemie Enke, Stuttgart, **1978**.

[87] E. A. C. Neeft*, et al.*, The EFTTRA-T3 irradiation experiment on inert matrix fuels*, J. Nucl. Mater.* **2003**, *320*, 106-116.

[88] P. Pöml*, et al.*, Inert Matrix Fuel*,* in *Comprehensive Nuclear Materials* (Ed.: R. J. M. Konings), Elsevier, Oxford, **2012**, 237-256.

[89] R.L. Segall*, et al.*, Ionic oxides: distinction between mechanisms and surface roughening effects in the dissolution of magnesium oxide*, J. Chem. Soc. Farad. T 1* **1978**, *1*.

[90] D. A. Vermilyea, The Dissolution of MgO and $Mg(OH)_2$ in Aqueous Solutions*, J. Electrochem. Soc.* **1969**, *116*, 1179-1183.

[91] A. Fedoročková, P. Raschman, Effects of pH and acid anions on the dissolution kinetics of MgO*, Chem. Eng. J.* **2008**, *143*, 265-272.

[92] R. A. Wogelius*, et al.*, Periclase surface hydroxylation during dissolution*, Geochim. Cosmochim. Ac.* **1995**, *59*, 1875-1881.

[93] M. F. Suárez, R. G. Compton, Dissolution of Magnesium Oxide in Aqueous Acid: An Atomic Force Microscopy Study*, J. Phys. Chem. B* **1998**, *102*, 7156-7162.

[94] A. Fedorockova, P. Raschman, Effects of pH and acid anions on the dissolution kinetics of MgO*, Chem. Eng. J.* **2008**, *143*, 265-272.

[95] C. Agte, J. Vacek, *Wolfram und Molybdän*, Akademie Verlag, Berlin, **1959**.

[96] É. Esbelin, *Étude de la complexation et de la précioitation du molybdène(VI) par le zirconium(IV) en milieu très acide. Application à la dissolution du combustible nucléaire irradié*, **1999**.

[97] S. Y. F. Chu*, et al. The Lund/LBNL Nuclear Data Search Version 2.0*. **1999**; Available from: http://nucleardata.nuclear.lu.se/nucleardata/toi/.

[98] W. W. Schulz, *Reprocessing Uranium-Molybdenum Alloy Fuels -- Dissolution in Concentrated Nitric Acid*, Hanford Atomic Products Operation, Richland, **1960**.

[99] W. W. Schulz*, et al.*, Nitric acid dissolution of uranium molybdenum alloy reactor fuels*, Ind. Eng. Chem. Proc. Des. Dev.* **1962**, *1*, 156-160.

[100] K. H. Tytko, *Mo: Molybdenum. System number 53. Molybdenum oxide hydrates, oxomolybdenum species in aqueous solutions,* Gmelin handbook of inorganic chemistry Springer, Berlin, **1989**.

[101] E. Best, *Mo: molybdenum. System Nummer 53. Metal, chemical reactions,* Gmelin-Handbuch der anorganischen Chemie, Springer, Berlin, **1983**.

[102] I. I. Suponitskaya, I. N. Putilova, Influence of Thiourea on the Kinetics of Molybdenum Dissolution in Nitric Acid*, Russ. J. of Appl. Chem.* **1972**, *45*, 741-745.

[103] I. N. Putilova, I. I. Suponitskaya, Kinetics of the Dissloution of Molybdenum in 2N HNO_3 Containing Urea*, Prot. Met.* **1970**, *6*, 571-572.

[104] A. Clearfield, R. H. Blessing, Preparation and Crystal-Structure of a Basic Zirconium Molybdate and Its Relationship to Ion-Exchange Gels*, J Inorg Nucl Chem* **1972**, *34*, 2643-&.

[105] G. Thomas*, et al.*, Kinetics of dissolution of synthetic digenite and chalcocite in aqueous acidic ferric sulphate solutions*, Can. Metall. Quart.* **1967**, *6*, 281-292.

[106] A. G. Sykes, Molybdenum: The Element and Aqueous Solution Chemistry*, Coordination Chemistry of the s, p, and f metals. In: Comprehensive Coordination Chemistry* **1987**, *3*, 1229.

[107] L. Gmelin, G. Czack, *Mo: molybdenum. system number 53. Physical properties Electrochemistry: XVII,* Gmelin handbook of inorganic chemistry; Mo Suppl. A2B, Springer, Berlin, **1988**.

[108] K. H. Tytko, H. Katscher, *Mo: molybdenum. system number 53. Oxomolybdenum species in aqueous solutions (continued), oxomolybdenum species in nonaqueous solvents, oxomolybdenum species in melts, peroxomolybdenum species,* Gmelin handbook of inorganic chemistry Suppl. B3B, Springer, Berlin, **1989**.

[109] E. I. Stiefel, Molybdenum(VI)*,* in *Comprehensive Coordination Chemistry, Vol. 3*, **1987**, 1375-1420.

[110] T. Fujii*, et al.*, Extraction of molybdenum from nitric acid by octyl(phenyl)-N,N-diisobutylcarbamoylmethylphosphine oxide*, Solvent Extr. Ion Exc.* **2001**, *19*, 127-141.

[111] P. Tkac, A. Paulenova, Speciation of molybdenum(VI) in aqueous and organic phases of selected extraction systems*, Separ. Sci. Technol.* **2008**, *43*, 2641-2657.

[112] I. A. Demet'ev*, et al.*, Mononuclear, Polynuclear, and Cluster Complexes of Molybdenum and Their Reactions as Models of Biochemical Systems and Processes*, Russ. J. General Chemistry* **2007**, *77*, 822-843.

[113] E. I. Stiefel, The Coordination and Bioinorganic Chemistry of Molybdenum*, Prog. Inorg. Chem.* **1977**, *22*, 1-223.

[114] G. P. Haight, D. R. Boston, Molybdenum Species in Aqueous Solution - A Brief Summary*, J. Less-Common Met.* **1974**, *36*, 95-102.

[115] C. Knobler*, et al.*, Molybdenum(VI) Complexes from Diols and Aminoalcohols: the Occurrence of MoO_2, Mo_2O_3, and Mo_2O_5 Core Structures*, J. Chem. Soc.* **1980**, *2*, 248-252.

[116] J. J. Cruywagen, J. B. B. Heyns, Spectrophotometric determination of the thermodynamic parameters for the first two protonation reactions of molybdate: An advanced undergraduate laboratory experiment*, J. Chem. Educ.* **1989**, *66*, 861.

[117] H. K. Fun*, et al.*, Tetrakis(triethylammonium) octamolybdate(VI) dihydrate*, Acta Crystallogr. C* **1996**, *52*, 506-509.

[118] M. T. Pope, A. Müller, Polyoxometalate Chemistry: An Old Field with New Dimensions in Several Disciplines*, Angew. Chem. Int. Edit.* **1991**, *30*, 34-48.

[119] M. T. Pope, *Introduction to polyoxometalate chemistry,* Polyoxometalated Molecular Science, **2003**.

[120] M. T. Pope, 4.10 - Polyoxo Anions: Synthesis and Structure*,* in *Comprehensive Coordination Chemistry II* (Ed.: J. A. M. J. Meyer), Pergamon, Oxford, **2003**, 635-678.

[121] L. Krumenacker, Study of Highly Acidic Sodium Molybdate Solutions by Ultravoilet Absorption Spectroscopy .3. Influence of Acidity on Absorption Spectrum of Dimeric Form Predominant in Concentrated Molybdate Solutions*, B. Soc. Chim. Fr.* **1971**, 362-365.

[122] L. Krumenacker, Study of Highly Acidic Sodium Molybdate Solutions by Voltamperometric Polarography*, B. Soc. Chim. Fr.* **1971**, 368-371.

[123] L. Krumenacker, Very Acidic Sodium Molybdate Solutions by Ultraviolet Spectrophotometry .4. New Interpretation of Measurements - Very Dilute Solutions*, B. Soc. Chim. Fr.* **1971**, 2820-2823.

[124] L. Krumenacker, Acidic sodium molybdate solutions 5 - Solubility of MoO_3*$2H_2O$ at 25°C in solutions - 3M $(H^+,Na^+)ClO_4^-$*, B. Soc. Chim. Fr.* **1971**, 2824-2828.

[125] L. Krumenacker, Study of Highly Acidic Sodium Molybdate Solutions*, Annales De Chimie France* **1972**, *7*, 425-434.

[126] L. Krumenacker, J. Bye, Ultraviolet Spectrophotometric Study of Sodium Molybdate Solutions of High Acidity .I. Experimental First Interpretation*, B. Soc. Chim. Fr.* **1968**, 3099-3103.

[127] L. Krumenacker, J. Bye, Ultraviolet Spectrophotometric Study of Sodium Molybdate Solutions of High Acidity .2. More Elaborate Interpretation of Experimental Data*, B. Soc. Chim. Fr.* **1968**, 3103-3107.

[128] L. Krumenacker, C. Heitz, Study of Autodiffusion in Highly Acidic Molybdate Solutions*, B. Soc. Chim. Fr.* **1971**, 365-368.

[129] F. Chauveau*, et al.*, Etudes des Composes Permolybdiques*, B. Soc. Chim. Fr.* **1955**, 1519-1524.

[130] J. J. Cruywagen*, et al.*, Dimeric Cations of Molybdenum(VI)*, J. Inorg. Nucl. Chem.* **1978**, *40*, 53-59.

[131] J. F. Ojo*, et al.*, Kinetics of the rapid monomer-dimer equilibration of molybdenum(VI) in aqueous perchloric acid solutions*, J. Chem. Soc. Dalton* **1975**, 500-505.

[132] J. M. Coddington, M. J. Taylor, Mo-95 Nuclear Magnetic-Resonance and Vibrational Spectroscopic Studies of Molybdenum(VI) Species in Aqueous-Solutions and Solvent Extracts from Hydrochloric and Hydrobromic Acid - Evidence for the Complexes $Mo_2O_5(H_2O)_6^{2+}$, $MoO_2X_2(H_2O)_2$ (X = Cl or Br), and $MoO_2Cl_4^{2-}$*, J. Chem. Soc. Dalton* **1990**, 41-47.

[133] K. Y. S. Ng, E. Gulari, Spectroscopic and scattering investigation of isopoly-molybdate and tungstate solutions*, Polyhedron* **1984**, *3*, 1001-1011.

[134] P. G. Dickens*, et al.*, Hydrogen insertion compounds of transition metal oxides*, J. Electron. Mater.* **1981**, *10*, 999-1009.

[135] V. B. Goncharov, E. F. Fialko, Structure and Reactivity of Gas-Phase Molybdenum Oxide Cluster Ions*, J. Struc. Chem.* **2002**, *43*, 777-782.

[136] C. J. Cassady*, et al.*, Production and fragmentation of molybdenum oxide ions*, J. Chem. Phys.* **1992**, *96*, 691-699.

[137] V. G. Pitsyuga*, et al.*, Nature of water in hydrated molybdenum and tungsten oxides*, Russ. J. Inorg. Chem.* **1980**, *25*, 496-498.

[138] J. B. B. Heyns*, et al.*, Yellow Molybdenum(VI) Oxide Dihydrate*,* in *Inorg. Syn.*, John Wiley & Sons, Inc., **2007**, 191-192.

[139] L. M. Ferris, Solubility of Molybdic Oxide and Its Hydrates in Nitric Acid, Nitric Acid-Ferric Nitrate, and Nitric Acid-Uranyl Nitrate Solutions*, J. Chem. Eng. Data* **1961**, *6*, 600-603.

[140] M. L. Freedman, Precipitation of Molybdenum (VI) in Strongly Acid Solutions*, J. Chem. Eng. Data* **1963**, *8*, 113-116.

[141] K. Y. Shapiro, I. V. Volk-Karachevskaya, Solubility of molybdic acid in hydrochloric, sulfuric, and nitric acids*, Russ. J. Inorg. Chem.* **1969**, *14*, 571-573.

[142] S. P. Vorob'ev, I. P. Davydov, Solubility of molybdenum trioxyde in nitric acid*, Russ. J. Inorg. Chem.* **1966**, *11*, 1087-1089.

[143] M. Schmid, *Untersuchungen an primären und sekundären Löserückständen hochabgebrannter Kernbrennstoffe*, Technischen Universität München (München), **1986**.

[144] P. Cannon, The Solubility of Molybdenum Trioxide in Various Mineral Acids*, J. Inorg. Nucl. Chem.* **1959**, *11*, 124-127.

[145] G. A. Meerson, V. G. Mikhailova, Solubility of tungstic and molybdic acids in nitric acid*, Russ. J. Inorg. Chem.* **1967**, *12*, 849-851.

[146] A. Vizsolyi, E. Peters, Nitric Acid Leaching of Molybdenite Concentrates*, Hydrometallurgy* **1980**, *6*, 103-119.

[147] R. L. Fellows*, et al.*, X-Ray-DIffraction and Thermal Anlysis of Molybdenum(VI) Oxide Hemihydrate - Monoclinic $MoO_3*^1/_2$ H_2O*, Inorg. Chem.* **1983**, *22*, 2468-2470.

[148] J. Li*, et al.*, Recovery of Mo from Ni–Mo ore leach solution with carrier co-precipitation method*, Int. J. Refract. Met. H.* **2012**, *30*, 180-184.

[149] K.-H. Park*, et al.*, Recovery of molybdenum from spent catalyst leach solutions by solvent extraction with LIX 84-I*, Sep. Purif. Technol.* **2010**, *74*, 294-299.

[150] J. A. M. van den Berg*, et al.*, Comprehensive processing of low grade sulphidic molybdenum ores*, Minerals Engineering* **2002**, *15*, 879-883.

[151] B. B. Kar*, et al.*, Spent catalyst: secondary source for molybdenum recovery*, Hydrometallurgy* **2004**, *72*, 87-92.

[152] F. Pagnanelli*, et al.*, Adsorption onto activated carbon for molybdenum recovery from leach liquors of exhausted hydrotreating catalysts*, Hydrometallurgy* **2011**, *110*, 67-72.

[153] O. N. Kononova*, et al.*, Ion exchange recovery of molybdenum from nitric acidic solutions using macroporous anion exchangers with long-chained cross-linking agents*, Hydrometallurgy* **2003**, *68*, 83-87.

[154] S. V. Kotov*, et al.*, Some molybdenum-containing chelating ion-exchange resins (polyampholites) as catalysts for the epoxidation of alkenes by organic hydroperoxides*, J. Mol. Catal. A-Chem.* **2000**, *154*, 121-129.

[155] Z. Zhao*, et al.*, Recovery and purification of molybdenum from Ni-Mo ore by direct air oxidation in alkaline solution*, Hydrometallurgy* **2010**, *103*, 68-73.

[156] J. Wu*, et al.*, Selective extraction of Mo using Cyanex-272 and tributyl phosphate from low grade Ni-Mo ore leach liquor*, Sep. Purif. Technol.* **2012**, *99*, 120-126.

[157] N. D. Goletskii*, et al.*, Extraction of Molybdenum from Supersaturated Solutions in Nitric Acid with Tributyl Phosphate Solutions*, Radiochemistry* **2010**, *52*, 180-188.

[158] F. Benesovsky, E. Lell, *Molybdän. System Nummer 53. Metall, Technologie* Gmelin-Handbuch der anorganischen Chemie, Springer, Berlin, **1977**.

[159] A. Bremer*, et al.*, Extraction of molybdenum from CERMET target dissolution solutions using CYANEX® 600*,* in proceedings of *GLOBAL 2015*, Paris, France, **2015**.

[160] C. J. Maher, *Options for Treatment of Legacy and Advanced Nuclear Fuels*, PhD thesis, **2014**.

[161] C. Guéneau*, et al.*, Thermodynamic and Thermophysical Properties of the Actinide Oxides Comprehensive Nuclear Materials*,* in *Comprehensive Nuclear Materials* (Ed.: R. J. M. Konings), **2012**, 21-59.

[162] W. Runde, W. Schulz, Americium*,* in *The Chemistry of the Actinide and Transactinide Elements* (Eds.: L. Morss, N. Edelstein, J. Fuger), Springer Netherlands, **2006**, 1265-1395.

[163] N. N. Greenwood, A. Earnshaw, *Chemistry of the elements*, Pergamon Pr., Oxford, **1986**.

[164] L. R. Morss*, et al.*, *The Chemistry of the Actinide and Transactinide Elements edited by Lester R. Morss, Norman M. Edelstein, Jean Fuger [E-Book]*, Springer Science+Business Media B.V., Dordrecht, **2011**.

[165] *Institut für Arbeitsschutz der Deutschen Gesetzlichen Unfallversicherung, GESTIS-Stoffdatenbank*. **2013**; Available from: http://www.dguv.de/ifa/ Gefahrstoffdatenbanken/ GESTIS-Stoffdatenbank/index.jsp.

[166] *UNI TERRA - Kindler & Gliech GbR Germany, Berlin*. **2013**; Available from: http://www.uniterra.de/rutherford/tab_ior.htm.

[167] H. C. Yang*, et al.*, Behavior of radioactive metal surrogates under various waste combustion conditions*, Journal of the Korean Nuclear Society* **2002**, *34*, 80-89.

[168] H. S. Kim*, et al.*, Applicability of CeO2 as a surrogate for PuO2 in a MOX fuel development*, J. Nucl. Mater.* **2008**, *378*, 98-104.

[169] A. K. Tyagi*, et al.*, Simulation of lattice thermal expansion behaviour of $Th_{1-x}Pu_xO_2$ (0.0≤x≤1.0) using CeO_2 as a surrogate material for PuO_2*, J. Alloy. Compd.* **2002**, *337*, 277-281.

[170] J. L. Ryan*, et al.*, *Catalyzed Electrolytic Plutonium Oxide Dissolution (CEPOD): The past seventeen years and future potential*, American Chemical Society, United States, **1990**.

[171] A. L. Uriarte, R. H. Rainey, *Dissolution of high-density UO_2, PuO_2, and UO_2-PuO_2 pellets in inorganic acids*, Oak Ridge National Laboratory, Oak Ridge, Tenn, **1965**.

[172] X. Machuron-Mandard, C. Madic, Plutonium dioxide particle properties as a function of calcination temperature*, J. Alloy. Compd.* **1996**, *235*, 216-224.

[173] A. Inoue, Enhanced Dissolution of PuO_2 in Nitric Acid using Uranium(IV)*, Journal of the Chemical Society, Faraday Transactions 1* **1988**, *84*, 1195-1197.

[174] S. G. Thompson*, et al.*, The New Element Berkelium (Atomic Number 97)*, Physical Review* **1950**, *80*, 781-789.

[175] K. E. Sickafus*, et al.*, Radiation Tolerance of Complex Oxides*, science* **2000**, *289*, 748-751.

[176] N. N. Greenwood, A. Earnshaw, *Chemistry of the elements. %7 Repr. with corr*, Pergamon Pr., Oxford, **1986**.

[177] Gmelin, Seltenerdelemente TeilC1 Sc, Y, La und Lanthanide, Verbindungen*,* in *Handbuch der Anorganischen Chemie, Vol. 8*, Springer Verlag Berlin, Berlin, **1974**, 261.

[178] M. Dole*, et al.*, Molecular Beams of Macroions*, J. Chem. Phys.* **1968**, *49*, 2240-2249.

[179] M. Yamashita, J. B. Fenn, Electrospray ion-source - Another variation on the free-jet theme*, Journal of Physical Chemistry* **1984**, *88*, 4451-4459.

[180] J. S. Becker, *Inorganic mass spectrometry: Principles and applications*, Wiley, New York, NY, **2007**.

[181] E. d. Visser-Týnová, *ASGARD Partner Interim Report No. 4*, NRG, **2013**.

[182] W. E. C. Creyke*, et al.*, *Design with non-ductile materials*, Applied Science Publishers London and New York, **1982**.

[183] R. J. Brook, *Concise Encyclopedia Of Advanced Ceramic Materials*, Pergamon Press, **1991**.

[184] D. Munz, T. Fett, *Ceramics Mechanical Properties, Failure Behaviour, Materials Selection*, Springer, Berlin, **1999**.

[185] A. Bukaemskiy, Physical properties of ceramic in the CeO_2-8YSZ and Nd_2O_3-8YSZ systems*,* in *CALPHAD XXXVIII, Prague*, **2009**.

[186] E. A. C. Neeft*, et al.*, Mechanical behaviour of macro-dispersed inert matrix fuels*, J. Nucl. Mater.* **2003**, *317*, 217-225.

[187] C. Jinju, Indentation-based methods to assess fracture toughness for thin coatings*, J. Phys. D* **2012**, *45*.

[188] D. W. Richerson, *Modern Ceramic Engineering: Properties, Processing And Use In Design*, Marcel Dekker, INC. New York and Basel, **1992**.

[189] P. Chhillar*, et al.*, Sintering of molybdenum metal powder using microwave energy*, Powder Metall.* **2008**, *51*, 182-187.

[190] T. Bergmann*, et al.*, High-Resolution Time-of-Flight Mass-Spectrometers .2. Cross Beam Ion Optics*, Rev. Sci. Instrum.* **1990**, *61*, 2585-2591.

[191] T. Bergmann*, et al.*, High-Resolution Time-of-Flight Mass-Spectrometer*, Rev. Sci. Instrum.* **1989**, *60*, 792-793.

[192] T. Bergmann*, et al.*, High-Resolution Time-of-Flight Mass-Spectrometers .1. Effects of Field Distortions in the vicinity of Wire Meshes*, Rev. Sci. Instrum.* **1989**, *60*, 347-349.

[193] T. Bergmann*, et al.*, High-Resolution Time-of-Flight Mass-Spectrometers .2. Reflector Design*, Rev. Sci. Instrum.* **1990**, *61*, 2592-2600.

[194] C. Walther*, et al.*, Investigation of polynuclear Zr(IV) hydroxide complexes by nanoelectrospray mass-spectrometry combined with XAFS*, Anal Bioanal Chem* **2007**, *388*, 409-431.

[195] W. F. M. G. Zevert*, et al.*, Powder preparation and compaction behavior of fine-grained Y-TZP*, J. Mater. Sci.* **1990**, *25*, 3449-3455.

[196] K. Kawakita, K. H. Ludde, Some considerations on powder compression equations*, Powder Technol.* **1971**, *4*, 61-68.

[197] W.M.Haynes, *Handbook of Chemistry and Physics*, **2013-2014**.

[198] C. A. Brookes, B. Moxley, A pentagonal indenter for hardness measurements*, J. Phys. E: Sci. Instrum.* **1975**, *8*, 456.

[199] D. W. Stollberg*, et al.*, Nanoindentation measurements of combustion CVD Al_2O_3 and YSZ films*, Mater. Sci. Eng. A* **2003**, *359*, 112-118.

[200] Robert L. Segall*, et al.*, Ionic oxides: distinction between mechanisms and surface roughening effects in the dissolution of magnesium oxide*, J. Chem. Soc. Farad. T 1* **1978**, *1*.

[201] A. C. Lasaga, Fundamental approaches in describing mineral dissolution and precipitation rates*, Chemical Weathering Rates of Silicate Minerals* **1995**, *31*, 23-86.

[202] R. A. Berner, Rate Control Of Mineral Dissolution Under Earth Surface Conditions*, Am. J. Sci.* **1978**, *278*, 1235-1252.

[203] G. Jordan, W. Rammensee, Dissolution rates and activation energy for dissolution of brucite (001): A new method based on the microtopography of crystal surfaces*, Geochim. Cosmochim. Ac.* **1996**, *60*, 5055-5062.

[204] J. Guspiel, W. Riesenkampf, Kinetics of dissolution of ZnO, MgO and their solid solutions in aqueous sulfuric acid solutions*, Hydrometallurgy* **1993**, *34*, 203-220.

[205] C. F. Jones*, et al.*, Initial dissolution kinetics of ionic oxides*, Proc. R. Soc. London, Ser. A* **1981**, *374*, 141-153, 142 plates.

[206] C. F. Jones*, et al.*, The effect of irradiation on the dissolution rate of magnesium oxide*, Radiat. Eff.* **1982**, *60*, 167-171.

[207] D. Staicu*, et al.*, Fast neutron irradiation impact on thermophysical properties of inert materials intended as support matrix for transmutation targets bearing minor actinides, in proceedings of *GLOBAL 2009*, Paris, France, **2009**, 2016-2022.

[208] S. Finkeldei*, et al.*, Dissolution of ZrO_2 based pyrochlores in the acid pH range: A macroscopic and electron microscopy study*, Appl. Geochem.* **2014**, *49*, 31-41.

[209] H. Salmang, H. Scholze, *Die physikalischen und chemischen Grundlagen der Keramik*, Springer Berlin Heidelberg, **2007**.

[210] A. J. Barker, A. J. Barker, *Introduction to Metamorphic Textures and Microstructures*, S. Thornes, **1998**.

[211] L. Priester, *Grain boundaries : from theory to engineering,* Springer series in materials science, Springer, Dordrecht, **2013**.

[212] H. Onishi*, et al.*, Adsorption of sodium atoms and oxygen-containing molecules on magnesia(100) and (111) surfaces*, Surf. Sci.* **1987**, *191*, 479-491.

[213] N. H. de Leeuw*, et al.*, Atomistic Simulation of the Effect of Dissociative Adsorption of Water on the Surface Structure and Stability of Calcium and Magnesium Oxide*, J. Phys. Chem.* **1995**, *99*, 17219-17225.

[214] B. Eiliazadeh*, et al.*, Effects of punch geometry on powder movement during pharmaceutical tabletting processes*, Int. J. Solids Struct.* **2004**, *41*, 5967-5977.

[215] N. Dacheux*, et al.*, Reactive sintering of the thorium phosphate-diphosphate. Study of physical, thermal, and thermomechanical properties and chemical durability during leaching tests*, Chem. Mater.* **2002**, *14*, 2953-2961.

[216] D. Horlait*, et al.*, Environmental SEM monitoring of $Ce_{1-x}Ln_xO_{2-x/2}$ mixed-oxide microstructural evolution during dissolution*, J. Mater. Chem.* **2014**, *2*, 5193-5203.

[217] M. J. Carrott*, et al.*, The Chemistry of (U,Pu)O2 Dissolution in Nitric Acid*, Procedia Chemistry* **2012**, *7*, 92-97.

[218] T. Fukasawa, Y. Ozawa, Relationship between dissolutionrate of uranium dioxide pellets in nitric acid solutions and their porosity, *Journal of Nuclear Chemistry* **1986**, *106*, 345-356.

[219] I. M. Kolthoff, *et al.*, The Volumetric Determination of Nitrates with Ferrous Sulfate as Reducing Agent, *Journal of the American Chemical Society* **1933**, *55*, 1454-1457.

[220] I. R. Epstein, *et al.*, A kinetics study of the oxidation of iron(II) by nitric acid, *Journal of the American Chemical Society* **1980**, *102*, 3751-3758.

[221] G. A. Chappelle, *et al.*, Kinetic investigation of the cerium(IV) oxidation of the bis(µ-oxo)bis(oxo-molybdenum(V)) ion, *Inorg. Chem.* **1984**, *23*, 2768-2771.

[222] Y. Ikeda, *et al.*, Kinetic-study on Dissolution of UO_2 Powders in Nitric Acid, *J. Nucl. Mater.* **1995**, *224*, 266-272.

[223] R. F. Taylor, *et al.*, Dissolution Rates of Uranium Dioxide Sintered Pellets in Nitric Acid Systems, *Journal of Applied Chemistry* **1963**, *13*, 32-40.

[224] M. Shabbir, R. G. Robins, Kinetics of the dissolution of uranium dioxide in nitric acid. II, *Journal of Applied Chemistry* **1969**, *19*, 52-56.

[225] Y. M. Kulyako, *et al.*, New approaches to reprocessing of oxide nuclear fuel, *Radiochemistry* **2010**, *52*, 344-349.

[226] M. S. Farrell, S. R. Isaacs, *Laboratory developement of the grind leach process for the HTGCR Fuel Cycle, Part 1: Dissolution of urania-thoria fuel particles in nitric acid solutions*, Australian Atomic Energy Commission Research Establishment Lucas Heights, Sydney, **1965**.

[227] R. E. Blanco, *et al.*, Chemical Processing of Irradiated Fuels, in proceedings of *AEC Symposium*, Richland, Washington, **1959**.

[228] J. L. Ryan, L. A. Bray, Dissolution of Plutonium Doxide a Critical-Review, *Abstr. Pap. Am. Chem. S.* **1979**, 14-14.

[229] V. V. Romanovski, *et al.*, Potential agents for removal of actinides from waste solutions, in proceedings, *Vol. 3*, **1996**, 2330-2334.

[230] K. N. Raymond, *et al.*, Specific sequestering agents for the actinides, *ACS Symp. Ser.* **1980**, *131*, 143-172.

[231] M. Cheng, *et al.*, On the dissolution behavior of new Mo fuel matrices for Generation IV Ractors, in *GDCh Wissenschaftsforum 2013*, Darmstadt, **2013**.

[232] S. Himeno, M. Hasegawa, Raman spectroscopic evidence of dimeric molybdenum(VI) species in acidic solutions, *Inorg. Chim. Acta* **1984**, *83*, L5-L6.

[233] J. J. Cruywagen, J. B. B. Heyns, Molybdenum(VI) equilibria at high perchloric acid concentration, *Polyhedron* **2000**, *19*, 907-911.

[234] J. J. Cruywagen, Protonation, oligomerization, and condensation reactions of vanadate(V), molybdate(VI), and tungstate(VI), *Adv. Inorg. Chem.* **2000**, *49*, 127-182.

[235] E. Rohwer, *et al.*, Spectrophotometric Study of Dimerization of of Molybdenum(VI) in Perchloric-Acid Medium, *Journal of the South African Chemical Institute* **1972**, *25*, 338-348.

[236] A. Saito, G. R. Choppin, Complexation of uranyl(VI) with polyoxometalates in aqueous solutions, *J. Alloy. Compd.* **1998**, *271–273*, 751-755.

[237] H. Suzuki, *et al.*, Extraction and separation of Am(III) and Sr(II) by N,N,N',N'-tetraoctyl-3-oxapentanediamide (TODGA), *Radiochim. Acta* **2004**, *92*, 463-466.

[238] S. A. Ansari, *et al.*, N,N,N ',N '-Tetraoctyl diglycolamide (TODGA): a promising extractant for actinide-partitioning from high-level waste (HLW), *Solvent Extr. Ion Exch.* **2005**, *23*, 463-479.

[239] C. Cuillerdier, *et al.*, Malonamides as New Extractants for Nuclear Waste Solutions, *Separ. Sci. Technol.* **1991**, *26*, 1229-1244.

[240] C. Cuillerdier, *et al.*, Diamides as Actinide Extractants for Various Waste Treatments, *Separ. Sci. Technol.* **1993**, *28*, 155-175.

[241] Y. N. Wu, *et al.*, Solid state reaction of MoO_3-CeO_2 complex oxide studied by Raman spectroscopy, *Solid State Sciences* **2011**, *13*, 2096-2099.

[242] J. C. J. Bart, N. Giordano, Phase relationships in the cerium-molybdenum oxide system, *J. Less-Common Met.* **1976**, *46*, 17-24.

[243] O. A. Ustinov*, et al.*, Molybdenum trioxide-cerium dioxide system*, Zh. Neorg. Khim.* **1970**, *15*, 2549-2551.

[244] P. Gougeon*, et al.*, Structural trends and the electronic structure of the rare-earth oxomolybdates RMo5O8 (R = La, Ce, Pr, Nd, Sm, Eu and Gd) containing chains of bioctahedral Mo10 clusters*, Acta Crystallogr., Sect. B: Struct. Sci.* **2003**, *B59*, 472-478.

[245] A. D. Prokoshin*, et al.*, Molybdenum trioxide-plutonium dioxide system*, Zh. Neorg. Khim.* **1976**, *21*, 1565-1568.

7 Acknowledgements

Besonderer Dank gilt Herrn Prof. Dr. Dirk Bosbach, der mir als Doktorvater diese Arbeit am Institut für Nukleare Entsorgung und Reaktorsicherheit (IEK-6) ermöglicht hat. Vielen Dank für die Betreuung und für die Unterstützung während meiner Doktorarbeit. Ebenso danke ich Herrn Prof. Dr. Rainer Telle, der sich bereit erklärt hat Zweitgutachter dieser Arbeit zu sein.

Bei Herrn PD Dr. Giuseppe Modolo bedanke ich mich herzlich für die hervorragende Betreuung und die stete Hilfsbereitschaft bei wissenschaftlichen und experimentellen Fragestellungen, sowie die TG/DSC-Messungen. Vielen Dank für dein Verständnis und dein Vertrauen in einer schweren Zeit.

Financial support for this research was provided by the European Atomic Energy Community‘s 7th Framework Program (FP7 2007-2011), project ASGARD – grant agreement No. 295825. I would like to thank all members of the consortium for the fruitful discussions. Special thanks to Dr. Chris J. Maher for proofreading of this thesis.

Weiterhin möchte ich mich bei Herrn Dr. Andrey Bukaemskiy für die viele Zeit, die wir gemeinsam im Labor verbracht haben bedanken, sowie für die vielen Diskussionen, Anregungen und ausgezeichneten Ideen, die zum Gelingen dieser Arbeit beigetragen haben.

Bei Herrn Fabian Sadowski bedanke ich mich für die unzähligen ICP-MS Messungen und seine Hilfsbereitschaft in allen Belangen des Labors.

Bei Herrn Prof. Dr. Clemens Walther, Herrn Dr. Michael Steppert, Frau Meijie Cheng, Herrn Andreas Hartmann und Herrn Sebastian Büchner bedanke ich mich für die gute Zusammenarbeit bei der Mo-Speziation mit dem ALBATROS ESI-ToF-MS.

Herrn Dr. Andreas Geist, Frau Claudia Stauch und Frau Manuela Casutt danke ich für ihre Unterstützung bei den Auflösungsversuchen an PuO_2-haltigen Pellets.

Ich danke Herrn Tobias Wegener, Herr Rainer Engelmann und Herrn Markus Gerdes und meiner ehemaligen Masterandin Elena Lichte. Eure fleißigen Hände haben zum Gelingen dieser Arbeit beigetragen.

Herrn Dr. Stephan Küppers, Herrn Dr. Volker Nischwitz und Frau Dr. Beatrix Santiago-Schüble danke ich für die Entwicklung des Messprotokolls für eine kommerzielle ESI-MS und die entsprechenden Messungen.

Herrn Dr. Stefan Neumeier, Herrn Dr. Felix Brandt, Frau Dr. Sarah Finkeldei, Herrn Dr. Andreas Wilden und allen weiteren Mitarbeitern der AG Modolo möchte ich für die konstruktive Diskussion meiner Arbeit und die hilfreichen Anregungen danken.

Bei Herrn PD Dr. Hartmut Schlenz und seiner Arbeitsgruppe bedanke ich mich für die Röntgendiffraktometrie- und die Ramanmessungen.

Frau Dr. Martina Klinkenberg und Herrn Murat Güngör danke ich für die Elektronenmikroskopieaufnahmen und EDX-Messungen.

Für die Hilfsbereitschaft in allen Angelegenheiten des Strahlenschutzes danke ich Herrn R. König und Herrn C. Schreinemachers.

Allen nicht namentlich genannten Mitarbeitern des IEK-6 danke ich für die gute Zusammenarbeit und das angenehme Arbeitsklima. Besonders bedanken möchte ich mich bei Frau Dr. Carole Babelot, Frau Jana Assenmacher, Herrn Peter Kaufholz, Herrn Holger Schmidt und Frau Simone Weigelt. Ich hatte viel Spaß mit euch und ihr seid zu echten Freunden geworden.

Ich danke meinen Freunden vom Studium Universale und aus der Ruhrtalbahn, die mich durch alle Höhen und Tiefen dieser Arbeit begleitet haben. Mein besonderer Dank gilt Herrn Dr. Stephan Lehnen für den zuverlässigen Kaffeeservice. Du hast mir so manchen Start in den Tag erleichtert.

Meiner Familie danke ich für ihre Unterstützung während dieser Arbeit und meines gesamten Studiums. Danke Julian, dass du mich immer unterstütz und motiviert hast. Ich freue mich auf den 13.08. und alles was die Zukunft für uns bereithält.

Publications and Presentations of this Work

Journal Articles

E.L. Ebert, A. Bukaemskiy, F. Sadowski, S. Lange, A. Wilden, G. Modolo, Reprocessability of molybdenum and magnesia based inert matrix fuels, *Nukleonika*, **2015**, *60*, 871-878.

Conference Proceedings

E. L. Ebert, G. Modolo, A. Bukaemskiy, F. Sadowski, D. Bosbach, Dissolution behavior of MgO and Mo-based inert Matrix fuel for the Transmutation of Plutonium and minor actinides, Proceedings of the 13th Information Exchange Meeting on Actinide and Fission Product Partitioning and Transmutation – IEMPT13, Seoul, Korea, 09/23/2014 – 09/26/2014.

E. L. Ebert, A. Bukaemskiy, G. Modolo, Dissolution Behavior of MgO- and Mo-Based Inert Matrix Fuel for the Transmutation of Plutonium and Minor Actinides, Proceedings of Global 2015, Paper 5199, Paris, France, 09/20/2015 – 09/24/2015.

E. De Visser-Týnová, G. Ménard, **E. L. Ebert**, G. Modolo, M. Cheng, C. Walther, K. V. Mareš, J. John, A. Geist, Dissolution Behavior of Inert Matrix Fuels, Proceedings of TopFuel 2015, Zurich, Switzerland, 09/13/2015 – 09/17/2015.

Conference Presentation

S. Neumeier, F. Brandt, A. Bukaemskiy, S. Finkeldei, Y. Arinicheva, J. Heuser, **E. L. Ebert**, C. Schreinemachers, A. Wilden, G. Modolo, D. Bosbach, Ceramic Waste Forms: Present status and perspectives, International Conference and exposition on Advanced Ceramics and Composites, ICACC2014, Daytona Beach, Florida, US, 01/26/2014 – 01/31/2014.

E. L. Ebert, M. Cheng, M. Steppert, C. Walther, G. Modolo, D. Bosbach: Dissolution of Mo-based CerMet fuel: ESI-TOF MS speciation in nitric acid medium, 17th Radiochemical Conference, Marianske Lazne, Czech Republic, 05/11/2014 – 05/16/2014.

S. Neumeier, F. Brandt, A. Bukaemskiy, S. Finkeldei, Y. Arinicheva, J. Heuser, **E. L. Ebert**, C. Schreinemachers, A. Wilden, G. Modolo, D. Bosbach, Ceramic Waste Forms in Innovative Waste Management Strategies: Present Status and Perspectives, MRS Fall Meeting, Boston, USA, 11/30/2014 – 12/05/2014.

E. L. Ebert, G. Modolo, D. Bosbach, M. Cheng, M. Steppert, C. Walther, Dissolution studies on molybdenum-based inert matrix fuels for the transmutation of minor actinides, First SACSESS International Workshop, Warsaw, Poland, 04/22/2015 – 04/24/2015.

M. Steppert, M. Cheng, **E. L. Ebert**, C. Walther, Investigations on the solution behavior of new Mo fuel matrices for generation IV reactors by means of electrospray ionization mass spectrometry, E-MRS Spring Meeting 2015, Lille, France, 05/11/2015 – 05/15/2015.

E. De Visser-Týnová, G. Ménard, **E. L. Ebert**, G. Modolo, M. Cheng, C. Walther, K. V. Mareš, J. John, A. Geist, Dissolution Behavior of Inert Matrix Fuels, TopFuel 2015, Zurich, Switzerland, 09/13/2015 – 09/17/2015.

E. L. Ebert, M. Cheng, M. Steppert, C. Walther, A. Bukaemskiy, G. Modolo, D. Bosbach, Dissolution Behavior of MgO- and Mo-Based Inert Matrix Fuel for the Transmutation of Plutonium and Minor Actinides, Global 2015, Paris, France, 09/20/2015 – 09/24/2015.

Presentation (invited)

M. Steppert, M. Cheng, **E. L. Ebert**, X. Chen, C. Walther, Ionic solution species of molybdenum in strongly acidic media characterized by means of electrospray ionization mass spectrometry, Institutsseminar HZDR IRE, 01/10/2014.

S. Neumeier, F. Brandt, A. Bukaemskiy, S. Finkeldei, J. Heuser, Y. Arinicheva, **E. L. Ebert**, C. Schreinemachers, A. Wilden, G. Modolo, D. Bosbach, Ceramic materials for innovative nuclear waste management strategies, Seminar Institut für Ressourcenökologie, Helmholtz-Zentrum Dresden-Rossendorf, Dresden, Germany, 03/28/2014.

E. L. Ebert, G. Modolo, Dissolution studies on Mo- and MgO-based inert matrix fuels for the transmutation of minor actinides, Seminar Institut für Radioökologie und Strahlenschutz, Leibniz Universität Hannover, Germany, 11/12/2015.

Poster

E. L. Ebert, E. Lichte, M. Cheng, M. Steppert, A. Bukaemskiy, F. Sadowski, S. Neumeier, G. Modolo, D. Bosbach, Auflösungsverhalten von Mo- und MgO-basierten ADS Inertmatrixbrennstoffen, GDCh Wissenschaftsforum Chemie 2013, Darmstadt, Germany, 09/01/2013 – 09/04/2013.

E. L. Ebert, A. Bukaemskiy, S. Neumeier, G. Modolo, D. Bosbach, Dissolution behavior of MgO and Mo based ADS inert matrix fuel, E-MRS Spring Meeting, Strasbourg, France, 05/27/2013 – 05/31/2013.

E. L. Ebert, A. Bukaemskiy, F. Sadowski, F. Brandt, M. Cheng, M. Steppert, C. Walther, G. Modolo, D. Bosbach: Dissolution behavior of MgO and Mo based Inert Matrix Fuel for the transmutation of plutonium and minor actinides, First joint workshop on f-element chemistry, University of Manchester, UK 04/28/2014 – 04/30/2014.

E. L. Ebert, A. Bukaemskiy, F. Sadowski, F. Brandt, G. Modolo, D. Bosbach: Dissolution studies on molybdenum-based inert matrix fuel targets for the transmutation of minor actinides, 17th Radiochemical Conference, Marianske Lazne, Czech Republic, 05/11/2014 – 05/16/2014.

E. L. Ebert, A. Bukaemskiy, F. Sadowski, F. Brandt, G. Modolo, D. Bosbach: Dissolution behavior of MgO based Inert Matrix Fuel for the transmutation of plutonium and minor actinides, 17th Radiochemical Conference, Marianske Lazne, Czech Republic, 05/11/2014 – 05/16/2014. (**Poster Certificate**)

E. L. Ebert, M. Cheng, M. Steppert, C. Walther, G. Modolo, D. Bosbach, Electrospray Ionization Time-of-Flight Mass Spectrometry: Dissolution of Mo-based CerMet fuel, 8th European Summer School on Separation Chemistry and Conditioning as well as Supramolecular, Intermolecular, Interaggregate Interactions, Bonn, Germany, 07/07/2014 – 07/09/2014 (2014)

E. L. Ebert, G. Modolo, A. Bukaemskiy, F. Brandt, D. Bosbach, M. Cheng, M. Steppert, c. Walther, Dissolution behavior of MgO and Mo based inert Matrix fuel for the Transmutation of Plutonium and minor actinides, 13th Information Exchange Meeting on Actinide and Fission Product Partitioning and Transmutation – IEMPT13, IEMPT13, Seoul, Korea, 09/23/2014 – 09/26/2014.

M. Cheng, **E. L. Ebert**, M. Steppert, C. Walther, How does Iron influence the dissolution behavior of Mo based generation IV reactor fuel? New insights using nanoESI-TOF-MS, E-MRS Spring Meeting 2015, Lille, France, 05/11/2015 – 05/15/2015. **(Posterpreis)**

M. Cheng, M. Steppert, **E. L. Ebert**, C. Walther, How does Iron influence the dissolution behavior of Mo based generation IV reactor fuel? New insights using nanoESI-TOF-MS, GDCh Wissenschaftsforum Chemie 2015, Dresden, Germany, 08/30/2015 – 09/02/2015.

Band / Volume 364
Intragruppentrennung Seltener Erden mittels neuer phosphororganischer Liganden
S. Hadić (2017), VIII, 164 pp
ISBN: 978-3-95806-215-3

Band / Volume 365
Automated Magnetic Divertor Design for Optimal Power Exhaust
M. Blommaert (2017), xxiv, 220 pp
ISBN: 978-3-95806-216-0

Band / Volume 366
PEM-Elektrolyse-Systeme zur Anwendung in Power-to-Gas Anlagen
G. Tjarks (2017), IV, 135 pp
ISBN: 978-3-95806-217-7

Band / Volume 367
Fundamental Insights into the Radium Uptake into Barite by Atom Probe Tomography and Electron Microscopy
J. Weber (2017), IX, 160 pp
ISBN: 978-3-95806-220-7

Band / Volume 368
Entwicklung von elektronenleitenden Schutzschichten gegen die anodische Auflösung von Stromsammlern in neuartigen „Dual-Ionen“-Energiespeichern
G. Teucher (2017), VIII, 119 pp
ISBN: 978-3-95806-222-1

Band / Volume 369
Herstellung und Charakterisierung oxiddispersionsverstärkter Haftvermittlerschichten
J. Bergholz (2017), V, 133, II pp
ISBN: 978-3-95806-223-8

Band / Volume 370
Performance of Plasma Facing Materials under Thermal and Plasma Exposure
I. Steudel (2017), XVI, 150 pp
ISBN: 978-3-95806-226-9

Band / Volume 371
The Impact of Transient Thermal Loads on Beryllium as Plasma Facing Material
B. Spilker (2017), XII, 134 pp
ISBN: 978-3-95806-227-6

Band / Volume 372
Analysis and Simulation of Macroscopic Defects in $Cu(In,Ga)Se_2$ Photovoltaic Thin Film Modules
B. Misic (2017), iv, 147 pp
ISBN: 978-3-95806-228-3

Band / Volume 373
Chemical and physical properties of sodium ionic conductors for solid-state batteries
M. Guin (2017), ix, 126 pp
ISBN: 978-3-95806-229-0

Band / Volume 374
Prediction of Oxidation Induced Life Time for FCC Materials at High Temperature Operation
R. Duan (2017), vi, 180 pp
ISBN: 978-3-95806-230-6

Band / Volume 375
Microstructure Evolution of Laves Phase Strengthened Ferritic Steels for High Temperature Applications
J. K. Lopez Barrilao (2017), XVI, 134 pp
ISBN: 978-3-95806-231-3

Band / Volume 376
Drying front formation in topmost soil layers as evaporative restraint
Non-invasive monitoring by magnetic resonance and numerical simulation
S. Merz (2017), xxii, 108 pp
ISBN: 978-3-95806-234-4

Band / Volume 377
Low Temperature Thin-Film Silicon Solar Cells on Flexible Plastic Substrates
K. Wilken (2017), 194 pp
ISBN: 978-3-95806-235-1

Band / Volume 378
Dissolution Behaviour of Innovative Inert Matrix Fuels for Recycling of Minor Actinides
E. L. Mühr-Ebert (2017), xii, 164 pp
ISBN: 978-3-95806-238-2

Weitere ***Schriften des Verlags im Forschungszentrum Jülich*** unter
http://wwwzb1.fz-juelich.de/verlagextern1/index.asp

Energie & Umwelt /
Energy & Environment
Band / Volume 378
ISBN 978-3-95806-238-2